Théorie de l'électrofiltration: nouveaux développements, validation expérimentale et applications à l'hydrogéologie et au volcanisme.

Agnès Crespy

UNIVERSITE PAUL CEZANNE
FACULTE DE DROIT, D'ECONOMIE ET DES SCIENCES D'AIX MARSEILLE III

N° attribué par la bibliothèque:

THEORIE DE L'ELECTROFILTRATION : NOUVEAUX DEVELOPPEMENTS, VALIDATION EXPERIMENTALE, APPLICATIONS A L'HYDROGEOLOGIE ET AU VOLCANISME

Pour le grade de:

DOCTEUR DE L'UNIVERSITE DE DROIT D'ECONOMIE ET DES SCIENCES D'AIX MARSEILLE III

Discipline: GEOSCIENCES DE L'ENVIRONNEMENT

Présentée et soutenue publiquement par :

AGNES CRESPY

le **26 novembre 2008**, dans l'amphithéâtre du CEREGE (Aix en Provence)

Directeur de Thèse:
André REVIL

Jury

Laurence Jouniaux	CR, Institut de Physique du Globe de Strasbourg	Rapporteur
Alain Tabbagh	Pr., Sisyphe, Université Paris VI	Rapporteur
Claude Doussan	CR, INRA, Avignon	Examinateur
André Revil	DR., Université Joseph Fournier Grenoble	Directeur de Thèse
Pierre Henry	DR., Collège de France Université Aix-Marseille III	Co-directeur

Remerciements

Ces trois années de thèse furent vraiment d'une grande richesse tant d'un point de vue scientifique qu'humain. J'ai fait la connaissance de personnes vraiment exceptionnelles et je sais que pour certaines il n'est que peu probable que je les revoie un jour mais je ne les oublierai jamais. La liste des personnes à remercier est longue et je tiens d'ores et déjà à m'excuser si j'ai la maladresse d'omettre quelqu'un.

En premier lieu, je tiens à remercier André Revil pour avoir été à l'initiative de ce travail de thèse et pour m'avoir accordé sa confiance pour mener à terme ce travail. Je lui suis vraiment reconnaissante de m'avoir fait partager sa passion pour les volcans qui m'a permis de découvrir des endroits extraordinaires. Je remercie également Pierre Henry, pour son soutien, sa patience et les nombreuses discussions qui m'ont vraiment éclairée. Il m'a soutenue dans les périodes les plus délicates et j'ai toujours pu compter sur lui malgré son emploi du temps surchargé.
Je remercie les membres du jury pour l'attention qu'ils ont bien voulu prêter à mon travail. Monsieur Alain Tabbagh et Madame Laurence Jouniaux pour avoir accepté d'en être les rapporteurs et Monsieur Claude Doussan pour avoir assumé l'examen de ma thèse.

Les expériences en cuve n'auraient peut être pas été aussi réussies sans l'aide de Pierre Henry avec qui nous avons longuement réfléchi sur la méthode à adopter afin d'adapter à la géophysique un appareil conçu pour la recherche médicale. Un grand merci à Nicklas qui m'a apporté son aide afin d'exploiter toutes ces données et surtout pour sa gentillesse et sa générosité. Merci à Alexandre pour m'avoir, à maintes reprises, consacré du temps pour les simulations numériques. Ah ce Comsol!! Merci à Anthony F. pour tous ses conseils.

J'ai éprouvé un grand plaisir à travailler sur le Stromboli et Vulcano. Ce sont des lieux empreints d'une force qui nous dépasse mais qui, et je ne saurais l'expliquer, vous apporte une certaine paix intérieure, un "je ne sais quoi" qui vous prend et ne vous lâche plus.
La bonne ambiance qui a toujours régné au sein de notre groupe a su rendre les douleurs musculaires supportables. Enzo merci pour ta constante bonne humeur, Anthony pour tes super plats de riz au fromage, grazie Sabatino, merci à toute la "PS team"… Grâce à ces nombreuses missions, j'ai connu et appris à connaître deux personnes qui me sont aujourd'hui très chères : merci Basia d'avoir été mon "Bradipo" et d'avoir réussi à me donner de ta force pour surmonter les pentes et merci d'être venue de Suisse pour me soutenir le jour J! Merci Tullio pour ta patience, ton soutien et toute ton attention!

L'un des aspects les plus positifs de cette thèse a été la possibilité de partir souvent à l'étranger et pour cela encore merci André. Notre mission dans l'Idaho a été géniale. Pour leur grande gentillesse je remercie Warren Barrash qui a su royalement organiser cette campagne de terrain et Leah, une personne d'une générosité rare que je suis vraiment heureuse d'avoir rencontrée.
Après l'Idaho, passons au Colorado où j'ai fait la connaissance de Donna qui m'a hébergée pendant plus d'un mois comme si je faisais partie de sa famille, j'ai été vraiment touchée par son attention de tous les jours.

Un grand merci à mes voisins de bureau, Barbara bien sûr, Philippe pour son soutien, ses conseils et son aide sur Matlab, Ludo pour m'avoir fait découvrir la spéléo, Christophe Morhange pour ses grands sourires, Alexandre, Damien pour son inébranlable bonne humeur. Je remercie également Tanvi pour m'avoir fait découvrir une infime partie de la culture indienne.

Finalement durant ces trois dernières années, ce sont mes amis du CEREGE que je voyais le plus. Merci à Julie, tu vas beaucoup me manquer mais t'inquiète je viendrai te voir et tu sais que ma porte est grande ouverte! Merci Prisc pour ta patience et ton soutien dans mes moments de stress, t'inquiète je te renverrai l'ascenseur. Merci à Magali pour son sourire de tous les jours et son petit brin de folie! Merci à ma Floflo pour tous ces cinés. Merci à Benoît pour sa "cool attitude", merci à Adrien pour nos petites pauses "aquarium". Merci Yannick, Guillaume, Mel, Irène, Cyrille, Sophie, Nico, Anne Lise, Lucie, Mica, Julien et tous les autres.
Merci à Marie Magdeleine pour sa grande gentillesse et sa vitalité, j'ai rarement vu quelqu'un régler les problèmes de façon si efficace.
Je tiens à remercier chaleureusement les personnes du bâtiment Villemin et plus particulièrement Marie, toujours à l'écoute, pour ses côtés chaleureux et rassurant, Laurence qui est l'une des seules personnes que je connaisse qui vous donne envie de sourire même si vous vous être levée du pied gauche. Merci à Maryse, Gilbert, Michel, Fred, Gilles, Max pour leur grande gentillesse. Un petit clin d'œil à Gérard qui adore faire partager sa passion et qu'on ne se lasse jamais d'écouter!

Ah et puis, même si mes proches vont encore m'appeler Brigitte Bardot, je remercie ma Dido pour ses ronrons et ses calins qui après une dure journée sont vraiment bienvenus et merci à mon toutou du Stromboli, Rocky, pour son affection!

Enfin je garde le meilleur pour la fin, ma famille, merci à mes parents qui ont toujours fait en sorte que je puisse réaliser tout ce que je désirais en me soutenant, me rassurant et me conseillant, merci ma sœur adorée d'être toujours là! Merci Jean-François! Merci à ma mamie pour les pauses détente et merci tantine. Ah et puis merci à mon Bibou qui a su me supporter malgré les coups de stress, ton soutien et ta présence me sont précieux. Attention je compte sur toi pour la suite…

Résumé

La méthode de polarisation spontanée (PS) consiste en la mesure du potentiel électrique naturellement présent dans le sol. Elle est la seule méthode sensible aux écoulements d'eau souterrains. Les principaux objectifs de cette thèse ont été de (1) déterminer l'influence de la conductivité de surface et du régime d'écoulement sur le coefficient de couplage électrocinétique (paramètre crucial pour l'interprétation des signaux de PS), (2) de montrer l'efficacité de la PS dans la mise en évidence des phénomènes hydromécaniques et (3) de caractériser les écoulements de fluides en contexte volcanique. Nous avons développé un modèle corrigeant le coefficient de couplage électrocinétique à la fois des effets de la conductivité de surface et du nombre de Reynolds. La validité de ce modèle a été confirmée grâce à des expériences réalisées sur billes de verre. Lors d'expériences en cuve, la méthode du potentiel spontané associée à un appareillage de haute sensibilité nous a permis de caractériser la signature électrique liée à des phénomènes hydromécaniques. Utilisées à partir des enregistrements de PS réalisés à la surface de la cuve les méthodes d'analyse en ondelettes et d'intercorrelation ont montré la nature dipolaire de la source électrique liée à de telles perturbations et ont permis sa localisation. Sur le Stromboli en Italie, nous avons utilisé une approximation au premier ordre de la relation entre l'épaisseur de la zone vadose et l'anomalie de PS afin de déterminer la profondeur d'un aquifère situé sur le flanc est du volcan.

Mots clés: **Potentiel Spontané, PS, électrofiltration, coefficient de couplage électrocinétique, aquifère.**

Abstract

The self-potential method consists on the passive measurement of the electrical potential distribution at the ground surface of the Earth. This is the only method thqt is sensitive to the flow of the ground water. The main objectives of this work were (1) to determine the influence of the surface conductivity and the flow regime upon the streaming coupling coefficient (a critical parameter to interpret SP signals), (2) to show the efficiency of the SP in the localization of hydromechanical disturbances, (3) to characterize ground water flow and aquifers in a volcanic context. For indifferent electrolytes, like sodium chloride, we derived two simple scaling laws for the dependence of the streaming potential coupling coefficient with the surface conductivity and Reynolds number. The validity of these laws was checked successfully against a new set of experimental data using glass bead. In sandbox experiments, the self-potential method associated with a high sensitivity equipment has enabled us to characterize the electrostatic signature of hydromechanical disturbances. The wavelet analysis and the cross-correlation method showed the dipolar nature of the electrical source linked to such disturbances and can be used to locate the source. On Stromboli in Italy, we used a relationship between the thickness of the vadose zone and the self-potential anomaly to determine the shape of the water table along the flank of the volcano.

Key words: **Self-potential, SP, electrofiltration, streaming potential coupling coefficient, aquifer.**

Tables des matières

Introduction 1

Chapitre 1 : Théorie du Couplage Hydroélectrique 7

1.1 Introduction 7
1.2. La Double Couche Electrique 8
1.3. Quantification du phénomène d'électrofiltration 10
1.3.1. L'équation d'Helmholtz-Smoluchowski 10
1.3.2. Les Equations constitutives du couplage électrocinétique 11
1.3.3. L'équation de Poisson 14
1.4. Le coefficient de couplage électrocinétique 16
1.4.1. Définition 16
1.4.2. Mesure du coefficient de couplage électrocinétique 17
1.4.2.1. Le zetacad® 17
1.4.2.2. Autres dispositifs expérimentaux 17
1.5. Conclusion 18
1.6. Références 19

Chapitre 2 : Le coefficient de couplage électrocinétique 21

2.1. Introduction 21
2.2. Influence de la Perméabilité 22
2.3. Influence de la Température 23
2.4. Influence de la salinité et du pH 25
2.4.1. La conductivité électrique 25
2.4.2. Influence du pH 25
2.5. Influence de la Conductivité de Surface 26
2.6. Influence du Nombre de Reynolds 28
2.7. Présentation de deux Articles Scientifiques 29
2.8. Conclusion 99
2.9. Références 100

Chapitre 3 : Localisation de sources hydromécaniques par la méthode du potentiel spontané 103

3.1. Introduction 103
3.2. Localisation de source de courant dans un milieu conducteur 104

3.2.1. L'analyse en ondelettes 104
3.2.2. La méthode d'intercorrélation 106
3.3. Validation Expérimentale 109
3.3.1. Description de la cuve et propriétés pétrophysiques du sable 109
3.3.2. Principe des mesures de potentiel spontané 110
3.3.2.1. Les électrodes 110
3.3.2.2. Acquisition et traitement des données 112
3.3.2.3. Expériences d'injection et de pompage 113
3.4. Résultats 114
3.6. Conclusion 172
3.7. Références 172

Chapitre 4 : Applications de la méthode de polarisation spontanée en volcanologie 175

4.1. Introduction 175
4.2. Les origines du potentiel spontané 177
4.2.1. Le potentiel électrochimique 177
4.2.2. Le couplage thermoélectrique 178
4.2.3. Le couplage électrocinétique 179
4.2.3.1. L'effet topographique 180
4.2.3.2. Les Remontées Hydrothermales 181
4.3. Les Principaux Types d'Anomalies de Potentiel Spontané 182
4.3.1. Les anomalies en V 182
4.3.2. Les anomalies en W 183
4.3.3. Les anomalies positives 184
4.4. Localisation d'un aquifère à Stromboli 185
4.4.1. Mesures géoélectriques et géochimiques réalisées sur le Stromboli 185
4.4.1.1. Les mesures de potentiel spontané 185
4.4.1.2. Les mesures de résistivité électrique 186
4.4.1.3. Les mesures de flux de CO_2 187
4.4.2. Signaux de Potentiel Spontané Associés à des Ecoulements Souterrains 187
4.4.2.1. La surface SPS 187
4.4.2.2. Le modèle de Fournier 189
4.5. Résultats et Interprétations 190
4.6. Etude de la Structure Interne de Vulcano 218
4.7. Conclusion 274
4.8. Références 275

Conclusions et Perspectives 279

Bibliographie 281

Liste des figures 291

Listes des symboles 293

Introduction

La méthode du potentiel spontané consiste en la mesure passive, à la surface de la Terre ou en forage, du champ électrique ou de la distribution de potentiel électrique associée à des mécanismes de polarisation naturels dans le sous-sol. Trois principales sources de courant existent dans le sous-sol : les couplages thermoélectriques (liés directement à un gradient de température), l'électrofiltration (couplage lié à une circulation hydrique dans un milieu poreux), et le couplage électrochimique associé à un gradient de potentiel chimique des porteurs de charges (ions et électrons). Nous verrons que la principale contribution en milieu volcanique est l'effet électrocinétique et plus particulièrement le phénomène d'électrofiltration (Ishido et Mizutani, 1981, Morgan et al., 1989, Michel et Zlotnicki, 1998). Ce phénomène est le résultat du déplacement de charges électriques à l'interface minéral/solution sous un gradient de pression de fluide poral dans une matrice rocheuse.

La méthode du potentiel spontané, avec plus de 170 ans d'histoire, est l'une des plus anciennes méthodes géophysiques (Fox, 1830). Longtemps considérée comme une curiosité scientifique, elle a connu, dans les années 70, un développement important de ces applications aux systèmes hydrothermaux et aux zones de failles (Corwin and Morrison, 1977 ; Fitterman, 1978 ; Corwin and Hoover, 1979). Ses nombreuses applications en hydrogéophysique ont fait récemment évoluer la méthode notamment dans la détermination des circulations hydriques dans le sous-sol (Fournier, 1989 ; Aubert et Atangana, 1996 ; Revil and Leroy, 2001 ; Doussan et al., 2002) ou en montrant la présence de zones contaminées par la distribution du potentiel rédox (Naudet et al. 2003, 2004; Arora et al., 2007; Linde et Revil, 2007). Elle a également connu de grands succès dans les domaines de la géothermie (Corwin, 1990) et de la volcanologie (Lénat et al., 1998 ; Finizola et al. 2004 ; Aizawa, 2008).

Le problème des ressources en eau est aujourd'hui un problème sociétal majeur. L'importance de cette problématique conduit à de nouveaux travaux de recherche concernant l'utilisation de méthodes géophysiques d'imagerie du sous-sol. Aux méthodes actives que sont le géoradar, la sismique haute résolution, la tomographie de résistivité électrique, se rajoute donc la méthode du potentiel spontané qui est une méthode passive et la seule à être directement sensible aux écoulements d'eau souterrains (Fournier, 1989 ; Corwin, 1990 ; Aubert et al., 1993).

Les principaux objectifs de cette thèse sont de déterminer l'efficacité de la méthode du potentiel spontané dans la mise en évidence des phénomènes hydromécaniques et dans la caractérisation des écoulements de fluides et des nappes d'eau en contexte volcanique. Pour répondre à ces objectifs, nous avons réalisé des expériences de laboratoire, élaboré un protocole pour des expérimentations en cuve et organisé quatre campagnes de terrain sur les édifices de Stromboli et de Vulcano (Iles Eoliennes, Italie).

Le premier objectif visait à étudier l'intérêt de la méthode du potentiel spontané pour localiser des perturbations hydromécaniques. Le Chapitre 1 fait un rappel sur l'état des connaissances de l'électrofiltration à l'échelle locale du milieu poreux. Nous y proposons une théorie de l'électrofiltration dans un milieu poreux déformable. En effet, la fracturation de roches et en général toutes sortes de perturbations hydromécaniques affectant une roche poreuse et perméable génèrent des signaux électromagnétiques (e.g., Surkov and Pilipenko, 1997 ; Moore et Glaser, 2006, 2007 ; Yoshida and Ogawa, 2004). En contexte volcanique, comprendre ces perturbations électromagnétiques pourrait permettre le développement de nouveaux dispositifs de surveillance des édifices volcaniques actifs.

Avant une éruption volcanique, les écoulements souterrains dans des milieux fracturés et résultants d'une variation brusque de la pression d'eau interstitielle et de l'état de contrainte ne sont pas toujours dans le régime laminaire visqueux. Il nous a donc semblé important, afin d'interpréter quantitativement les signaux de potentiel spontané, de connaître l'influence du nombre de Reynolds sur le phénomène d'électrofiltration. Dans le Chapitre 2, nous avons donc développé un modèle afin de corriger les valeurs de potentiel spontané de l'influence du nombre de Reynolds.

Nous avons élaboré un protocole de mesures en cuve afin de mettre en évidence la signature électrique associée à une variation brutale de pression par injection ou pompage

d'un très faible volume d'eau. Compte tenu des expériences envisagées, il était indispensable d'utiliser des électrodes de petite taille et d'une très grande précision. Une des nouveautés apportée par ces expériences a été l'utilisation d'un dispositif élaboré pour l'électroencéphalographie dont la sensibilité est de trois ordres de grandeur supérieurs aux systèmes utilisés antérieurement (Perrier et Morat, 2000 ; Rizzo et al., 2004). Il s'agit d'un voltmètre compact, associé à des électrodes Ag/AgCl d'une sensibilité de 0.1 μV. Dans le Chapitre 3, nous présentons nos expériences en cuve liées à l'étude des perturbations hydromécaniques et leurs résultats.

Dans le cas des zones volcaniques, les mesures de potentiel spontané sont essentiellement utilisées pour cartographier les limites lithologiques (failles, dykes, limites de cratère) et déterminer les configurations des circulations de fluides de subsurface (Zlotnicki et al., 1998 ; Aubert et al., 2000 ; Revil et al., 2004). Cette méthode est également de plus en plus utilisée comme méthode de surveillance. Les mesures spatio-temporelles de potentiel spontané ont non seulement l'avantage d'être sensibles à la dynamique des systèmes hydrothermaux, mais elles permettent également une meilleure compréhension de la configuration des écoulements d'eau météoritiques et du système hydrothermal. Ce dernier aspect a une dimension importante la présence d'aquifères pouvant engendrer des éruptions phréato-magmatiques de fortes intensités mais également devenir une ressource en eau pour les populations locales. Dans le Chapitre 4, nous présentons deux exemples d'applications de la méthode du potentiel spontané en contexte volcanique.

Références

Aizawa, K., 2008. Classification of self-potential anomalies on volcanoes and possible interpretations for their subsurface structure, *J. Volcanol. Geotherm. Res.*, 175(3), 253-268.

Arora, T., A. Revil, N. Linde, and J. Castermant, 2007. Non-intrusive determination of the redox potential of contaminant plumes using the self-potential method, *Contaminant Hydrology*, 92, 274-292.

Aubert, M. and Yene Atangana, Q., 1996. Self-potential method in hydrogeological exploration of volcanic areas, *Ground-water*, 34 (6), 1010–1016.

Aubert, M., P. Antraygues, E. Soler, 1993. Interpretation of the self-potential measurements in hydrogeological exploration of a volcanic massif. On the existence of groundwater flow paths on the south flank of the Piton de la Fournaise (Réunion Island), *Bull. Soc. Géol. France,* 164, 17-25.

Aubert, M., I. Dana and A. Gourgaud, 2000. Internal structure of the Merapi summit from self-potential measurements, *J. Volcanol. Geotherm. Res.,* 100, 337-343.

Corwin, R., and H. Morrison, 1977. Self-Potential Variations Preceding Earthquakes in Central California, *Geophys. Res. Lett.*, 4(4), 171-174.

Corwin, R.F., and D.B. Hoover, 1979. The Self-Potential method in geothermal exploration, *Geophysics,* 44, 226-245.

Corwin, R.F., 1990. The Self-Potential Method for Environmental and Engineering Applications in S. H. Ward (ed.), Geotechnical and Environmental Geophys., Vol. 1, *Soc. Explor. Geophys.,* Tulsa, 127.

Doussan, C., Jouniaux, L., and J.-L. Thony, 2002. Variations of self-potential and unsaturated water flow with time in sandy loam and clay loam soils, *Journal of Hydrology*, 267, 173–185.

Finizola, A., J. F. Lénat, O.Macedo, D. Ramos, J. C. Thouret, and F. Sortino, 2004. Fluid circulation and structural discontinuities inside Misti volcano (Peru) inferred from self-potential measurements, *J. Volcanol. Geotherm. Res.,* 135(4), 343– 360.

Fitterman, D., 1978. Electrokinetic and Magnetic Anomalies Associated With Dilatant Regions in a Layered Earth, *J. Geophys. Res.*, 83(B12), 5923-5928.

Fournier, C., 1989. Spontaneous potential and resistivity surveys applied to hydrogeology in a volcanic area : case history of the chaîne des puys (Puy-de-Dôme, France), *Geophys. Prospecting*. 37, 647-668.

Fox, R.W., 1830. The electromagnetic properties of metalliferous veins in the mines of Cornwall, *Proc. R. Soc. London* 2, 411.

Ishido, T., and H. Mizutani, 1981. Experimental and theoretical basis of electrokinetic phenomena in rock-water systems and its applications to geophysics, *J. Geophys. Res.,* 86, 1763-1775.

Lénat, J.F., B. Robineau, S. Durand and P. Bachélery, 1998. Etude de la zone sommitale du volcan Karthala (Grande Comore) par polarisation spontanée, *C.R. Acad. Sci.,* 327, 781-788.

Linde, N., D. Jougnot, A. Revil, S. Matthäi, T. Arora, D. Renard, and C. Doussan, 2007. Streaming current generation in two-phase flow conditions, *Geophys. Res. Lett.,* 34(3), L03306, doi: 10.1029/2006GL028878.

Michel, S., and J. Zlotnicki, 1998. Self-potential and magnetic surveying of La Fournaise volcano (Réunion Island): Correlations with faulting, fluid circulation and eruption, *J. Geophys. Res.* 103, 17,845-17,857.

Moore, J. R., and S.D. Glaser, 2006. The origins of the self-potential response during hydraulic fracturing, *Eos Trans.,* AGU Fall Meet. Suppl., Abstract NS21A-04.

Moore, J.R. and S.D. Glaser, 2007. Self-Potential Observations During Hydraulic Fracturing, *J. Geophys. Res.*, 112, B02204, 1-17.

Morgan, F. D., E.R. Williams and T.R. Madden, 1989. Streaming potential of westerly granite with applications, *J. Geophys. Res.,* 94, 12,449-12461.

Naudet, V., A. Revil, J.-Y. Bottero, and P. Bégassat, 2003. Relationship between self-potential (SP) signals and redox conditions in contaminated groundwater, *Geophys. Res. Lett.,* 30(21), 2091, doi : 10.1029/2003GL018096.

Naudet, V., A. Revil, E. Rizzo, J.-Y Bottero, and P. Begassat, 2004. Groundwater redox conditions and conductivity in a contaminant plume from geoelectric investigations, *Hydrology and Earth System Science*, 8 (1), 8-22.

Perrier, F., and P. Morat, 2000. Characterization of electrical daily variations induced by capillary flow in the non-saturated zone, *Pure Appl. Geophys.*, 157, 785-810.

Revil, A. and P. Leroy, 2001. Hydroelectric coupling in a clayey material, *Geophys. Res. Lett.*, 28, 1643–1646.

Revil, A. and P. Leroy, 2004. Governing equations for ionic transport in porous shales, *J. Geophys. Res.*, 109(B03208), doi 10.1029/2003JB002755.

Revil, A., A. Finizola, F. Sortino and M. Ripepe, 2004. Geophysical investigations at Stromboli volcano, Italy: implications for ground water flow and paroxysmal activity, *Geophys. J. Int.,* 157, 426–440.

Rizzo, E., B. Suski, A. Revil, S. Straface, and S. Troisi, 2004. Self-potential signals associated with pumping-tests experiments, *J. Geophys. Res.,* 109, B10202, doi:10.1029/2004JB003049.

Surkov, V.V., and V.A. Pilipenko, 1997. Magnetic effects due to earthquakes and underground explosions: a review, *Ann. Geofis.*, XL, 1-13.

Yoshida, S., and T. Ogawa, 2004. Electromagnetic emissions from dry and wet granite associated with acoustic emissions, *J. Geophys. Res.,* 109, B09204, doi:10.1029/2004JB003092.

Zlotnicki, J., G. Boubon, J.P. Viodé, J.F. Delarue, A. Mille, F. Bruère, 1998. Hydrothermal circulation beneath Mount Pelée inferred by self potential surveying. Structural and tectonic implications, *J. Volcanol. Geotherm. Res.,* 84, 73-91.

Chapitre 1 :

Théorie du Couplage Hydroélectrique

1.1 Introduction

Le potentiel spontané consiste en la mesure passive de champs électriques à la surface du sol et en forage. De nombreux phénomènes électromagnétiques peuvent induire des potentiels électriques observables à la surface de la Terre : les phénomènes d'induction magnétotellurique (Perrier et al., 1997), les phénomènes d'oxydoréduction associés à la présence d'un gradient de potentiel rédox et de conducteurs électriques dans le sous-sol (Naudet et al., 2003), le phénomène de couplage thermoélectrique (dû à l'effet thermique sur le gradient de potentiel chimique des porteurs de charges ioniques ou électroniques, Marshall and Madden, 1959), les couplages électrodiffusionels (donnant naissance aux potentiels de diffusion et de membrane, Hearst et al., 2000 ; Leroy et Revil, 2004 ; Revil et Linde, 2006), et le couplage électrocinétique associé à mouvement différentiel entre les minéraux chargés et l'eau porale (Gex, 1980 ; Ishido et Mizutani, 1981 ; Revil et al., 1999a). D'autres phénomènes de couplage existent comme la piézoélectricité (Freund et al., 2006). Enfin, les courants d'origine anthropique causent des perturbations dont l'intensité peut être très variable.

Ce premier chapitre est consacré à la présentation du phénomène d'électrofiltration encore appelé couplage hydroélectrique. En effet, parmi tous les phénomènes électromagnétiques qui peuvent être à l'origine des anomalies de potentiel spontané, l'électrofiltration permet la caractérisation des écoulements souterrains ou peut conduire à l'observation à distance d'autres phénomènes comme l'hydrofracturation dans les édifices volcaniques par exemple. L'électrofiltration correspond à la naissance d'un champ électrique en réponse à une circulation de fluide dans le milieu poreux ou fracturé d'une roche (Gex, 1980 ; Ishido et Mizutani, 1981 ; Revil et al., 1999a). Un champ magnétique peut également

être généré par le phénomène d'électrofiltration (Fitterman, 1979 ; Revil et al., 1999b) mais nous ne nous intéresserons pas à ce phénomène de couplage « hydromagnétique » dans cette thèse.

Dans un premier temps, nous allons expliquer l'origine du couplage hydroélectrique à l'échelle locale du milieu poreux. Nous allons ensuite discuter les équations constitutives à l'échelle du volume élémentaire d'un milieu poroélastique saturé en eau. Ceci nous permettra de quantifier les variations électriques associées à des perturbations hydromécaniques. Enfin nous nous attarderons particulièrement sur le coefficient de couplage électrocinétique qui permet de quantifier l'intensité du couplage hydroélectrique.

1.2. La Double Couche Electrique

Avant de décrire l'électrofiltration à l'échelle d'un volume élémentaire de milieu poreux, nous allons décrire le phénomène de double couche électrique à l'origine du couplage hydroélectrique à l'échelle microscopique. La Figure 1.1 montre le phénomène de Double Couche Electrique (DCE) à la surface des minéraux. La surface de tout minéral en contact avec l'eau possède des sites réactifs (par exemple des sites silanols >Si-OH à la surface de la silice, > représente le réseau crystallin). Ces sites réactifs sont le lieu d'échanges de protons entre la surface du minéral et l'eau ainsi que des sites d'adsorption des ions présents en solution suivant leur affinité pour les sites de surface. Par exemple, à la surface de la silice, les réactions dites de complexation peuvent être les suivantes,

$$> SiO^- + H^+ \Leftrightarrow > SiOH \, , K_1,$$

$$> SiOH + H^+ \Leftrightarrow > SiOH_2^+ \, , K_2,$$

$$> SiO^- + Na^+ \Leftrightarrow > SiONa \, , K_3,$$

où les constantes K_1, K_2, K_3 sont des constantes d'équilibre pour les différentes réactions chimiques et les phénomènes d'adsorption (par exemple la troisième des réactions écrites ci-dessus).

Il résulte de ces réactions chimiques, une charge nette à la surface des minéraux. Pour de nombreux minéraux en contact avec l'eau, cette charge est négative à pH=7. Les

phénomènes d'adsorption se produisent dans une couche dite couche de Stern. La couche de surface et la couche de Stern forment la couche fixe attachée à la surface des minéraux. Afin de respecter les conditions d'électroneutralité, cette charge fixe est compensée par un excès de contre-ions dans l'eau porale. Il en résulte une modification locale de la concentration ionique de la solution dans une couche dite diffuse également appelée couche de Gouy-Chapman dont l'épaisseur dépend de la force ionique de la solution aqueuse. Le premier modèle de la double couche électrique est attribué à Helmholtz (1879). Mathématiquement, il a assimilé la double couche à un condensateur. Mais ce modèle ne prend pas en compte l'effet de la couche diffuse. Plus tard, Gouy (1910) et Chapman (1913) ont apporté des améliorations significatives à ce modèle, en développant séparément la théorie de la couche diffuse. Le modèle utilisé aujourd'hui est le modèle de Gouy-Chapman-Stern (Stern, 1924 ; Ishido et Mizutani, 1981 ; Morgan et al., 1989 ; Revil et al., 1999a), qui combine les deux modèles en faisant intervenir la couche dense de Helmholtz (appelée alors couche de Stern) et la couche diffuse de Gouy-Chapman (Figure 1.1).

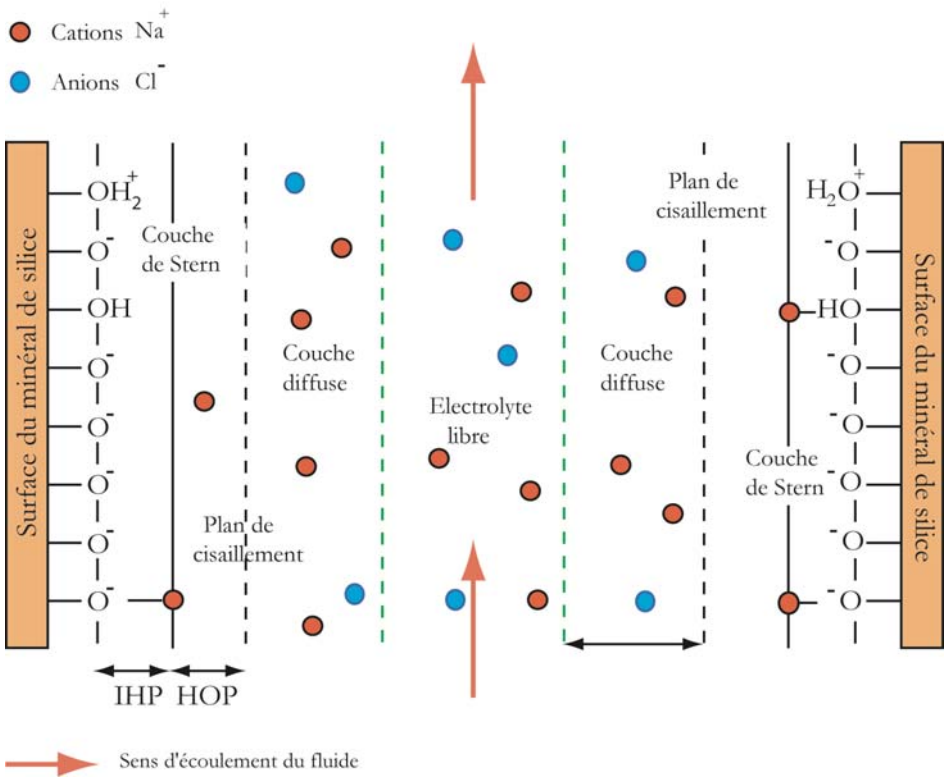

Figure 1.1 : Schéma de la distribution ionique de la double couche électrique.

La Figure 1.1 nous montre un schéma de la double couche électrique qui se compose donc :

- D'une couche interne appelée couche de Stern où les ions sont fixés au solide. On distingue : (1) le plan interne de Helmholtz (IHP) constitué essentiellement d'ions partiellement dissous et (2) le plan externe de Helmholtz (OHP), occupé par des ions hydratés, qui sépare la couche de Stern de la couche diffuse.
- une couche externe ou couche diffuse de Gouy-Chapman où les ions potentiellement mobiles compensent le déficit de charges de la surface du minéral et obéissent à une loi de Boltzmann. L'épaisseur de la couche diffuse est caractérisée par la longueur de Debye χ_D (m). Cette longueur correspond à la distance à partir de laquelle les perturbations associées à la surface chargée du minéral sont négligeables. Cette longueur est de l'ordre de l'Angström (Revil & Glover, 1997) et dépend fortement de la concentration des espèces ioniques et de la charge des ions de l'électrolyte :

$$\chi_d = \sqrt{\frac{\varepsilon_r \varepsilon_0 k_b T}{2e^2 NI}}, \tag{1.1}$$

avec ε_0 la permittivité électrique du vide (ε_0= 8, 84.10^{-12}), ε_r la constante diélectrique relative de l'eau, e la charge élémentaire de l'électron (1.602×10^{-19} C), N le nombre d'Avogadro (6, 023 × 10^{23} mol L^{-1}), I la force ionique de l'eau (mol m^3), k_b la constante de Boltzman (k_b=1,3806 × 10^{-23} J K^{-1}). L'équation (1.1) montre que l'épaisseur de la couche diffuse diminue avec l'augmentation de la concentration en espèces ioniques. Ainsi la longueur de Debye sera plus grande pour une eau douce que pour une eau salée.

Au-delà de la couche diffuse, la solution aqueuse qui n'est plus affectée par les effets d'intéraction coulombienne avec la surface chargée des minéraux est appelée électrolyte libre.

1.3. Quantification du phénomène d'électrofiltration

1.3.1. L'équation d'Helmholtz-Smoluchowski

Lorsque la solution aqueuse s'écoule au travers du milieu poreux, l'excès de charge de la couche diffuse est entraîné par la circulation de la solution. Il se produit une densité de

courant dans les pores du milieu poreux, appelé courant d'électrofiltration (e.g., Overbeek, 1952). Le potentiel électrique (microscopique) de la double couche électrique situé sur le plan hydrodynamique où la vitesse entre les grains et l'électrolyte est nulle est appelé le potentiel zêta (ζ). C'est un paramètre fondamental dans la mesure des potentiels d'électrofiltration (potentiel électrique entre les extrémités de l'échantillon). L'équation d'Helmholtz-Smoluchowski décrit le potentiel d'électrofiltration dans le cas d'un flux laminaire percolant à l'intérieur d'un tube où l'épaisseur de la couche de Stern est petite devant le rayon de courbure des grains et la conductivité de surface négligeable devant celle du fluide. L'entraînement par le fluide des ions présents dans la couche diffuse engendre un courant de convection I'. Le déséquilibre des charges causé par ce courant crée un champ électrique et on voit apparaître un courant de conduction I dû à la migration des ions dans ce champ. En régime stationnaire, I et I' sont égaux mais de signe opposé et il existe un rapport de proportionnalité décrit par l'équation d' Helmoltz-Smoluchowski (Overbeek, 1952):

$$C_{HS} = \left(\frac{\Delta\varphi}{\Delta p}\right)_{\vec{j}=0} = \frac{\varepsilon_f \zeta}{\eta_f \sigma_f}, \tag{1.2}$$

où Δp (en Pa) est la différence de pression contrôlant le débit hydrique, $\Delta\varphi$ (en V) est la différence de potentiel électrique (potentiel d'électrofiltration) mesurée sur les faces opposées du milieu poreux, σ_f (en S m^{-1}) est la conductivité électrique du fluide, ε_f (en F m^{-1}) est la constante diélectrique du fluide, ζ (en V) est le potentiel zêta, η_f (en Pa s) est la viscosité dynamique du fluide. A densité de courant nulle, le rapport $\Delta\varphi/\Delta p$ est communément appelé coefficient de couplage électrocinétique C_{HS}. Nous pouvons constater que cette équation ne fait pas intervenir de paramètres texturaux ; dans le cas d'un milieu poreux, sous les conditions de validité de cette équation, cela signifie que le coefficient de couplage électrocinétique est indépendant de la microstructure du milieu poreux. On notera que le signe du potentiel ζ correspond au signe de la charge de surface du minéral et détermine le signe du coefficient de couplage électrocinétique.

1.3.2. Les Equations constitutives du couplage électrocinétique

Considérons un volume poreux Ω isotrope et saturé avec un électrolyte en équilibre avec les grains. Quand le fluide interstitiel monophasique s'écoule dans le régime laminaire visqueux

(à faible nombre de Reynolds) à travers la roche, les processus hydrauliques et électriques sont couplés par les équations constitutives macroscopiques (Ishido et Mizutani, 1981) :

$$\mathbf{J} = -L_{11}\nabla\varphi - L_{12}(\nabla p - \rho_f \mathbf{g}), \tag{1.3}$$

$$\mathbf{U} = -L_{21}\nabla\varphi - L_{22}(\nabla p - \rho_f \mathbf{g}), \tag{1.4}$$

où $\boldsymbol{J}$ représente la densité de courant (A m^{-2}), σ la conductivité électrique du milieu (S m^{-1}), φ est le potentiel électrique macroscopique (V), ρ_f est la masse volumique du fluide (kg m^{-3}), $\mathbf{g}$ est l'accélération due à la gravité (m s^{-2}), $\boldsymbol{U}$ est la vitesse de Darcy (m s^{-1}) (flux hydrique), p est la pression du fluide poral (Pa), L_{ij} sont des termes de couplage électrocinétique (en m^2 V^{-1} s^{-1}) entre la loi de Darcy et la loi d'Ohm. L_{11} et L_{22} sont des coefficients de conductivité tandis que L_{12} et L_{21} sont des coefficients de couplage. La loi de réciprocité d'Onsager, impose L_{12}= L_{21}, on notera ($L = L_{12} = L_{21}$), $L_{ij} \geq 0$ et $L^2 \leq L_{11}\, L_{22}$. Le coefficient de couplage L, dans le cas d'un milieu poreux isotrope homogène, s'écrit (e.g., Revil 1999b) :

$$L = -\frac{\varepsilon_f \zeta}{\eta_f F}, \tag{1.5}$$

où ε_f (en F m^{-1}) est la constante diélectrique du fluide, ζ (en V) est le potentiel zêta, η_f (en Pa s) est la viscosité dynamique de l'eau et F est le facteur de formation qui est défini par le rapport de la conductivité électrique de l'eau porale sur la conductivité du milieu poreux saturé et seulement lorsque la conduction de surface dans la double couche électrique peut être considérée comme négligeable par rapport à la conductivité de l'électrolyte. La loi empirique d'Archie (1942) relie le facteur de formation à la porosité par la relation : $F = \Phi^{-m}$ où en général $1.5 < m < 2.5$ est appelé le facteur de cimentation (Mendelson et Cohen, 1982). Ce facteur de cimentation dépend de la texture du milieux poreux. Dans le cas d'un milieu granulaire, il dépend de la forme des grains (m=1.5 pour des grains sphériques).

La loi d'Ohm impose $L_{11} = \sigma$ où σ est la conductivité électrique du milieu poreux (S m^{-1}) et la loi de Darcy que $L_{22} = k/\eta_f$ où k est la perméabilité (intrinsèque) du milieu poreux (m^2). Nous pouvons donc écrire les équations (1.3) et (1.4) sous la forme :

$$\mathbf{J} = \underbrace{-\sigma \nabla \varphi}_{\text{Loi d'Ohm}} \underbrace{- L(\nabla p - \rho_f \mathbf{g})}_{\text{Courant de convection}}, \tag{1.6}$$

$$\mathbf{U} = \underbrace{-L\nabla\varphi}_{\text{Electro osmose}} \underbrace{- \frac{k}{\eta_f}(\nabla p - \rho_f \mathbf{g})}_{\text{Loi de Darcy}}, \tag{1.7}$$

L'équation (1.6) est la somme d'un courant de conduction régit par la loi d'Ohm et d'un courant de convection induit par le mouvement des charges électriques de la double couche électrique.

L'équation (1.7) correspond à la loi de Darcy généralisée, le premier terme est associé à l'effet électro-osmotique où le flux hydraulique est induit par le champ électrique. Dans la majorité des cas, exception faite des argiles fortement compactées, le champ électrique généré par le couplage électrocinétique n'a pas d'effet important sur la vitesse de Darcy, l'effet électro-osmotique est donc négligeable :

$$-L\nabla\varphi << \frac{k}{\eta_f}(\nabla p - \rho_f \mathbf{g}). \tag{1.8}$$

On retrouve alors l'équation classique de Darcy :

$$\mathbf{U} = -\frac{k}{\eta_f}(\nabla p - \rho_f \mathbf{g}) = K\nabla h, \tag{1.9}$$

Avec h la charge hydraulique (m) et K la conductivité hydraulique (m s^{-1}) définie par :

$$K = \frac{k\rho_f g}{\eta}, \tag{1.10}$$

Ainsi en combinant les équations (1.6) et (1.9) on exprime la densité de courant totale $\mathbf{J}$ en fonction du gradient de potentiel électrique $\nabla\varphi$ (loi d'Ohm) et du gradient de pression hydraulique ∇p :

$$\mathbf{J} = -\sigma\nabla\varphi + \mathbf{J_s}, \tag{1.11}$$

Avec J_s la densité de courant source définie par :

$$\mathbf{J}_s = -L\nabla p, \tag{1.12}$$

En l'absence d'accumulation de charges dans le milieu poreux les équations de conservation de la charge et de la masse de l'eau porale sont (Sill, 1983):

$$\nabla \cdot \mathbf{J} = 0, \tag{1.13}$$

$$\nabla \cdot (\rho_f \mathbf{U}) = -\frac{\partial}{\partial t}\left(\rho_f \phi\right). \tag{1.14}$$

En utilisant la théorie de Biot, l'équation de conservation de la masse du fluide poral dans un milieu poreux déformé peut être écrite en terme de déformation volumique ε du matériau poreux et en variation dans le temps de la pression de fluide (Palciauskas and Domenico, 1989),

$$\nabla \cdot (\rho_f \mathbf{U}) = -\rho_f \left[\xi \frac{d\varepsilon}{dt} + \left(\frac{1}{R} - \frac{\xi}{H}\right)\frac{dp}{dt}\right], \tag{1.15}$$

$$\frac{1}{R} - \frac{\xi}{H} = \frac{1}{\rho_f}\left(\frac{\partial m_f}{\partial p}\right)_\varepsilon, \tag{1.16}$$

$$\frac{1}{H} = \frac{1}{\rho_f}\left(\frac{\partial m_f}{\partial \sigma}\right)_p, \tag{1.17}$$

$$\frac{1}{R} = \frac{1}{\rho_f}\left(\frac{\partial m_f}{\partial p}\right)_\sigma, \tag{1.18}$$

où σ est la contrainte élastique de confinement moyenne (en Pa) et ε est la déformation volumique du milieu poreux. Les coefficients R, ξ, et H sont appelés coefficients de Biot (en Pa). Le coefficient $1/R$ représente le changement de teneur en eau pour une variation donnée de pression de fluide. Le coefficient $(1/R - \xi/H)$ est la quantité d'eau qui peut être stockée dans un matériel poreux soumis à une variation de pression de fluide tandis que le volume du milieu est maintenu constant. Le coefficient $1/H$ représente la variation de quantité d'eau pour une variation de contrainte du matériel drainé.

1.3.3. L'équation de Poisson

D'après le modèle développé par Revil et al. (2005) (voir Crespy et al., 2007 ; Revil and Linde, 2006 ; and Linde et al., 2007), la densité de courant source peut également être

écrite sous la forme $\mathbf{J}_S = \overline{Q_V}\mathbf{U}$ où $\overline{Q_V}$ est l'excès de charge effectif de la couche diffuse par unité de volume de pore (en C m^{-3}) qui peut être entraîné par la circulation hydrique. La combinaison des équations (1.11) et (1.13) donne une équation de Poisson pour le potentiel spontané φ (en V) qui va nous permettre de déterminer les différentes sources possibles des signaux de potentiel spontané,

$$\nabla \cdot (\sigma \nabla \varphi) = \Im, \tag{1.19}$$

où $\Im$ est la densité de courant volumique (en A m^{-3}) donnée par,

$$\Im = \nabla \cdot \mathbf{J}_S, \tag{1.20}$$

$$\Im = \nabla L \cdot \nabla p + L \nabla^2 p. \tag{1.21}$$

A partir de cette expression, on voit que des sources naturelles de courant électrique de nature électrocinétique peuvent être créées soit par un gradient de pression non perpendiculaire à une variation du coefficient de couplage électrocinétique, soit par des variations horizontales du coefficient de couplage électrocinétique et par un Laplacien non nul du gradient de pression de l'eau porale.

En utilisant $\mathbf{J}_S = \overline{Q_V}\mathbf{U}$, l'équation de la densité de courant volumique peut également s'écrire sous la forme:

$$\Im = \overline{Q_V} \nabla \cdot \mathbf{U} + \nabla \overline{Q_V} \cdot \mathbf{U}, \tag{1.22}$$

$$\Im = -\overline{Q_V} \xi \frac{d\varepsilon}{dt} - \overline{Q_V} \left(\frac{1}{R} - \frac{\xi}{H} \right) \frac{dp}{dt} + \nabla \overline{Q_V} \cdot \mathbf{U}, \tag{1.23}$$

où l'équation (1.23) est définie pour un fluide poral légèrement compressible comme l'eau. Suivant l'équation (1.23), il y a trois termes sources électrocinétiques capables de générer des signaux de potentiel spontané dans un milieu poreux déformable saturé. La première contribution résulte de la déformation volumique $d\varepsilon / dt$ du milieu poreux. Si le milieu a des grains incompressibles, on a $d\varepsilon / dt = [1/(1-\phi)] d\phi / dt$. Si le milieu est affecté par le phénomène de dilatance ($d\varepsilon / dt \geq 0$), cette contribution $\Im_1 = -\overline{Q_V} \xi d\varepsilon / dt$ est négative car

$\overline{Q_V}$ est généralement positive (voir Revil et al. (2005) pour les minéraux argileux et Linde et al. (2007) pour le sable). La seconde contribution $\Im_2 = -\overline{Q_V}(1/R - \xi/H)dp/dt$, est le résultat des variations de pression de fluide dans le temps. Dans les zones où la pression de fluide augmente dans le temps, cette contribution est négative. La troisième composante $\Im_3 \approx \nabla\overline{Q_V} \cdot \mathbf{U}$ est liée à l'écoulement de fluide poral dans des domaines caractérisés par un gradient de densité de charges volumique $\overline{Q_V}$. Nous verrons dans le Chapitre 3 que cette contribution joue un rôle clé dans l'étude de perturbations hydromécaniques provoquées, par exemple, par la brève injection d'eau dans un milieu poreux saturé en eau.

1.4. Le coefficient de couplage électrocinétique

1.4.1. Définition

A partir des équations (1.11) et (1.12) on définit le coefficient de couplage électrocinétique en prenant $\mathbf{J} = 0$:

$$C \equiv \left(\frac{\partial\varphi}{\partial p}\right)_{\vec{j}=0} = -\frac{L}{\sigma}, \tag{1.24}$$

$$C' \equiv \left(\frac{\partial\varphi}{\partial h}\right)_{\vec{j}=0} = \rho_f g C, \tag{1.25}$$

où C est exprimé en mV/Pa (e.g. Revil 2002b). En hydrogéologie, on préférera utiliser le coefficient C' (en mV m^{-1}) qui représente le coefficient de couplage d'électrofiltration associé à une différence de charge hydraulique. Avec le modèle développé par Revil et Linde (2006), on peut noter la relation entre le coefficient de couplage électrocinétique et l'excès de densité de charges du fluide poral selon :

$$C = \frac{\overline{Q}_v k}{\eta_f \sigma}, \tag{1.26}$$

1.4.2. Mesure du coefficient de couplage électrocinétique

Nous pouvons facilement mesurer le coefficient de couplage électrocinétique en laboratoire grâce au zetacad® (Figure 1.2). Toutefois si les grains de l'échantillon ont un diamètre inférieur à 50 μm ou si nous voulons faire des mesures sur des échantillons rocheux intacts il faut utiliser un autre dispositif comme celui developpé par Suski et al. (2006) (Figure 1.3).

1.4.2.1 Le zetacad®

Cet appareil est un zêta-mètre conçu spécialement pour la mesure automatique du coefficient de couplage électrocinétique par la technique du potentiel d'écoulement. Il est applicable aux matériaux poreux avec des grains d'un diamètre supérieur à 50 μm. L'appareillage se compose d'une cellule dans laquelle est placé l'échantillon. L'eau circule à l'intérieur de la cellule et on mesure le potentiel électrique et la différence de pression aux bornes de la cellule (Figure 1.2). Ceci permet de calculer le potentiel zêta moyen de la surface des grains.

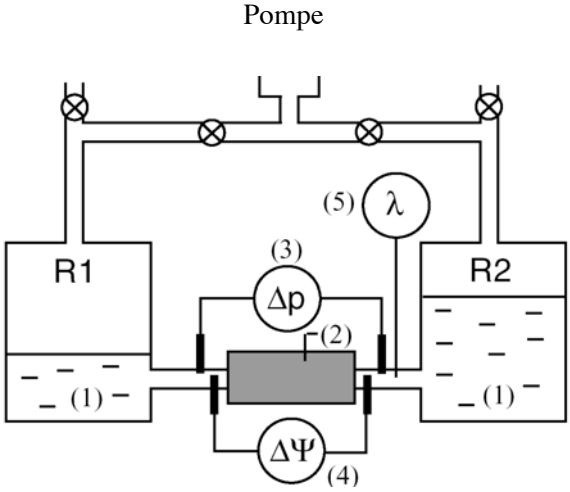

Figure 1.2 : Système de mesure de laboratoire du coefficient de couplage électrocinétique (1) Réservoirs de fluide poral R1 et R2. (2) Echantillon. (3) Capteurs de pression. (4) Electrodes non-polarisables reliées à un voltmètre permettant la mesure de la différence de potentiel. (5) Mesures de la conductivité électrique de l'électrolyte. La pression est contrôlée par de l'azote qui n'a aucun effet sur le pH et la salinité de l'électrolyte.

1.4.2.2. Autres dispositifs expérimentaux

L'échantillon, placé en bas d'une colonne de plexiglas de 2 m de hauteur, est en équilibre avec de l'eau à conductivité électrique donnée (figure 1.3a). Deux électrodes non

polarisables Ag/AgCl de type REF321 de chez Radiometer Analytical sont positionnées aux bornes de l'échantillon afin de mesurer la différence de potentiel électrique.

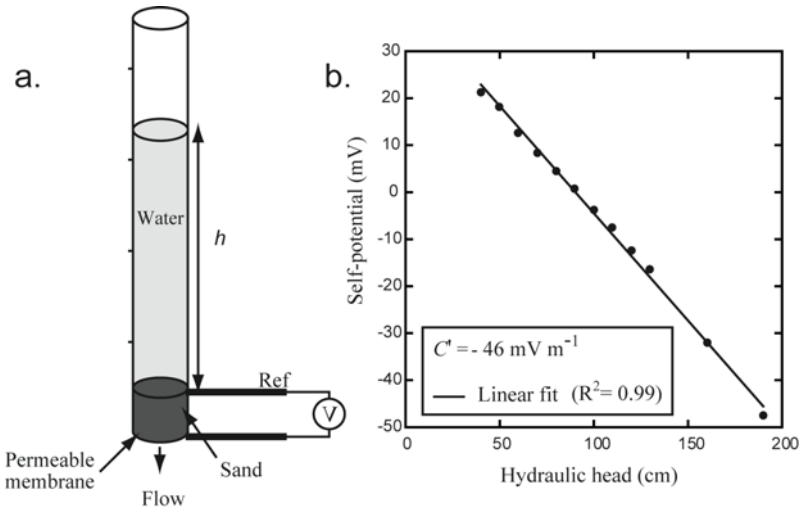

Figure 1.3: Dispositif expérimental pour déterminer le coefficient de couplage électrocinétique. **a.** Dispositif expérimental montrant l'échantillon situé en bas d'un tube de plexiglass. La différence de potentiel électrique aux bornes de l'échantillon est mesurée avec un voltmètre Metrix MX-20 et de deux électrodes non polarisables $Ag/AgCl_2$. **b.** Représentation graphique de la réponse de potentiel électrique en fonction de différentes charges hydrauliques. Le coefficient de couplage correspond à la pente de la tendance linéaire.

Une quantité d'eau est injectée à un temps *t*, et on mesure la différence de potentiel induite par la différence de hauteur d'eau (Figure 1.3b). Le coefficient de couplage électrocinétique *C'* associé aux hauteurs d'eau est déterminé à partir de l'équation (1.25).

1.5. Conclusion

A l'échelle microscopique, les réactions chimiques de complexation entre la surface d'un minéral et l'électrolyte poral est à l'origine de la création de la double couche électrique. L'entraînement de l'excès de charges contenu dans la couche diffuse par l'écoulement du fluide donne naissance à une densité de courant électrocinétique. Dans les équations de Maxwell, le potentiel électrique quasi-statique associé à la divergence de cette densité de courant correspond au phénomène d'électrofiltration. Nous avons vu que nous pouvons adapter cette théorie à des milieux déformables par l'application de la théorie de Biot. Nous verrons dans le Chapitre 3, le cas d'une distribution de potentiel électrique associé à une perturbation hydromécanique à l'échelle d'une cuve analogique. Le coefficient de couplage

électrocinétique est un paramètre indispensable afin de quantifier l'électrofiltration et d'interpréter les signaux de potentiel spontané. Nous allons donc étudier dans le chapitre suivant les différents paramètres qui peuvent l'influencer afin d'améliorer l'interprétation des données de potentiel spontané.

1.6. Références

Crespy, A., A. Bolève, and A. Revil, 2007. Influence of the Dukhin and Reynolds numbers on the apparent zeta potential of granular media, *J. Colloid Interface Sci.,* 305, 188-194, 2007.

Fitterman, D. V., 1979. Theory of electrokinetic-magnetic anomalies in a faulted half-space, *J. Geophys. Res.*, *84*, 6031-6041.

Freund, F., A. Takeuchi, and B.W.S. Lau, 2006. Electric currents streaming out of stressed igneous rocks. A step toward understanding pre-earthquake low frequency EM emissions, *Physics and Chemistry of the Earth*, 31, 389-396.

Gex, P., 1980. Electrofiltration phenomena associated with several dam sites, *Bulletin of the Society Vaud Science and Nature*, 357(75), 39-50.

Hearst, J.R., P.H. Nelson, and F.L. Paillett, 2000. Well logging fot physical properties, Wiley-VCH Verlag GmBH, Germany.

Ishido, T., and H. Mizutani, 1981. Experimental and theoretical basis of electrokinetic phenomena in rock-water systems and its applications to geophysics, *J. Geophys. Res.,* 86, 1763-1775.

Leroy, P., and A. Revil, 2004. A triple-layer model of the surface electrochemical properties of clay minerals, *J.Colloid Interface Sci.*, 270, 371-381.

Linde, N., D. Jougnot, A. Revil, S. Matthäi, T. Arora, D. Renard, and C. Doussan, 2007. Streaming current generation in two-phase flow conditions, *Geophys. Res. Lett.,* 34(3), L03306, doi: 10.1029/2006GL028878.

Marshall, D.J., and T.R. Madden, 1959. Induced polarization, a study of its causes, *Geophysics,*4(4),790-816.

Mendelson, K. S., and M. H. Cohen, 1982. The effect of grain anisotropy on the electrical properties of sedimentary rocks, *Geophysics*, 47(2), 257–263.

Morgan, F. D., Williams, E. R., and T. R. Madden, 1989. Streaming potential of westerly granite with applications, *J. Geophys. Res.,* 94, 12,449-12461.

Naudet, V., A. Revil, J.-Y. Bottero, and P. Bégassat, 2003. Relationship between self-potential (SP) signals and redox conditions in contaminated groundwater, *Geophys. Res. Lett.,* 30(21), 2091, doi : 10.1029/2003GL018096.

Overbeek, J.T.G., 1952. Electrochemistry of the double layer, *Colloïd Science*, 1, 115-193.

Palciauskas, V. V., and P. A. Domenico, 1989. Fluid pressures in deforming porous rocks, *Water Resour. Res.*, 25, 203-213.

Perrier, F., G. Petiau, G. Clerc, V. Bogorodsky, E. Erkul, L. Jouniaux, D. Lesmes, J. Macnae, J, Meunier, D. Morgan, D. Nascimento, G. Oettinger, G. Schwartz, H. Toh, M. Valiant, K. Vozoff, and O. Yazici-Çakin, 1997. A one-year systematic study of electrodes for long period measurements of the electric field in geophysical environments, *J. Geomag. Geoelectr.*, 49, 1677-1696.

Revil, A. & Leroy, P., 2004. Governing equations for ionic transport in porous shales, *J. of Geophys. Res.*, 109(B03208), doi 10.1029/2003JB002755.

Revil and N. Linde, 2006. Chemico-electromechanical coupling in microporous media, *J. Colloid Interface Sci.,* 302, 682–694.

Revil, A., Pezard, P.A., Glover, P.W.J., 1999a. Streaming potential in porous media: 1. Theory of the zeta potential. *J. Geophys. Res.* 104, 20021–20031.

Revil, A., H. Schwaeger, L. Cathles III, and P. Manhardt, 1999b. Streaming potential in porous media 2. Theory and application to geothermal systems, *J. Geophys. Res.*, 104(B9), 20033-20048.

Revil, A., and P.W.J. Glover, 1997. Theory of the ionic-surface conduction in porous media, *Phys. Review, B*, 55(3), 1,757-1,773.

Revil, A., P. Leroy, and K. Titov, 2005. Characterization of transport properties of argillaceous sediments. Application to the Callovo-Oxfordian Argillite, *J. Geophys. Res.*, 110, B06202.

Revil, A., D. Hermitte, E. Spangenberg, and J.J Cochmé, 2002b. Electrical properties of zeolitized volcaniclastic materials, *J. Geophys Res.*, 107(B8), 2168, doi:10.1029/2001JB000599.

Sill, W. R., 1983. Self-potential modeling from primary flows, *Geophysics, 48*, 76– 86.

Suski, B., A. Revil, K. Titov, P. Konosavsky, M. Voltz, C. Dagès, O. Huttel, 2006. Monitoring of an infiltration experiment using the self-potential method, *Water Resources Research,* 42.

Chapitre 2 :

Le coefficient de couplage électrocinétique

2.1. Introduction

Nous avons vu dans le chapitre précédent que le principal paramètre qui permettait d'interpréter les signaux de potentiel spontané était le coefficient de couplage électrocinétique. Dans l'hypothèse classique où la conductivité de surface est négligeable, ce coefficient est lié au potentiel ζ par l'équation d'Helmholtz Smolukovski (Equation 1.2, Chapitre 1). Toutefois, des études montrent que lorsque d'autres effets comme la conductivité de surface des grains et l'influence d'un écoulement inertiel non visqueux ne sont pas pris en compte, cette équation à tendance à sous-estimer l'amplitude du potentiel ζ (Somasundaran and Kulkarni, 1973). La loi linéaire de Darcy n'est valable que pour un régime laminaire visqueux, mais qu'en n'est-il des régimes inertiel laminaire et turbulent ? Dans les milieux volcaniques, avant une éruption, les écoulements souterrains résultant d'une variation brusque de la pression de l'eau interstitielle ne sont pas toujours dans le régime laminaire visqueux. Il paraît donc indispensable, afin d'interpréter quantitativement les signaux de potentiel spontané, de connaître l'influence du nombre de Reynolds sur le potentiel zêta apparent ou sur le coefficient de couplage électrocinétique.

Dans ce chapitre, nous discutons les différents paramètres pouvant influencer le coefficient de couplage électrocinétique, puis nous présenterons un modèle corrigeant le potentiel ζ apparent à la fois de la conductivité de surface, par l'intermédiaire du nombre de Dukhin, et du nombre de Reynolds dépendant du régime d'écoulement. Cette étude a fait l'objet de deux articles dans les revues scientifiques *Journal of Colloid and Interface Science* (2007) et *Journal of Geophysical Research* (2007).

2.2. Influence de la Perméabilité

Lorne et al. (1999a) ont étudié le potentiel ζ à partir de mesures de potentiel d'électrofiltration sur des échantillons broyés de grès de Fontainebleau. Ils ont mis en évidence les variations du potentiel ζ apparent (et par extension celles du coefficient de couplage électrocinétique) en fonction de la perméabilité. Afin de démontrer cette dépendance, ils ont utilisé des conductivités de fluides et des pH différents. Pour des perméabilités inférieures à 10 Darcy, le coefficient de couplage reste constant tandis qu'il diminue fortement pour des perméabilités supérieures à 50 Darcy. Comme aucune correction du nombre de Reynolds n'a été appliquée à ces données, il est très probable qu'elles reflètent un effet de ce nombre sans dimension pour les hautes perméabilités.

Moore et Glaser (2007) ont étudié en laboratoire la réponse du potentiel spontané sur des échantillons intacts de granite Sierra soumis à fracturation hydraulique. Ils ont remarqué qu'à des pressions basses, la variation de potentiel spontané en fonction des sauts de pression est linéaire, indiquant un coefficient de couplage constant (comme le prévoit l'équation de Helmholtz-Smolukovski). Cependant pour des pressions d'injection approchant la pression de rupture, la relation n'est plus linéaire et l'amplitude du coefficient de couplage électrocinétique augmente exponentiellement de 80%. L'augmentation du coefficient de couplage et sans doute liée à la dilatance des microfractures à haute pression. Ils ont montré que pendant l'injection précédant la fracturation hydraulique, la valeur du coefficient de couplage augmente suivant la relation :

$$|C| = 200 + 3{,}7 \times 10^{27} k^{1,5} \qquad (2.1)$$

où C est le coefficient de couplage électrocinétique (mV/MPa) et k est la perméabilité (m^2). La Figure 2.1 nous montre l'évolution du coeffcient de couplage en fonction de la perméabilité suivant la relation 2.1.

Selon Moore et Glaser (2007), le phénomène de dilatance causé par la microfracturation de l'échantillon cause une diminution de la tortuosité hydraulique, laquelle est inversement proportionnelle à la perméabilité. Les données de laboratoire obtenues suggèrent une diminution substantielle de la tortuosité et donc une augmentation du coefficient de couplage électrocinétique. Il se peut également que cette augmentation du

coefficient de couplage électrocinétique soit due à une diminution de la contribution de la conductivité de surface à la conductivité totale de l'échantillon.

A partir des deux exemples précédents, il est clair qu'il faut comprendre les effets du nombre de Reynolds et du nombre de Dukhin sur le comportement électrocinétique. C'est l'objet de l'article qui sera présenté en section 2.7 du présent chapitre.

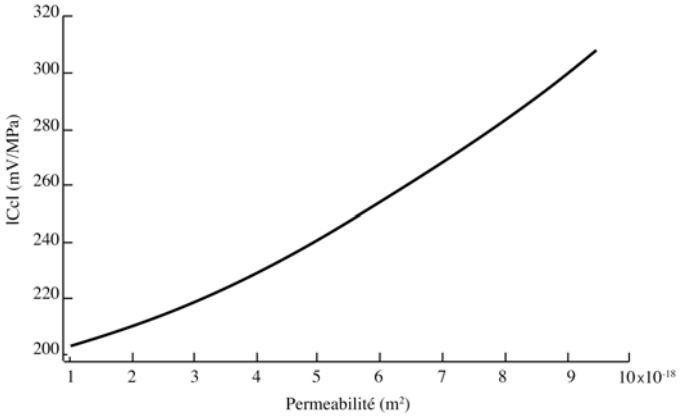

Figure 2.1 : Variation des valeurs du coefficient de couplage électrocinétique en fonction de la perméabilité suivant la relation $|Cc| = 200 + 3{,}7 \times 10^{27} k^{1,5}$. D'après Moore and Glaser (2007).

2.3. Influence de la Température

Les théories concernant l'influence de la température sur le potentiel ζ ont été pendant longtemps contradictoires. Morgan et al. (1989) ont montré que le potentiel ζ d'échantillons de granite était indépendant de la température. Ceci est en contradiction avec les données expérimentales de Somasundaran and Kulkani (1973) et de Ishido et Mizutani (1981). Ces derniers ont réalisé leurs expériences avec des solutions de Al-K-NO_3 à des températures allant de 20°C à 80°C, ils montrent une nette augmentation du potentiel ζ (ici positif) jusqu'à une température de 52°C puis une chute brutale. Ils expliquent cette forte décroissance par une probable desorption des ions Al^{3+} de la surface des grains de quartz. Toutefois, ils ne donnent aucune explication concernant le signe positif du potentiel ζ et son augmentation jusqu'à la température de 52°C. Guichet et Zuddas (2003) expliquent le signe postif du potentiel ζ par la précipitation de la gibbsite enrobant la surface du quartz et montrent que la précipitation d'un minéral secondaire peut cacher les propriétés électriques de la roche

primaire. Le couplage hydroélectrique est controlé par la phase minéralogique sur laquelle l'eau s'écoule.

Dans le cas où la surface n'est pas chimiquement altérée, Revil et al. (1999a) ont proposé un modèle mécanistique reposant sur la théorie de la double couche électrique. Leur modèle prédit que le potentiel ζ est influencé par la température selon la relation :

$$\zeta(T) = \zeta(T_0)\left[1 + \vartheta\zeta(T - T_0)\right], \tag{2.2}$$

où T_0 est la température de référence (25°C) et $\upsilon_\zeta = 1{,}71.10^{-2}$ °C^{-1}. Ce modèle correspond très bien aux données expérimentales d' Ishido et Mizutani (1981) pour une solution de KNO_3. Revil et al. (1999b) expliquent les différents résultats par la cinétique des réactions chimiques qui ont lieu dans la double couche électrique d'où la nécéssité de laisser saturer les échantillons dans l'électrolyte durant 48 heures pour atteindre l'équilibre thermodynamique. Ceci donne une idée de la cinétique des réactions de surface présentées brièvement dans le chapitre 1.

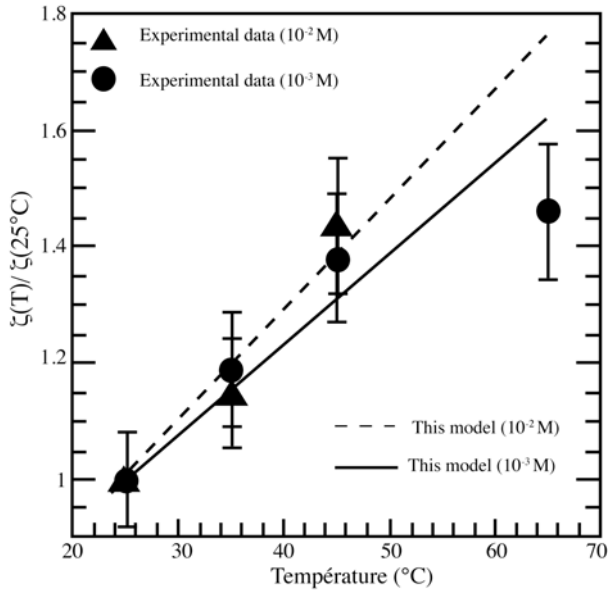

Figure 2.2 : Influence de la température sur le potentiel ζ (silice, pH 7, KNO_3). Données expérimentales de Somasundaran and Kulkarni (1973) et Ishido et Mizutani (1981).

2.4. Influence de la salinité et du pH

2.4.1. La conductivité électrique

La valeur absolue du potentiel ζ décroît lorsque la salinité de l'électrolyte augmente. Ce résultat peut être reproduit par la théorie de la Double Couche Electrique. Il en résulte que plus le fluide est conducteur, plus faible sera le coefficient de couplage électrocinétique. Lorne et al. (1999) ont mis en évidence une diminution du potentiel ζ avec la conductivité du fluide pour des échantillons broyés de grès de Fontainebleau trempés dans différentes solutions de KCl. La diminution du coefficient de couplage électrocinétique se retrouve sous la forme d'une relation linéaire dans un diagramme log-log. Une telle dépendance a été démontrée théoriquement par Revil et al. (1999) en utilisant un modèle de double couche. Il en ressort :

$$\zeta = a + b \log_{10} \sigma_f, \tag{2.3}$$

où a et b sont deux constantes indépendantes de la salinité mais dépendantes de la température. Grâce à l'équation d'Helmholtz-Smolukovski et l'équation (2.3), nous pouvons estimer la valeur du coefficient de couplage électrocinétique à une conductivité électrique donnée. Nous avons également mis en évidence cette relation dans Crespy et al. (2007) (voir section 2.7) sur des billes de verre saturées par des solutions de NaCl à différentes conductivités.

2.4.2. Influence du pH

Le pH influence la charge de surface des grains ainsi que les réactions électrochimiques entre la surface des grains et l'électrolyte. Le pH va donc agir sur le coefficient de couplage électrocinétique. De nombreuses études concernant la variation du potentiel d'électrofiltration en fonction du pH ont été réalisées (Ishido et Mizutani, 1981 ; Lorne et al., 1999 ; Morgan et al., 1989 ; Revil et al., 1999 ; Hase et al., 2003). Ces études montrent que plus le pH augmente, plus le potentiel ζ devient négatif (Figure 2.3). Leurs études montrent également que pour des valeurs de pH très faibles, on observe une inversion du signe du potentiel ζ au point isoélectrique (IEP) aussi appelé Point de Charge Nulle.

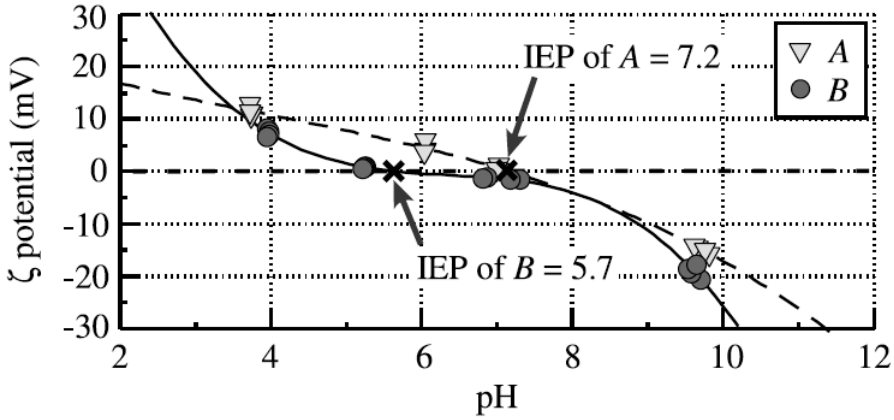

Figure 2.3 : Relation typique entre pH et valeurs du potentiel ζ (les échantillons A et B son issus des volcans Uwa-Komezuka et Mt Okamado respectivement. IEP représente le point isoélectrique valeur de pH pour laquelle le potentiel ζ est nul (selon Hase et al., 2003).

Les échantillons étudiés par Hase et al. contiennent peu de SiO_2 (point isoélectrique bas) mais de nombreux éléments ayant des points isoélectriques hauts. Les auteurs pensent que les valeurs positives du potentiel ζ pourraient être liées à une relative abondance d'éléments ayant un IEP élevé.

2.5. Influence de la Conductivité de Surface

Von Smolukovski fut le premier à mettre en évidence le rôle des ions présents dans la double couche qui participent à un accroissement de la conductivité électrique de l'échantillon (Dukhin and Derjaguin, 1974). La concentration des ions est plus importante à proximité de la

surface du minéral que dans l'électrolyte plus éloigné de la surface des grains. Une partie de ces ions contribue à la conductivité électrique. Cette contribution est appelée conductivité de surface σ_s. Smolukovski pensait en son temps que les ions de la double couche étaient mobiles uniquement au-delà du plan de cisaillement de cette dernière, si bien que le potentiel ζ qui apparaît dans son équation prend en compte la participation de la conductivité de surface.

Dans le milieu pétrolier, de nombreux modèles ont mis en évidence dès les années 50 le rôle de la conductivité de surface dans la conductivité des roches réservoirs. L'un des modèles les plus populaires est le modèle de Waxman et Smits (1968). Pour une roche isotrope et saturée en eau, la conductivité électrique σ peut être reliée à la conductivité électrique du fluide σ_f par (Waxman and Smits, 1968),

$$\sigma = \frac{\sigma_f}{F} + \sigma_s \tag{2.4}$$

où σ_s est la conductivité de surface et F le facteur de formation de la roche.

Nous avons vu dans le Chapitre 1 que lorsque la conductivité de surface peut être négligée et dans le cas d'un écoulement visqueux laminaire, le coefficient de couplage est lié au potentiel ζ par l'équation de Helmholtz-Smolukovski :

$$C_{HS} = \frac{\varepsilon_f \zeta}{\eta_f \sigma_f}. \tag{2.5}$$

Cette formulation est toujours la base de la détermination du potentiel ζ de beaucoup de matériaux même si nous savons qu'elle est sous-estimée. Lorsque d'autres effets (comme la conductivité de surface ou l'influence d'écoulement non-visqueux) doivent être pris en compte le potentiel ζ déterminé à partir de l'équation de HS est appelé « potentiel ζ apparent ».

$$\zeta_{app} = \frac{\eta_f \sigma_f}{\varepsilon_f} C. \tag{2.6}$$

Nous pouvons trouver, dans la littérature, de nombreux modèles pour corriger le potentiel ζ de l'effet de la conductivité de surface (Pengra et al., 1999). Cependant la plupart de ces corrections ont été réalisées selon l'hypothèse que la contribution principale de la conductivité de surface provenait de l'électromigration des ions dans la couche diffuse (Bernabé, 1998). Actuellement une série de travaux montre que la conductivité de surface agit dans la couche de Stern et non dans la couche diffuse (O'Brien and Rowlands, 1993 ; Leroy and Revil, 2004). Plusieurs auteurs supposent qu'il existe une relation linéaire entre la conductivité électrique de l'échantillon et la conductivité électrique du fluide (Pengra et al., 1999) mais il s'avère que cette linéarité est approximative à cause d'une modification des chemins préférentiels de migration des cations et des anions quand la conductivité électrique décroît

(Agapiou and De Vries, 1989 ; Bernabé and Revil, 1995 ; Revil et al., 2002).

Dans la Section 2.7 nous proposons un modèle pour corriger le potentiel ζ apparent de l'influence du nombre de Dukhin qui représente le ratio entre la conductivité de surface et la conductivité de l'électrolyte.

2.6. Influence du Nombre de Reynolds

Lorsque le flux hydrique augmente, la loi de Darcy, qui décrit une relation linéaire entre la conductivité hydraulique K (m s^{-1}) et la charge hydraulique h (m) n'est plus valide. D'un régime d'écoulement laminaire visqueux, nous passons à un écoulement inertiel laminaire pour lequel le terme inertiel domine dans l'équation de Navier-Stokes. Quant au régime turbulent il n'est atteint que pour des nombres de Reynolds (Re) très élevés (supérieurs à 200).

Teng et Zhao (2000) ont proposé une prise de moyenne volumique de l'équation de Navier-Stokes pour un volume élémentaire de milieu poreux saturé par un liquide Newtonien. En négligeant les forces électrostatiques et donc la contribution électro-osmotique à la vitesse d'infiltration, à l'état stationnaire, on peut réécrire une nouvelle loi de Darcy apparente sous la forme :

$$\mathbf{U} = -\frac{\rho_f g k_0}{\eta_f (1+\mathrm{Re})}\frac{h}{L}\mathbf{z}, \tag{2.7}$$

$$k / k_0 = 1/(1+\mathrm{Re}), \tag{2.8}$$

où k est une perméabilité apparente et k_0 une perméabilité intrinsèque du milieu poreux définit dans le régime d'écoulement visqueux laminaire. Cette équation n'est plus une relation linéaire entre flux et gradient de pression puisque le nombre de Reynolds dépend du gradient de pression du fluide. Nous verrons dans les articles suivants que le rôle du nombre de Reynolds dans le flux hydrique implique nécessairement un rôle du nombre de Reynolds dans la définition d'un coefficient de couplage électrocinétique apparent.

Dans leurs travaux publiés en 2008, Jardani et al. ont montré, lors d'expériences de pompage, que l'anomalie de PS n'était pas centrée sur le puits. Ils montrent grâce à des simulations numériques que cette assymétrie est directement liée à l'influence du nombre de Reynolds.

2.7. Présentation de deux Articles Scientifiques

L'étude de l'influence des nombres de Reynolds et de Dukhin a fait l'objet de la rédaction de deux articles scientifiques intitulés : « Influence of the Dukhin and Reynolds numbers on the apparent zeta potential of granular porous media » par Crespy A., A. Bolève and A. Revil, publié en 2007 dans *Journal of Colloid and Interface Science* et « Streaming potentials of granular media: Influence of the Dukhin and Reynolds numbers » par Bolève A., A. Crespy, A. Revil, F. Janod, J. L. Mattiuzzo, publié en 2007 dans *Journal of Geophysical Research*. Nous présentons le premier de ces deux articles dans les pages qui suivent. Le premier article est destiné aux électrochimistes et montre comment l'emploi de l'équation d'Helmholtz-Smoluchowski sans termes correctifs pour les effets des nombres de Dukhin et de Reynolds peut conduire à des valeurs erronées du potentiel zêta. Le second article est destiné aux géophysiciens et montre, outre le rôle des nombres de Dukhin et de Reynolds, sur les équations de couplage électrocinétique, comment utiliser cette théorie pour une application géophysique.

Influence of the Dukhin and Reynolds numbers on the apparent zeta potential of granular porous media

A. Crespy (1), A. Bolève (1, 2), and A. Revil (1)

(1) CNRS-CEREGE, Université Paul Cézanne, Dept. Hydrogeophysics and Porous Media, 13545 Aix en Provence, Cedex 4, France
(2) SOBESOL, Savoie Technolac, BP 230, F-73375 Le Bourget du Lac Cedex, France

Abstract. The Helmholtz-Smoluchowski (HS) equation represents a widely used equation to determine the apparent zeta potential of porous materials using the streaming potential method. We present a model able to correct this apparent zeta potential of granular media of the influence of the Dukhin and Reynolds numbers. The Dukhin number represents the ratio between the surface conductivity (mainly occurring in the Stern layer) and the pore water conductivity. The Reynolds number represents the ratio between inertial and viscous forces in the Navier-Stokes equation. We show here that the HS-equation can lead to serious errors if it is used to predict the dependence of zeta potential for flow in the inertial laminar flow regime without taking into account these corrections. For indifferent 1:1 electrolytes (like sodium chloride), we derived two simple scaling laws for the dependence of the streaming potential coupling coefficient (or the apparent zeta potential) with the Dukhin and Reynolds numbers. Our model is compared with a new set of experimental data obtained on glass bead packs saturated with NaCl solutions at different salinities and pH. We find a fairly good agreement between the model and these experimental data.

1. Introduction

The streaming current and streaming potential techniques measure electrical currents or electrical fields, respectively, occurring when pressure-driven flow in a porous material drags the excess charge contained in the electrical diffuse layer coating the surface of the grains (e.g., [1]). The characterization of the electrochemistry of the pore water / solid

interface is often based on these techniques because of their simplicity. This is done despite the fact that the actual position of the shear plane (defined as the surface for which the relative velocity between the solid grains and the fluid is null) is not well known. The measurement of the streaming potential coupling coefficient C (expressed in V Pa^{-1}) characterizes the sensitivity between the streaming potential and the pore fluid pressure driving the flow of the pore water ([1, 2]). When surface conductivity of the grains can be neglected and in the case of viscous-inertial flow, the streaming potential coupling coefficient is related to the zeta potential by the well-known Helmholtz Smoluchowski (HS-) equation (e.g., [3]):

$$C_{HS} = \frac{\varepsilon_f \zeta}{\eta_f \sigma_f}, \tag{1}$$

where ε_f is the dielectric constant of water (ε_f = 80 x $8.84.10^{-12}$ F m^{-1}), ζ is the zeta potential (a key parameter characterizing the electrical potential of the inner part of the electrical diffuse layer or more precisely the electrical potential of the shear plane defined above), η_f is the dynamic viscosity of the pore water (in Pa s), and σ_f is the electrical conductivity of the brine (in S m^{-1}). Equation (1) is still the basis for the determination of the zeta potential of various materials by numerous researchers even if it is know that this equation tends to underestimate the magnitude of the zeta potential [3-5].

When other effects (like surface conductivity of the grains or the influence of non-viscous flow) need to be taken into account, the zeta potential determined from the HS-equation can only be called an “apparent zeta potential”. The apparent zeta potential is therefore defined by

$$\zeta_{app} = \frac{\eta_f \sigma_f}{\varepsilon_f} C, \tag{2}$$

A number of models were developed in the literature to correct the apparent zeta potential of the effect of surface conductivity (e.g., [1]). However most of these corrections were performed under the assumption that the main contribution to surface conductivity is

coming from electromigration of the ions in the electrical diffuse layer (e.g., [6]). In addition, several authors assumed a linear relationship between the bulk electrical conductivity and the conductivity of the pore water solution [1]. Nowadays, a set of evidences indicate that most of surface conductivity occurs in the Stern layer and not in the diffuse layer (e.g., [7-9]). It is also known that the relationship between the effective conductivity of the porous medium and the conductivityof the pore water solution is not linear because of the change in the preferential migration pathways of the cations and anions when the electrical conductivity decreases [10-17].

We propose below a model to correct the apparent zeta potential of the influence of two dimensionless numbers, the Dukhin and the Reynolds numbers, in the case of brine-saturated granular media (however we suspect that our method would work for any type of porous materials if the length scale associated with surface conductivity can be properly defined).

2. Influence of the Dukhin Number

We consider in this section, the electrical conductivity σ of a granular medium. The electrical conductivity of water-saturated granular media has been the subject of numerous investigations in the literature (e.g., [10] and references therein). As shown below, electrical conductivity of the porous composite depends on the conductivity of the pore water, the tortuosity of the connected pore space, the porosity, and the surface conductivity due to electro-migration and electro-osmotic transport in the electrical double layer coating the surface of the grains. Surface conductivity has two contributions. Historically, surface conduction was supposed to be located in the Gouy-Chapman diffuse layer [11]. More recently, several researchers have shown that surface conductivity occurs mainly in the Stern layer [9, 11-12, 17-21]. For a long-time, the electrical conductivity of granular composites

was obtained by solving the local boundary value problem of electrical conduction for simplified geometries (see [13]) However, these formulations were not general enough. A key-textural parameter controlling the electrical conductivity of a water-saturated porous medium was defined by petrophysicists and is called the electrical formation factor. The formation factor is equal to the tortuosity of the path of the ions through the connected porosity divided by the porosity (see [14-16], and references therein). The electrical formation factor can be obtained by volume-averaging the local current density (obtained from the Nernst-Planck equation) or by volume-averaging the Joule dissipation occurring during electrical conduction [14] as both fluxes and dissipation are upscalable quantities.

If we do not distinguish between the different paths taken by the cations and anions (see [7] and [17]), the electrical conductivity of a water-saturated granular medium is ([2], [17]):

$$\sigma = \sigma_f \mathrm{Du}\,, \text{ as } \mathrm{Du} \geq 1, \tag{3}$$

$$\sigma = \frac{\sigma_f}{F}\left[F\mathrm{Du} + \frac{1}{2}(1-\mathrm{Du})\left(1-\mathrm{Du}+\sqrt{(1-\mathrm{Du})^2+4F\mathrm{Du}}\right)\right], \text{ as } \mathrm{Du} \leq 1. \tag{4}$$

These equations result from the application of the differential effective medium theory. In Equation (4), F is the electrical formation factor ($F = \alpha/\phi$, α is the tortuosity of the pore space and ϕ is the porosity of the medium). The parameter Du is a dimensionless number called the Dukhin's number. It represents the ratio between the surface conductivity of the grains to the electrical conductivity of the pore water (e.g., [9]):

$$\mathrm{Du} \equiv \sigma_S / \sigma_f\,. \tag{5}$$

For packing of spheres of diameter d_0, the macroscopic surface conductivity σ_S is related to the specific surface conductivity Σ_S, by ([18]),

$$\sigma_S = \frac{6\Sigma_S}{d_0}\,. \tag{6}$$

The specific surface conductivity can be independently determined from double or triple layer models [7].

The streaming potential coupling coefficient is defined by,

$$C = \left(\frac{\partial \psi}{\partial p} \right)_{\mathbf{J}=0}, \tag{7}$$

$$C = -\frac{L}{\sigma}, \tag{8}$$

$$C = \frac{\varepsilon_f \zeta}{\eta_f F \sigma}, \tag{9}$$

In these equations, **J** is the total current density (expressed in A m^{-2}) including Ohm conduction and a source current density of electrokinetic nature, ψ is the streaming potential (in V), p is the fluid pressure (in Pa), L is the streaming current coefficient (in A Pa^{-1} m^{-3}), and ζ is the intrinsic zeta potential (in V). From Eqs. (2) and (9), the ratio between the intrinsic zeta potential and the apparent zeta potential is therefore related to the Dukhin number by,

$$\frac{\zeta_{app}}{\zeta} = \frac{1}{H(\mathrm{Du})}, \tag{10}$$

where the function H(Du) (dimensionless) is defined by,

$$H(\mathrm{Du}) = F\mathrm{Du}\ , \text{ as } \mathrm{Du} \geq 1, \tag{11}$$

$$H(\mathrm{Du}) = F\mathrm{Du} + \frac{1}{2}(1-\mathrm{Du})\left(1-\mathrm{Du}+\sqrt{(1-\mathrm{Du})^2+4F\mathrm{Du}}\right), \text{ as } \mathrm{Du} \leq 1, \tag{12}$$

Equation (10) provides the first correction function for the zeta potential. It is easy to check that sign(ζ) = sign(ζ_{app}) (where sign(a) is the sign of the value of the parameter a) and that $|\zeta| \geq |\zeta_{app}|$. Therefore the magnitude of the intrinsic zeta potential is always larger or equal to the magnitude of the apparent zeta potential.

3. Influence of the Reynolds Number

Gorelik [22] recently used dimensional analysis to demonstrate that the influence of the Reynolds number upon the streaming potential coupling coefficient corresponds to a multiplication of the Helmholtz-Smoluchowski equation by an unspecified function that depends solely on the Reynolds number. We look below for an explicit (quantitative) relationship between the streaming potential coupling coefficient and the Reynolds number. The Reynolds number expresses the ratio of inertial to viscous forces in the Navier-Stokes equation (e.g., [23]). For a capillary of radius R (in m), U being the strength of the (Darcy) seepage velocity (in m s^{-1}), the Reynolds number is defined by (e.g., [23]),

$$\mathrm{Re} = \frac{\rho_f U R}{\eta_f}. \tag{13}$$

In a porous material, the radius of the capillary R should be replaced by a corresponding characteristic length scale of the porous material, e.g., the Λ-length defined by [14-16] and discussed in [24, 25]). There are three distinct flow regimes based on the value of the Reynolds number [23]. The domain Re << 0.1 corresponds to the viscous-laminar flow regime, the domain 0.1 << Re << 100 corresponds to the inertial-laminar flow regime, while the domain Re >> 100 corresponds to the turbulent flow regime, which is not investigated in this paper because of no practical interests.

Teng and Zhao [26] derived a generalized Darcy equation valid for the two first domains. They volume-averaged the local Navier-Stokes momentum equation over a representative elementary volume of a porous material. Neglecting the electrostatic force in this equation, and therefore the electro-osmotic contribution in the seepage velocity, the generalized Darcy equation in steady state conditions of flow is ([26]),

$$\mathbf{U} = -\frac{k}{\eta_f}\nabla p, \tag{14}$$

$$k / k_0 = 1/(1 + \mathrm{Re}), \tag{15}$$

where k is an apparent permeability entering the Darcy law extended in the inertial-flow regime and k_0 is the intrinsic permeability of the porous medium, defined in the viscous laminar flow regime.

At the scale of a representative elementary volume of the porous material, the streaming current density is given by (e.g., [27]),

$$\mathbf{J}_S = \overline{Q_V}\,\mathbf{U}. \tag{16}$$

where $\overline{Q_V}$ corresponds to the volumetric excess charge density per unit pore volume. If the shear plane is coincident with the Helmholtz plane, this charge density is equal to the excess of charge of the diffuse layer per unit pore volume. Therefore Equation (17) expresses the fact that the source current density is equal to the excess of charge of the pore fluid $\overline{Q_V}$ time the seepage velocity **U**. Using Eq. (14) yields,

$$\mathbf{J}_S = -\frac{k\overline{Q_V}}{\eta_f}\nabla p, \tag{17}$$

and k is the apparent permeability defined above. The streaming potential coupling coefficient can be related to the electrical conductivity of the porous pack σ by $C_0 = k_0\overline{Q_V}/\eta_f\sigma$ [27]. As the Darcy velocity is influenced by the increase of the Reynolds number (for Re > 0.1), the Reynolds number also influences the value of the streaming potential coupling coefficient. Using Eqs. (15) and (17), the streaming potential coupling coefficient is related to the Reynolds number by,

$$C / C_0 = 1/(1 + \mathrm{Re}), \tag{18}$$

where C_0 is the streaming potential coupling coefficient in the viscous laminar flow regime and C is the measured coupling coefficient. The apparent zeta potential (obtained by using an expression for the streaming potential coupling coefficient that do not account for the

Reynolds number) is related to the true (intrinsic or corrected) zeta potential ζ_0 by

$$\zeta_{app} = \zeta_0 \left(\frac{1}{1 + \mathrm{Re}} \right). \tag{19}$$

We have sign(ζ_0) = sign(ζ_{app}) and $|\zeta_0| \geq |\zeta_{app}|$.

4. Comparison with Experimental Data

The model developed for the streaming potential coupling coefficient (or the apparent zeta potential) in Sections 2 and 3 can be summarized by the following equation,

$$C = C_{HS} \frac{G(\mathrm{Re})}{H(\mathrm{Du})}, \tag{20}$$

where C is the measured or true coupling coefficient, G(Re) = 1/ (1 + Re), and H(Du) is defined in Section 2. In this section, we test the accuracy of equation (20) to determine the streaming potential coupling coefficient and therefore to demonstrate that the coupling coefficient is entirely controlled by the Dukhin and Reynolds dimensionless numbers.

4.1. Experimental Setups

The experimental setup for the measurement of the streaming potential coupling coefficient consists simply of a Plexiglas tube (2.5 cm in diameter) with an insulating permeable membrane placed at its bottom, with a coarse mesh (50 μm). Consequently the permeability of this membrane is always much larger than the permeability of the porous packs (for the beads with a diameter of 3000 μm, we used a coarser mesh). The glass beads are packed at the bottom of the tube and a given water pressure head is set up in the tube. We let the brine flowing through the sample, and the electrical (streaming) potential is measured at the end faces of the tubes and is reported as a function of the pressure head in the tube. This

protocol is described with more details in [28]. The resulting electrical potential is measured with two non-polarizable $Ag/AgCl_2$ electrodes (Ref321/XR300, Radiometer Analytical) located at the end-faces of the sample. We found that these electrodes are very stable over time and produce repeatable measurements. The voltages are measured with a voltmeter Metrix MX-20 (internal impedance 100 MOhm, sensitivity of 0.1 mV).

Each sample corresponds to a packing of glass beads of a given grain size. These samples are manufactured by Sigma-Aldrich. They are seven glass bead packs investigated here with mean grain size varying in the range 56-3000 μm. Each pack is chosen to have a very narrow log normal grain size distribution. The chemical composition of the glass is SiO_2 ~60.5%, Na_2O ~12 to 18 %, CaO ~5 to 12%, MgO ~4%, and Al_2O_3 ~1%. The measured porosity of the packs is $\phi = 0.40 \pm 0.02$ and this value is independent of the mean grain diameter of the pack.

The measurements of the streaming potential coupling coefficient were performed at different background pore water electrical conductivities using NaCl solutions with varying ionic strengths. We use the following set of brine conductivities ($3x10^{-2}$, 10^{-2}, $3x10^{-3}$, 10^{-3}, $3x10^{-4}$, and 10^{-4} S m^{-1}) at 25 ± 1°C. These solutions were prepared by measuring the weight of NaCl salt to add to a given solution of deionized or demineralized water or by measuring directly the conductivity of the solution with a conductivity meter (CDM-230, MeterLab™). The pH of the solution, measured with the pH-meter pH-330 (SET1-Fisher), is in the range 5.6 to 5.9 at 24.5 °C because of the solubility of the atmospheric CO_2. A set of measurements of the streaming potential coupling coefficient are reported on Figure 1. In this figure, we show the predictions of Eq. (20) and those made with the Helmholtz-Smoluchowski equation, Eq. (1).

We also measure the electrical conductivity of the porous packs using a frequency-dependent impedancemeter (Waynekerr Analyser 6425 performing measurements in the frequency range 30 Hz-300 kHz). For the electrical conductivity measurements, we use the

following set of brine conductivities (10^{-1}, $6x10^{-2}$, $3x10^{-2}$, 10^{-2}, $3x10^{-3}$, 10^{-3}, $3x10^{-4}$, and 10^{-4} S m^{-1}) at 25 ± 1°C. Electrical conductivity measurements were performed in this frequency domain with a two-electrode device (using stainless electrodes) according to the protocol described in [17]. The accuracy of the measurement is estimated to be 5% [17]. Typically, the measurements are obtained at the frequency for which the polarization of the electrodes can be neglected, generally few kHz.

4.2. Electrical Conductivity

In Figure 2, we plot the electrical conductivity of two glass bead packs, with mean grain diameter 86 and 151 μm, as a function of the electrical conductivity of the brine. We use Eqs. (3) and (4) to fit these experimental data in the purpose to determine the value of the surface conductivity and the electrical formation factor. The mean formation factor is 3.4 ± 0.1. This yields a tortuosity of the pore space of 1.36. Measurements made with the five other packs confirm this value.

The value of surface conductivity of each glass bead pack is reported as a function of the mean grain diameter of each pack on Figure 3. We see very clearly that surface conductivity is inversely proportional to the mean diameter of the medium as predicted by the most of the models [3, 13]. The value of the specific surface conductivity obtained from this trend, Σ_S = $4.0x10^{-9}$ S (at 25°C), is consistent with the double layer model prediction of [29] at a salinity of 10^{-3} S m^{-1}. A linear temperature correction for this specific surface conductivity is discussed in [17].

The “conductivity ratio” of the porous samples is defined by the ratio between the electrical conductivity of the porous pack to the conductivity of the brine. The conductivity ratios are plotted on Figure 4 as a function of the Dukhin numbers for all the samples. As discussed by [17], this provides a way to normalize electrical conductivity plots. We observe indeed that all the data fall on the same trend, which is well reproduced by the model. Linear

models are very often used to describe the electrical conductivity of a porous material as a function of the electrical conductivity of the brine [1]. However these models fail in reproducing this trend.

4.3. Coupling Coefficient

Using Eq. (9), we combine the measurements of the streaming potential coupling coefficient and the measurements of the electrical conductivity to determine the values of the zeta-potential in viscous-laminar flow conditions. For each experiment, the Reynolds number was accurately determined with a new equation determined in [30]:

$$\mathrm{Re} = \frac{1}{2}\left(\sqrt{1+c}-1\right), \tag{21}$$

$$c = \frac{d\rho_f}{\eta_f{}^2}\frac{{d_0}^3}{F(F-1)^3}\left(\frac{p}{H}\right), \tag{22}$$

where $d \approx 2.25 \times 10^{-3}$ is a dimensionless numerical constant, ρ_f is the bulk mass density of the pore water (1000 kg m^{-3}), H is the thickness of the porous pack (in m) (length of the sample), d_0 is the mean grain diameter of the pack (in m), and p is the fluid pressure at the bottom of the column. The values of the intrinsic zeta potential (corrected from the measured electrical conductivity of the investigated packs and corrected for the Reynolds numbers) are reported as a function of the logarithm of the electrical conductivity of the pore water on Figure 5. For simple supporting electrolytes, the zeta potential depends on the logarithm of the salinity (and therefore on the logarithm of the electrical conductivity) of the pore water over a wide range of salinity (see [3, 29] and references therein). Such a dependence was demonstrated theoretically in [29] using an electrical double layer model. So we can write,

$$\zeta = a + b\log_{10}\sigma_f\,, \tag{23}$$

where a and b are two constants. The constants a and b of Eq. (23), corresponding to the best

fit of the zeta-potential values, are reported on Figure 5. With the values of *a* and *b* and Eqs. (1) and (23), we can estimate the value of the Helmholtz-Smoluchowski equation for the streaming potential coupling coefficient at a given electrical conductivity of the pore water.

We first check the relationship between the streaming potential coupling coefficient and the Dukhin number ξ. On Figure 6, we plot the ratio between the apparent zeta potential and the intrinsic zeta potential as a function of the Dukhin number for the seven packs. Note that because the formation factor is roughly the same for all the samples, all the data fall on the same curve. There is a fairly good match between the theory and the experimental data.

We investigate now the relationship between the apparent zeta potential and the Reynolds number Re. On Figure 7, we plot the ratio between the apparent zeta potential and the intrinsic zeta potential versus the Reynolds number for the seven samples investigated in this study. All the data fall on the same curve while the measurements were performed at different salinities and with packs having different mean grain diameters. We found again a fairly good agreement between the theory and the experimental data.

4.4. Application to the pH dependence of the Zeta Potential

We make a last test of the present model to observe how the correction of the Reynolds number developed above is important to determine the intrinsic pH dependence of the zeta potential of glass bead packs. We measured the streaming potential coupling coefficient of coarse glass bead packs (with a mean grain diameter of 3000 μm) at various heads and with the same lengths of the packs. All the measurements were made at 25°C and performed with a background electrolyte (NaCl) conductivity of 10^{-3} Mol L^{-1}. Then, we used the Helmholtz-Smoluchowski equation to determine the apparent zeta potential and Eq. (19) to determine the intrinsic zeta potential corrected for the effect of the Reynolds number. The results are reported on Figure 8. There is clearly a strong difference between the two estimates. Clearly, the correction proposed in this paper is very promising to obtain reliable

estimate of the intrinsic zeta potential from electrokinetic measurements.

5. Concluding Statements

In experiments made with granular materials, the zeta potential needs very often to be corrected for the influence of two key dimensionless parameters, the Dukhin and the Reynolds numbers. The former account for the influence of surface conductivity and the second accounts for the influence of inertial forces in the flow rate. While a vast body of models and experimental data were already available in the literature to evaluate the influence of the Dukhin number upon the electrical conductivity of bead packs [10-16], it appears that the model presented in this paper is the first attempt to correct the zeta potential (or the streaming potential coupling coefficient) from the effect of both the Dukhin and Reynolds numbers. In the present paper, we offer two simple scaling laws that can be used to perform these corrections. The validity of these laws was checked successfully against a new set of experimental data made with seven glass bead packs with different mean grain diameters. Extension of the present work will concern heterogeneous media with packing of wide distributions of grain diameters, non-spherical particles, anistropy, electrokinetic measurements in the frequency domain (e.g. [1]), and the study of the influence of an interface between two homogeneous glass bead packs with very different grain diameters upon the electrokinetic generation of a magnetic field (see [18]).

Acknowledgments. This work is supported by ANR Project “ERINOH” and ANR-ECCO-PNRH Project “POLARIS” in France. The Ph-D Thesis of Agnès Crespy is supported by the Ministère de la Recherche et de l’Enseignement in France and the Ph-D Thesis of A. Bolève by SOBESOL and ANRT in France.

References

[1] Pengra, D.B., S.X. Li, P.-Z. Wong, Journal of Geophysical Research, 104(B12) (1999) 29,485-29,508.

[2] Revil A., Journal of Colloid and Interface Science, 212 (1999) 503-522.

[3] (a) Overbeek, J.T.G., Adv. Colloid Sci., 3 (1950) 97. (b) Kirby, B.J., E.F. Hasselbrink, Electrophoresis, 25 (2004) 187-202.

[4] (a) Somasundaran, P., R.D. Kulkarni, J. Colloid Interface Sci., 45 (1973) 591-600; (b) Alkafeef S. F., R.J. Gochin, and A.L. Smith, Colloids and Surfaces A: Physicochemical and Engineering Aspects, 159 (2-3)(1999) 263-270.

[5] Berlin, T.S., A.V. Khabakov, Geochemistry, 3 (1961) 217-230.

[6] Bernabé, Y., J. Geophys. Res., 103 (1998) 20,827-20,841.

[7] Leroy, P. A. Revil, J. Colloid Interface Sci., 270(2) (2004) 371-380.

[8] O'Brien R.W., W. N. Rowlands, J. Colloid Interface Sci., 159(2) (1993) 471-476.

[9] Shilov, V.N., A.V. Delgado, F. Gonzalez-Caballero, C. Grosse, Colloids and Surfaces A: Physicochemical and Engineering Aspects, 192 (2001) 253-265.

[10] (a) McPhedran, R.C., D.R. McKenzie, Proc. R. Soc. Lond. A. 359 (1978) 45-63. (b) Agapiou, J.S., M.F. De Vries, Journal of Heat Transfer 111 (1989) 281-286. (c) Torquato, S., I.C. Kim, D. Cule, Journal of Applied Physics, 85 (1999) 1471-1560. (d) Argento, C., D. Bouvard, International Journal of Heat and Mass Transfer, 39 (1996) 1343-1350.

[11] (a) Bikerman, J.J., Z. Phys. Chem. A, 163 (1933) 378. (b) Bikerman, J.J., Kolloid-Z, 72 (1935) 100.

[12] Zukovski, C.F., D.A. Saville, J. Colloid Interface Sci., 114 (1986) 32.

[13] Dukhin S.S., B.V. Derjaguin Electrokinetic Phenomena, in: Surface and Colloid Science, (E. Matievich, Ed.), Wiley Interscience, New York, 1974.

[14] Avellaneda, M., S. Torquato, Phys. Fluids A, 3(11) (1991) 2529-2540.

[15] Johnson, D.L., J. Koplik, L.M. Schwartz, Phys. Rev. Lett., 57 (1986) 2564.

[16] Kostek, S., L.M. Schwartz, D.L. Johnson, Phys. Rev. B, 45(1) (1992) 186-195.

[17] Revil, A., D. Hermitte, E. Spangenberg, J. J. Cochémé, J. Geophys. Res., 107(B8) (2002), doi:10.1029/2001JB000599, 2168.

[18] Revil, A., N. Linde, J. Colloid Interface Sci., 302 (2006) 682-694.

[19] Ennis J. L. R. White, J. Colloid Interface Sci., 178(2) (1996) 446-459.

[20] Revil, A., and Glover, P.W.J., Physical Review B., 55(3) (1997) 1757-1773.

[21] Revil, A., Glover, P.W.J., Geophysical Research Letters, 25(5) (1998) 691-694.

[22] Gorelik, L.V., J. Colloid Interface Sci., 274 (2004) 695-700.

[23] (a) Batchelor, G.K. An Introduction to Fluid Dynamics, Cambridge University Press, Cambridge (1972); (b) Scheidegger, A.E., The Physics of Flow Through Porous Media, 3rd ed., University of Toronto Press, Toronto (1974) 353 pp.

[24] Macevoy, W., M. Avellaneda, J. Colloid Interface Sci., 188 (1997) 139-149.

[25] Revil, A., Geophysical Journal International, 151(3) (2002) 944-949.

[26] Teng, H., T.S. Zhao, Chemical Engineering Science, 55 (2000) 2727-2735.

[27] (a) Revil, A., P. Leroy, K. Titov, J. Geophys. Res., 110 (2005) doi:10.1029/2004JB003442, B06202. (b) Revil, A., P. Leroy, J. Geophys. Res., 109 (2004) doi : 10.1029/2003JB002755, B03208.

[28] Suski, B., A. Revil, K. Titov., P. Konosavsky, M. Voltz, O. Huttel, Water Resources Research, 42 (2006) doi:10.1029/2005WR004840, W08418.

[29] (a) Revil, A., Pezard, P.A., P.W.J., Glover, J. Geophys. Res., 104(B9) (1999), 20,021-20,031; (b) Revil, A., Schwaeger, H., Cathles, L.M., P. Manhardt, J. Geophys. Res., 104(B9) (1999) 20,033-20,048,.

[30] Bolève A., A. Crespy, A. Revil, F. Janod, J. L. Mattiuzzio, submitted to J. Geophys. Res., (2006).

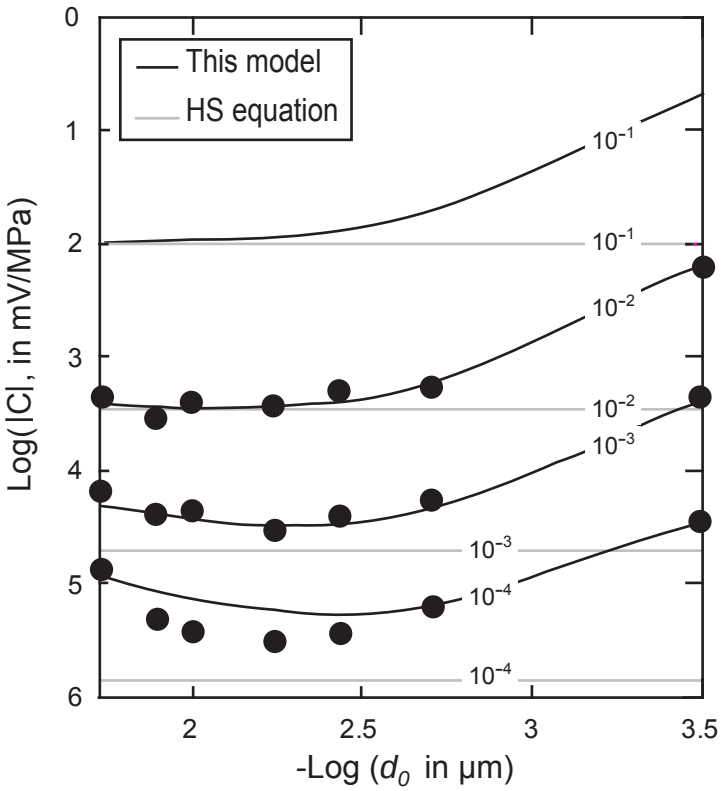

Figure 1. Comparison between the prediction of Eq. (20), the prediction from the Helmholtz-Smoluchowski equation, and experimental data (the filled circles) made on glass beads. The numbers on the plot correspond to the values of the electrical conductivity of the saturating electrolyte σ_f expressed in S m^{-1}. We observe that at low ionic strengths, the model never reach the Helmholtz-Smoluchowski asymptotic behavior because of the influence of the Dukhin and Reynolds numbers (value taken for the computation: Σ_S = 4.0x10^{-9} S, thickness of the sample 10 cm, pressure head 2 m, and we consider the logarithm scaling dependence between the zeta potential and the conductivity of the brine, see Figure 5).

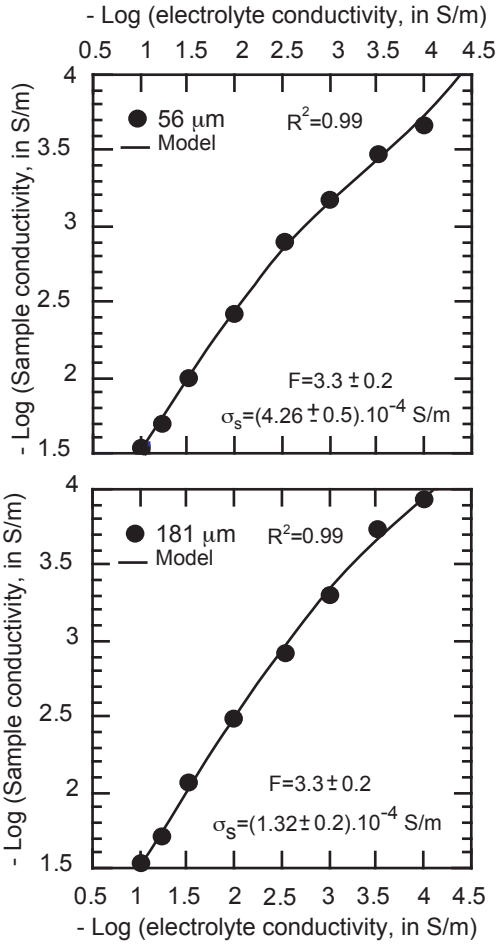

Figure 2. Comparison between the electrical conductivity model (equations 3 and 4) and the experimental data for two glass bead packs. The best fit of the model yields the value of the formation factor *F* and the value of the surface conductivity σ_S for each glass bead pack (the experiments are made at 25 ± 1 °C).

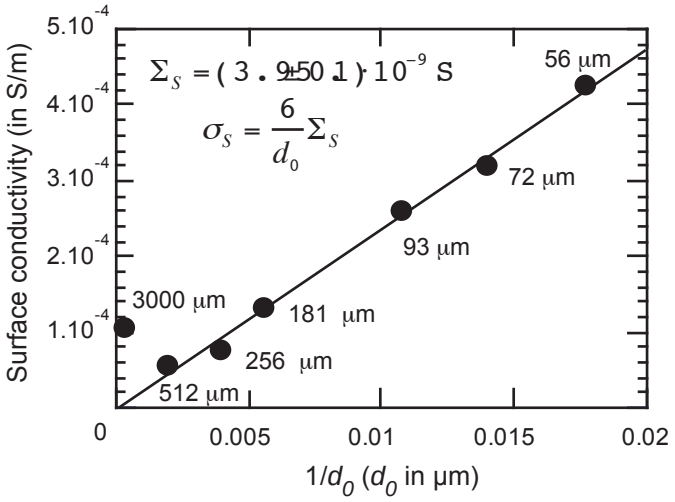

Figure 3. Surface conductivity determined from the best fit of the electrical conductivity data (see Figure 2) and the mean diameter of the glass bead packs. As predicted by the theory, the surface conductivity is inversely proportional to the mean grain diameter of the glass bead packs. The slope of this trend allows determining the specific surface conductance Σ_S.

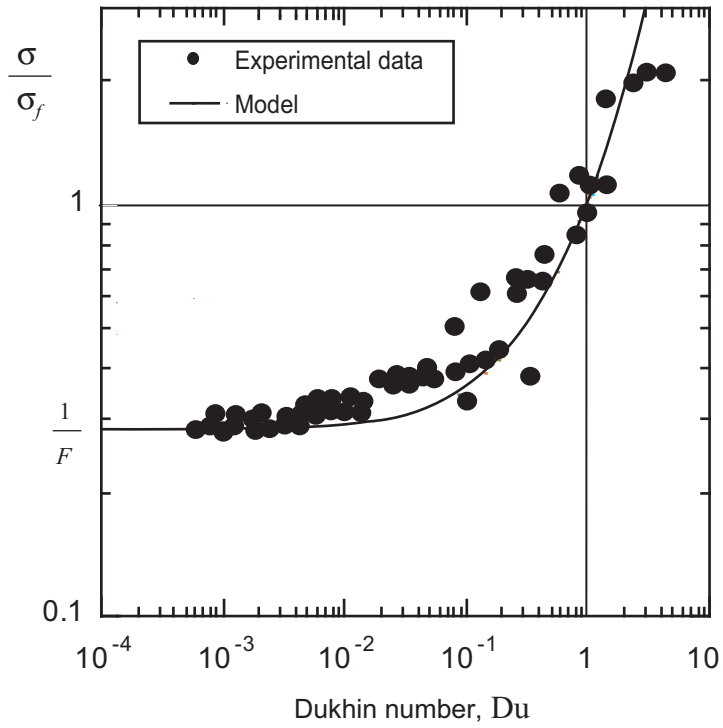

Figure 4. Comparison between the electrical conductivity model and the electrical conductivity data. The non-linearity of the trend and the existence of an iso-conductivity point are well reproduced by the model. The uncertainty on the electrical conductivity data is approximately 5%. Linear conductivity models (e.g., [1]) cannot reproduce this type of non-linear trend.

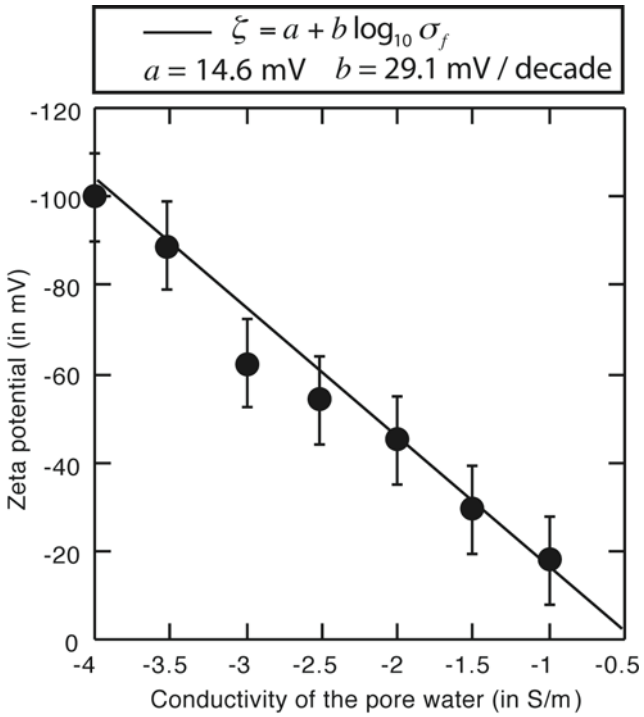

Figure 5. Determination of the intrinsic value of the zeta potential of the glass beads at pH = 5.6-5.9 and T = 25 ± 1°C. A logarithmic scaling between the zeta potential and the electrical conductivity of the brine is predicted by the model developed by [22]. This scaling matches very well the observations for sodium chloride solutions.

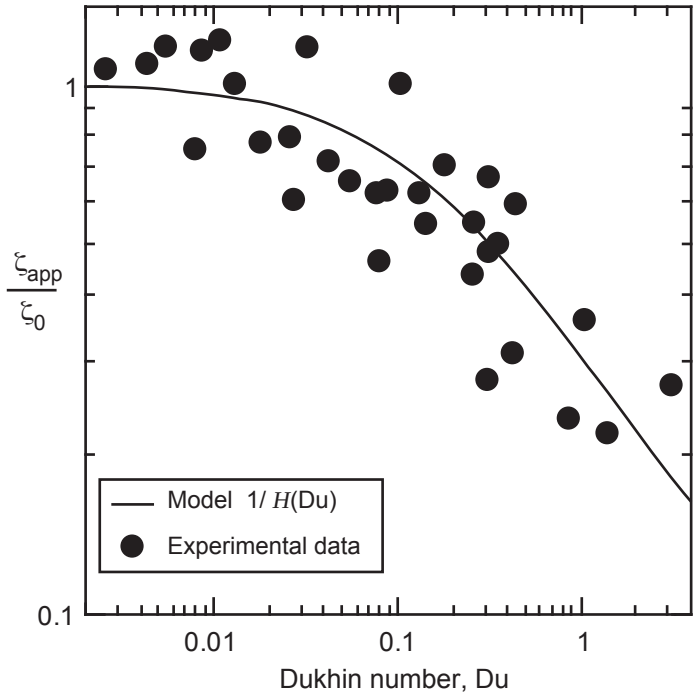

Figure 6. Comparison between the model and the experimental data regarding the influence of the Dukhin number on the apparent zeta potential of glass bead packs. The uncertainty of the ratio between the apparent zeta potential and the intrinsic zeta potential is approximately 15%. The slope of this trend would depend on the value of the electrical formation factor, which has here the same value for all the samples. For each experiment, the Reynolds number is determined from Eqs. (21) and (22)

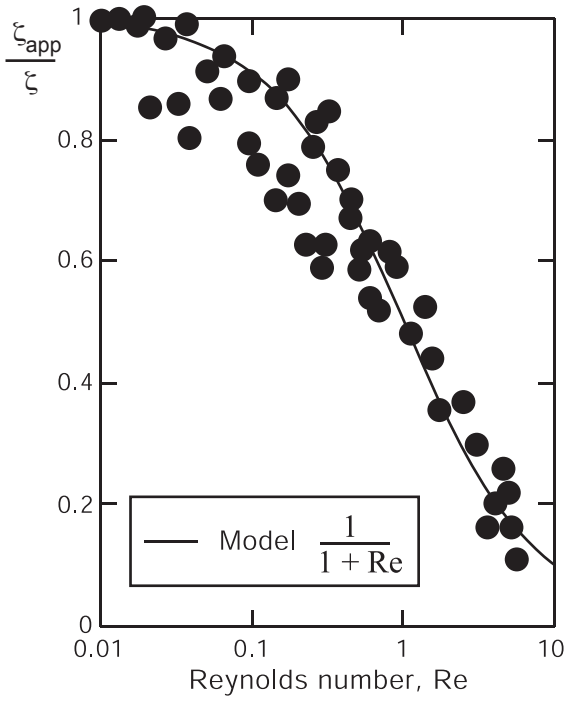

Figure 7. Comparison between the model and the experimental data regarding the influence of the Reynolds number on the apparent zeta potential of glass bead packs. The uncertainty on the ratio between the apparent zeta potential and the intrinsic zeta potential is approximately 10%. Different salinities have been used here showing the universal character of this trend.

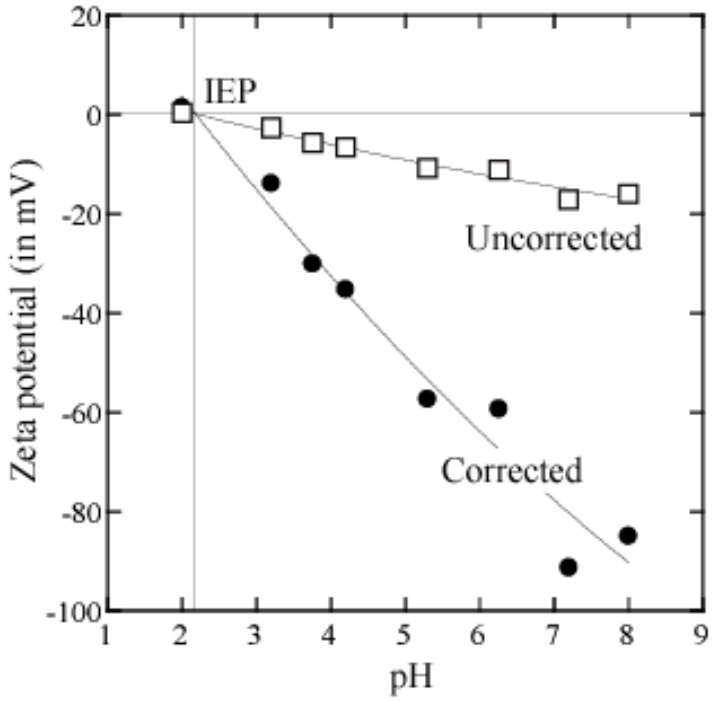

Figure 8. Comparison between the apparent zeta potential (the coupling coefficient is determined with a head of 1.80 meters) and the zeta potential determined using the coupling coefficient corrected for the Reynolds number. The experiments have been performed with the glass bead packs of 3000 μm (lines are guides to the eye) (IEP is the isoelectric point of the mineral).

Streaming potentials of granular media. Influence of the Dukhin and Reynolds numbers

A. Bolève (1, 3), A. Crespy (1), A. Revil (1, 2), F. Janod (3), and J. L. Mattiuzzo (3)

(1) CNRS-CEREGE, Université Paul Cézanne, IRD, Aix-en-Provence, France

(2) Colorado School of Mines, Golden, United States

(3) SOBESOL, Savoie Technolac, BP 230, F-73375 Le Bourget du Lac Cedex, France

Abstract. Laboratory experiments are performed to understand the controlling parameters of the electrical field associated with the seepage of water through a porous material. We use seven glass bead packs with varying mean grain size in an effort to obtain a standard material for the investigation of these electrical potentials. The mean grain size of these samples is in the range 56-3000 μm. We use pure NaCl electrolytes with conductivity in the range 10^{-4} to 10^{-1} S m^{-1} at 25°C. The flow conditions cover viscous and inertial laminar flow conditions but not turbulent flow. In the relationship between the streaming potential coupling coefficient and the grain size, three distinct domains are defined by the values of two dimensionless numbers, the Dukhin and the Reynolds numbers. The Dukhin number represents the ratio between the surface conductivity of the grains (due to conduction in the electrical double layer coating the surface of the grains) and the pore water electrical conductivity. At high Dukhin numbers (>>1) and low Reynolds numbers (<<1), the magnitude of the streaming potential coupling coefficient decreases with the increase of the Dukhin number and depends on the mean grain diameter (and therefore permeability) of the medium. At low Dukhin and Reynolds numbers (<<1), the streaming potential coupling coefficient becomes independent of the microstructure and is given by the well-known Helmholtz-Smoluchowski equation widely used in the literature. At high Reynolds numbers, the magnitude of the streaming potential coupling coefficient decreases with the increase of the Reynolds number in agreement with a new model developed in this paper. A numerical

application is made illustrating the relation between the self-potential signal and the intensity of seepage through a leakage in an embankment.

1. Introduction

The generation of electrical signals associated with the movement of water in porous/fractured materials is related to the viscous drag of the excess charge contained in the pore water of the porous medium (e.g., Bull and Gortner, 1932). The record of these electrical fields provides a powerful geophysical method for tracking the pattern of ground water flow. Applications in geohydrology concern the forced movement of water associated with deformation of porous rocks (e.g., Lorne et al., 1999a, b; Revil et al., 2003), the determination of preferential flow paths over karstic areas (Jardani et al., 2006a, b), the determination of transmissive properties of unconfined aquifers (Titov et al., 2000), the determination of subglacial flow patterns (Kulessa et al., 2003a, b), CO_2 sequestration (Moore et al., 2004), and the detection of leakages in embankments and dams and the interpretation of the resulting self-potential signals in terms of seepage velocity (e.g., Bogoslovsky and Ogilvy, 1970; Gex, 1980; Panthulu et al., 2001; Sheffer, 2002; Sheffer and Howie, 2001, 2003; Titov et al., 2005; Rozycki et al., 2006). These works have also recently driven the development of new algorithms of self-potential tomography (e.g., Revil et al. 2001; Long and Hao, 2005; Minsley et al., 2007) and tank-scale laboratory measurements in well-controlled conditions to check the underlying physics of these processes (Maineult et al., 2005, 2006; Moore and Glaser, 2007). Similar types of analysis were carried out recently in medical imaging to study the flow of electrolytes in cartilage submitted to mechanical loads (Sachs and Grodzinsky, 1995; Garon et al., 2002) and in plant sciences to monitor the flow of sap in trees (Gibert et al., 2006).

There are a number of works published in the literature regarding the measurement of streaming potentials associated with the flow of water through granular porous materials (e.g., Ahmad, 1964; Lorne et al., 1999a, b; Guichet et al., 2006). The streaming potential coupling

coefficient is a material property arising in the coupled hydroelectric problem of porous material. It represents the variation of the electrical potential to a variation in pore fluid pressure. For example, Bull and Gortner (1932) show a decrease of the strength of the streaming potentials by two orders of magnitude when the grain size decreases by two orders of magnitude from ~5 to 500 μm at low ionic strengths (~10^{-4} N NaCl at 25°C). This decrease was explained by Revil et al. (1999b) as resulting from the influence of the surface conductivity of the grains on the streaming potential coupling coefficient in the viscous laminar flow regime.

However, very few researchers have investigated the effect of non-viscous laminar flow upon the electrokinetic process. Streaming potential measurements have been made in capillaries of different radii to see the influence of the viscous sublayer upon the electrokinetic process at high Reynolds numbers (Bocquet et al., 1956; Kurtz et al., 1976). The Reynolds number is a key-dimensionless number that expresses the ratio of inertial to viscous forces in the Navier-Stokes equation. However, as far as we know, there were no works investigating quantitatively the influence of the Reynolds number upon the value of the streaming potential coupling coefficient at the transition between the viscous-laminar flow regime and the inertial-laminar flow regime in porous media.

In this paper, we propose a new formulation regarding the influence of the Reynolds number upon the coupled hydroelectric problem of porous material. In this formulation, we also account for the influence of surface conductivity of the grains on both the electrical conductivity and the streaming potential coupling coefficient. To check the validity of this model, we measure the streaming potential coupling coefficient and electrical conductivity of glass bead packs at different salinities. We investigate a set of seven well calibrated glass bead packs that can be considered as a standard material for the investigation of electrokinetic phenomena. The mean grain size of each sample is in the range 56 to 3000 μm (the permeability of these samples covers approximately four orders of magnitude and the porosity

ϕ is approximately that of a random packing of spherical particles, $\phi = 0.40$). We used NaCl solutions with electrical conductivities in the range 10^{-4} to 10^{-1} S m^{-1} at 25°C, corresponding to the conductivity of surface and ground waters often encountered in nature. Our goal in this paper is to provide a model explaining the variations of the streaming potential with the mean grain diameter of the sample at different salinities. An illustration is made by simulating the intensity of self-potential signals associated with the leakage of water through an embankment. We show that a quantitative relationship exists between the intensity of the self-potential signals and the intensity of seepage.

2. Theoretical Background

In this section, we discuss a theoretical model able to capture the influence of two key dimensionless numbers, namely the Dukhin and the Reynolds numbers, upon the value of the streaming potential coupling coefficient. The streaming potential coupling coefficient is the key parameter that controls the magnitude of self-potential signals associated with the percolation of water through a porous material. This electrokinetic or hydroelectrical phenomenon stems from the existence of an electrical double layer coating the surface of the grains. Indeed, when in contact with water, the surface of the minerals becomes charged. The fixed charge of the mineral surface is counterbalanced by sorbed charges in the Stern layer plus charges located in the diffuse layer. The counterions correspond to the excess of ions (generally cations) located in the pore space of the porous material. The flow of water through the porous material drags the excess charge contained in the pore space, creating a net source of current density (the streaming current) (e.g., Lorne et al., 1999a, b). The opposite mechanism exists and corresponds to the flow of pore water in response to the application of an electrical field. This is due to viscous drag of the pore water by the movement of the counterions associated with the application of the electrical field. This mechanism is known as electro-osmosis.

2.1. Viscous Laminar Flow

We consider a granular medium with a narrow particle size distribution centered on a mean particle diameter d_0. If the distribution of the size of the particles corresponds to a log normal distribution, d_0 corresponds to the peak of this distribution. We denote p the pore fluid pressure (in Pa) and φ the electrical potential (in V). We consider that the pore water is an electrolyte with N ionic species (the mobility of species i is b_i and their charge q_i). The boundary-value problem describing the hydroelectric coupling through a granular porous material is given by the Nernst-Planck and Stokes equations (e.g., Pride, 1994; Revil and Linde, 2006),

$$\mathbf{j}_f = \sum_{i=1}^{N} q_i \left[-b_i q_i \overline{C}_i \nabla\varphi + \overline{C}_i \frac{\partial \mathbf{u}_f}{\partial t} \right], \tag{1}$$

$$-\nabla p + \eta_f \nabla^2 \left(\frac{\partial \mathbf{u}_f}{\partial t} \right) + \mathbf{F} = 0, \tag{2}$$

$$\frac{\partial \mathbf{u}_f}{\partial t} = 0, \text{ on } S, \tag{3}$$

$$\mathbf{j}_f \cdot \mathbf{n} = 0, \text{ on } S \tag{4}$$

where $\mathbf{j}_f$ is the electrical current density in the pore water (in A m^{-2}), $\partial \mathbf{u}_f / \partial t$ is the velocity of the pore fluid (in m s^{-1}) and $\nabla \cdot (\partial \mathbf{u}_f / \partial t) = 0$ (incompressibility of the flow), $\mathbf{F} = -\overline{Q}_V \nabla\varphi$ is the electrostatic microscopic body force per unit volume acting on the pore water, $\mathbf{n}$ is the unit vector normal to the surface of the grains, $\overline{Q}_V$ is the excess charge per unit pore volume (expressed in Coulomb m^{-3}), η_f is the dynamic viscosity of the pore water (in Pa s), and $\overline{C}_i$ is the concentration of species i per unit pore volume. In the following, the pressure will be equal to the hydrostatic fluid pressure (in Pa), $p = \rho_f g h$, where h is the hydraulic head (in m), g is the acceleration due to gravity (in m s^{-2}), and ρ_f is the bulk density of the pore water (in kg m^{-3}).

There are several ways to upscale Eqs. (1) and (2), which are subjected to the local boundary conditions given by Eqs. (3) and (4) plus specified macroscopic boundary conditions. Examples are volume-averaging and differential-effective-medium approaches (see Pride, 1994; Revil, 2002). In all cases, theories developed in the vicinity of thermodynamic equilibrium yield macroscopic linear constitutive equations between the macroscopic current density **J** (in A m^{-2}) and the seepage velocity **U** (in m s^{-1}). In the viscous laminar flow regime, this yields,

$$\mathbf{J} = -\sigma(\nabla\varphi - C_0\nabla h), \tag{5}$$

$$\mathbf{U} = -K_0\nabla h + C_0\sigma\nabla\varphi, \tag{6}$$

where $K_0 = k_0\rho_f g/\eta_f$ is the hydraulic conductivity of the porous medium (in m s^{-1}), k_0 is its permeability (in m^2), σ is the DC-electrical conductivity of the porous material (in S m^{-1}), and C_0 is its streaming potential coupling coefficient, expressed here in Volts per meter of hydraulic head and defined by

$$C_0 = \left(\frac{\partial\varphi}{\partial h}\right)_{\mathbf{J}=0}. \tag{7}$$

Revil (2002) proposed to use a differential-effective-medium approach to obtain an expression for the electrical conductivity and then for the streaming potential coupling coefficient. This model can be written as (Revil et al., 2002)

$$k_0 = \frac{{d_0}^2}{\alpha F(F-1)^2}, \tag{8}$$

$$C_0\sigma = \rho_f g\frac{\varepsilon_f\zeta}{\eta_f F}, \tag{9}$$

$$\sigma = \sigma_f\xi, \text{ as } \xi \geq 1, \tag{10}$$

$$\sigma = \frac{\sigma_f}{F}\left[F\xi + \frac{1}{2}(1-\xi)\left(1-\xi+\sqrt{(1-\xi)^2+4F\xi}\right)\right], \text{ as } \xi \leq 1, \tag{11}$$

where ε_f is the dielectric constant of water (ε_f = 80 x ε_0 where ε_0 = 8.84.10^{-12} F m^{-1} is the dielectric constant of free space), ζ is the so-called zeta potential (a key parameter

characterizing the electrical potential of the inner part of the electrical diffuse layer, see Leroy and Revil, 2004), α is an empirical constant (see Revil and Cathles, 1999), $F = \phi^{-m}$ is the electrical formation factor, and σ_f is the electrical conductivity of the brine. The exponent *m* is often called the cementation exponent or first Archie's exponent, ξ is a dimensionless number called the Dukhin number, the ratio between the surface conductivity of the grains to the electrical conductivity of the pore water (e.g., Shilov et al., 2001):

$$\xi \equiv \sigma_S / \sigma_f \, . \tag{12}$$

As shown below, Eq. (10) is used to capture the non-linear behavior of the relationship between the electrical conductivity of the porous material and the electrical conductivity of the pore water (see discussion in Niwas et al., 2006). Eqs. (10) and (11) imply the existence of an iso-conductivity point characterized by $\sigma = \sigma_f = \sigma_S$. At this point, the conductivity of the material is equal to the conductivity of its pore water.

For packing of spheres, the macroscopic surface conductivity σ_S is related to the specific surface conductivity, Σ_S, by (Revil and Linde, 2006),

$$\sigma_S = \frac{6\Sigma_S}{d_0} , \tag{13}$$

where the numerical constant 6 corresponds to spherical grains. Surface conductivity includes conduction in the Stern layer of sorbed counterions and in the diffuse (Gouy-Chapman) layer (Ennis and White, 1996; Revil and Glover, 1997, 1998).

All the material properties entering the constitutive equations depend on only two textural parameters, the mean grain diameter and the formation factor, and two electrical double layer properties, the zeta potential ζ and the specific surface conductivity Σ_S. For simple supporting electrolytes, the zeta potential depends usually on the logarithm of the salinity (and therefore on the logarithm of the electrical conductivity) of the pore water (e.g., Kirby and Hasselbrink, 2004) over a wide range of salinity. Such a dependence was

demonstrated theoretically by Revil et al. (1999a) using an electrical double layer model. So we can write

$$\zeta = a + b \log_{10} \sigma_f \,, \tag{14}$$

where *a* and *b* are two constants.

The dependence of the specific surface conductivity on salinity is not well known. Most authors consider the surface conductivity to be a constant that is independent of the mineralization and composition of the ground water. Revil et al. (1997), Revil and Glover (1998), and Leroy and Revil (2004) have proposed double-layer models for silica and aluminosilicates to determine the salinity dependence of surface conductivity. They found that most of the surface conductivity is due to electrical conduction in the Stern layer and that the salinity dependence of the surface conductivity is relatively weak (the situation would be very different if surface conduction occurred mainly in the diffuse Gouy-Chapman layer of counterions). The uncertainty in the electrical conductivity and streaming potential measurements does not allow a salinity dependence of the surface conductivity to be determined so it is customary to assume that surface conductivity is independent of salinity. Because this dependence is probably weak as discussed above, we will adopt this assumption below.

When the Dukhin number is very small, the streaming potential coupling coefficient is given by the Helmholtz-Smoluchowski equation:

$$\lim_{\xi \to 0} C_0 \equiv C_{HS} = \frac{\varepsilon_f \zeta}{\eta_f \sigma_f}, \tag{15}$$

According to this equation, the streaming potential coupling coefficient is independent of the texture of the porous material and therefore independent of the permeability.

2.2. Inertial Laminar Flow

Darcy's law in its classical form implies a linear relationship between the flux and the gradient of the fluid pressure when the flow is laminar and the viscous (friction) force dominates at the interface between the grains and the pore water. As the Reynolds number increases, we pass from this viscous-laminar flow regime to another laminar flow regime in which the inertial force controls the flow. For a Reynolds number higher than 100-200, flow starts to become turbulent and vorticities appear in the flow lines in the pore space of the material. However, we will not consider the turbulent regime in this paper, as it does not seem to have practical applications in geohydrology of porous media.

Teng and Zhao (2000) derived recently a generalized Darcy equation by volume-averaging the local Navier-Stokes momentum equation over a representative elementary volume of a porous material, given by

$$\rho_f \frac{d\mathbf{U}}{dt} + \frac{1+\mathrm{Re}}{k_0}\eta_f \mathbf{U} = -\nabla p + \mathbf{F}\,, \tag{16}$$

where **F** is a macroscopic body force and Re is the Reynolds number, a key-dimensionless number that expresses the ratio of inertial to viscous forces in the Navier-Stokes equation (e.g., Batchelor, 1972). For a capillary of radius *R*, *U* being the strength of the seepage velocity, the Reynolds number is then defined by (e.g., Batchelor, 1972),

$$\mathrm{Re} = \frac{\rho_f U R}{\eta_f}\,. \tag{17}$$

In a porous material, the radius of the capillary should be replaced by a corresponding length scale of the porous material. The Reynolds number is defined by,

$$\mathrm{Re} = \frac{\rho_f U \Lambda}{\eta_f}\,, \tag{18}$$

where Λ is a characteristic length of the flow (for capillaries $\Lambda = R$ where *R* is the radius of the capillary). If we replace *U* by the Darcy equation (neglecting the electroosmotic

contribution), we can approximate the Reynolds number,

$$\mathrm{Re} = \frac{\rho_f{}^2 g k_0 \Lambda}{\eta_f{}^2 (1+\mathrm{Re})} \frac{h}{L}, \tag{19}$$

where h is the hydraulic head and L is the length of the cylindrical core pack. For a granular medium with a unimodal particle size distribution, the length scale Λ is given by (Revil, 2002)

$$\Lambda = \frac{d_0}{2m(F-1)}. \tag{20}$$

From Eqs. (19) and (20), the Reynolds number is the solution of the following equation,

$$\mathrm{Re}^2 + \mathrm{Re} - \frac{\rho_f{}^2 g}{2m\alpha\eta_f{}^2} \frac{d_0{}^3}{F(F-1)^3} \left(\frac{h}{L}\right) = 0. \tag{21}$$

The positive root of Eq. (21) is,

$$\mathrm{Re} = \frac{1}{2}\left(\sqrt{1+c} - 1\right), \tag{22}$$

$$c = \frac{\beta \rho_f{}^2 g}{\eta_f{}^2} \frac{d_0{}^3}{F(F-1)^3} \left(\frac{h}{L}\right), \tag{23}$$

where $\beta \approx 2.25 \times 10^{-3}$ is a numerical constant (determined from the constants given above). Equation (22) is a new equation that has a strong practical value since it can be easily used to determine the Reynolds number in a porous material from the knowledge of the pressure gradient.

In the present case, the macroscopic body force corresponds to the electrostatic force associated with the excess of electrical charge per unit pore volume. Therefore the generalized Darcy equation, Eq. (16), can be written as,

$$\mathbf{U} = -\frac{k}{\eta_f} \nabla p - \overline{Q}_V \nabla \varphi, \tag{24}$$

where *k* is an apparent permeability that is related to the Reynolds number by

$$k / k_0 = 1/(1 + \mathrm{Re}), \tag{25}$$

$$\lim_{\mathrm{Re}\to 0} k / k_0 = 1, \tag{26}$$

where k_0 is the permeability in viscous laminar flow conditions.

The influence of inertial flow upon electrokinetic coupling has been the subject of very few publications (see recently Watanabe and Katagishi, 2006 and references therein). Gorelik (2004) used dimensional analysis to demonstrate that the effect of the Reynolds number corresponds to a multiplication of the Helmholtz-Smoluchowski equation by an unspecified function of the Reynolds number. In this paper, we look for an explicit (quantitative) relationship between the streaming potential coupling coefficient and the Reynolds number. At the scale of a representative elementary volume, the current density is given by (Revil et al., 2005; Linde et al., 2007)

$$\mathbf{J} = -\sigma \nabla \varphi + \overline{Q}_V \mathbf{U}, \tag{27}$$

$$\mathbf{J} = -\sigma \nabla \varphi - \frac{k \overline{Q}_V}{\eta_f} \nabla p, \tag{28}$$

where *k* is the apparent permeability defined above. The streaming potential coupling coefficient can be related to the excess charge of the diffuse layer per unit pore volume, $\overline{Q}_V$, by $C_0 = k_0 \overline{Q}_V / \eta_f \sigma$ (Revil et al., 2005). Equation (27) expresses the fact that the source current density is equal to the excess of charge of the pore fluid $\overline{Q}_V$ times the seepage velocity **U**. As the seepage velocity is influenced by the increase of the Reynolds number (for Re > 0.1), the Reynolds number also influences the value of the streaming potential coupling coefficient. Following Eqs. (25) and (28), the streaming potential coupling coefficient is related to the Reynolds number by,

$$C / C_0 = 1/(1 + \mathrm{Re}), \tag{29}$$

$$\lim_{\mathrm{Re}\to 0} C / C_0 = 1, \tag{30}$$

where C_0 is the streaming potential coupling coefficient in viscous laminar flow conditions and C is the measured coupling coefficient.

In summary, the generalized coupled constitutive equations between the seepage velocity and the electrical current density are,

$$\mathbf{J} = -\sigma\left(\nabla\varphi - \frac{C_0}{1+\mathrm{Re}}\nabla h\right), \tag{31}$$

$$\mathbf{U} = -\frac{K_0}{1+\mathrm{Re}}\nabla h + \frac{C_0}{1+\mathrm{Re}}\sigma\nabla\varphi, \tag{32}$$

with a preserved symmetry of the coupling term. This means that Onsager's reciprocity holds. The situation would likely be different in the turbulent flow regime where a magnetic field is probably associated with vortices of the local flow lines in the pore space.

3. Experimental Methods

The experimental setup for the measurement of the streaming potential coupling coefficient is shown in Figure 1a. It consists simply of a Plexiglas tube with a permeable and electrically insulating membrane, placed at its bottom, with a mesh of 50 μm. We check that the permeability of this membrane is always at least ten times larger than the permeability of the sample (for the highly permeable sample S6, we use a coarser mesh). Each sample corresponds to a packing of glass beads (manufactured by Sigma-Aldrich) of a given particle size. They are seven glass bead packs investigated in this study with mean particle size in the range 56-3000 μm, so approximately covering two orders of magnitude in size (Table 1). The chemical composition of the glass is SiO_2 ~60.5%, Na_2O ~12 to 18 %, CaO ~5 to 12%, MgO ~4%, Al_2O_3 ~1%. The measured mass density of the grains is 2430 kg m^{-3}. The measured porosity of the packs is ϕ = 0.40 irrespective of the size of the glass beads. The other properties of the glass bead packs are reported in Table 1.

To measure the streaming potential coupling coefficient, we use the following

protocol. In some cases, a given hydraulic head is imposed on the cylindrical sample inside the tube by adding water to the water column in the tube in such a way that the hydraulic head is maintained constant. We use also for some experiments a falling head method during which the electrical potential is measured during the decrease of the hydraulic head in the tube associated with the flow of the water through the porous pack. The gradient of the fluid pressure is controlled by the hydraulic head in the tube and the length of the porous pack (typically between 1 to 60 centimeters). In both cases, the brine is flowing through the porous sample. The resulting electrical potential is measured with two non-polarizable $Ag/AgCl_2$ electrodes (Ref321/XR300, Radiometer Analytical) located in the vicinity of the end faces of the sample. The difference of the electrical potential measured between the end faces of the porous pack divided by the length of the sample is the streaming electrical field associated with the flow of the brine through the pack. The voltages are measured with a data logger (Easy Log, internal impedance of 10 MOhm, sensitivity of 0.1 mV) or with a voltmeter (Metrix MX-20, internal impedance 100 MOhm, sensitivity of 0.1 mV). Both provided consistent measurements.

Streaming potential data from a typical run are shown at Figures 2 and 3. In viscous laminar flow conditions, the differences of the electrical potential measured in the vicinity of the end-faces of the porous medium are proportional to the imposed hydraulic heads, as shown on Figures 2 and 3. The slope of the linear trend of streaming potential vs. head is the streaming potential coupling coefficient, defined from Eq. (5) by

$$C = \left(\frac{\partial \varphi}{\partial h} \right)_{\mathbf{J}=0} . \tag{33}$$

In addition to the streaming potential coupling coefficient, we determine the intrinsic permeability in viscous-laminar flow conditions by measuring the seepage per unit time at a given hydraulic head (when the flow was not in the viscous-laminar flow regime, we performed a correction using the estimated value of the Reynolds number as explained

below). Measurements of the streaming potential coupling coefficient and permeability were performed for different pore water electrical conductivities using different NaCl solutions. These solutions were prepared by measuring the weight of NaCl salt to add to a given solution of deionized water or by measuring directly the conductivity the solution with a calibrated impedancemeter. We use the following set of brine conductivities ($3x10^{-2}$, 10^{-2}, $3x10^{-3}$, 10^{-3}, $3x10^{-4}$, and 10^{-4} S m^{-1}) for the streaming potential measurements. The electrical conductivity of the electrolytes was measured with a conductivity meter (CDM-230, MeterLab™). The pH of the solution, measured with the pH-meter (pH-330, SET1-Fisher), is in the range 5.6 to 5.9 at 24.5 °C. Values of the streaming potential coupling coefficients are reported in Table 2.

We also measure the electrical conductivity using a frequency-dependent impedancemeter (Waynekerr Analyser 6425) in the frequency range 30 Hz-300 kHz. Electrical conductivity measurements were performed in the frequency domain with a two-electrode device (with stainless steel electrodes) according to the protocol described in Revil et al. (2002). We use the following set of brine conductivities (10^{-1}, $6x10^{-2}$, $3x10^{-2}$, 10^{-2}, $3x10^{-3}$, 10^{-3}, $3x10^{-4}$, and 10^{-4} S m^{-1}) for the electrical conductivity measurements. The description of this protocol will not be repeated here. Accuracy of the measurement is estimated to be 5%. Values of the electrical conductivity are reported in Table 3. They are obtained at a frequency of a few hundreds of Hertz to a few kHz.

Permeability is determined using Darcy's law and measuring the volume of water passing through the glass packs per unit time. Measurements were reproducible with an uncertainty of 10%. Values of the measured intrinsic permeability (in the viscous laminar flow regime) are reported in Table 1.

4. Results and Discussion

4.1. Intrinsic Permeability

In Figure 4, we plot the measured intrinsic permeabilities versus the intrinsic permeabilities predicted by Eq. (8) corrected for the influence of the Reynolds number (see

Eqs. (22) and (25)). There is very good agreement between the measured data and the prediction of Eq. (8).

4.2. Electrical Conductivity

In Figure 5, we plot the electrical conductivity of the samples as a function of the electrical conductivity of the pore water. We use Eq. (11) to fit these experimental data in order to determine the value of the surface conductivity and the electrical formation factor. The mean formation factor is 3.4 ± 0.1 (see Table 1). Using Archie's law, $F = \phi^{-m}$ and a porosity of 0.40, we obtain a cementation exponent m = 1.34 (this is consistent with the cementation exponent of unconsolidated sands and glass beads reported by Sen et al., 1981).

The value of surface conductivity of each pack is reported as a function of the mean diameter of each pack on Figure 6. We see very clearly that surface conductivity is inversely proportional to the mean diameter of the beads as predicted by the theory. The value of the specific surface conductivity obtained from this trend, Σ_S = 4.0x10^{-9} S, is consistent with the double layer model prediction of Revil et al. (1999a) for a salinity of 10^{-3} S m^{-1}, and with previous experimental data (O'Brien and Rowlands, 1993). Other estimates of the specific surface conductance are reported in Table 4. They are consistent with the above estimate. Brovelli et al. (2006) used a finite-element code to simulate electrical conduction in a partially water-saturated sandstone. They obtained Σ_S = 3.3x10^{-7} S. Wildenschild et al. (2000) obtained Σ_S in the range (0.5-1.5)x10^{-7} S using electrical conductivity data on mixtures of sand and clay particles. Block and Harris (2006) found Σ_S = 4.2x10^{-8} S with sand with a small amount of clay particles. However, none of these authors discussed the discrepancy between their estimates and those obtained from electrical triple layer calculations (see Revil and Glover, 1997, 1998; Revil and Leroy, 2001; Leroy and Revil, 2004). Our conclusion is that the values derived by Wildenschild et al. (2000), Brovelli et al. (2006), and Block and Harris (2006) are strongly overestimated by one to two orders of magnitude because of the

inappropriate mean grain size used by these authors to estimate the surface conductance from the macroscopic surface conductivity.

The "conductivity ratio" of the porous samples is defined as the ratio between the electrical conductivity of the porous pack to the conductivity of the brine. These conductivity ratios are plotted on Figure 7 as a function of the Dukhin numbers for all the samples. As discussed by Revil et al. (2002), this provides a way to normalize electrical conductivity plots. We observe that all the data fall on the same curve that is well reproduced by our model. This shows the power of our electrical conductivity model to represent accurately the electrical conductivity response of granular materials. We point out that popular electrical conductivity models such as the Waxman and Smits (1968) model (or all the family of "linear conductivity models", see Niwas et al., 2006) cannot reproduce these experimental data as they do not explain the occurrence of an iso-conductivity point.

4.3. Coupling Coefficient

The model developed for the streaming potential coupling coefficient in Section 2 can be summarized by the following equation,

$$C = C_{HS} \frac{G(\mathrm{Re})}{H(\xi)}, \tag{34}$$

where $G(\mathrm{Re}) = 1/(1+\mathrm{Re})$ and $H(\xi) = F\sigma_0(\xi)/\sigma_f$. In this section, we test the accuracy of Equation (34) to determine the streaming potential coupling coefficient and therefore to demonstrate that the coupling coefficient is controlled by the Dukhin and Reynolds numbers.

A preliminary step is to determine the dependence of the zeta potential on the conductivity of the pore water as discussed in Section 2. Using Eq. (9), we combined the measurements of the streaming potential coupling coefficient and the measurements of the electrical conductivity to determine the values of the zeta potential in viscous-laminar flow conditions. The results are reported as a function of the logarithm of the electrical

conductivity of the pore water on Figure 8. These results are consistent with the values usually reported for silica and glasses (e.g., Kirby and Hasselbrink, 2004). The constants *a* and *b* of Eq. (14) corresponding to the best fit of the zeta-potential values are reported in Figure 8. With the values of *a* and *b* and Eq. (14), we can estimate the value of the streaming potential coupling coefficient via the Helmholtz-Smoluchowski equation at a given electrical conductivity of the pore water. These values are reported in the last line of Table 2.

We first check the relationship between the streaming potential coupling coefficient and the Dukhin number ξ. In Figure 9, we plot the reduced streaming potential coupling coefficient C_0 / C_{HS} versus the Dukhin number for the seven packs. The measured value of the streaming potential coupling coefficient *C*, determined from Eq. (33), is corrected for the influence of the Reynolds number using Eqs. (29) and (22) . Note that because the formation factor is roughly the same for all the samples, all the data fall on the same curve. There is a good match between the theory and the experimental data (see Figure 9).

Finally, we check the relationship between both the streaming potential coupling coefficient and the Reynolds number Re. In Figure 10, we plot the reduced streaming potential coupling coefficient C / C_0 (where $C_0 = C_{HS} / H(\xi, F)$) and the reduced permeability k / k_0 versus the Reynolds number for the seven samples investigated in this study. All the data fall on the same curve. The curves correspond to Eq. (33) for the ratio C / C_0. Again, we found a good agreement between the theory and the experimental data. It is clear from these data that the decrease of the streaming potential coupling coefficient with the increase of the Reynolds number is entirely due to the increase of the flow rate in the sample during the transition from viscous- to inertial-laminar flows. However, the situation could be different for turbulent flow.

We can summarize our findings in the following way. At high Dukhin numbers (>>1) and low Reynolds numbers (<<1), the magnitude of the streaming potential coupling coefficient decreases with the increase of the Dukhin number and depends on the mean grain

diameter (and therefore permeability) of the medium. At low Dukhin and Reynolds numbers (<<1), the streaming potential coupling coefficient becomes independent of the microstructure and is given by the well-known Helmholtz-Smoluchowski equation widely used in the literature. At high Reynolds numbers, the magnitude of the streaming potential coupling coefficient decreases with the increase of the Reynolds number in agreement with the new model developed in Section 2.

A recent paper by Kuwano et al. [2006] investigated how the apparent permeability and the apparent streaming current coupling coefficient depend on the Reynolds number like in the present work. These authors realized experiments showing a decrease of the streaming current coupling coefficient L and permeability k of glass bead packs with the Reynolds number Re. They also noted qualitatively that L decreases less than k with Re and suggested that this difference could be related to the increase in the efficiency of charge transport in the vicinity of the surface of the minerals when the Reynolds number increases. This effect could reflect a change in the shape of the velocity profile of the water in the pores when the Reynolds number increases. According to Revil (2007), the data presented by Kuwano et al. [2006] can be fitted with the following parametric function $L(\mathrm{Re}) = L_0 (1 + \mathrm{Re})^{-n}$ where n = ½. Additional investigations will be performed to test this point further.

5. Example of Geophysical Application

The modified form of the constitutive equations described above could be applied to the study of electromagnetic signals associated with fracturing (see the recent paper by Moore and Glaser, 2007, this field will be explored in a future contribution) and to the study of leakage in embankments and dams. In this section, we simulate a leakage problem. The geometry of the basin in which the leakage occurs is shown on Figure 3. Previous simulations of such hydroelectric problem were mainly 2D and were not accounting for the influence of the Reynolds number (see Wilt and Corwin, 1988; Titov et al., 2000, 2005 and references

therein and recently Suski et al., 2006). In this paper, we use the finite element code Comsol Multiphysic 3.2 to simulate the 3D distribution of the self-potential signals associated with the leakage of water through a highly permeable pipe located in the wall of the basin. Dimensions of the pool are reported in Table 5. The basin is assumed to be filled with water with an electrical conductivity equal to 3.7×10^{-2} S m^{-1} (at 20°C). We assume that the material used for the basin is a clay material. The pipe is filled with the gravel with a formation factor equal to 2.9 and an intrinsic permeability equal to $k_0 = 4.6 \times 10^{-9}$ m². Because of the strong contrast of permeability between the material filling the pipe and the clay, the leakage of water occurs mainly through the pipe.

Comsol Multiphysic 3.2 is first used to solve the continuity equation $\nabla \cdot \mathbf{U} = 0$ with appropriate boundary conditions for the pressure head in the basin and Eq. (32) for the Darcy velocity and neglecting electro-osmosis. At the entrance of the pipe, we impose the seepage velocity according to the modified Darcy's law that account for the Reynolds number, Eq. (32) where h / L is the hydraulic gradient and L is now equal to the length of the pipe and h is the total hydraulic head (including the length of the pipe), k_0 is the permeability of the gravel filling the pipe. At the exit of pipe, we also imposed the flux that is conservative (in steady-state conditions), assuming therefore no exchange of water between the pipe and the surrounding clay material. Therefore the magnitude of the seepage velocity at the entrance of the pipe is equal to the magnitude of the seepage velocity of the exit of the pipe. For all other boundary conditions, we have no flux (only a given head).

For the electrical problem, we solve the continuity equation for the electrical charge $\nabla \cdot \mathbf{J} = 0$ combined with Eq. (31). This lead to a Poisson's equation for the electrical potential with a source term depending on the distribution of the fluid pressure (e.g., Titov et al., 2000 and 2005 and references therein). The values of the electrical conductivity of three materials (tap water, clay, and gravel), voltage and current coupling coefficients and dimensions of the system are reported in Table 5. At the outer boundaries of the basin, we use $\mathbf{n} \cdot \nabla \varphi = 0$ as an

appropriate boundary condition (contact with an insulating body like the atmosphere). A reference for the voltage is placed at a reference station chosen arbitrarily in the basin but far enough from the leaking pipe (see “Ref” on Figure 11).

Figures 12 and 13 show the distribution of the equipotentials for the self-potential in the pool (for $k_0 = 4.6 \times 10^{-9}$ m²). The leakage is clearly associated with a negative self-potential anomaly centered on the area of leakage in agreement with field observations (e.g., Bogoslovsky and Ogilvy, 1970; Sheffer, 2002; Sheffer and Howie, 2001, 2003). The magnitude of this anomaly at the entrance of the pipe is equal to four millivolts. This anomaly can be well resolved using filtering analysis and a sensitive voltmeter (e.g., the Metrix MX20 has a sensitivity of 0.1 mV). Simulations indicate that applying our model for poorly mineralized water (e.g., 10^{-3} S m^{-1} at 20°C), the intensity of the self-potential anomaly can reach very easily 100 mV.

To test the evolution of a self-potential anomaly associated with the evolution of a leaking area, we modeled the intensity of the self-potential anomaly resulting from an increase of the intrinsic permeability k_0 over time. In this case, the model shows a decrease of the maximum of the self-potential anomaly when the intrinsic permeability increases (Figure 14). This variation is due to the decrease of the streaming potential coupling coefficient with the Reynolds number. There is clearly a domain of intrinsic permeability for which the magnitude of the self-potential anomaly can be used to retrieve the magnitude of the seepage velocity. The self-potential method could be also combined with other methods (e.g., thermal methods) to improve its ability to determine the seepage velocity of leaking areas though joint inversion of self-potential and temperature measurements.

6. Concluding Statements

In this paper, we show how the streaming potential coupling coefficient depends non-linearly on two key dimensionless parameters, the so-called Dukhin and Reynolds numbers. The Dukhin number characterizes the relative influence of the surface conductivity of the

grains (which depends on the grain size) to the conductivity of the pore water electrolyte. The Reynolds number characterizes the influence of the inertial force in the Navier-Stokes equation. In this paper, we have derived (i) a new expression for the Reynolds number and (ii) a general equation for the streaming potential coupling coefficient showing that the Helmholtz-Smoluchowski equation is recovered when both the Reynolds and the Dukhin numbers are much smaller than unity, that is, when viscous-laminar flow and pore water conduction dominate. In the transition between the viscous and inertial laminar flow regimes, the streaming potential coupling coefficient falls as 1 / (1+Re) with the increase of the Reynolds number. In addition, (iii) a new set of experimental data has been obtained and both these data and the model agree with each other. Finally (iv) for the first time, we show how surface conductivity varies with the size of the grains. We show that the value of the specific surface conductance agrees with that predicted by double-layer models. Finally, we show that our model can easily be incorporated in finite-element simulation software to determine the intensity of self-potential signals associated with leakage. We expect application of this theory also for the potential breaking of seals in the context of CO_2 sequestration.

Extension of the present work will concern mixtures of beads with different grain sizes and clay-bead mixtures, the study of heterogeneities with glass bead packs in series and in parallel, and the application of the present work to real rocks. However, we believe that we can already apply the present petrophysical model to the determination of the relationship between the seepage velocity and the self-potential anomalies measured in various environments and especially in geohydrology to interpret quantitatively self-potential anomalies related to leakage of water in embankments and dams for example (e.g., Sheffer and Howie, 2001, 2003) and to fracturing in active volcanoes (e.g., Revil et al., 2003; Finizola et al., 2004).

Acknowledgments. This work is supported by ANR Project ERINOH in France related to the

study of leakages in embankments dams and ANR-ECCO-PNRH Project POLARIS. The Ph-D Thesis of A. Bolève is supported by SOBESOL and the Ph-D thesis of Agnès Crespy by the Ministère de la Recherche et de l'Enseignement in France.

References

Ahmad, M. (1964), A laboratory study of streaming potentials, Geophys. Prospect., 12, 49-64.

Batchelor, G.K. (1972), An Introduction to Fluid Dynamics, Cambridge University Press.

Block, G. I., and J. G. Harris (2006), Conductivity dependence of seismoelectric wave phenomena in fluid-saturated sediments, J. Geophys. Res., 111, B01304, doi:10.1029/2005JB003798.

Bocquet, P.E., C.M. Sliepcevich, and D.F. Bohr (1956), Effects of turbulence on the streaming potential, Ind. Eng. Chem., 48, 197-200.

Bogoslovsky, V.A., and V.A. Ogilvy (1970), Natural potential anomalies as a quantitative index of the role of water seepage from reservoir, Geophysical Prospecting, 18, 261-268.

Brovelli, A., G. Cassiani, E. Dalla, F. Bergamini, D. Pitea, and A.M. Binley (2005), Electrical properties of partially saturated sandstones: novel computational approach with hydrogeophysical applications, Water Resources Res., 41, W08411, doi: 10.1029/2004WR003628.

Bull, H.B., and R.A. Gortner (1932), Electrokinetic potentials. X. The effect of particle size on potentials, J. Phys. Chem., 36, 111-119.

Ennis J. and L. R. White (1996), Dynamic Stern layer contribution to the frequency-dependent mobility of a spherical colloid particle: A low-zeta-potential analytic solution, Journal of Colloid and Interface Science, 178(2), 446-459.

Finizola, A., J.F. Lénat, O. Macedo, D. Ramos, J.C. Thouret, and F. Sortino (2004), Fluid circulation and structural discontinuities inside Misti volcano (Peru) inferred from self-potential measurements, J. Volcanology and Geothermal Research, 135(4), 343-360.

Garon, M., A. Légaré, R. Guardo, P. Savard, and M. D. Buschmann (2002), Streaming potentials maps are spatially resolved indicators of amplitude, frequency and ionic strength dependant responses of articular cartilage to load, Journal of Biomechanics, 35(2), 207-216.

Gex, P. (1980), Electrofiltration phenomena associated with several dam sites, Bulletin of the Society Vaud Science and Nature, 357(75), 39-50.

Gibert, D., J.-L. Le Mouël, L. Lambs, F. Nicollin, and F. Perrier (2006), Sap flow and daily electrical potential variations in a tree trunk, in press in Plant Science.

Gorelik, L.V. (2004), Investigation of dynamic streaming potential by dimensional analysis, J. Colloid and Interface Science, 274, 695-700.

Guichet, X., Jouniaux, L., and Catel, N. (2006), Modification of streaming potential by precipitation of calcite in a sand-water system: laboratory measurements in the pH range from 4 to 12, Geophysical Journal International, 166(1), 445-460.

Jardani, A., J.P. Dupont, and A. Revil (2006a), Self potential signals associated with preferential ground water flow pathways in sinkholes, Journal of Geophysical Research, 111, B09204, doi: 10.1029/2005JB004231.

Jardani, A. A. Revil, F. Akoa, M. Schmutz, N. Florsch, and J.P. Dupont (2006b), Least-squares inversion of self-potential (SP) data and application to the shallow flow of the ground water in sinkholes, Geophysical Research Letters, 33(19), L19306, doi: 10.1029/2006GL027458.

Kirby, B.J., and E.F. Hasselbrink (2004), Zeta potential of microfluidic substrates. 1. Theory, experimental techniques, and effects on separations, Electrophoresis, 25, 187-202.

Kulessa, B., B. Hubbard, and G.H. Brown, (2003a), Cross-coupled flow modeling of coincident streaming and electrochemical potentials, and application to subglacial self-potential (SP) data, J. Geophys. Res., 108(B8), 2381, doi: 10.1029/2001JB1167.

Kulessa, B., B. Hubbard, G.H. Brown, and J. Becker (2003b), Earth tide forcing of glacier drainage, Geophys. Res. Lett, 30(1), 1011, doi: 10.1029/2002GL105303.

Kurtz, R.J., E. Findl, Al. B. Kurtz, and L.C. Stormo (1976), Turbulent flow streaming potentials in large bore tubing, J. Colloid Interf. Sci., 57, 28-39.

Kuwano, O., M. Nakatani, and S. Yoshida (2006), Effect of the flow state on streaming current, Geophys. Res. Lett., 33, L21309, doi:10.1029/2006GL027712.

Leroy, P. and A. Revil (2004), A triple layer model of the surface electrochemical properties of clay minerals, Journal of Colloids and Interface Science, 270(2), 371-380.

Linde, N., D. Jougnot, A. Revil, S.K. Matthaï, T. Arora, D. Renard, and C. Doussan (2007), Streaming current generation in two-phase flow conditions, Geophysical Research Letters, 34(3), L03306, doi: 10.1029/2006GL028878.

Long, H.L., and J.Q. Hao (2005), Theoretical and experimental research on self-potential tomography, Chinese Journal of Geophysics – Chinese Edition, 48(6), 1343-1349.

Lorne, B, Perrier, F. and J.P.Avouac (1999a), Streaming potential measurements 1. Properties of the electrical double layer from crushed rock samples, Journal of Geophysical Research, 104, 17,857 –17,877.

Lorne, B, Perrier, F. and and J.P. Avouac (1999b), Streaming potential measurements 2. Relationship between electrical and hydraulic patterns from rock samples during deformation, J. Geophys. Res., 104, 17,879 –17,896.

Maineult, A., Y. Bernabé, and P. Ackerer (2006), Detection of advected concentration and pH fronts from self-potential measurements, J. Geophys. Res., 110(B11), B11205.

Maineult, A., Y. Bernabé, and P. Ackerer (2006), Detection of advected, reacting redox fronts from self-potential measurements, J. Contaminant Hydrology, 86(1-2), 32-52.

Minsley, B.J., J. Sogade, and F.D. Morgan (2007), Three-dimensional source inversion of self-potential data, J. Geophys. Res., 112, B02202, doi : 1029/2006JB004262.

Moore, J. R., and S. D. Glaser (2007), Self-potential observations during hydraulic fracturing, J. Geophys. Res., 112, B02204, doi:10.1029/2006JB004373.

Moore, J.R., S.D. Glaser, H.F. Morrison, and G.M. Hoversten (2004), The streaming potential of liquid carbone dioxide in Berea sandstone, Geophys. Res. Lett., 31(17), L17610, 2004.

Niwas, S., P.K. Gupta, and O.A.L. de Lima (2006), Nonlinear electrical response of saturated shaley sand reservoir and its asymptotic approximations, Geophysics, 71(3), G129-G133.

O'Brien R. W. and W. N. Rowlands (1993), Measuring the Surface Conductance of Kaolinite Particles, Journal of Colloid and Interface Science, 159(2), 471-476.

Panthulu, T.V., C. Krishnaiah, and J.M. Shirke (2001), Detection of seepage paths in earth dams using self-potential and electrical resistivity methods, Engineering Geology, 59, 281-295, 2001.

Revil, A. (2007), Comment on “Effect of the flow state on streaming current” by O. Kuwano, M. Nakatani, and S. Yoshida, submitted to Geophysical Research Letters.

Revil, A. and N. Linde (2006), Chemico-electromechanical coupling in microporous media, Journal of Colloid and Interface Science, 302, 682-694.

Revil, A., P. Leroy, and K. Titov (2005), Characterization of transport properties of argillaceous sediments. Application to the Callovo-Oxfordian Argillite, J. Geophys. Res., 110, B06202, doi: 10.1029/2004JB003442.

Revil, A., G. Saracco, and P. Labazuy (2003), The volcano-electric effect, Journal of Geophysical Research, 108(B5), 2251, doi: 10.1029/2002JB001835.

Revil, A., D. Hermitte, E. Spangenberg, and J. J. Cochémé (2002), Electrical properties of zeolitized volcaniclastic materials, J. Geophys. Res., 107(B8), 2168, 10.1029/2001JB000599.

Revil, A., L. Ehouarne, and E. Thyreault (2001), Tomography of self-potential anomalies of electrochemical nature, Geophysical Research Letters, 28(23), 4363-4366.

Revil, A., and P. Leroy (2001), Hydroelectric coupling in a clayey material, Geophysical Research Letters, 28(8), 1643-1646.

Revil, A. (2002), The hydroelectric problem of porous rocks: thermodynamic approach and introduction of a percolation threshold, Geophysical Journal International, 151(3), 944-949.

Revil, A., Pezard, P.A., and P.W.J., Glover (1999a), Streaming potential in porous media. 1. Theory of the zeta-potential, J. Geophys. Res., 104(B9), 20,021-20,031.

Revil, A., Schwaeger, H., Cathles, L.M., and P. Manhardt (1999b), Streaming potential in porous media. 2. Theory and application to geothermal systems, J. Geophys. Res., 104(B9), 20,033-20,048.

Revil, A., and Cathles (1999), L.M., Permeability of shaly sands, Water Resources Research, 35(3), 651-662.

Revil, A., and Glover, P.W.J. (1998), Nature of surface electrical conductivity in natural sands, sandstones, and clays, Geophysical Research Letters, 25(5), 691-694.

Revil, A., and Glover, P.W.J. (1997), Theory of ionic surface electrical conduction in porous media, Physical Review B., 55(3), 1757-1773.

Rozycki, A., J.M.R. Fonticiella, and A. Cuadra (2006), Detection and evaluation of horizontal fractures in Earth dams using self-potential method, Engineering Geology, 82(3), 145-153.

Sachs J. R. and A. J. Grodzinsky (1995), Electromechanical spectroscopy of cartilage using a surface probe with applied mechanical displacement**,** Journal of Biomechanics, 28(8), 963-976.

Sen, P.N., C. Scala, and M.H. Cohen (1981), A self-similar model for sedimentary rocks with application to the dielectric constant of fused glass beads, Geophysics, 46(5), 781-795.

Sheffer, M.R. (2002), Response of the self-potential method to changing seepage conditions in embankments dams, M.A.Sc. Thesis, Dept. of Civil Eng., University of British Columbia, April 2002.

Sheffer, M.R., and J.A. Howie (2001), Imaging subsurface seepage conditions through the modeling of streaming potential, Proceedings of 54th Canadian Geotechnical Conference, Calgary, P. 1094-1101.

Sheffer, M.R., and J.A. Howie (2003), A numerical modelling procedure for the study of the streaming potential phenomenon in embankment dams, Symposium on the Application of Geophysics to Engineering and Environmental Problems, San Antonio, p. 475-487.

Shilov, V.N., A.V. Delgado, F. Gonzalez-Caballero, and C. Grosse (2001), Thin double layer theory of the wide-frequency range dielectric dispersion of suspensions of non-conducting spherical particles including surface conductivity of the stagnant layer, Colloids and Surfaces A: Physicochemical and Engineering Aspects, 192, 253-265.

Suski, B., A. Revil, K. Titov, P. Konosavsky, M. Voltz, C. Dagès, and O. Huttel (2006), Monitoring of an infiltration experiment using the self-potential method, Water Resour. Res., 42, W08418, doi:10.1029/2005WR004840.

Teng, H., and T.S. Zhao (2000), An extension of Darcy's law to non-Stokes flow in porous media, Chemical Engineering Science, 55, 2727-2735.

Titov, K., Loukhmanov, and A. Potapov (2000), Monitoring of water seepage from a reservoir using resistivity and self-polarization methods: case history of the Petergoph fountain water supply system, First Break, 18, 431-435.

Titov, K., A. Levitski, P.K. Konosavski, A.V. Tarasov, Y. Ilyin, and M.A. Buès (2005), Combined application of surface geoelectrical methods for groundwater flow modeling: a case history, Geophysics, 70(5), H21-H31.

Watanabe, T., and Y. Katagishi (2006), Deviation of linear relation between streaming potential and pore fluid pressure difference in granular material at relatively high Reynolds numbers, Earth, Planets and Space, 58(8), 1045-1051.

Waxman, M.H., and L.J.M. Smits (1968), Electrical conductivity in oil-bearing sands, Journal of the Society of Petroleum Engineers, 8, 107-122

Wildenschild, D., Roberts, and E. Carlberg (2000), On the relationship between microstructure and electrical and hydraulic properties of sand-clay mixtures, Geophys. Res. Lett., 27(19,), 3085-3088.

Wilt M.J., and R.F. Corwin (1989), Numerical modeling of self-potential anomalies due to leaky dams: Model and field examples. In: Lecture Notes in Earth Sciences, vol. 27, ed. Merkler GP et al., Detection of subsurface flow phenomena, Springer-Verlag, Berlin Heidelberg: 73-89.

Table 1. Measured properties of the glass bead packs

Sample	d range (in μm)	d_0 (in μm)	F (1)	σ_S (in mS m^{-1}) (1)	k_0 (in m^2) (2, 3)
S1a	50-60	56	3.3 ± 0.2	0.43 ± 0.05	2.0 x 10^{-12}
S1b	60-80	72	3.2 ± 0.2	0.32 ± 0.05	3.1 x 10^{-12}
S2	80-106	93	3.4 ± 0.2	0.26 ± 0.04	4.4 x 10^{-12}
S3	150-212	181	3.3 ± 0.2	0.13 ± 0.02	2.7 x 10^{-11}
S4	212-300	256	3.4 ± 0.2	0.08 ± 0.02	5.6 x 10^{-11}
S5	425-600	512	3.4 ± 0.2	0.05 ± 0.02	1.2 x 10^{-10}
S6	3000	3000	3.6 ± 0.2	0.10 ± 0.02	1.4 x 10^{-8}

(1) The uncertainty is determined from the best fit of the electrical conductivity data using Eq. (11)

(2) Determined from Eq. (25) where k is the measured value and Re the Reynolds number.

(3) The uncertainty is roughly equal to 10% of the reported value

Table 2. Values of the streaming potential coupling coefficient C_0 (expressed in mV m^{-1}). The coefficient C_0 is determined from Eq. (29) where C is the measured coupling coefficient and Re is the Reynolds number determined using Eq. (22) (Measurements made at 25± 1 °C).

Sample	$3x10^{-2}$ (S m^{-1})	10^{-2} (S m^{-1})	$3x10^{-3}$ (S m^{-1})	10^{-3} (S m^{-1})	$3x10^{-4}$ (S m^{-1})	10^{-4} (S m^{-1})
S1a	-12.5	-22.0	-75	-159	-454	-647
S1b	-8.5	-36.0	-142	-245	-748	-1944
S2	-8.1	-24.0	-87	-224	-477	-3215
S3	-7.6	-30.5	-137	-319	-1219	-4793
S4	-7.5	-23.0	-82	-317	-1132	-4502
S5	-11.1	-36.0	-107	-331	-1451	-3483
S6	-17.2	-43.0	-159	-510	-1014	-
C_{HS} (1)	-6.9	-30.2	-136	-504	-2033	-7063

(1) Values predicted by the Helmholtz-Smoluchowski equation (in mV/m).

Table 3. Measurements of the electrical conductivity of the samples σ (in 10^{-4} S m^{-1}) as a function of the electrical conductivity of the solution

Sample	10^{-1} (S m^{-1})	$6x10^{-2}$ (S m^{-1})	$3x10^{-2}$ (S m^{-1})	10^{-2} (S m^{-1})	$3x10^{-3}$ (S m^{-1})	10^{-3} (S m^{-1})	$3x10^{-4}$ (S m^{-1})	10^{-4} (S m^{-1})
S1a	289.5	199.0	100.9	38.4	12.61	6.59	3.38	2.11
S1b	291.4	199.0	101.3	38.6	12.30	6.62	2.54	1.94
S2	291.4	195.6	91.6	32.6	11.77	6.20	2.29	1.78
S3	290.9	193.0	86.8	32.7	11.74	5.11	1.81	1.19
S4	288.0	188.7	86.5	31.9	11.47	3.78	1.33	1.08
S5	283.1	187.3	84.6	31.5	11.14	3.31	1.14	0.94
S6	279.8	182.0	75.6	31.6	9.61	3.59	2.28	0.91

Table 4. Surface Conductivity – grain size relationship (NaCl solutions) (S: Silica, GB: Glass beads)

Study	Material	σ_S (in 10^{-4} S m^{-1})	d_0 (in μm)	σ_f (in S m^{-1})	T (in °C)	pH	Σ_S (in 10^{-9}S)
(1)	S-NaCl	71 ± 4	4.5	$2.4x10^{-3}$	24.5	5.7	5.3
(2)	S-KCl	1.03 ± 0.04	80	10^{-4}	25.0	5.7	1.4
(3)	GB-NaCl	1.3 ± 0.1	115	10^{-4}	23.0	7.5	2.5

(1) Bull and Gortner (1932) (using measurements of the streaming potential coupling coefficient).

(2) Lorne et al. (1999a) (using measurements of the electrical conductivity).

(3) Watanabe and Katagishi (2006) (using measurements of the electrical conductivity).

Table 5. Value of the variables used to compute the self-potential response to the seepage flow through the pipe

Property	Symbol	Value	Units
Length of the pipe	L_p	8.5	m
Diameter of the pipe	d	0.15	m
Length of the basin	L	34.5	m
Width of the basin	l	21	m
Height of the basin	h	3.5	m
Water conductivity	σ_f	$3.7\text{x}10^{-2}$	S m^{-1}
Clay conductivity	σ_c	$5.8\text{x}10^{-2}$	S m^{-1}
Gravel conductivity	σ_g	$1.3\text{x}10^{-2}$	S m^{-1}
Gravel EK current coefficient	L_g	$7.75\text{x}10^{-9}$	A m^{-1} Pa^{-1}

Captions

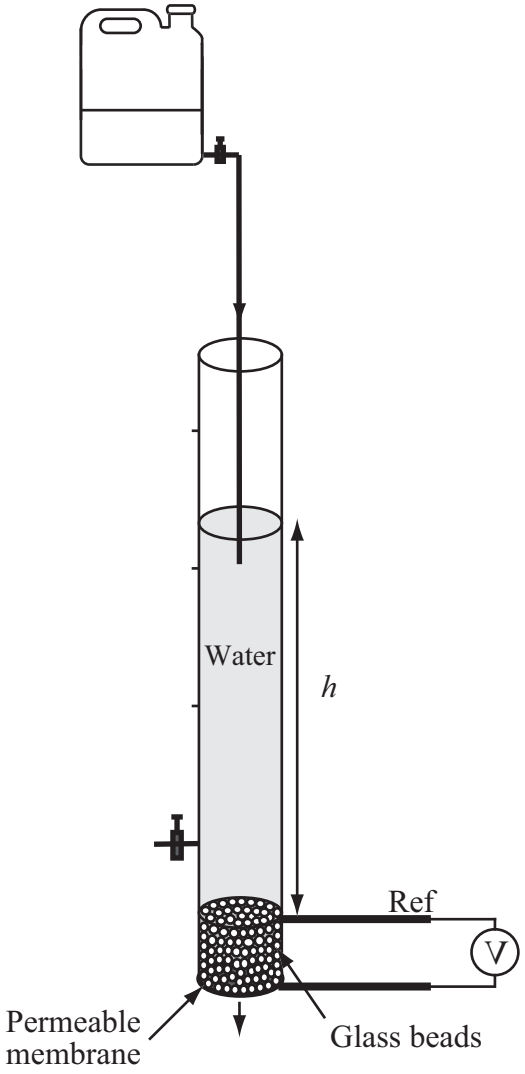

Figure 1. Sketch of the experimental setup. The sample is packed at the bottom of a Plexiglas tube and is maintained in the tube by a permeable membrane with a coarse mesh (the mesh is, however, finer than the diameter of the grains). The record of the self-potentials during the flow of the electrolyte through the sample is done with $Ag/AgCl_2$ electrodes ("Ref" is the reference electrode). The hydraulic heads are maintained constant at different levels and the streaming potentials are recorded at these levels at the end-faces of the sample.

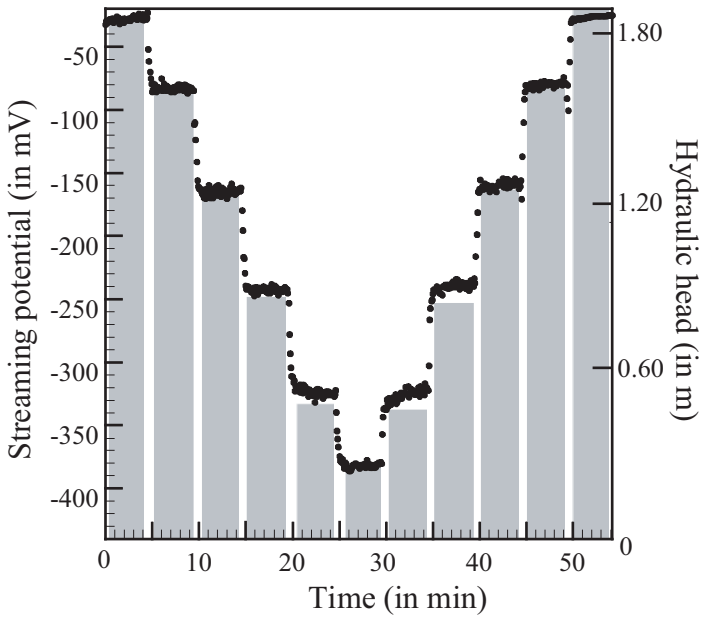

Figure 2. Example of a typical run for sample S3 (grain size of 150-212 μm) and a water conductivity of 10^{-3} S m^{-1}. The filled circles correspond to the measurements of the streaming potential at the two end-faces of the sample while the grey columns correspond to the measurement of the hydraulic heads.The streaming potentials are proportional to the imposed hydraulic heads. The results are reproducible. This means that there is no drift of the electrical potential of the electrodes during the duration of the experiment.

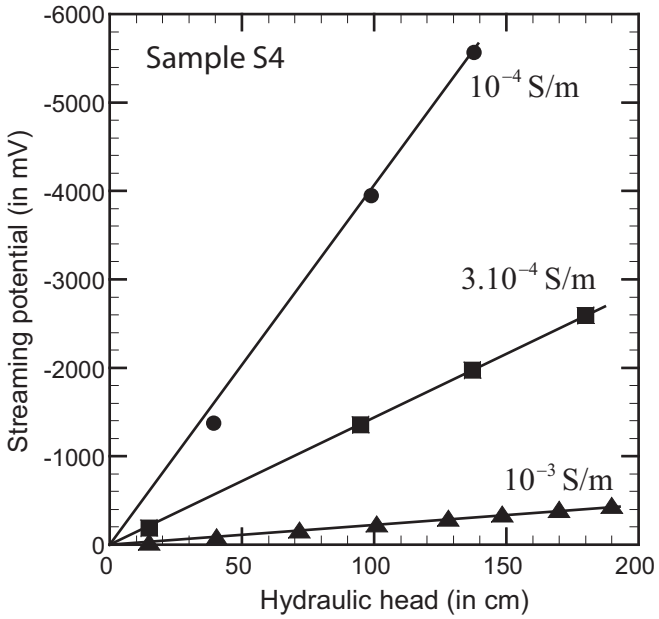

Figure 3. Example of typical runs for sample S4 (grain size of 212-300 μm) at three water conductivities. We observe linear relationships between the variation of the streaming potentials and the variation of the hydraulic heads at these different salinities. At each salinity, the streaming potential coupling coefficient is equal to the slope of the linear trend.

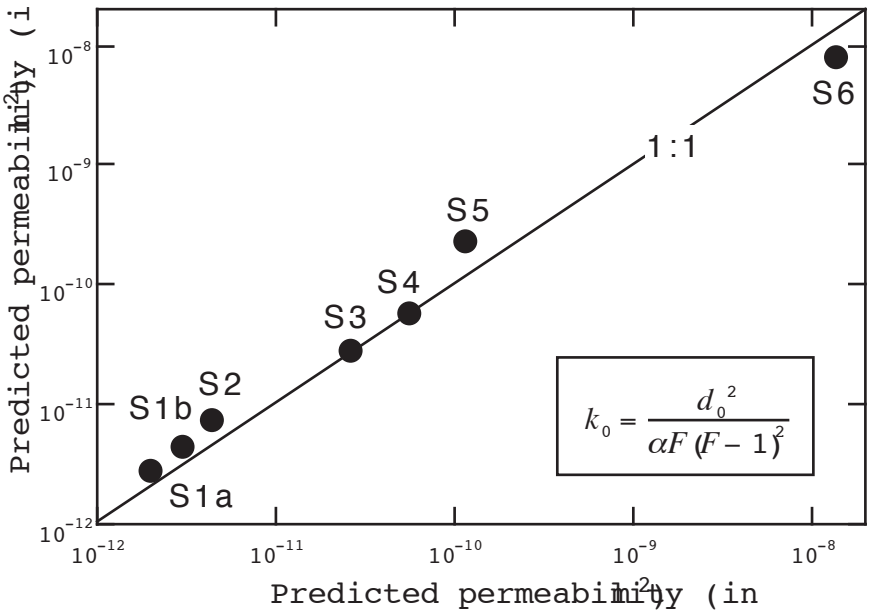

Figure 4. Measured versus modeled intrinsic permeability for the samples investigated in this study. We use $\alpha = 53$, and the formation factor is equal to 3.4. For sample S6, the measured permeability is corrected for the value of the Reynolds number using the formulae given in the main text, Equations (22) and (25).

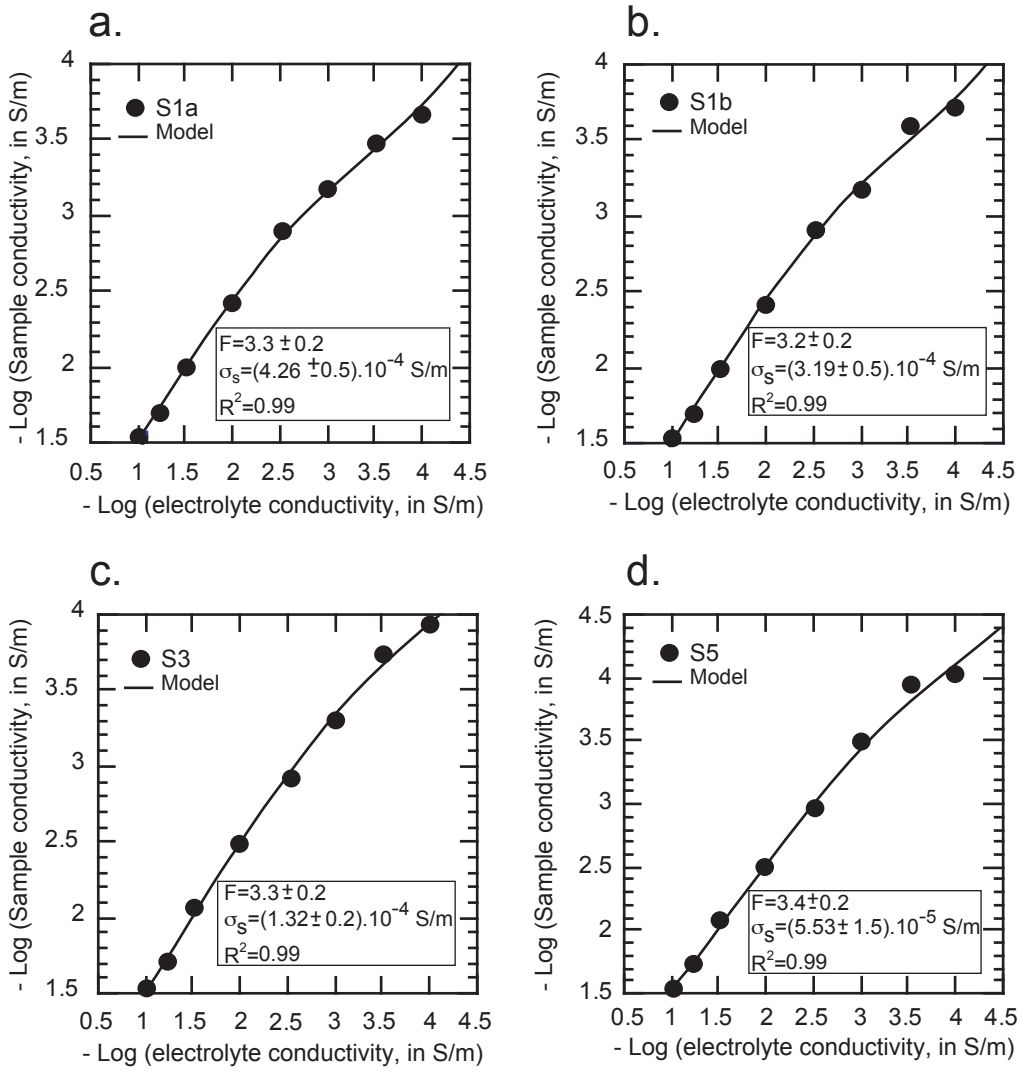

Figure 5. Plots showing the logarithm of the electrical conductivity of four samples σ versus the logarithm of the electrical conductivity of the brine σ_f. The iso-conductivity point is defined by the condition $\sigma = \sigma_f$ for which we also have $\sigma_S = \sigma_f$. The surface conductivity σ_S and the electrical formation factor *F* are inverted from Eq. (11) and the experimental data. The plain lines represent the best fit of the model. Note the very good agreement between the model and the experimental data.

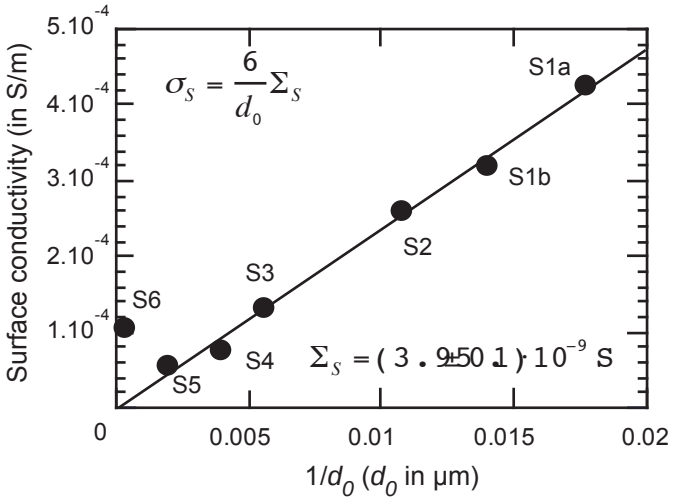

Figure 6. Surface conductivity σ_S versus the inverse of the mean bead size. The linear trend is used to determine the specific surface conductivity, which is equal to Σ_S = 4.0x10^{-9} S. Note the excellent correlation between the surface conductivity data and the mean diameter of the beads in the packs (except for sample S6), in agreement with the theory.

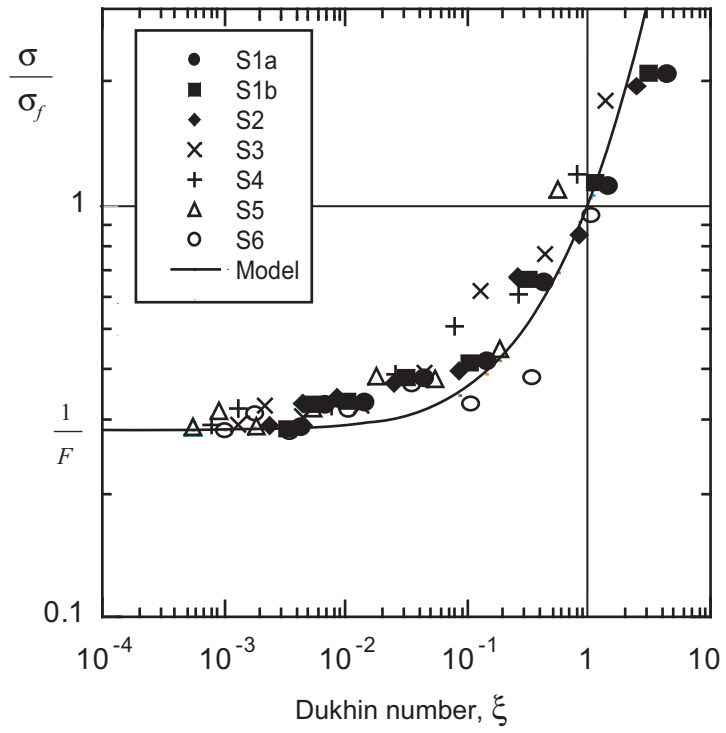

Figure 7. Reduced conductivity ratio σ/σ_f versus the Dukhin number ξ for all the glass bead packs investigated in this study (F is the electrical formation factor). The curve corresponds to the electrical conductivity model discussed in the main text, Eq. (11). Note the existence of an iso-conductivity point, (1, 1) in the coordinates of the plot. Note that the existence of this iso-conductivity point is not predicted by classical models like the Waxman and Smits (1968) formula.

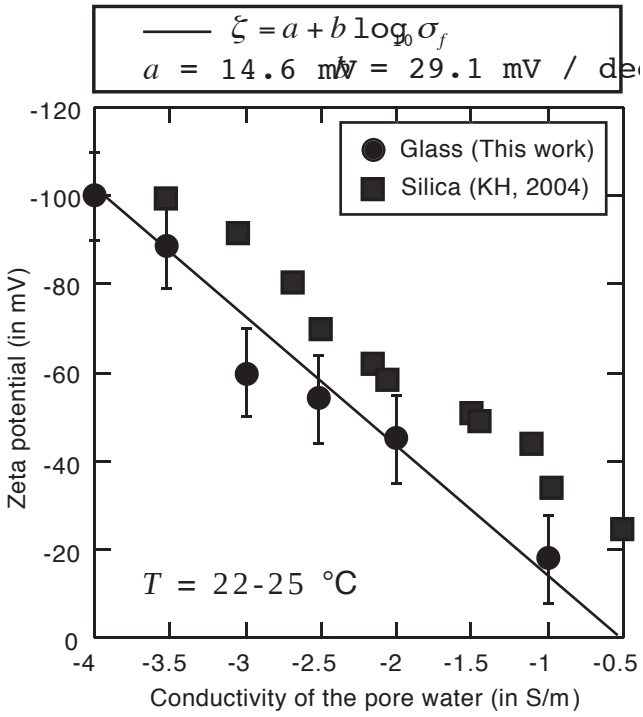

Figure 8. Zeta potential (in mV) versus the logarithm of the electrical conductivity of the pore water (r = 0.95) (NaCl, pH 5.6-5.9, 24°C). For comparison, we include the data reported for silica by Kirby and Hasselbrink (KH, 2004) (NaCl, pH 7, 25°C).

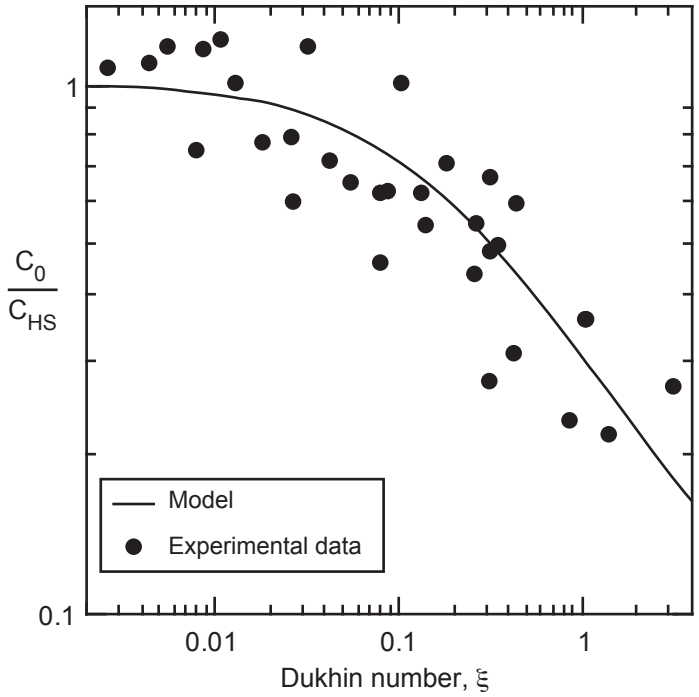

Figure 9. Reduced streaming potential coupling coefficient C_0 / C_{HS} versus the Dukhin number ξ (determined from the measured surface conductivity divided by the conductivity of the brine) for all the samples investigated in this study (see Table 2). Note that because the formation factor is roughly the same for all the samples, all the data fall on the same trend. The curve corresponds to the model discussed in the main text.

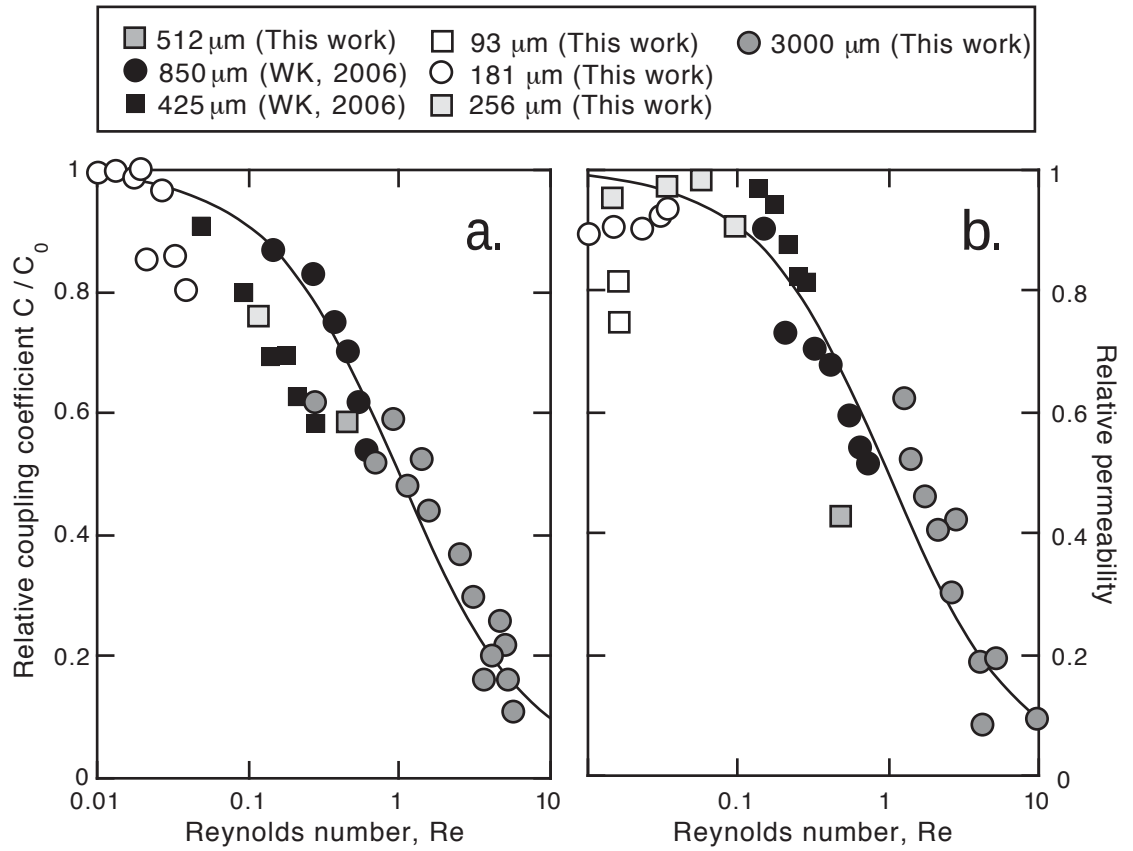

Figure 10. Influence of the Reynolds number, determined from Eqs. (22) and (23), upon the relative coupling coefficient C/C_0 (where C is the measured apparent streaming potential coupling coefficient and C_0 is given by Eq. (15)) and the relative permeability k/k_0 (where k is the measured apparent permeability (using Darcy's law) and k_0 is given by Eq. (8)). These measurements have been made at different salinities showing the universal character of this trend.

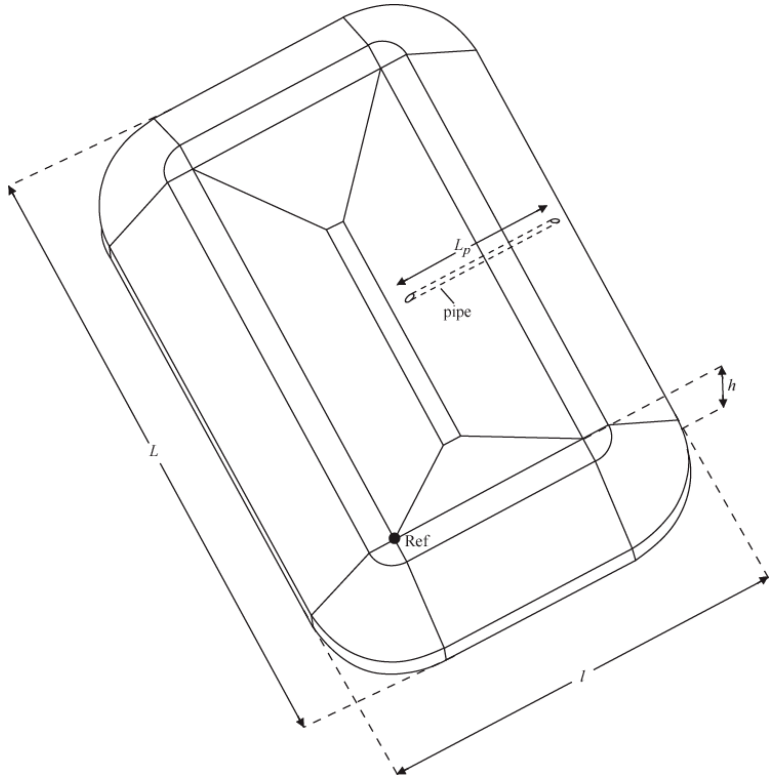

Figure 11. Geometry of water-filled basin with the position of the gravel-filled pipe, which constitutes the preferential fluid flow pathways for the water. The embankment is made of clay (permeability 10 mD). The reference for the electrical potential (position of the reference electrode where the electrical potential is taken equal to zero) is placed at the point Ref (ideally it should be located as far as possible from the self-potential anomaly resulting from the pipe).

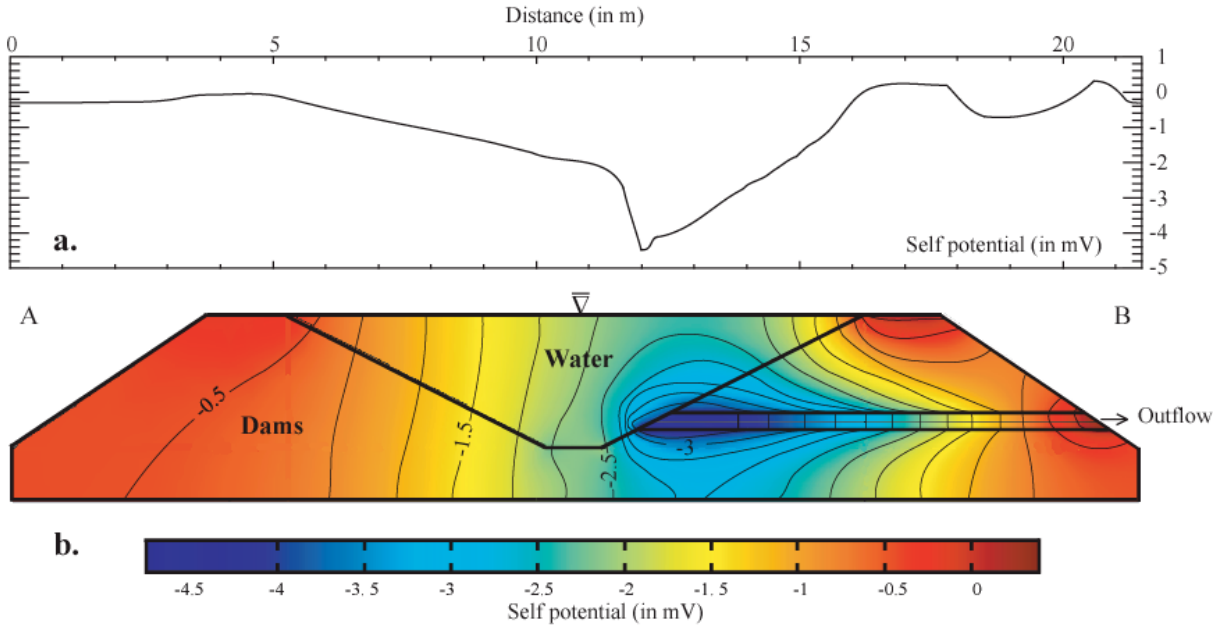

Figure 12. Plot showing the distribution of the electrical potential along a cross-section parallel to the pipe (the reference for the self-potential signals is shown on Figure 4). **a.** Distribution at the surface of the dams. The minimum of the self-potential distribution is located at the entrance of the pipe where a negative self-potential anomaly is observed (with an amplitude of few mV). Note that in water, the sensitivity of the measurements is typically 0.2 mV, which warranties a good signal-to-noise ratio. **b.** Distribution of the streaming equipotentials.

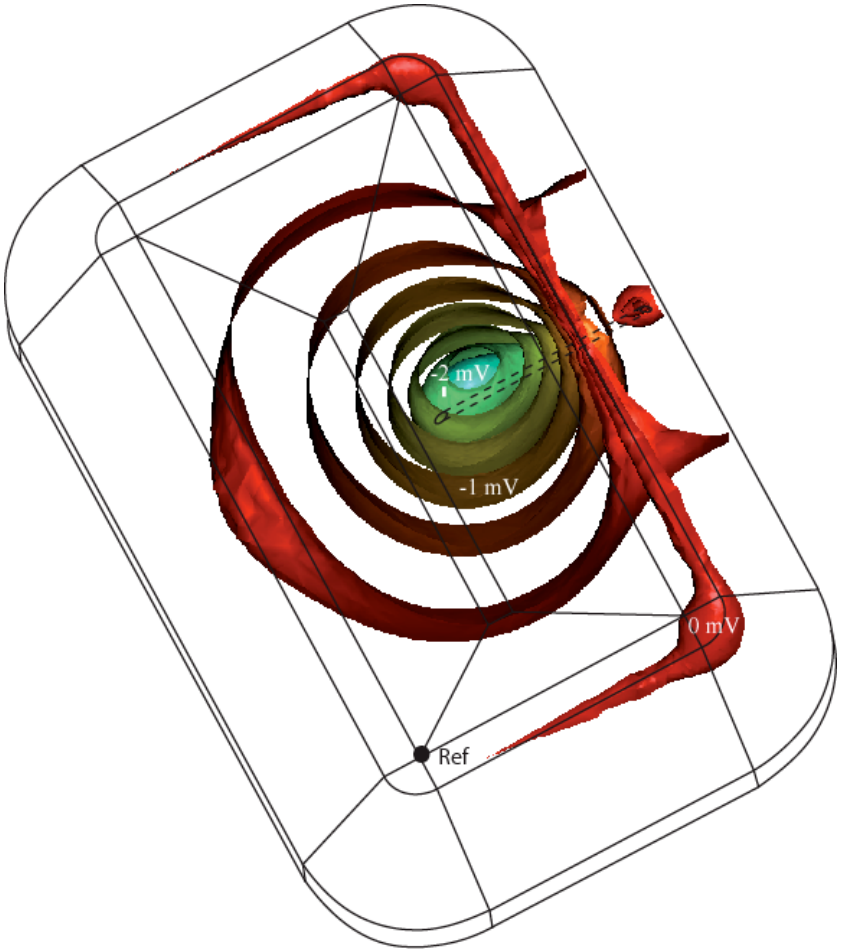

Figure 13. 3D-distribution of the electrical equipotentials in the basin due to the leakage of water through the pipe. The maximum intensity of the self-potential anomaly is 4 mV at the entrance of the leaking area.

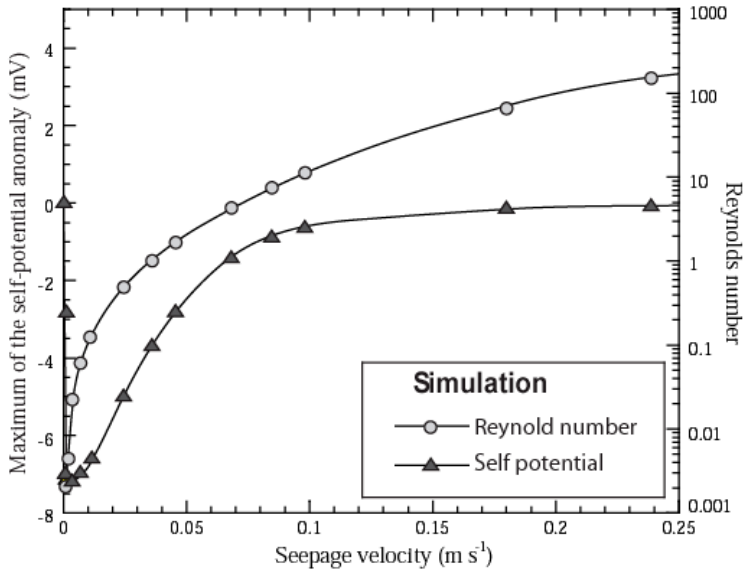

Figure 14. Maximum of the self potential anomaly at the entrance of the pipe versus the seepage velocity for different value of intrinsic permeability k_0. When the intrinsic permeability k_0 increases over time, there is a decrease of the magnitude of the self-potential anomaly due to the increase of the Reynolds number.

2.8. Conclusion

Nous avons vu que de nombreux travaux ont été menés sur différents paramètres pouvant influencer le potentiel zêta et le coefficient de couplage électrocinétique. Toutefois l'influence de la conductivité de surface était prise en compte en se basant sur l'hypothèse que sa principale contribution était dans la couche diffuse et non dans la couche de Stern. La loi de Darcy n'est valable que dans le cas d'un écoulement laminaire, il faut donc tenir compte de l'influence du nombre de Reynolds sur le potentiel zêta dans le cas d'un régime d'écoulement plus important. Grâce au modèle développé dans cet article, il est possible de corriger le potentiel zêta de l'influence des nombres de Reynolds et de Dukhin. La validité de ces lois a été vérifiée avec succès en comparant nos données expérimentales à nos modèles.

Aujourd'hui il serait intéressant des se rapprocher du milieu naturel en réalisant ce type d'expériences sur des milieux hétérogènes avec une large distribution de la taille des grains… Nous pourrions inclure l'étude de l'influence d'une interface entre deux types de billes dont les diamètres seraient très différents sur la naissance du phénomène d'électrofiltration ou d'un champ magnétique. Nous pensons que nous pouvons déjà utiliser ce modèle pétrophysique dans la détermination de la relation entre la vitesse d'infiltration et les anomalies de potentiel spontané mesurées dans divers cas et spécialement en hydrogéologie pour interpréter quantitativement les anomalies liées aux fuites d'eau dans les barrages et les digues ou à la fracturation dans les volcans actifs (e.g. Revil et al., 2003; Finizola et al., 2004).

2.9. Références

Agapiou J.S. and M.F. De Vries, 1989. An experimental determination of the thermal conductivity of a 304L stainless steel powder metallurgy material, *J. Heat Transfer,* 111, 281–286.

Bernabé, Y., and A. Revil, 1995. Pore-scale heterogeneity, energy dissipation and the transport properties of rocks, *Geophys. Res. Lett.*, 22, 1529-1532.

Bernabé Y., 1998. Streaming potential in heterogeneous networks, *J. Geophys. Res.*, 103 20827–20841.

Crespy, A., A. Boleve and A. Revil, 2007. Influence of the Dukhin and Reynolds numbers on the apparent zeta potential of granular porous media, *J. of Colloid Interface Sci.,* 305(1), 188-194.

Dukhin, S. S. and B. V Derjaguin, 1974. Surface and Colloid Science (Wiley-Interscience, New York).

Finizola, A., J. F. Lénat, O.Macedo, D. Ramos, J. C. Thouret, and F. Sortino, 2004. Fluid circulation and structural discontinuities inside Misti volcano (Peru) inferred from self-potential measurements, *J. Volcanol. Geotherm. Res.,* 135(4), 343– 360.

Guichet X., and P. Zuddas, 2003. Effets of secondary minerals on electrokinetic phenomena during water-rock interation, *Geophys. Res. Lett, 30*, No. 13, 1714, doi : 10.1029/2003GL017480.

Ishido, T., and H. Mizutani, 1981. Experimental and theoretical basis of electrokinetic phenomena in rock-water systems and its applications to geophysics, *J. Geophys. Res.,* 86, 1763-1775.

Hase, H., T. Ishido, S. Takakura, T. Hashimoto, K. Sato, and Y. Tanaka, 2003. Zêta potential measurement of volcanic rocks from Aso caldera, *Geophys. Res. Lett.*, 30(23), 2210.

Jardani, A., Revil, A., Barrash, W., Crespy, A., Rizzo, E., Straface, S., Cardiff, M., Malama, B., Miller, C., and Johnson, T. (2008) Reconstruction of the Water Table from Self-Potential Data: A Bayesian Approach, Ground Water, doi:10.1111/j.1745-6584.2008.00513.x

Leroy, P. and A. Revil, 2004. A triple-layer model of the surface electrochemical properties of clay minerals, *J. Colloid Interface Sci.*, 270 (2), 371–380.

Lorne, B, F. Perrier and J.P. Avouac, 1999a. Streaming potential measurements 1. Properties of the electrical double layer from crushed rock samples, *J. Geophys. Res.,* 104, 857–877.

Moore, J.R. and S.D. Glaser, 2007. Self-Potential Observations During Hydraulic Fracturing, *J. Geophys. Res.*, 112, B02204, 1-17.

Morgan, F. D., Williams, E. R., and T. R. Madden, 1989. Streaming potential of westerly granite with applications, *J. Geophys. Res.,* 94, 12,449-12461.

O'Brien R.W. and W.N. Rowlands, 1993. Measuring the surface conductance of kaolinitic particles, *J. Colloid Interface Sci.*, 159 (2), 471–476.

Pengra, D., S. Xi Li, and P. Wong, 1999. Determination of rock properties by low-frequency AC electrokinetics, *J. Geophys. Res.*, 104(B12), 29485-29508.

Revil, A., Pezard, P.A., Glover, P.W.J., 1999a. Streaming potential in porous media: 1. Theory of the zeta potential. *J. Geophys. Res.* 104, 20021–20031.

Revil, A., Schwaeger, H., Cathles, L.M., et P. Manhardt, 1999b. Streaming potential in porous media. 2. Theory and application to geothermal systems, *J. Geophys. Res.,* 104, 20033–20048.

Revil A., 1999. Ionic diffusivity, electrical conductivity, membrane and thermoelectric potentials in colloids and granular porous media: a unified model, *Journal of Colloid and Interface Science*, 212, 503-522.

Revil, A. D. Hermitte, E. Spangenberg, and J.J. Cochémé, 2002. Electrical properties of zeolitized volcaniclastic materials, *J. Geophys. Res.*, B 107(8), 2168–2184.

Revil, A., G. Saracco, and P. Labazuy, 2003. The volcano-electric effect, *J. Geophys. Res.,* 108(B5),2251.

Somasundaran, P., R. D. Kulkarni, 1973. A New Streaming Potential Cell and Study of Temperature Effects Using It, *J. Coll. Interf. Sci.,* 45, 591-600.

Teng, H., and T.S. Zhao, 2000. An extension of Darcy's law to non-Stokes flow in porous media, *Chemical Engineering Science,* 55, 2727-2735.

Waxman, M.H., and L.J.M. Smits, 1968. Electrical conductivities in oil-bearing shaly sands, *Journal of the Society of Petroleum Engineering,* 8, 107–122.

Chapitre 3:

Localisation de sources hydromécaniques par la méthode du potentiel spontané

3.1. Introduction

De nombreux auteurs (e.g., Surkov and Pilipenko, 1997 ; Moore and Glaser, 2006, 2007 ; Yoshida and Ogawa, 2004) ont montré que la fracturation de roches et en général toutes sortes de perturbations hydromécaniques affectant une roche poreuse et perméable génèrent des signaux électromagnétiques. En contexte volcanique, comprendre ces perturbations électromagnétiques pourrait permettre le développement de nouveaux dispositifs de surveillance des édifices.

Il existe au moins trois phénomènes physiques qui peuvent être responsables des signaux électromagnétiques observés durant ce type de manifestations : l'effet piézoélectrique, la migration des porteurs de charge électriques mobiles activée par une augmentation de la contrainte mécanique, et l'effet électrocinétique. Cependant, il semble peu probable que les deux premiers soient responsables des signaux de potentiel spontané observés car leur amplitude est inférieure à celle associée à l'effet d'électrofiltration dont nous avons discuté la physique dans les deux chapitres précédents (Nitsan et al., 1977 ; Yoshida et al., 1994, 1997 ; Moore et al., 2007).

Le défi principal posé par l'étude des signaux de potentiel spontané associés à des sources hydromécaniques est de comprendre (1) la physique de ces phénomènes et (2) de développer des algorithmes mathématiques afin de localiser les sources de ces signaux

électromagnétiques dans le sous-sol. Il est primordial de valider ces algorithmes en les comparant à des données expérimentales acquises dans des conditions bien connues comme en laboratoire.

Dans ce chapitre, nous ferons un rappel sur les techniques de localisation des sources de potentiel spontané (transformée en ondelettes, intercorrélation) puis nous verrons leurs applications dans le cadre d'une série d'expériences en cuve analogique. Ces dernières ont été réalisées dans la perspective de comprendre la signature électrique associée à un changement très rapide de pression par l'injection ou le pompage d'un très faible volume d'eau dans une cuve remplie de sable saturé d'eau.

3.2. Localisation de sources de courant dans un milieu conducteur

Nous analysons dans ce chapitre deux techniques de localisation de sources électriques dans un milieu conducteur. Ces deux méthodes sont l'analyse en ondelettes et la méthode d'intercorrélation. Nous discuterons des avantages et inconvénients de ces deux méthodes et nous les appliquerons à deux expériences de laboratoire.

3.2.1. L'analyse en ondelettes

L'analyse par ondelettes est une méthode de traitement du signal permettant de déterminer les propriétés d'une source multipolaire ayant une signature électrique à la surface du sol. Cette approche a l'avantage de ne pas requérir la connaissance de l'ordre du multipôle responsable des signaux de potentiel spontané enregistré à la surface du sol. Une fois l'ordre du multipôle connu, la technique d'intercorrélation que nous présenterons plus loin peut être utilisée pour trouver la profondeur de la source.

Les transformées en ondelettes ont été mises au point récemment pour l'interprétation des anomalies de champ de potentiel (Hornby et al., 1999). En utilisant les ondelettes de Poisson, nous pouvons estimer la profondeur des sources homogènes et déterminer la nature de la source (Moreau et al., 1997, 1999). Soit ψ une ondelette analysante (ondelette mère). Une ondelette $\psi(x)$ est une fonction avec support compact, de moyenne nulle, normalisée

telle que $\|\psi\|=1$ et centrée autour de 0. La transformée en ondelettes d'un champ de potentiel mesuré $\varphi_0(x)$ est définie par :

$$W_{\psi|\varphi_0}(b,a) = \int_{-\infty}^{\infty} \frac{1}{a}\psi\left(\frac{b-x}{a}\right)\varphi_0(x)dx \tag{3.1}$$

$$= (D_a\psi * \varphi_0)(b) \tag{3.2}$$

où b est un paramètre de position et a un paramètre de dilatation, a et b varient continûment et * désigne le produit de convolution. Chaque coefficient d'ondelette $W(b,a)$ apporte des informations sur le comportement de φ_0 au voisinage du point b et à l'échelle a. L'opérateur de dilatation est défini par :

$$D_a\psi(x) = \frac{1}{a}\psi\left(\frac{x}{a}\right). \tag{3.3}$$

Moreau et al. (1997, 1999) montrent qu'une classe spéciale d'ondelettes sont obtenues quand un multiplicateur homogène de Fourier de degré γ et une dilatation sont appliqués au noyau du semi groupe de Poisson. Ce noyau défini en fait le filtre de prolongement vers le haut $P_a(x)$, qui étend le champ harmonique mesuré du niveau z au niveau $z+a$:

$$P_a(x) = \frac{1}{\pi}\frac{a}{a^2+x^2}. \tag{3.4}$$

Les ondelettes horizontales et verticales sont donc définies par :

$$\psi_x^\gamma(x) = \frac{\partial^\gamma}{\partial x^\gamma}\left[\frac{1}{\pi}\frac{1}{(1+x^2)}\right], \tag{3.5}$$

$$\psi_z^\gamma(x) = \frac{\partial^{\gamma-1}}{\partial x^{\gamma-1}}\frac{\partial}{\partial a}\left[\frac{1}{\pi}\frac{a}{(a^2+x^2)}\right], \tag{3.6}$$

avec γ l'ordre de l'ondelette analysante. Une ondelette complexe est définie par (Moreau, 1995) :

$$\psi_c^\gamma(x) = \psi_x^\gamma(x) - i\psi_z^\gamma(x). \tag{3.7}$$

Le premier ordre des ondelettes complexes (appelées ondelettes de Cauchy) permet d'estimer l'orientation de la source (angle d'inclinaison). Moreau et al. (1997,1999) montrent que pour une source homogène localisée en $x = 0$, $z = z_0$, la loi d'échelle suivante lie les coefficients d'ondelettes à deux niveaux, a et a' :

$$W_{\psi^\gamma|\varphi(.,z=0)}(x,a) = \left(\frac{a}{a'}\right)^{\gamma} \left(\frac{a'+z_0}{a+z_0}\right)^{\beta} W_{\psi^\gamma|\varphi(.,z=0)}\left(x\frac{a'+z_0}{a+z_0}, a'\right), \tag{3.8}$$

où $\beta = -(\gamma-\alpha)$ est lié à la géométrie de la source (avec α le degré d'homogénéité du terme source).

Moreau et al. (1997) proposent d'estimer la profondeur de la source à partir du point d'intersection du maximum local des coefficients d'ondelettes. Une autre approche est développée par Moreau et al. (1999) et Sailhac et al. (2000) en estimant la profondeur de la source pour laquelle $\left|\log(W_a)/a^\gamma\right|$ varie linéairement en fonction de l'augmentation de $\log(a+z_0)$. Une fois la profondeur connue, on peut déterminer le coefficient β comme la pente de $\left|\log(W_a)/a^\gamma\right|$ versus $\log(a+z_0)$. Nous présenterons un peu plus loin un exemple d'application de cette méthode au champ de potentiel spontané associé à une infiltration pulse dans une cuve remplie de sable.

3.2.2. La méthode d'intercorrélation

Patella (1997a) propose une approche de localisation de source monopolaire rapide et simple pour localiser les sources ponctuelles de potentiel spontané dans le sous-sol. Il montre que la solution de l'équation de conservation du courant électrique peut se mettre sous une forme discrétisée. Le potentiel électrique mesuré en un point *P(x)* à la surface du sol peut s'écrire comme la somme de contributions élémentaires de monopôles, distribués en profondeur. La forme discrétisée du potentiel électrique s'écrit alors :

$$\varphi(P) = \sum_{q=1}^{Q} \frac{\Gamma_q}{r_q} \tag{3.9}$$

où φ est le potentiel électrique (V), Q est le nombre de frontières de l'espace discrétisé, Γ_q l'intensité de l'accumulation de charges électriques à l'interface q et $\boldsymbol{r}_q$ la distance entre la charge q et le point d'observation P. Les sources Γ_q peuvent être primaires c'est-à-dire issues de couplages électrocinétiques, ou bien secondaires, c'est-à-dire induites par des contrastes de

conductivité électrique.

Patella (1997a) définit une fonction d'intercorrélation entre un champ électrique associé à une charge ponctuelle (fonction scanante) et le champ électrique mesuré à la surface du sol :

$$\eta(x_q, z_q) = C \int_{-\infty}^{+\infty} E_x(x) I_x(x - x_q, z_q) dx \,, \tag{3.10}$$

avec $E_x = -\partial\varphi / \partial x$ est le champ électrique horizontal mesuré en surface et I_x est la fonction scannante, dérivée horizontale de la fonction de Green d'une source ponctuelle dans un espace homogène :

$$I_x(x - x_q, h_q) = \frac{(x - x_q)}{\left[(x - x_q)^2 + {z_q}^2\right]} dx \,. \tag{3.11}$$

et où (x_q, z_q) représente les coordonnées de la source et (x, z =0) le point d'observation. Le coefficient C de l'équation (3.10) est un terme de normalisation qui dépend de l'énergie du signal de potentiel spontané à la surface du sol,

$$C = \left[\int_{-\infty}^{+\infty} {E_x}^2(x) dx \int_{-\infty}^{+\infty} I_x^2(x - x_q, h_q) dx \right]^{-1/2} \tag{3.12}$$

Le principe de cette méthode consiste à discrétiser la zone étudiée et à calculer à chaque noeud de la grille les coefficients d'intercorrelation. Les valeurs de la probabilité d'occurrence de charges ainsi calculée sont représentées sous forme de contours montrant les zones à plus forte probabilité d'occurrence. Patella (1997b) a généralisé cette approche au cas tridimensionnel pour prendre en compte les effets de la topographie. Toutefois, la méthode de Patella n'est pas adaptée pour localiser des sources étendues, des sources trop proches les unes des autres ou des sources dipolaires. Revil et al. (2001) ont modifié cette approche afin de rechercher des sources dipolaires en démontrant que les signaux de potentiel spontané sont en général associés à des sources de nature dipolaire. Iuliano et al. (2002) ont généralisé les résultats obtenus par Revil et al. (2001) en 3D.

Considérons un système de coordonnées cartésiennes (x,y,z) où l'axe des z est positif vers le haut. Supposons que le champ électrique $\boldsymbol{E}(\boldsymbol{r})$ est dû à P dipôles de moment $\boldsymbol{d}_p$ (p $\in$

{1,2, …., P}) le p^{ième} élément est localisé en $\mathbf{r}\equiv(x_p,y_p,z_p)$. Le champ électrique associé à un dipôle est:

$$\mathbf{E}(\mathbf{r}) = \mathbf{d}\nabla\mathbf{G}(\mathbf{r}) \tag{3.13}$$

où G est la fonction de green de la source supposée être dipolaire.

$$\mathbf{E}(\mathbf{r}) = \sum_{p=1}^{p}(\mathbf{d}_p\nabla_p)\mathbf{G}(\mathbf{r}_p - \mathbf{r}) \tag{3.14}$$

avec

$$\mathbf{G}(\mathbf{r}_p - \mathbf{r}) = \frac{\mathbf{r}_p - \mathbf{r}}{|\mathbf{r}_p - \mathbf{r}|^3} \tag{3.15}$$

on note E le module du champ électrique $\boldsymbol{E}(\boldsymbol{r})$, l'énergie associée au champ électrique s'écrit :

$$\wp(E) = \int_S E^2(\mathbf{r})dS \tag{3.16}$$

$$= \sum_{\upsilon} d_\upsilon \int_S \mathbf{E}(\mathbf{r})\frac{\partial\mathbf{G}}{\partial\upsilon_p}dS \tag{3.17}$$

où $\upsilon=x,y,z$ et $\upsilon_p=x_p,y_p,z_p$, la projection de S sur le plan horizontal (x,y) est adaptée à un rectangle dont les côtés ont une dimension de 2X et de 2Y respectivement suivant les axes x et y correspondant, par exemple, aux dimensions de notre cuve. On note $g(z)$ le facteur de correction topographique défini par :

$$g(z) = \left[1 + \left(\frac{\partial z}{\partial x}\right)^2 + \left(\frac{\partial z}{\partial y}\right)^2\right]^{1/2} \tag{3.18}$$

En applicant l'inégalité de Schwarz, Iuliano et al. (2002) ont introduit le produit d'intercorrelation suivant :

$$\eta_\upsilon(r_p) = C_\upsilon^p \int_{-X}^{X}\int_{-Y}^{Y}\mathbf{E}(\mathbf{r})\frac{\partial\mathbf{G}(\mathbf{r}_p - \mathbf{r})}{\partial\upsilon_p}g(z)dxdy \tag{3.19}$$

Le coefficient de normalisation C_v^p est définit par :

$$C_v^p = \left[\int_{-X}^{X} \int_{-Y}^{Y} E^2(\mathbf{r}) g(z) dxdy \int_{-X}^{X} \int_{-Y}^{Y} \frac{\partial \mathbf{G}(\mathbf{r}_p - \mathbf{r})}{\partial \upsilon_p} g(z) dxdy \right]^{-1/2} \quad (3.20)$$

à chaque $\boldsymbol{r}_p$ correspond trois valeurs $\eta^{(d)}$ qui peuvent être calculées, $\eta_x^{(d)}$, $\eta_y^{(d)}$, $\eta_z^{(d)}$.
Étant donné que la fonction qui définit le coefficient d'intercorrelation peut être négative, nous ne pouvons pas directement utiliser le terme de densité de probabilité. Nous utilisons ici l'hypothèse selon laquelle la position du maximum de la valeur absolue de la fonction d'intercorrelation correspond au maximum de probabilité de présence d'un dipôle.
La fonction DOP s'écrit alors comme la norme de la somme vectorielle de ces trois composantes vectorielles :

$$\eta(r_p) = \sqrt{\eta_x(r_p)^2 + \eta_y(r_p)^2 + \eta_z(r_p)^2} \quad (3.21)$$

Nous présenterons un exemple de cette méthode plus loin pour le cas d'une injection pulse d'eau dans une cuve remplie de sable.

3.3. Validation Expérimentale

3.3.1. Description de la cuve et propriétés pétrophysiques du sable

La cuve de verre utilisée pour les expériences a pour dimensions 70 cm de longueur, 50 cm de hauteur et 50 cm de largeur. Le verre nous permet de limiter les effets électrostatiques et les dimensions de la cuve nous offre la possibilité de traiter les données en 3D. La cuve est remplie d'un sable homogène dont les propriétés physiques ont été déterminées indépendamment (conductivité électrique, perméabilité, porosité, coefficient de couplage électrocinétique). Le sable utilisé dans la cuve est un sable de grains de quartz fin, calibré, de diamètre compris entre 100 et 160 µm avec un diamètre moyen de 132 µm. Des analyses aux rayons X ont permis de déterminer la composition du sable. Il est composé de silice SiO_2 (~ 95 %), d'orthoclase KSi_3AlO_8 (4%) et de plagioclase $NaAlSi_3O_8$ (< 1%). La densité des grains

est considérée égale à celle du quartz pur soit 2650 kg m^{-3}. La porosité ϕ, la perméabilité k et le facteur de formation électrique F ont été mesuré au laboratoire (voir Suski et al., 2006). Les résultats sont $\phi = 0.34 \pm 0.02$, $k = 7.3x10^{-12}$ m^2, et $F = 4.3 \pm 0.01$. Ce qui donne une conductivité hydraulique $K = 7.1\ 10^{-5}$ m s^{-1} en considérant la viscosité du fluide égale à 10^{-3} Pa s à 20 °C. Toutes les expériences ont été réalisées avec un électrolyte composé d'eau et d'une très légère quantité d'hypochlorite de sodium (NaClO) de conductivité électrique σ_f=5.6 10^{-3} S m^{-1} à 25°C et de pH=6.8. L'hypochlorite a été utilisé pour limiter la croissance de bactéries. Le coefficient de couplage électrocinétique C' a été déterminé selon la même méthode que celle développée par Suski et al. (2006) et décrite dans le chapitre 1 section 1.3.2.2. Lorsque le sable est saturé par notre électrolyte, le coefficient de couplage C' est égal à –46 ± 2 mV/m.

3.3.2. Principe des mesures de potentiel spontané

Dans cette section, nous allons décrire le dispositif expérimental dont la figure 3.1 nous donne une vue d'ensemble.

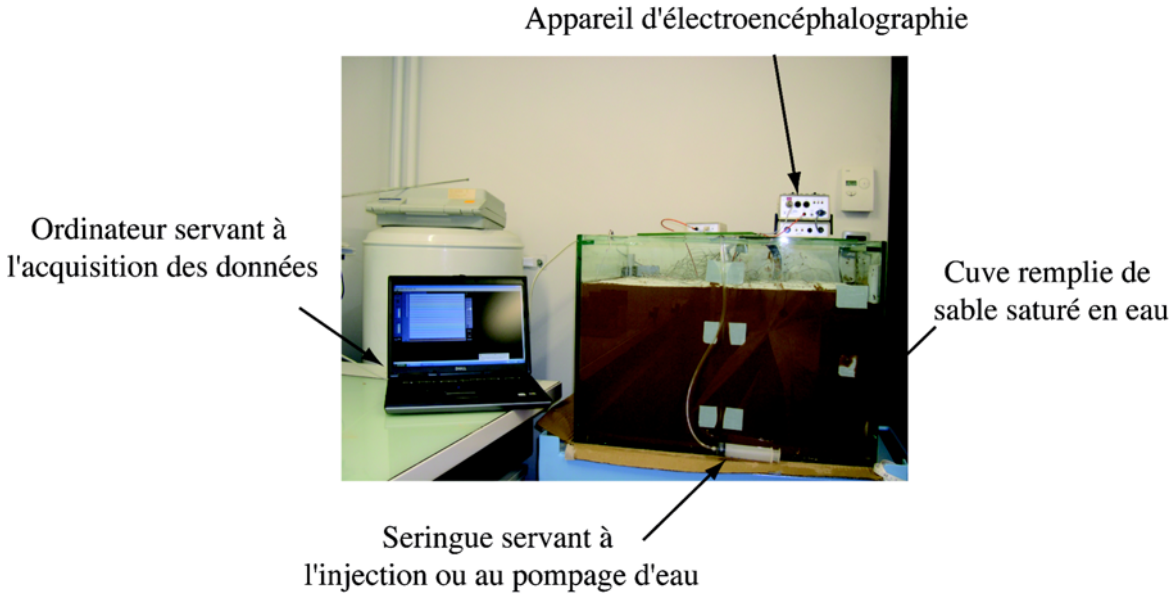

Figure 3.1. Vue d'ensemble du dispositif expérimental.

3.3.2.1. Les électrodes

Jusqu'au début du XXème siècle, le potentiel spontané était mesuré par de simples tiges de métal ou d'alliage (cuivre, acier, laiton) directement plantées dans le sol. Leur facilité

d'utilisation et leur faible coût étaient leurs principaux avantages. Cependant la variation de la nature des porteurs de charge entre le sol et le métal de l'électrode génère une accumulation de charges à l'interface sol/électrode et donc une polarisation de celle-ci.
Afin de limiter ces bruits instrumentaux, souvent non-quantifiables, Schlumberger en 1920, a développé le concept d'électrodes non-polarisables. L'élément métallique baigne dans une solution saline contenant l'ion métallique correspondant. Un élément poreux comme de la céramique ou du sable assure le bon contact entre la solution saline et le sol. La solution saline étant en équilibre avec l'élément métallique, le potentiel de l'élément métallique est le même que dans la solution et que dans l'élément poreux en contact avec sol.

Compte tenu des expériences envisagées, il était indispensable d'utiliser des électrodes de petite taille et d'une très grande précision. Les électrodes que nous avons utilisées (Figure 3.2) ont été mises au point par Biosemi (www.biosemi.com). En associant une première étape d'amplification à des électrodes Ag/AgCl des mesures avec un bruit réduit et exemptes d'interférences sont possibles. Ce sont des capteurs avec une impédance de sortie très faible où tous les problèmes liés au couplage capacitif entre les câbles et les sources des interférences sont éliminés. L'impédance d'entrée du voltmètre de 300 MOhm est très importante. L'encapsulation des électrodes les rend totalement résistantes à l'eau. Leur petite taille (proche de 1 cm de diamètre) implique une grande facilité d'utilisation à l'échelle de la cuve.

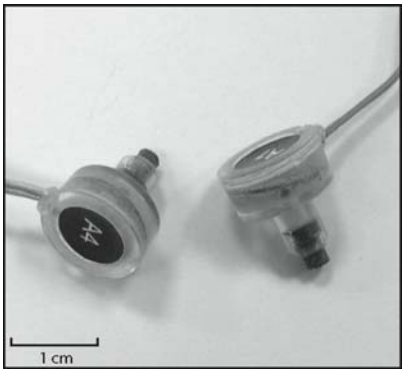

Figure 3.2: Photographie des électrodes Ag/AgCl.

3.3.2.2. Acquisition et traitement des données

Jusqu'à présent, les signaux de potentiel spontané liés à de la déformation ont été difficilement mesurables à cause de la sensibilité insuffisante des appareils de mesures. La plupart des systèmes utilisés en géophysique ont une sensibilité de 0.1 mV. La grande nouveauté apportée par ces expériences est l'utilisation d'un appareil, à l'origine élaboré pour l'électroencéphalographie, dont la sensibilité est de trois ordres de grandeurs supérieurs aux systèmes précédents (Perrier et Morat, 2000 ; Rizzo et al., 2004). Il s'agit d'un voltmètre compact (Figure 3.3), associé aux électrodes Ag/AgCl d'une sensibilité de 0.1 μV, dont la gamme de fréquence d'acquisition va de 256 Hz à 2048 Hz, la bande passante de DC à 7 kHz. Dans le cas de nos expériences, nous avons utilisé une fréquence d'acquisition de 1024 Hz suffisante à l'obtention de données de qualité.

Figure 3.3 : Appareil d'électro-encéphalographie d'après www.biosemi.com.

Les données de potentiel spontané ont été transformées dans le domaine fréquentiel par Transformée de Fourier Rapide. Nous avons remarqué que le 50 Hz (et ses harmoniques) du courant électrique d'EDF dominait fortement les données brutes de potentiel spontané. Nous avons donc utilisé un filtre passe bas avec une fréquence de coupure à 30 Hz afin d'atténuer les hautes fréquences. Les signaux filtrés sont ensuite ramenés au domaine temporel par transformée de Fourier inverse.

3.3.2.3. Expériences d'injection et de pompage

Nous avons réalisé quatre expériences afin d'observer et d'analyser les signaux électriques résultant d'une très brève injection ou d'un retrait d'eau au centre de la cuve (Figure 3.4). L'eau est injectée à 15 cm de profondeur à travers un capillaire rempli avec l'électrolyte et connecté à une seringue.

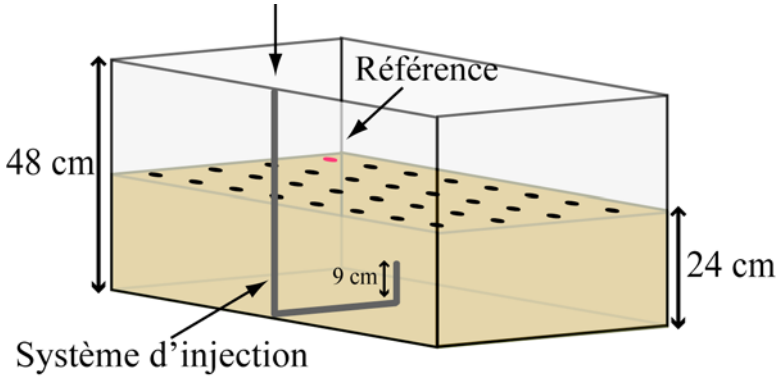

Figure 3.4 : Représentation 3D de la cuve. Un total de 32 électrodes est réparti à trois cm de la surface de la cuve. La cuve est remplie de sable bien calibré et saturé par une solution dont la conductivité électrique et la composition est de l'électrolyte. L'électrode de référence est figurée en rouge.

L'injection est faite grâce à coup de marteau sur le piston de la seringue. Nous nous sommes bien assurés que l'eau injectée était de même composition chimique que celle contenue dans la cuve en extrayant directement l'eau de la cuve quelques minutes avant l'expérience. Ainsi nous évitons des effets de diffusion ou de membrane qui pourraient être associés à une différence de composition chimique entre l'eau injectée et l'eau qui sature le sable. Dans les deux premières expériences, les 32 électrodes non-polarisables ont été également réparties à 3 cm en dessous de la surface (Figure 3.5.a) tandis que pour les expériences 3 et 4, les électrodes sont réparties sur un plan vertical contenant le système d'injection (Figure 3.5.b).

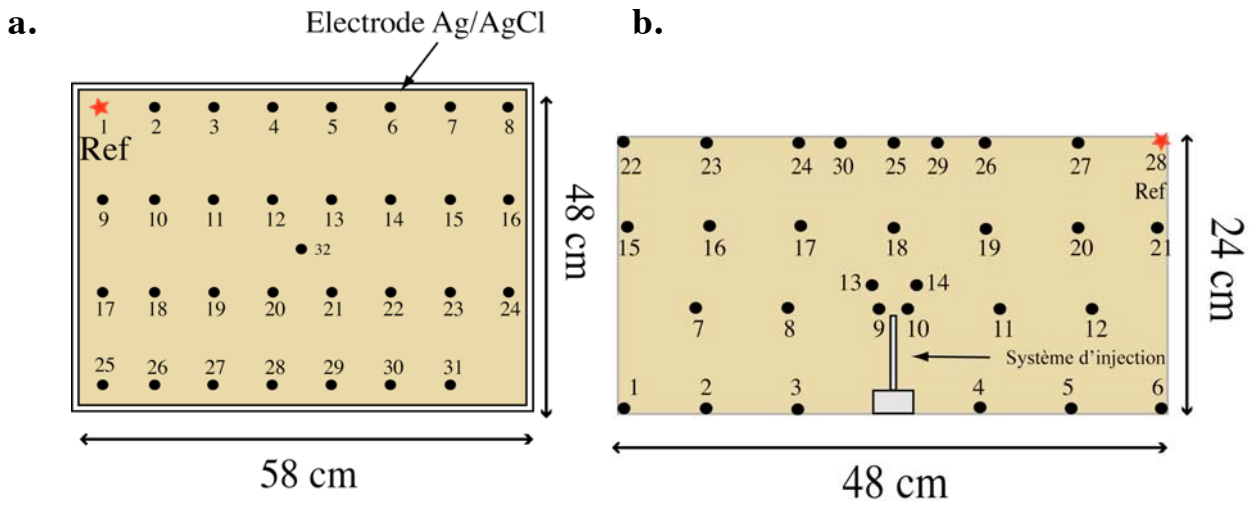

Figure 3.5 : (**a**) Vue de dessus de la surface de la cuve montrant la position des électrodes (Expériences 1 et 2). Les électrodes sont placées à une profondeur de 3 cm. L'étoile rouge représente la position de l'électrode de référence. L'électrode 32 est placée juste au-dessus de la sortie du capillaire. (**b**) Schéma représentant la position des électrodes sur un plan vertical (Expériences 3 et 4).

3.4. Résultats

Les résultats des ces expériences réalisées en cuve ont fait l'objet d'un article, publié dans *Journal of Geophysical Research* en 2008, intitulé « Detection and localization of hydromechanical disturbances in a sandbox using the self-potential method » par Crespy A., A. Revil, N. Linde, S. Byrdina, A. Jardani, A. Bolève, P. Henry.

Après la publication de cet article, nous nous sommes rendus compte qu'il y avait quelques imprécisions dans la section 4.1, il est écrit que le terme prépondérant de l'équation 11 est $\nabla\overline{Q}_V \cdot \mathbf{U}$ (lié au flux d'eau porale et au gradient de charges) mais il faut également tenir compte du deuxième terme $\overline{Q}_V \nabla \cdot \mathbf{U}$. La densité de courant volumique obtenue lors de l'expérience d'injection étant négative, le champ observé (négatif à tous les points de mesure) résulte du fait que la densité de courant à l'exutoire n'est que partiellement compensée par les charges positives réparties dans le milieu.

Nous avons montré en utilisant les transformées en ondelettes et les fonctions d'intercorrelation que le potentiel électrostatique mesuré en surface était identique au champ d'un dipôle situé à l'exutoire. Dans le modèle hydroélectrique nous avons fait l'hypothèse que le moment de ce dipôle était proportionnel au flux d'eau à l'exutoire.

Detection and localization of hydromechanical disturbances in a sandbox using the self-potential method

A. Crespy (1), A. Revil (2, 8, 9), N. Linde (3), S. Byrdina (4), A. Jardani (5, 6), A. Bolève (7, 8), and P. Henry (10)

(1) CNRS-CEREGE, Université Aix Marseille III, Aix en Provence, France

(2) Colorado School of Mines, dept of Geophysics, Golden, Colorado, United States

(3) Swiss Federal Institute of Technology, Institute of Geophysics, Zurich, Switzerland

(4) IPGP, 4 Place Jussieu, Paris, France

(5) Laboratoire de Géologie, Faculté des Sciences, Université de Rouen, Mont Saint Aignan, France

(6) Bureau d'Etude ALISE, Saint Jacques-sur-Darnétal, France

(7) SOBESOL, Savoie Technolac, BP 230, F-73375 Le Bourget du Lac Cedex, France

(8) LGIT (UMR 5559), University of Savoie, Equipe Volcan, Chambéry, France

(9) GdR FORPRO 0788, CNRS-ANDRA, France.

(10) Collège de France, Université Aix Marseille III, France.

Abstract. Four sandbox experiments were performed to understand the self-potential response to hydro-mechanical disturbances in a water-infiltrated controlled sandbox. In the first two experiments, ~0.5 mL of water were abruptly injected through a small capillary at a depth of 15 cm using a syringe impacted by a hammer stroke. In the second series of experiments, ~0.5 mL of pore water were quickly pumped out of the tank, at the same depth, using a syringe. In both type of experiments, the resulting self-potential signals were measured using 32 sintered Ag/AgCl medical electrodes. In two experiments, these electrodes were located 3 cm below the top surface of the tank. In two other experiments, they were placed along a vertical section crossing the position of the capillary. These electrodes were connected to a voltmeter with a sensitivity of 0.1 μV and an acquisition frequency of 1.024 kHz. The injected/pumped volumes of water produced hydro-mechanical disturbances in the sandbox. In turn, these disturbances generated dipolar electrical anomalies of electrokinetic nature with an amplitude of few microvolts. The source function is the product of the dipolar Green's function by a source intensity function that depends solely on the product of the streaming potential coupling coefficient of the sand to the pore fluid overpressure with respect to the hydrostatic pressure. Numerical modeling using a finite element code was performed to solve the coupled hydro-mechanical problem and to determine the distribution of the resulting self-potential during the course of these experiments. We use 2D and 3D algorithms based on the cross-correlation method and wavelet analysis of potential fields to show that the source was a vertical dipole. These methods were also used to localize the position of the source of the hydromechanical disturbance from the self-potential signals recorded at the top surface of the tank. The position of the source agrees with the position of the inlet / oulet of the capillary showing the usefulness of these methods for application to active volcanoes.

1. Introduction

Distinct electromagnetic (EM) signals are generated during rock fracturing, steam injection in Hot Dry Rock (HDR) reservoirs, detonation of explosive charges in boreholes, and generally speaking any kind of hydro-mechanical disturbances affecting the porous and conductive ground [e.g., *Surkov and Pilipenko*, 1997; *Ushijima et al*., 1999; *Yoshida*, 2001; *Gaffet et al.* 2003; *Yoshida and Ogawa*, 2004; *Soloviev and Sweeney*, 2005; *Moore and Glaser*, 2006, 2007; *Park et al.*, 2007]. In addition, possible EM signals in various frequency ranges have been reported preceding earthquakes [e.g., *Tate and Daily*, 1989; *Fraser-Smith et al*., 1990; *Dea et al*., 1991; *Park et al*., 1993, *Fenoglio et al.* 1995, and references therein]. The self-potential method consists in passively recording the fluctuations of the electrical at the surface of the Earth or in boreholes to evidence polarization mechanisms occurring at depth. *Byrdina et al.* (2004) observed well-defined time variations of the self-potential correlated with ultra long period seismic signals associated with ongoing fracturing at the Merapi volcano. Self-potential signals have also been observed in geothermal fields (e.g., *Ishido* [1981, 1989]; *Revil and Pezard* [1998]; *Revil et al.* [1999a, b]; *Yasukawa et al*. [2002]).

Understanding of these EM disturbances could be used to develop new geophysical methods to monitor fracturing and hydro-mechanical disturbances in real time in the Earth to a depth of few kilometers. These signals could be also very important in the growing field of CO_2 sequestration to monitor in real-time the migration of CO_2 in a sedimentary reservoir or the rupturing of a pressure seal (e.g., *Moore et al.* [2004]). Similar researches are presently carried out in biomechanics (*Garon et al.* [2002]), in the study of deformation of glacier by earth tides (*Kulessa et al.* [2003]), and in the study of deformation and leakage in earth dams (*Wilt and Corwin* [1989]; *Titov et al.* [2000]; *Sheffer and Howie* [2003]).

The main challenges in the study of self-potential signals associated with hydromechanical disturbances are (1) to understand the physics underlying these phenomena and (2) to propose mathematical algorithms to locate the source of these EM disturbances in

the ground. It is also important to validate these algorithms against experimental data recorded in well-controlled conditions (*Minsley et al.* [2007]). However, observations of self-potential signals corresponding to deformation were probably not available before because of the sensitivity of the apparatus used. Most apparatus used in geophysics have a sensitivity of 0.1 mV. In the present work, we use a highly sensitive voltmeter with sintered Ag/AgCl electrodes with a sensitivity better than 0.1 μV.

There are, at least, three physical phenomena that could be responsible for electromagnetic signals during fracturing and hydro-mechanical disturbances. They are the piezoelectric effect [e.g., *Nitsan*, 1977; *Yoshida et al.*, 1994, 1997]; the migration of mobile electronic charge carriers activated by stress drops [*Freund et al.*, 2006a, b]; and the electrokinetic effect [e.g., *Fedorov et al.* 2001; *Yoshida and Ogawa*, 2004; *Moore and Glaser*, 2006, *Revil and Linde*, 2006]. However, it seems unlikely that the piezoelectric effect and the migration of mobile electronic charge carriers activated by stress drops can be responsible for observed self-potential signals in the shallow Earth since the magnitude of these two phenomena are much smaller the electrokinetic effect (see *Nitsan*, [1977], *Yoshida et al.*, [1994, 1997], and *Moore and Glaser* [2007]). *Yoshida et al.*, [1994, 1997] and *Moore and Glaser* [2007] provided convincing arguments that the electrokinetic effect is the most likely physical mechanism susceptible to produce large EM signals in the first kilometers of the Earth crust. In a porous pack of sand grains, the piezometric effect can be ruled out as generating any electromagnetic effects because the quartz crystals are randomly oriented. At depths greater than a few kilometers, the migration of mobile electronic charge carriers activated by stress drops could be the main current-driving mechanism [*Freund et al.*, 2006a, b].

In this paper, we are interested in performing well-constrained sandbox experiments for the purpose of understanding the electrostatic signature associated with hydro-mechanical disturbances caused by a sudden change in fluid pressure in a water-saturated controlled

sandbox. To our knowledge, this is the first time that such type of experiment is undertaken. A very sensitive voltmeter with a high acquisition frequency and connected to very small (~ 1 mm) non-polarizing silver / silver chloride electrodes was used. This novel system was initially developed in the context of electro-encephalography. It has a sensitivity 3 orders of magnitude better than previous systems used for similar experiments in geophysics (see *Butler et al.* [1990], *Perrier et al.* [1997, 1998], *Perrier and Morat* [2000], *Rizzo et al.* [2003]).

In addition, an analytical model and finite element numerical simulations were used to simulate the sandbox experiments. This approaches were based on the recently developed model of self-potential signals developed by *Revil and Linde* [2006] for electroporoelastic media.

Finally, we applied wavelet analysis to the self-potential field to demonstrate that the source, in the initial stage of the experiments, was equivalent to a vertical dipole. We also used a cross-correlation method between the self-potential field (normalized by the power of the signal) and the Green's function of a dipole to retrieve the position of the hydro-mechanical disturbance in the sandbox.

2. Electrokinetic Coupling

The surface of any mineral in contact with water is charged. This charge is attached to the grains. This fixed charge comprises the surface sites (e.g., silanol and aluminol surface groups) plus the counterions sorbed onto the surface. A complete description of this electrical double layer can be found in *Lorne et al.* [1999], *Revil and Leroy* [2001]; *Leroy and Revil* [2004], *Leroy et al.* [2007] and will not be repeated here. This fixed charge is counterbalanced by mobile charges located in the vicinity of the surface of the grains, inside the water phase, in the so-called electrical diffuse layer [*Gouy,* 1910]. The drag of the mobile electrical charge

of the electrical diffuse layer by the flow of the pore water causes a net current density $\mathbf{J}_S$ (expressed in A m^{-2}) [e.g., *Haartsen and Toksöz*, 1996; *Block and Harris*, 2006]. This current source density represents the net charge passing per unit surface area of a cross-section of the porous material and per unit time. To our knowledge, the first rigorous attempt to combine the theory of self-potential to poro-elastic deformation of a porous material was made by *Chandler* [1981]. *Chandler* [1981] was interested by using the self-potential method to probe the existence of Biot's slow wave. The formulation we adopted below is quite different from the classical formulation based on the so-called zeta potential and the pressure field. Following *Revil et al.* [2005], *Crespy et al.* [2007], *Revil and Linde* [2006], and *Linde et al.* [2007], our formulation of the coupled hydroelectric problem will be based on the excess of charge per unit pore volume and the seepage velocity.

Neglecting electro-osmosis in the macroscopic momentum equation [e.g., *Sill*, 1983], the constitutive equations for **J** (in A m^{-2}) and the Darcy velocity **U** (in m s^{-1}) are given by [e.g., *Sill*, 1983],

$$\mathbf{J} = -\sigma \nabla \psi + \mathbf{J}_S , \tag{1}$$

$$\mathbf{U} = -\frac{k}{\eta_f} \nabla p , \tag{2}$$

where $\mathbf{J}_S$ is the streaming current density (the subscript "s" stands for the fact that this current density is a source current density), p (in Pa) is the pore fluid pressure, ψ(in V) is the electrical potential, σ (in S m^{-1})is the electrical conductivity, k (in m^2) is the permeability of the porous medium, and η_f (in Pa s) is the dynamic viscosity of the pore water. The continuity equations for the charge and the mass of the pore water are [e.g., *Sill*, 1983],

$$\nabla \cdot \mathbf{J} = 0 , \tag{3}$$

$$\nabla \cdot (\rho_f \mathbf{U}) = -\frac{\partial}{\partial t}\left(\rho_f \phi\right), \tag{4}$$

where ρ_f is the density of the pore water (in kg m^{-3}), and ϕ the porosity ($m_f = \rho_f \phi$ is the mass of the pore water per unit volume of the porous material).

Using Biot's theory, the continuity equation for the mass of the pore fluid in a deforming porous medium can be written in term of the bulk deformation ε of the porous material and time variation of the fluid pressure by [*Palciauskas and Domenico*, 1989],

$$\nabla \cdot (\rho_f \mathbf{U}) = -\rho_f \left[\xi \frac{d\varepsilon}{dt} + \left(\frac{1}{R} - \frac{\xi}{H} \right) \frac{dp}{dt} \right], \tag{5}$$

$$\frac{1}{R} - \frac{\xi}{H} = \frac{1}{\rho_f} \left(\frac{\partial m_f}{\partial p} \right)_\varepsilon, \tag{6}$$

$$\frac{1}{H} = \frac{1}{\rho_f} \left(\frac{\partial m_f}{\partial \sigma} \right)_p, \tag{7}$$

$$\frac{1}{R} = \frac{1}{\rho_f} \left(\frac{\partial m_f}{\partial p} \right)_\sigma, \tag{8}$$

where ε is the trace of the deformation tensor, σ is the mean stress (in Pa) and ε is the bulk deformation of the medium. The coefficients R, ξ, and H are the so-called Biot coefficient of linear poro-elasticity (all expressed in Pa). The coefficient $1/R$ represents a measure of the change in water content for a given change in pore fluid pressure when the porous material is permitted to drain freely. The coefficient $(1/R - \xi/H)$ represents a measure of the amount of water which can be forced into a porous material under pressure while the volume of the material is kept constant. The coefficient $1/H$ represents a measure of the change in water content for a given change in confining stress when the material is permitted to drain freely. Despite the fact that these equations were initially derived to model poro-elastic deformation, they can also be used in the case of irreversible deformations as shown by *Palciauskas and Domenico* [1989].

According to the model developed by *Revil et al.* [2005] (see also *Crespy et al.* [2007], *Revil and Linde* [2006], and *Linde et al.* [2007]), the source current density is given by $\mathbf{J}_S = \overline{Q}_V \mathbf{U}$ where $\overline{Q}_V$ is the excess of charge of the diffuse layer per unit pore volume (in C m^{-3}). An alternative and more classical approach is to express the source current density in terms of pressure gradient $\mathbf{J}_S = -L\nabla p$ [e.g., *Ishido and Mizutani*, 1981; *Sill*, 1983; *Haartsen and Toksöz*, 1996; *Block and Harris*, 2006; *Jardani et al.*, 2006] where L is the streaming

current coupling coefficient. In all cases, the streaming potential coupling coefficient is defined by $C = (\partial\psi / \partial p)_{\mathbf{J}=0}$. With the model developed by *Revil and Linde* [2006], an explicit relationship between the streaming potential coupling coefficient and the excess charge density of the pore water is $\overline{Q_V}$ is $C = -\overline{Q_V} k /(\eta_f \sigma)$. In the classical approach, the streaming potential coupling coefficient is given by the Helmholtz-Smoluchowski equation or a similar equation (e.g., *Pengra and Wong* [1995] and *Szymczyk et al.* [2002]).

Combining Eqs. (1) and (3) yields a generalized Poisson equation for the self-potential ψ (expressed in V),

$$\nabla \cdot (\sigma \nabla \psi) = \Im, \tag{9}$$

where $\Im$ is the volumetric current density (in A m^{-3}) given by,

$$\Im = \nabla \cdot \mathbf{J}_S, \tag{10}$$

$$\Im = \overline{Q_V} \nabla \cdot \mathbf{U} + \nabla \overline{Q_V} \cdot \mathbf{U}, \tag{11}$$

$$\Im = -\overline{Q_V} \xi \frac{d\varepsilon}{dt} - \overline{Q_V} \left(\frac{1}{R} - \frac{\xi}{H} \right) \frac{dp}{dt} + \nabla \overline{Q_V} \cdot \mathbf{U}, \tag{12}$$

where Eq. (5) has been used for a slightly compressible pore fluid. According to Eq. (12), there are three electrokinetic sources terms able to generate self-potential signals in a deforming water-saturated porous medium. The first contribution results from the bulk deformation $d\varepsilon / dt$ of the porous body. If the medium has incompressible grains, we have $d\varepsilon / dt = [1/(1-\phi)] d\phi / dt$. If follows that if the medium is affected by dilatancy ($d\varepsilon / dt \geq 0$), the first contribution $\Im_1 = -\overline{Q_V} \xi d\varepsilon / dt$ is negative because $\overline{Q_V}$ is generally positive (see *Revil et al.* [2005] for clay minerals and *Linde et al.* [2007] for sand). The second contribution, $\Im_2 = -\overline{Q_V} (1/R - \xi / H) dp / dt$, results from time variation of the fluid pressure. In areas where the fluid pressure increases over time, this contribution is negative. The third contribution $\Im_3 \approx \nabla \overline{Q_V} \cdot \mathbf{U}$ is related to flow of the pore water in domains characterized by a gradient of the volumetric charge density $\overline{Q_V}$. As shown below, this contribution plays a key-role during

a pulse injection/pumping of water.

3. Sandbox Experiments

Four sandbox experiments were carried out to observe and analyze the electrical signals resulting from the pulse injection or pumping of water in a controlled sandbox. The experiments were performed in an unshielded room using a glass tank to limit electrostatic effects. The tank was open at the top and partially filled with a well-sorted sand mixed with an electrolyte.

3.1. Properties of the Sand

The sandbox was partially filled with a well-calibrated silica sand. The grain diameters were in the range 100-160 μm with a mean diameter of 132 μm and a standard deviation of 20 μm. From X-ray diffraction, the sand was composed mainly of silica SiO_2 (≈ 95 %), KSi_3AlO_8 (4 %), and $NaAlSi_3O_8$ (<1%). The porosity of the compacted sand was ϕ= 0.34 ± 0.02. Steady-state flow in a permeameter yielded a mean permeability $k = 7.3 \times 10^{-12}$ m^2 (the hydraulic conductivity K was therefore equal to 7.1×10^{-5} m s^{-1} with a dynamic viscosity η_f of 10^{-3} Pa s at 20°C). The electrical formation factor F determined from electrical conductivity measurements with brine solutions (NaCl) at various salinities was equal to 4.3 ± 0.1 (see *Suski et al*. [2004]).

The streaming potential coupling coefficient of the sand was determined using the same experimental setup of *Suski et al.* [2006]. All the experiments reported in the present paper were made with an electrolyte composed of sodium hypochlorite (NaClO) with an electrical conductivity $\sigma_f = 5.6\ 10^{-3}$ S m^{-1} at 25°C and a pH of 6.8. This electrolyte was used to avoid the growth of bacteria in the tank. The coupling coefficient determined using the experimental setup shown in Figure 1 was -46 ± 2 mV m^{-1}. The conductivity of the saturated

sand was equal to 1.31×10^{-3} S m^{-1}. The streaming current coupling coefficient was therefore $L = -C\sigma = 5.6 \times 10^{-9}$ A $(Pa\ m)^{-1}$. Using $C = -\overline{Q_V} k/(\eta_f \sigma)$ (see Section 2) and $\eta_f = 10^{-3}$ Pa s, we obtain $\overline{Q_V} = 0.77$ C m^{-3}. This value is very similar to the value obtained independently by *Linde et al.* [2007] ($\overline{Q_V}$ =0.48 C m^{-3}), who studied the primary drainage of a sand column using the same sand, but saturated by tap water rather than the solution described above.

3.2. The Voltmeter and the Active Electrodes

The self potential signals were monitored with 32 sintered Ag/AgCl electrodes developed for electroencephalography, that is for the study of electrical signals at the surface of the scalp due to polarization processes occurring in the brain. By integrating an amplifier with the sintered Ag-AgCl electrode, extremely low-noise measurements free of interference are possible (see www.biosemi.com). These « active » electrodes have very low output impedance and therefore all problems with regards to capacitive coupling between the cable and sources of interference are eliminated. Using this approach, noise levels as low as the thermal noise level of the electrode impedance were achieved. These electrodes are also water-proof and their size is close to 1 mm. This small size (with respect to the size of the array) implies that these electrodes can be treated as point measurements.

In the two first experiments (termed Experiments #1 and #2 below), these electrodes were regularly distributed at 3 cm below the top surface of the tank (see Figure 2) and connected to the ActiveTwo voltmeter manufactured by Biosemi. This voltmeter has 280 channels, a DC amplifier, and 24-bit resolution (see www.biosemi.com). This voltmeter has a resolution of ~0.1 μV, a maximum frequency of acquisition of 2.048 kHz, a bandwidth from DC to 7 kHz, and an input impedance for the electrode of 300 MOhm at 50 Hz. In the third and fourth experiments (Experiments #3, and #4), the electrodes were placed on a vertical plane, so it was possible to sample the variations of the electrical potential around the end of

the capillary. The characteristics of the ActiveTwo voltmeter are much better than the characteristic of the multichannel used usually in the field or in the laboratory for self-potential monitoring and which have a sensitivity on the order of 0.1 mV (see *Perrier et al.* [1997, 1998], *Perrier and Morat* [2000], *Rizzo et al.* [2004], *Maineult et al.* [2005], and *Suski et al.* [2006]).

3.3. Injection Experiment

We injected ~0.5 mL of solution in the central part of the tank at a depth of 15 cm. The water was injected through a relatively rigid capillary filled with water and connected to a Syria syringe. Injection was done by the impact of a hammer stroke on the syringe end-face. The diameter of the capillary was 2 mm. It was ensured that the injected water had the same chemical composition as the water in the tank by extracting the water directly from the tank a few minutes before the experiment. In this way, we avoided any membrane / diffusion polarization effects that could be associated with a difference of the chemical potential between the injected solution and the pore water filling the sand (e.g., *Maineult et al.* [2005, 2006a, b], *Revil et al.* [2005]). The self-potential response was measured with a sampling frequency of 1.024 kHz. The self-potential data was referenced and transformed to the frequency domain using a Fast Fourier Transform (FFT). We observed that the 50 Hz (and harmonics) of the anthropic electrical current strongly dominated the raw self-potential data. In order to remove these components of the self-potential time series, the signals were low-pass filtered with a cut-off frequency of 30 Hz and an attenuation of 5 decades at 50 Hz. The filtered signals were then back-transformed to the time domain (see also *Rizzo et al.* [2004]).

Snapshots of the filtered self-potential distribution at the surface of the tank are shown on Figure 3. These data exhibit a well-defined negative self-potential anomaly with a maximum amplitude of -6 μV. This anomaly is centered right above the injection point. We

observed a change in the polarity of the self-potential anomaly 0.35 s after the time of the injection (Figure 4). However, this experiment was repeated several times and the reverval of the self-potential signal was found to be non-reproducible if the shock of the hammer on the syringe is softer than for Experiment #1 (see an example in Section 3.5 below).

3.4. Pumping Test Experiment

A second experiment was performed by quickly pumping out of the tank a prescribed amount of water (~0.5 mL) from the capillary (Experiment #2). This was done by hand and by using the same syringe as previously. A rough estimate of the pumping rate is 2.0 ± 0.5 mL s^{-1}. The filtered data reveal a positive self-potential anomaly (with respect to the reference electrode) centered above the pumping point (Figure 5). Consequently, injecting and pumping produce sign inverted self-potential anomalies. The maximum amplitude of the self-potential anomaly was +5 μV (Figure 6), which is a magnitude similar to the injection experiment. This implies that a relatively similar mechanism is at play during these two experiments. In this experiment, there was no reversal of the polarity of the anomaly over time (Figure 6). We observed a relaxation of the anomaly after it reached its maximum amplitude with a duration of few seconds. This experiment was performed three times and was reproducible.

3.5. Additional Experiments

In order to test the distribution of the self-potential in a vertical plane passing by the capillary, we performed two additional experiments. Experiment #3 is an infiltration test but with an initial shock smaller than in Experiment #1 (Figures 7 and 8). For this experiment, we observed no reversal of the electrical potential anomaly during the experiment. This maybe indicates that the observed reserval of the self-potential signal is due to a dashpot behavior of the syringe. The distribution of the electrical potential through a vertical section of the tank shows clearly that the maximum of the amplitude of the anomaly is associated with the

position of the inlet of the capillary.

Experiment #4 is a pumping test experiment but with an initial shock smaller than in Experiment #2 (Figures 9 and 10). The distribution of the self-potential signals during this experiment shows very clearly that the maximum of the self-potential anomaly is initially associated with the outlet of the capillary (at a depth of 15 cm). However, it seems that the maximum of the self-potential anomaly shifts upward over time after the initial phase.

4. Forward Modeling

4.1 Infiltration and Pumping Experiments

Inside the capillary, the water obeys to electroneutrality ($\overline{Q_V} = 0$) while the pore water of the sand is not neutral as discussed above ($\overline{Q_V}$ = 0.77 C m^{-3}). Therefore during the injection or the pumping experiments, the water has to go through the interface between the capillary and the sand (see Figure 11). As this interface corresponds to a finite drop in the value of $\overline{Q_V}$, the dominant source term in Eq. (12) is:

$$\Im_3 \approx \nabla \overline{Q_V} \cdot \mathbf{U} . \tag{13}$$

An analytical solution of this problem is developed in Appendix A. A comparison between this solution and the measured values for Experiment #1 is displayed on Figure 12a. A comparison with the measurements of Experiment #1 taken at the time where the self-potential signals reached their minima is shown on Figure 12b.This solution suggests that the source, in the initial stage of the experiment, was dipolar for Experiment #1.

The analytical solution developed in Appendix A requires a value of the excess fluid pressure at a given time. To model the evolution of the fluid pressure over time, we need to solve the hydrodynamic problem coupled with the poro-elastic equations and then to use the solution to solve the Poisson equation for the electrostatic potential. We use the commercial

finite-element code Comsol Multiphysics 3.3 to solve Darcy's law including deformation of the porous medium (e.g., *Leake and Hsieh* [1997]):

$$S_\alpha \frac{\partial \delta H}{\partial t} + \nabla \cdot (-K \nabla \delta H) = \xi \frac{\partial}{\partial t}(\nabla \cdot \mathbf{u}), \tag{14}$$

where $\delta H = \delta p / \rho_f g$ is the change in hydraulic head (above or below the hydrostatic initial distribution H_0), $S_\alpha = \rho_f g S$ is the poroelastic storage coefficient (S_α is expressed in m^{-1} while S is expressed in Pa^{-1}), K is the hydraulic conductivity (in $m\ s^{-1}$), $\mathbf{u}$ is the total displacement (in m), ξ is the Biot coefficient (dimensionless, see Section 2), and $\partial(\nabla \cdot \mathbf{u})/\partial t$ is the time rate change in strain from the following equation for the displacement in plane strain for the solid grains (e.g., *Leake and Hsieh* [1997]).

The equilibrium condition for the stress tensor is $\nabla \cdot \overline{\overline{\sigma}} = -\mathbf{F}$ where $\overline{\overline{\sigma}}$ is the stress tensor and $\mathbf{F}$ is the total body force plus the gradient of the pore fluid pressure. Indeed, the gradient of the pore fluid pressure acts as a force acting on the grains and responsible for the deformation of the medium. The total displacement in plane strain is given by solving (e.g., *Leake and Hsieh* [1997]),

$$\frac{E}{2(1+\upsilon)} \nabla^2 \mathbf{u} + \frac{E}{2(1+\upsilon)(1-2\upsilon)} \nabla \cdot (\nabla \mathbf{u}) = \xi \rho_f g \nabla \delta H\ , \tag{15}$$

where E is the Young modulus and υ is the Poisson's ratio. We use fixed head at the top surface of the tank and no-flow conditions on the other boundaries ($\mathbf{n} \cdot K \nabla \delta H = 0$) including the surface of the tank and the surface of the capillary. The specific storage, the Young's modulus and the Poisson's ratio are not independent parameters. For incompressible solid grains and pores, the poroelastic storage coefficient is given by $S_\alpha = 1/K + \phi / K_f$ where $1/K$ and $1/K_f$ are the compressibility of the porous medium and the compressibility of the pore water (K_f = 3.3 GPa), respectively. Using the relationship given by *Wang* [2000] (see his Table B1, Appendix B), we have $S_\alpha = 3(1-2\upsilon)/E + \phi / K_f$. The initial condition for the fluid pressure was the hydrostatic distribution. The displacement of the medium was equal to zero

on the walls of the tank. We adopted a free deformable surface at the top surface of the tank. Equations (14) and (15) are discretized using the finite-element method and triangular meshing.

The 2D numerical simulations were performed according to the following procedure. We first solved the hydromechanical problem (Eqs. (14) and (15)) and then used the solution of the hydromechanical problem to determine the streaming current source density $\mathbf{J}_S$. Finally, we solved the Poisson's equation for the streaming potential ψ. We used the values of the electrical conductivity and the voltage and current coupling coefficients reported in Section 3.2. We assigned the boundary condition $\mathbf{n} \cdot \nabla \psi = 0$ at all the insulating boundaries of the tank. The voltage reference was placed at the same location as the reference electrode in the laboratory experiment (see Figure 2). To perform the simulations, we used the following set of parameters: E = 6 x 10^7 Pa, υ = 0.4, S_α = 1.3 x 10^{-8} Pa^{-1}, k = 2.5 x 10^{-12} m^2, and ξ = 1 for the sand (determined from the values reported in Section 2 and the data published in the literature) and a dynamic viscosity for the pore water equal to η_f = 10^{-3} Pa s for water.

The overpressure ($\delta p = p - p_H$ where p is the total fluid pressure and p_H is the hydrostatic pressure) at the end of the capillary was estimated by trial and error to be 17 Pa (1.2 cm of pressure head). These results show that the hydromechanical model discussed above is consistent with the measured self-potential distribution just after the pulse injection of water and over time.

Using an excess fluid pressure of 17 Pa at the end of the capillary, we obtain the displacement and the fluid pressure distribution shown on Figures 13. The self-potential signal computed at electrode #32 is shown on Figure 14. It shows clearly a change in polarity of the self-potential signal over time in agreement with the observed self-potential signals (see Figure 4). This implies a change in the polarity of the excess pore fluid pressure (with respect to the hydrostatic pressure) inside the capillary. A profile of the self-potential signal at a depth

of 3 cm is shown on Figure 15 at two characteristic times corresponding to the occurrence of the extrema of the development of the self-potential anomaly.

The influence of permeability upon the self-potential signals at electrode #32 is shown on Figure 16. Clearly the permeability of the medium controls not only the intensity of the self-potential signal at time t_2 but also the relaxation of the self-potential anomaly over time after time t_2. This means that the time variation of the self-potential signals can be used to invert the hydraulic diffusivity and therefore the poro-elastic storage and the hydraulic conductivity of the medium.

4.2 Pumping Experiment

In the pumping experiment (Experiment #2), the drop in the charge density through the inlet of the capillary is responsible for a vertical dipole oriented upward. To test this assumption, a comparison between the analytical solution developed in Appendix A and the measured potentials is given on Figure 12c. The measured self-potential data and those determined from the numerical model were found to be in fair agreement (see Figure 12d). Therefore, the mechanism that yields to the development of the self-potential anomalies is similar for both the injection and the pumping experiments. The change of the sign of the anomaly between the two experiments is due to the direction of the flow of the water at the inlet / outlet of the capillary.

5. Source Localization

Source localization of self-potential data is a relatively new and challenging field. Source localization can be performed using signal analysis algorithms (such as wavelet analysis or cross-correlation methods) or by minimization of a cost function using regularization (e.g., compactness applied to the inverted source) as shown recently by *Minsley*

et al. [2007]. Minimization techniques can also be applied by specifying a simple source model and invert the properties of this source model (such as depth of the source, direction of the dipolar moment, and intensity of the source, see *Paul* [1965], *Rao and Babu* [1984], *Murty and Haricharan* [1985]). In the analysis made below, we apply the wavelet technique to determine the properties of the source. This approach has the advantage that it does not require specifying the order of the multipole responsible for the self-potential signals recorded at the top surface of the tank. Once the order of the multipole has been determined, a cross-correlation technique can be used to infer the position of the source at depth.

5.1. Use of Wavelet Analysis

We now consider one self-potential profile passing through the peak of the 2D self-potential anomaly. This self-potential profile is taken just after the injection or the pumping of water. Continuous wavelet analysis is used to locate the position of the source and its multipolar index (*Grant and West* [1965]; *Holschneider* [1995], Fedi and Quarta [1998] ; *Mallat* [1999]).

In the initial stage of the deformation of the medium and for both injection and pumping experiments, the dominant source term in Eq. (12) is $\Im_3 \approx \nabla \overline{Q}_V \cdot \mathbf{U}$. If the distance between the observation electrode and the source volume is much larger than the size of the source (here the diameter of the capillary), we can assume that the self-potential field is created by a single homogeneous point source. This is the case here. In addition, we considered two-dimensional space to simplify the geometrical presentation and we assume that the electrical resistivity is constant in space, so that the equation (9) can be simplified to $\nabla^2 \varphi = \Im_3 / \sigma$. To show that these assumptions are compatible with the conditions of the experiment described in section 3, we first derive the source depth, and then estimate the multipolar index of the source.

The idea of the method is to use a special type of wavelets called Poisson wavelets. These wavelets are related to the upward continuation filter *Pa(x)*, transforming the potential field $\varphi(x)$ measured at a distance *Z* to the values at the depth *Z+a*. Due to the scaling properties of wavelets and homogeneity property of the source, the wavelet coefficients *W(a, u)* of potential fields at different scales *a* exhibit a conelike structure converging to the location of the source, while the attenuation of the local maxima of the wavelet coefficients reveal the multipolar index of the source. In two-dimensional space, if the potential field $\psi(x)$ is excited by an homogeneous source $\Im$ located at depth z_0 and measured at the surface $(z = 0)$, the corresponding wavelet coefficients in the upper half plane obey a power law, with the exponent $\beta = -\gamma + \alpha + 1$ related to the order γ of the chosen wavelets, the nature of the field and the multipolarity index α of the source.

The depth z_0 can be obtained as the intersection point of the local maxima of the wavelet coefficients (wavelet ridges). Once the depth is known, the exponent β can be determined as the slope of $\log(|W(a)|/a^{\gamma})$ versus $\log(a + z_0)$.

The Poisson wavelets are obtained with the help of the upward continuation filter [*Grant and West*, 1965],

$$P_a(x) = \frac{1}{\pi}\frac{a}{a^2 + x^2}. \tag{16}$$

Differentiating $P_a(x)$ with respect to *x* and *a* yields the corresponding first-order "horizontal" $g_x^{\gamma}(x)$ and "vertical" $g_z^{\gamma}(x)$ wavelets. Then the following γ-order derivative over *x* gives the γ order horizontal wavelets:

$$g_x^{\gamma} = \partial_x^{\gamma} P^1(x), \tag{17}$$

$$\hat{g}_x^{\gamma}(u) = \left(i2\pi|u|\right)^{\gamma} e^{-2\pi|u|}, \tag{18}$$

where $\hat{g}_x^{\gamma}(u)$ is the Fourier transform of g_x^{γ}. Similarly the vertical wavelet of order γ is,

$$g_z^{\gamma-1} = \partial_x^{\gamma-1}\partial_a P_a(x)\big|_{a=1}, \tag{19}$$

$$\hat{g}_z^{\gamma}(u) = \left(i2\pi|u|\right)^{\gamma-1}(-2\pi|u|)e^{-2\pi|u|},. \tag{20}$$

The first order complex analytic wavelet $g_c^{\gamma} = g_x^{\gamma} + ig_z^{\gamma}$ (named the "Cauchy wavelet") is used to estimate also the orientation of the source. In Fourier domain, this wavelet is,

$$\hat{g}_c^{\gamma}(u) = (-2\pi|u|)^{\gamma} e^{-2\pi|u|}. \tag{21}$$

In both sanbox experiments, the self potential anomaly along the diagonal attenuates almost totally at the sides of the sandbox. The self-potential profile is linearly interpolated to obtain two self-potential values per centimeter (113 points in total). The position x = 0 corresponds to the center of the tank, above the position of the capillary. The self-potential data are zero-padded on both sides of the profile to fill a 1024 points vector (Figure 17a). Figure 17b shows the wavelet transform using a first order (γ = 1) vertical g_z^1-wavelet. In this case, Equation (15) yields,

$$W(u,a) = \left(\frac{a}{a'}\right)\left(\frac{a'+z_0}{a+z_0}\right)^{\alpha} W\left(u\frac{a'+z_0}{a+z_0}, a'\right). \tag{22}$$

Areas in dark grey scales in Figure 17b corresponds to low values of the wavelet coefficients, while clear grey scales in Figure 17b show high values of the wavelet coefficients. The local maxima of the wavelet coefficients are shown by a dotted line. The cone-line structure of the wavelet coefficients converges to the source position z_0 = 12 cm. This depth is consistent with the position of the inlet/outlet end of the capillary. The value of the coefficient β is equal to slope of $\log(|W(a)|/a^{\gamma})$ versus $\log(a+z_0)$. We find $\beta = \alpha = -2.2$ (see Figure 17c). This value corresponds approximately to a dipole source ($\beta = -2$ for a perfect dipole). Finally, the phase iso-value of the complex wavelet transform g_c^1, at the source position, gives the directivity of the polarization vector from the vertical direction. This angle is about 1° (at the position x = 0), which means that the dipole is nearly vertical.

Analysis of the self-potential data related to the pumping experiment (see Figure 18) yields a source depth equal to z_0 = 13 cm (the depth of the inlet of the capillary is 12 cm) and

we find $\beta = \alpha = -2.3$ (the source is nearly dipolar in nature) (see Figure 18c). From the wavelet analysis, the source appears to be a vertical dipole pointing upward, in agreement with the model developed in Section 4.

5.2. Semblance Function

The wavelet analysis presented in Figures 17 and 18 cannot accommodate information concerning the topography and the electrical resistivity distribution of the conductive medium. Therefore, for the purpose of elaborating a method that could be applied to an active volcano, we tested another method based on the cross-correlation between the Green function derived from the linear operator associated with Poisson equation and the measured self-potential anomaly divided by its power. This approach has been used recently by *Revil et al.* [2003] to determine the geometry of the water table of unconfined aquifers. We used the 3D generalization of the cross-correlation density algorithm developed by *Revil et al.* [2001] to locate a dipolar source inside the medium [see *Iuliano et al*., 2002]. We considered a cartesian coordinate system (*x, y, z*) with the z-axis positive downwards. We assumed that the electrical field **E**(**r**) was due a single dipole with a moment **d**,

$$\mathbf{E}(\mathbf{r}) = \mathbf{d}\nabla\mathbf{G}\,, \tag{23}$$

where **G** is the Green function of the source assumed to be dipolar. G can be obtained using the derivation of the source function described in Appendix A. We note *E* the modulus of the electrical field **E**(**r**). The power associated with the electrical field is,

$$\wp(E) = \int_S E^2(\mathbf{r})dS\,, \tag{25}$$

$$\wp(E) = \sum_{\upsilon} d_{\upsilon} \int_S \mathbf{E}(\mathbf{r}) \frac{\partial \mathbf{G}}{\partial \upsilon_P} dS\,, \tag{26}$$

where $\upsilon = x, y, z$, $\upsilon_p = x_p, y_p, z_p$. The projection of *S* onto the (*x*, *y*) horizontal plane is adapted to a rectangle with sides of total length 2*X* and 2*Y* along the *x*- and *y*-axis, respectively, and

corresponding to the horizontal dimensions of the tank. We note g(z) the topography regularization factor defined by,

$$g(z) = \left[1 + \left(\frac{\partial z}{\partial x}\right)^2 + \left(\frac{\partial z}{\partial y}\right)^2\right]^{1/2}, \tag{27}$$

which in the present case is $g(z) = 1$ (no topography). *Iuliano et al.* [2002] introduced the following cross-correlation product,

$$\eta_\upsilon(r_p) = C_\upsilon^p \int_{-X}^{X}\int_{-Y}^{Y} \mathbf{E}(\mathbf{r}) \frac{\partial \mathbf{G}(\mathbf{r}_p - \mathbf{r})}{\partial \upsilon_p} g(z) dxdy . \tag{28}$$

The normalization constant C_υ^p is defined by,

$$C_\upsilon^p = \left[\int_{-X}^{X}\int_{-Y}^{Y} E^2(\mathbf{r}) g(z) dxdy \int_{-X}^{X}\int_{-Y}^{Y} \frac{\partial \mathbf{G}(\mathbf{r}_p - \mathbf{r})}{\partial \upsilon_p} g(z) dxdy\right]^{-1/2} . \tag{29}$$

The semblance function is therefore the normalized scalar product between the form-anomaly factor indicated by the self-potential measurements at the ground surface and the form-factor associated with a hypothetical dipolar source located in the source volume. These cross-correlation densities have the following property,

$$-1 \le \eta_\upsilon(r_p) \le 1. \tag{30}$$

The norm of the cross-correlation vector $\boldsymbol{\varsigma}(\eta_x, \eta_y, \eta_z)$ is given by,

$$\eta(r_p) = \sqrt{\eta_x(r_p)^2 + \eta_y(r_p)^2 + \eta_z(r_p)^2} . \tag{31}$$

If the distribution of the electrical resistivity is heterogeneous (or possibly anisotropic), the Green function **G** should be computed at the locations of each electrode using a numerical method assessing the self-potential response obtained by putting elementary dipoles along the three Cartesian directions for each elementary cell of the ground.

Then, it is possible to use the cross-correlation algorithm as above to determine the distribution of the cross-correlation densities (and its associated probability density) in the scanned subsoil.

For the canonical problem of finding a dipole in a homogeneous ground, the position of the source is given by $\mathrm{Max}[\eta(r_p)]_V$ (where $\mathrm{Max}[f(x)]_{x_1}^{x_2}$ is the maximum of the function $f(x)$ over the support (x_1, x_2)). In other words, the position of the source is obtained by maximizing the semblance between the form-anomaly factor and the form-factor associated with the dipolar source distribution. The coordinates of the vector $\mathbf{ç}(\eta_x, \eta_y, \eta_z)$ at this point provides the direction of the dipole moment **d** at the source. The cross-correlation density of finding a dipole responsible for the observed self-potential anomaly is shown on Figure 19 for the injection experiment and on Figure 20 for the pumping experiment. In the first case, the maximum of the cross-correlation density is located at position *S*(0 ± 2 cm, 0 ± 2 cm, 14 ± 2 cm) (so at a depth of 11 ± 2 cm below electrode #32). This is consistent with the actual position of the outlet of water in the tank, which is located at position *S*(0 cm, 0 cm, 15 cm). As explained in Section 3, it is not surprising to localize the source slightly above the outlet of the capillary.

In the case of the pumping test (Figure 20), the maximum of the probability density is located at position *S*(0 ± 2 cm, 0 ± 2 cm, 16 ± 1 cm) (so at a depth of 13 ± 2 cm below electrode #32 in the second experiment). Accounting for the uncertainty given above, this is also consistent with the actual position of the inlet of water in the tank *S*(0 cm, 0 cm, 15 cm). Therefore, the cross-correlation algorithm is capable of identitying the position of the source responsible for the self-potential anomaly with a reasonable accuracy.

6. Discussion

In this section, we discuss the level of sensitivity required to locate transient self-potential signals associated with fracturing in an active volcano. We consider a vertical

fracture located at a depth of H = 1 km with a cross-section area of S = 100 m^2. In volcanoes, a typical value of the voltage coupling coefficient C is -10 mV m^{-1} (e.g., *Revil et al.* [2003, 2004] and references therein). The overpressure associated with fracturing is taken equal to the difference between the lithostatic stress and the hydrostatic stress. According to the analysis made in Appendix A, the maximum of the self-potential anomaly is given by $\varphi_0 \approx (2S/\pi H)C$ (with C expressed in mV m^{-1}). With the parameters given above, this yields a self-potential transient signal of ~1 mV. This value is largely above the threshold sensitivity of electrical sensors (probably 1 μV once telluric and anthropic signals have been filtered out). For example in electroseismic investigations or for electromagnetic surveys, after filtering telluric currents and anthropic sources of noises, the sensitivity of measuring self-potential transient signals was found to be on the order of 1 μV (1 nV at the seafloor, Alumbaugh, D. L, personal communication, 2006). If the source is located at a depth of 100 m, the self-potential transient anomaly recorded at the ground surface amounts to ~10 mV, a value that can be easily monitored using a sensitive voltmeter and appropriate correction of the telluric currents in the frequency domain.

In addition, electrical disturbances associated with fracturing would occur in the band of few Hertz. Other self-potential sources like those associated with migration of water in the vadose zone and aquifers should occur at much lower frequencies (e.g., *Linde et al.* [2007]). In conclusion, it is likely that fracturing located at depths of a few hundreds meters to a few kilometers can be recorded by passive self-potential measurements. The determination of the properties of the source (direction and location) requires the knowledge of the distribution of the electrical resistivity of the volcano. This distribution can be obtained though electromagnetic data or DC-electrical resistance tomography (e.g., *Finizola et al.* [2004], *Finizola et al.* [2006]).

One may also worries about the frequency dependence of the source. Because we are in the quasi-static regime of the Maxwell equations, the frequency dependence of the

problems depends on the frequency dependence of the electrical resistivity and the streaming potential coupling coefficient. At frequencies lower than 1 kHz, the frequency dependence of the electrical resistivity and the frequency dependence of the streaming potential coefficient are very small and can be safely neglected (see *Olhoeft* [1985] and *Block and Harris* [2006], respectively).

Promising domains where this technique could also be applied are the monitoring of CO_2 sequestration operations (e.g., *Moore et al.* [2004]), dams and embankments (*Gex* [1980], *Merkler et al.* [1989], *Wilt and Corwin* [1989], *Butler et al.* [1990], *Triumf and Thunehed* [1996], *Sheffer and Howie* [2003], *Bolève et al.* [2007]), glaciers (*Kulessa et al.* [2003], and the activity of faults (*Park et al.* [2007]). All hydromechanical Earth processes occurring in the conductive ground can be monitored by this method if their signal-to-noise ratio is high enough.

7. Concluding Statements

We show that electric signals of electrokinetic nature are generated in response to hydromechanical disturbances in a water-filled electro-poro-elastic medium like a water saturated sand pack. To understand the underlying physics of this process, we performed two sandbox experiments. Prior to the experiments, the sandbox was filled with a well-sorted sand and infiltrated with an electrolyte of known composition and concentration. During the experiments, a known volume of electrolyte was injected or removed using a capillary located in the middle of the sandbox at a depth of 15 cm. In all cases, the source is dipolar and the dipole moment is proportional to the drop in charge density across the inlet / outlet of the capillary. Source localization algorithms based on the wavelet analysis of potential fields and the cross-correlation method were able to determine the position of the source in the sandbox. This opens very promising perspectives to use self-potential information to monitor continuously fracturing processes in a volcanic edifice and to monitor faults, glaciers, and

earth dams just to cite few examples. The next step will concern the development of a finer model of fracturing and diffusion of electromagnetic disturbances away from the source and the development of algorithms that can be used to retrieve the position of the source in the diffusive limit of the Maxwell equations including the distribution of the electrical resistivity in the inverse problem.

Acknowledgements. This work is supported by the French National Research Council (CNRS), the GDR-FORPRO (Research Action number 2005.II), ANR-Project POLARIS, and the French National Agency for Radioactive Waste Management (ANDRA). Joël Lancelot is strongly thanked for his support through the GDR FORPRO. This is GDR-FORPRO contribution 2007/05 A. S. Byrdina is supported by E2C2, A Specific Targeted Project of the European Community. We thank Stephen Park and two anonymous referees for their very constructive comments. AR thanks Terry Young for his support at CSM.

References

Block, G. I., and J. G. Harris (2006), Conductivity dependence of seismoelectric wave phenomena in fluid-saturated sediments, *J. Geophys. Res., 111*, B01304, doi:10.1029/2005JB003798.

Bolève, A., A. Crespy, A. Revil, F. Janod, and J. L. Mattiuzzo (2007), Streaming potentials of granular media: Influence of the Dukhin and Reynolds numbers, *J. Geophys. Res., 112*, B08204, doi:10.1029/2006JB004673.

Butler DK, Llopis JL, Dobecki TL, Wilt MJ, Corwin RF, Olhoeft G (1990), Comprehensive geophysical investigation of an existing dam foundation. (Part 2) The Leading Edge 1990(9): 44-53.

Byrdina, S., S. friedel, J. Wassermann, and J. Zlotnicki (2003), Self-potential variations associated with ultra-long period seismic signals at Merapi Volcano, *Geophysical Research Letters, 30*(22), 2156.

Chandler, R. N. (1981), Transient streaming potential measurements on fluid-saturated porous structures: An experimental verification of Biot's slow wave in the quasi-static limit, *J. Acoust. Soc. Am., 70*, 116–121.

Crespy, A., A. Bolève, and A. Revil (2007), Influence of the Dukhin and Reynolds numbers on the apparent zeta potential of granular media, *Journal of Colloid and Interface Science, 305*, 188-194, 2007.

Dea, J. Y., C. I. Richman, and W. M. Boerner (1991), Observation of seismo-electromagnetic earthquake precursor radiation signatures along Southern Californian fault zones: Evidence of long-distance precursor ULF signals observed before a moderate Southern California earthquake episode, *Can. J. Phys., 69*, 1138-1145.

Fedi M., T. Quarta (1998), Wavelet analysis for the regional-residual and local separation of potential field anomalies, *Geophysical Prospecting 46 (5)*, 507–525. doi:10.1046/j.1365-2478.1998.00105.x

Fedorov, E., V. Pilipenko, and S. Uyeda (2001), Electric and magnetic fields generated by electrokinetic processes in a conductive crust, *Phys. Chem. Earth, 26*(10-12), 793-799.

Fenoglio, M.A., M.J.S. Johnston, and J.D. Byerlee (1995), Magnetic and electric fields associated with changes in high pore pressure in fault zones: application to the Loma Prieta ULF emissions, *J. Geophys. Res., 100*, 12,951-12,958.

Finizola, A., J.F. Lénat, O. Macedo, D. Ramos, J.C. Thouret, and F. Sortino (2004), Fluid circulation and structural discontinuities inside Misti volcano (Peru) inferred from self-potential measurements, *J. Volcanology and Geothermal Research, 135*(4), 343-360.

Finizola, A. Revil A., E. Rizzo, B. Angeletti, S. Piscitelli, J. Morin, L. Mocochain, and F. Sortino (2006), Hydrogeological insights at Stromboli volcano (Italy) from geoelectrical, temperature, and CO_2 soil degassing investigations, *Geophys. Res. Lett., 33*, L17304, doi:10.1029/2006GL026842.

Fitterman, D. V. (1979), Theory of electrokinetic-magnetic anomalies in a faulted half-space, *J. Geophys. Res., 84*, 6031-6041.

Fitterman, D. V. (1981), Correction to « Theory of electrokinetic-magnetic anomalies in a faulted half-space », *J. Geophys. Res., 86*, 9585-9588.

Fraser-Smith, A.C., A. Bernardi, P.R. McGill, M.E. Ladd, R.A. Helliwell, and O.G. Villard Jr. (1990), Low frequency magnetic field measurements near the epicenter of the Ms 7.1 Loma Prieta earthquake, *Geophys. Res. Lett., 17*, 1465-1468.

Freund, F., M. A. Salgueiro da Silva, B.W.S. Lau, A. Takeuchi, and H. H. Jones (2006a), Electric currents along earthquake faults and the magnetization of pseudotachylite veins, *Tectonophysics*.

Freund, F., A. Takeuchi, and B.W.S. Lau (2006b), Electric currents streaming out of stressed igneous rocks. A step toward understanding pre-earthquake low frequency EM emissions, *Physics and Chemistry of the Earth*, 31, 389-396.

Gaffet S., Y. Guglielmi, J. Virieux, G. Waysand, A. Chwala, R. Stolz, C. Emblanch, M. Auguste, D. Boyer, and A. Cavaillou (2003), Simultaneous seismic and magnetic measurements in the Low-Noise Underground Laboratory (LSBB) of Rustrel, France, during the 2001 January 26 Indian earthquake, *Geophys. J. Int., 155*, 981–990.

Garon, M., A. Légaré, R. Guardo, P. Savard, and M. D. Buschmann (2002), Streaming potentials maps are spatially resolved indicators of amplitude, frequency and ionic strength dependant responses of articular cartilage to load, *Journal of Biomechanics, 35*(2), 207-216.

Gex, P. (1980), Electrofiltration phenomena associated with several dam sites, Bulletin of the Society Vaud Science and Nature, 357(75), 39-50.

Gouy, G. (1910), About the electric charge on the surface of an electrolyte, *J. Phys. A, 9*, 457– 468.

Grant, F.S., and West, G.F. (1965), *Interpretation Theory in Applied Geophysics*, McGraw-Hill Book.

Haartsen, M. W., and M. N. Toksöz (1996), Dynamic streaming currents from seismic point sources in homogeneous poroelastic media, *Geophys. J. Int., 132*, 256– 274.

Holschneider M. (1995), *Wavelets: An Analysis Tool*, Oxford University Press.

Ishido, T. (1981), Streaming potential associated with hydrothermal convection in the crust: a possible mechanism of self-potential anomalies in geothermal areas (in Jap., with Engl. Abstr.), *J. Geotherm. Res. Soc. Jpn., 3*, 87-100.

Ishido, T. (1989), Self-potential generation by subsurface water flow through electrokinetic coupling, in *Detection of Subsurface Flow Phenomena, Lecture Notes in Earth Sciences, 27*, edited by G.-P. Merkler et al., 121-131, Springer-Verlag, New York.

Ishido, T., and M. Mizutani, (1981), Experimental and theoretical basis of electrokinetic phenomena in rock-water systems and its application to geophysics: Journal of Geophysical Research, 86, 1763–1774.

Iuliano, T., P. Mauriello, and D. Patella (2002), Looking inside Mount Vesuvius by potential fields integrated probability tomographies, *J. Volcanology Geothermal Res., 113*, 363-378.

Jardani A., J.P. Dupont, and A. Revil (2006), Self-potential signals associated with preferential ground water flow pathways in sinkholes, *J. Geophys. Res.*, 111, B09204, doi: 10.1029/2005JB004231.

Kulessa, B., B. Hubbard, G.H. Brown, and J. Becker (2003), Earth tide forcing of glacier drainage, *Geophys. Res. Lett, 30*(1), 1011, doi: 10.1029/2002GL105303.

Leake, I.S.A., and P.A. Hsieh (1997), Simulation of deformation of sediments from decline of ground-water levels in an aquifer underlain by a bedrock step, U.S. Geological Survey Open File report 97-47.

Leroy, P., A. Revil, S. Altmann, and C. Tournassat (2007), Composition of the intersticial pore water of charged porous media. Theory and application to the Callovo-Oxfordian argilite, *Geochimica et Cosmochimica Acta, 71(5)*, 10.1016/j.gca.2006.11.009, 1087-1097.

Leroy, P. and A. Revil (2004), A triple layer model of the surface electrochemical properties of clay minerals, *Journal of Colloids and Interface Science, 270*(2), 371-380.

Linde, N., D. Jougnot, A. Revil, S. Matthäi, T. Arora, D. Renard, and C. Doussan (2007), Streaming current generation in two-phase flow conditions, *Geophysical Research Letters, 34(3*), L03306, doi: 10.1029/2006GL028878.

Lorne, B, Perrier, F. and J.P.Avouac (1999), Streaming potential measurements 1. Properties of the electrical double layer from crushed rock samples, *J. Geophys. Res.*, *104*, 17,857 – 17,877.

Maineult, A., Bernabé Y., Ackerer P. (2005), Detection of advected concentration and pH fronts from self-potential measurements. *J. Geophys. Res.*, *110*(B11), B11205, doi: 10.1029/2005JB003824.

Maineult, A., Y. Bernabé, and P. Ackerer (2006a), Detection of advected concentration and pH fronts from self-potential measurements, J. Geophys. Res., 110(B11), B11205.

Maineult, A., Y. Bernabé, and P. Ackerer (2006b), Detection of advected, reacting redox fronts from self-potential measurements, J. Contaminant Hydrology, 86(1-2), 32-52.

Mallat S. (1999), *A Wavelet Tour of Signal Processing*, Academic Press.

Merkler, G.P., H. Armbruster, H. Hötzl, P. Marshall, A. Kassel, and E. Ungar (1989), Modelling of streaming potentials and thermometrical measurements at a big laboratory channel, in Lecture Notes in Earth Sciences, Vol. 27, Edited by G.P. Merkler et al., Detection of Subsurface Flow Phenomena, Springer-Verlag Berlin Heidelberg.

Minsley, B.J., J. Sogade, and F.D. Morgan (2007), Three-dimensional source inversion of self-potential data, *J. Geophys. Res.*, *112*, B02202, doi : 1029/2006JB004262.

Moore, J. R., and S. D. Glaser (2006), The origins of the self-potential response during hydraulic fracturing, *Eos Trans. AGU, 87*(15), Fall Meet. Suppl., Abstract NS21A-04.

Moore, J. R., and S. D. Glaser (2007), Self-potential observations during hydraulic fracturing, *J. Geophys. Res., 112*, B02204, doi:10.1029/2006JB004373.

Moore, J.R., S.D. Glaser, H.F. Morrison, and G.M. Hoversten (2004), The streaming potential of liquid carbone dioxide in Berea sandstone, Geophys. Res. Lett., 31(17), L17610, 2004.

Murty B.V.S., and Haricharan P. (1985), Nomogram for the complete interpretation of spontaneous polarization profiles and sheet like and cylindrical two-dimensional sources; *Geophysics, 50*, 1127 – 1135.

Nitsan, U. (1977), Electromagnetic emission accompanying fracture of quartz-bearing rocks, *Geophys. Res., Lett., 4*, 333-336.

Olhoeft, G.R. (1985), Low-frequency electrical properties, *Geophysics, 50*, 2492-2503.

Palciauskas, V. V., and P. A. Domenico (1989), Fluid pressures in deforming porous rocks, Water Resour. Res., 25, 203-213.

Park S. K., W. Dalrymple, and J. C. Larsen (2007), The 2004 Parkfield earthquake: Test of the electromagnetic precursor hypothesis, *J. Geophys. Res., 112*, B05302, doi:10.1029/2005JB004196.

Park, S. K., M. J. S. Johnston, T. R. Madden, F. D. Morgan, and H. F. Morrison (1993), Electromagnetic precursors to earthquakes in the ULF band: A review of observations and mechanisms, *Rev. Geophys., 31(2)*, 117-132, 10.1029/93RG00820.

Paul M. K. (1965), Direct interpretation of self-potential anomalies caused by inclined sheets of infinite horizontal extensions, *Geophysics, 30*, 418 - 423.

Pengra, D., and P. Wong (1995), Pore size, permeability and electrokinetic phenomena, in *Access in Nanoporous Materials*, edited by T. J. Pinnavaia and M. F. Tho, pp. 295– 317, Springer, New York.

Perrier, F., G. Petiau, G. Clerc, V. Bogorodsky, E. Erkul, L. Jouniaux, D. Lesmes, J. Macnae, J, Meunier, D. Morgan, D. Nascimento, G. Oettinger, G. Schwartz, H. Toh, M. Valiant, K. Vozoff, and O. Yazici-Çakin (1997), A one-year systematic study of electrodes for long

period measurements of the electric field in geophysical environments, *J. Geomag. Geoelectr., 49*, 1677-1696.

Perrier, F., M. Trique, B. Lorne, J.-P. Avouac, S. Hautot, and P. Tarits (1998), Electrical potential variations associated with yearly lake level variations, *Geophys. Res. Lett., 25*, 1955-1959.

Perrier, F., and P. Morat (2000), Characterization of electrical daily variations induced by capillary flow in the non-saturated zone, *Pure Appl. Geophys., 157*, 785-810.

Rao A. D., and R. H. V.Babu (1984), Quantitative interpretation of self-potential anomalies due to two-dimensional sheet like bodies, *Geophysics, 48*, 1659 -1664.

Revil, A., and N. Linde (2006), Chemico-electromechanical coupling in microporous media, *J. Coll. Interf. Sci.*, 302, 682-694.

Revil, A., P. Leroy, and K. Titov (2005), Characterization of transport properties of argillaceous sediments. Application to the Callovo-Oxfordian Argillite, *J. Geophys. Res., 110*, B06202, doi: 10.1029/2004JB003442.

Revil, A. A. Finizola, F. Sortino and M. Ripepe (2004), Geophysical investigations at Stromboli volcano, Italy. Implications for ground water flow and paroxysmal activity, *Geophys. J. Int., 157*(1), 426-440.

Revil, A., V. Naudet, J. Nouzaret, and M. Pessel, Principles of electrography applied to self-potential electrokinetic sources and hydrogeological applications, *Water Resources Research, 39(5)*, 1114, doi: 10.1029/2001WR000916, 2003.

Revil, A., G. Saracco, and P. Labazuy (2003), The volcano-electric effect, *J. Geophys. Res., 108*(B5), 2251, doi: 10.1029/2002JB001835.

Revil, A., L. Ehouarne, and E. Thyreault (2001), Tomography of self-potential anomalies of electrochemical nature, *Geophys. Res. Lett., 28(23)*, 4363-4366.

Revil, A., and P. Leroy (2001), Hydroelectric coupling in a clayey material, *Geophysical Research Letters, 28(8)*, 1643-1646.

Revil, A., Pezard, P.A., and P.W.J., Glover (1999), Streaming potential in porous media. 1. Theory of the zeta-potential, *Journal of Geophysical Research, 104(B9)*, 20,021-20,031.

Revil, A., Schwaeger, H., Cathles, L.M., and P. Manhardt (1999), Streaming potential in porous media. 2. Theory and application to geothermal systems, *Journal of Geophysical Research, 104(B9)*, 20,033-20,048.

Revil, A., and Pezard, P.A.(1998), Streaming potential anomaly along faults in geothermal areas, *Geophysical Research Letters, 25(16)*, 3197-3200.

Rizzo, E., B. Suski, A. Revil, S. Straface, and S. Troisi (2004), Self-potential signals associated with pumping-tests experiments, *Journal of Geophysical Research, 109, B10203*, doi: 10.1029/2004JB003049.

Sheffer, M.R., and J.A. Howie (2003), A numerical modelling procedure for the study of the streaming potential phenomenon in embankment dams, Symposium on the Application of Geophysics to Engineering and Environmental Problems, San Antonio, p. 475-487.

Sill, W. R., Self-potential modeling from primary flows, *Geophysics, 48*, 76– 86, 1983.

Soloviev, S. P., and J. J. Sweeney (2005), Generation of electric and magnetic field during detonation of high explosive charges in boreholes, *J. Geophys. Res., 110*, B01312, doi:10.1029/2004JB003223.

Surkov, V. V., and V. A. Pilipenko (1997), Magnetic effects due to earthquakes and underground explosions: a review, *Ann. Geofis.*, XL, 1-13.

Suski, B., A. Revil, K. Titov., P. Konosavsky, C. Dagès, M. Voltz, and O. Huttel (2006), Monitoring of an infiltration experiment using the self-potential method, *Water Resour. Res.*, *42*, W08418, doi:10.1029/2005WR004840.

Suski, B., E. Rizzo, and A. Revil (2004), A sandbox experiment of self-potential signals associated with a pumping-test, *Vadose Zone J., 3*, 1193-1199, 2004.

Szymczyk, A., P. Fievet, and A. Foissy (2002), Electrokinetic characterization of porous plugs from streaming potential coupled with electrical resistance measurements, *Journal of Colloid and Interface Science, 255*, 323–331, doi:10.1006/jcis.2002.8591.

Tate, J. and W. Daily (1989), Evidence of electro-seismic phenomena, *Phys. Earth Planet. Inter., 57*, 1-10.

Titov, K., Loukhmanov, and A. Potapov (2000), Monitoring of water seepage from a reservoir using resistivity and self-polarization methods: case history of the Petergoph fountain water supply system, *First Break, 18*, 431-435

Triumf C. A., and H. Thunehed (1996), Two years of Self-Potential measurements on a large dam in northern Sweden. Procs. Repair and Upgrading of Dams, KTH, Stockholm: 307-315.

Ushijima K., H. Mizunaga, and T. Tanaka (1999), Reservoir monitoring by a 4-D electrical technique, *The Leading Edge, 12*, 1422-1424.

Wang, H.F. (2000), *Theory of Linear Poroelasticity with Applications to Geomechanics and Hydrogeology*, Princeton University Press, Princeton, 287 pp.

Wilt M.J., and R.F. Corwin (1989), Numerical modeling of self-potential anomalies due to leaky dams: Model and field examples. In: *Lecture Notes in Earth Sciences*, vol. 27, ed. Merkler GP et al., Detection of subsurface flow phenomena, Springer-Verlag, Berlin Heidelberg: 73-89

Yasukawa, K., Kusdinar, E. and Muraoka, H. (2002), Reservoir response to a well test identified through a self-potential monitoring at the Mataloko geothermal field, central Flores, Indonesia, *Geol. Surv. Japan, 53*, 355-363.

Yoshida, S., and T. Ogawa (2004), Electromagnetic emissions from dry and wet granite associated with acoustic emissions, *J. Geophys. Res., 109,* B09204, doi:10.1029/2004JB003092.

Yoshida, S. (2001), Convection current generated prior to rupture in saturated rocks, *J. Geophys. Res., 106,* 2103-2120.

Yoshida, S., M. Uyeshima, and N. Nakatani (1997), Electric potential changes associated with slip failure of granite: preseismic and coseismic signals, *J. Geophys. Res.*, 102, 14,883-14,897.

Yoshida, S., P. Manjgaladze, D. Zilpimiani, M. Ohnaka, and N. Nakatani (1994), Electromagnetic emissions associated with frictional sliding of rock, in *Electromagnetic Phenomena Related to Earthquake Prediction*, edited by M. Hayakawa and Y. Fujinawa, 307-322, Terrapub, Tokyo.

Appendix A

In this appendix, we model analytically the self-potential response associated with the pulse injection or pumping of water in the controlled sandbox. As all the boundaries of the tank are insulating, the electrical potential obeys $\mathbf{n}\cdot\nabla\psi = 0$ on these boundaries, where **n** is the outward normal unit vector. We note *S* the surface area of the cross section of the inlet / outlet of the capillary. The electrical conductivity and the streaming potential coupling coefficient of the electrolyte inside the capillary are $\sigma_i = \sigma_f$ and $C_i = 0$, respectively, where the subscript *i* denotes the interior of the capillary. We introduce the effective potential $\Psi_i = \psi_i$ and $\Psi_e = \psi_e - Cp$ where ψ_i and ψ_e are the electrical potentials inside and outside the ellipsoidal inclusion, respectively. The streaming potential current density is given by,

$$\mathbf{J}_S = \begin{cases} -\sigma_f C\nabla p, \text{on } \partial\Omega \\ 0, \text{outside } \partial\Omega \end{cases}, \tag{A1}$$

where $\partial\Omega$ denotes the interface between the capillary and the sand. The corresponding boundary value problem to solve is given by the solution of Laplace equation $\nabla^2\Psi = 0$ supplemented by boundary conditions that ensures the continuity of the potential Ψ and the normal component of the total current density **J** at the boundary $\partial\Omega$. Using the approach developed by *Fitterman* [1979, 1981] and *Fedorov et al.* [2001], the analytical solution for the electrical potential at position P for an infinite space is,

$$\psi(P) = \frac{S}{\pi}(C\delta p)\frac{\mathbf{e}_z\cdot\mathbf{r}}{r^3}. \tag{A2}$$

where $\mathbf{e}_z$ is the vertical unit vector perpendicular to the surface of the inlet of the capillary and $r = \sqrt{x^2 + y^2 + (z-h)^2}$ correspond to the distance between the electrode P and the center of the boundary $\partial\Omega$. Therefore the electrical potential is,

$$\psi(P) = \frac{S}{\pi}(C\delta p)\frac{z-h}{\left[x^2 + y^2 + (z-h)^2\right]^{3/2}}. \qquad \text{(A3)}$$

Using the method of images to satisfy the boundary conditions $\mathbf{n}\cdot\nabla\psi = 0$ at all the boundaries and we remove the potential at the position of the reference electrode to compare the model to the experimental data.

Captions

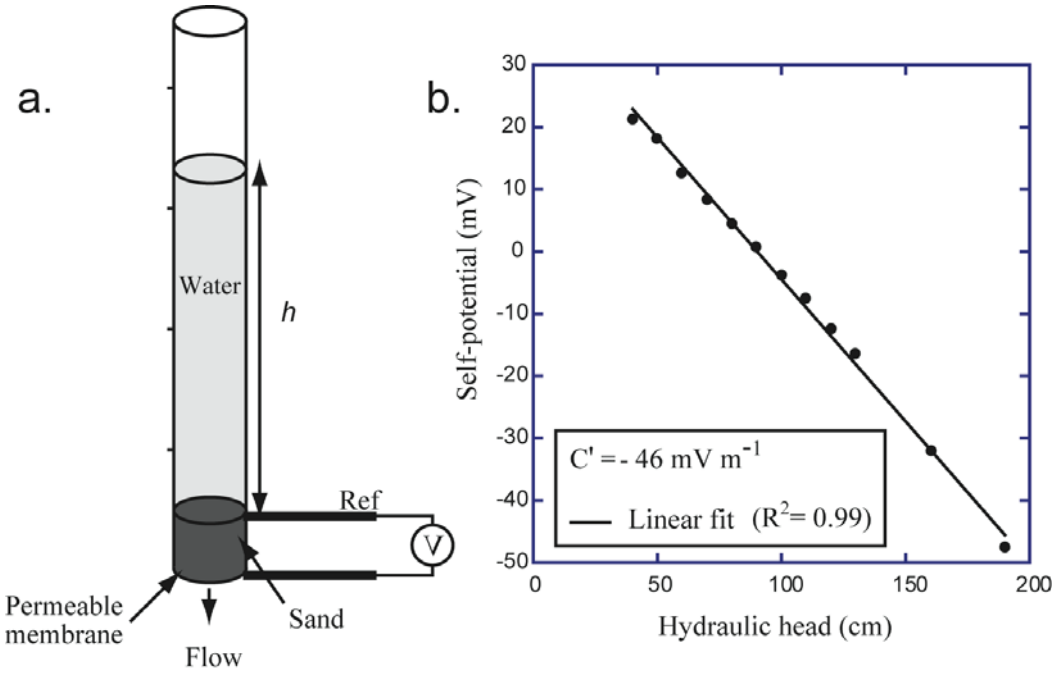

Figure 1. Experimental determination of the streaming voltage coupling coefficient of the sand filling the tank. **a.** Experimental setup showing the sample located at the bottom of a Plexiglas tube. The electrical potential difference at the end-faces of the sample (called the streaming potential) is recorded with a calibrated Metrix MX-20 voltmeter and two non-polarizing $Ag/AgCl_2$ electrodes. **b.** Measured streaming potentials versus the imposed hydraulic heads. The streaming potential coupling coefficient corresponds to the slope of the linear trend.

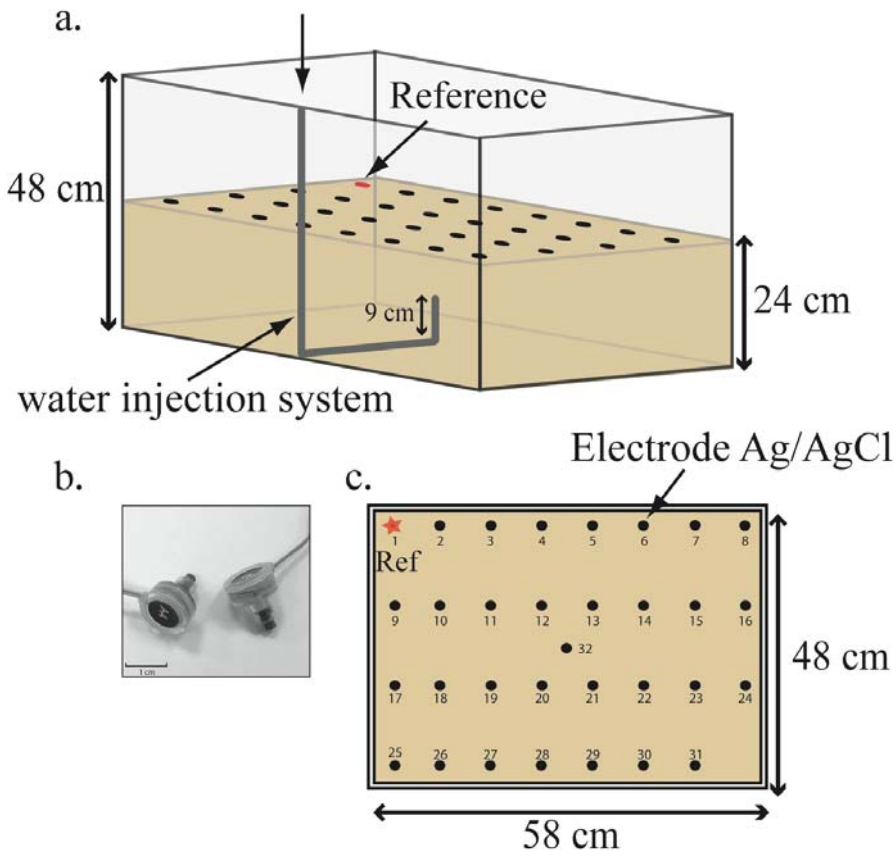

Figure 2. Sketch of the geometry of the sandbox experiment. A total of 32 non-polarizing electrodes are located at the top surface of the tank, which is partially filled with a well-calibrated sand and saturated by a solution of known composition and electrical conductivity. **a.** Geometry of the tank. **b.** Picture of the self-potential sintered Ag/AgCl electrodes developed by BioSemi. These electrodes are very sensitive thanks to a built in amplifier. **c.** Sketch of the top surface of the tank showing the position of the electrodes in the vicinity of the top surface of the tank. The electrodes are located at a depth of 3 cm. “Ref” indicates the position of the reference electrode. Electrode #32 is located just above the inlet/outlet of the capillary.

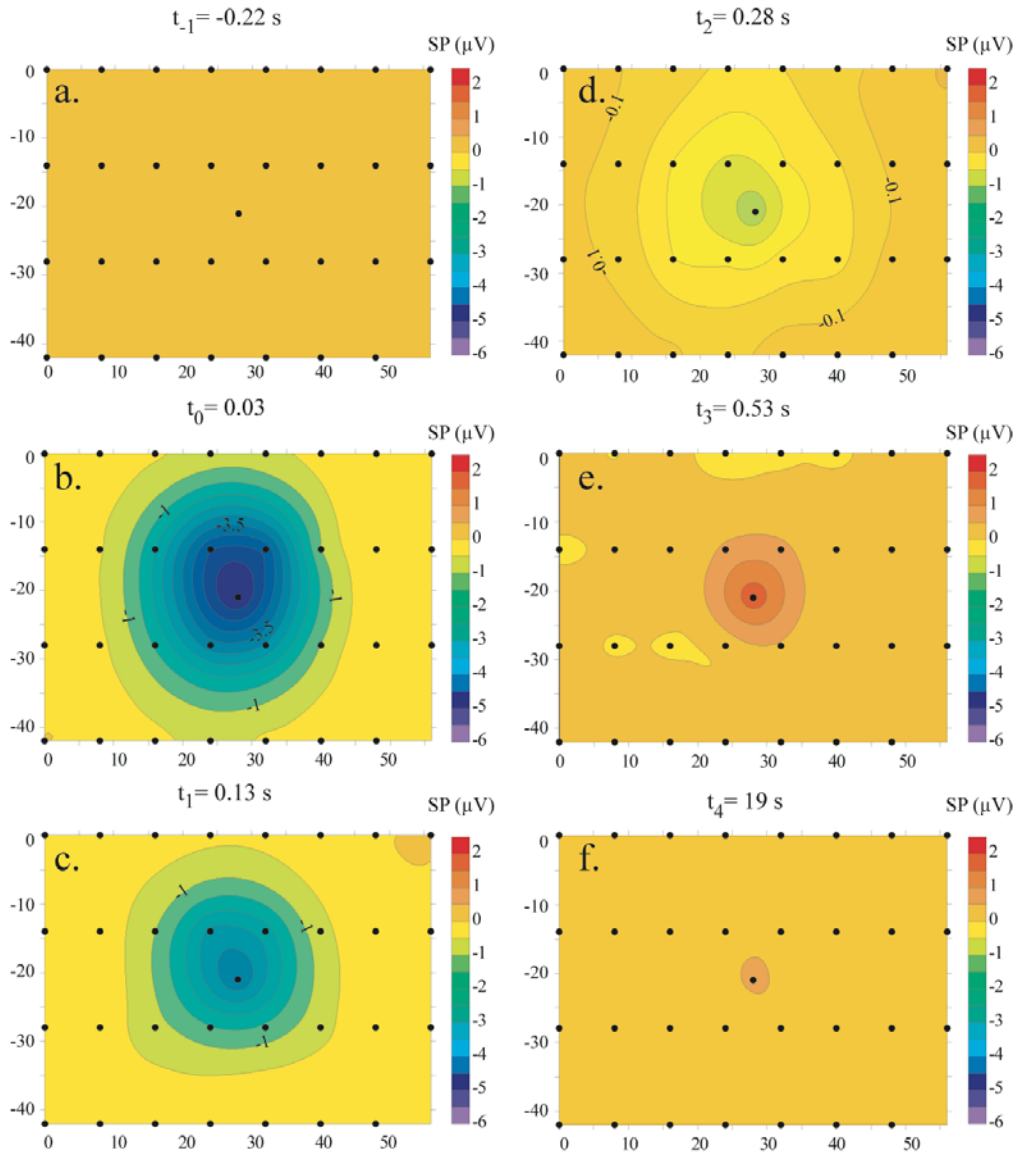

Figure 3. Time-lapse distribution of the self-potential measured at a depth of 3 cm below the ground surface (t = 0 corresponds to the injection of the pressure pulse, Experiment #1). Note the change of polarity over time in the self-potential distribution. At t = 1.9 s, the self-potential anomaly has vanished.

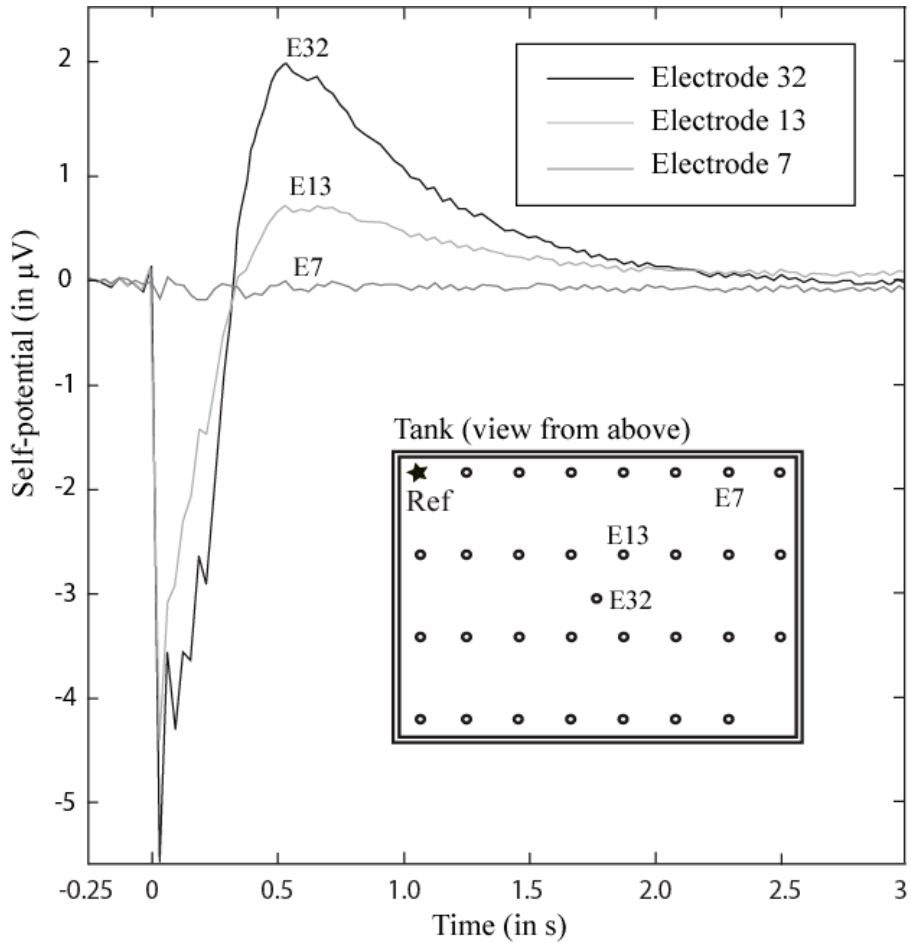

Figure 4. Electrograms for some selected electrodes (electrodes E32, E13, and E7) during the injection experiment (Experiment #1). Electrode E32 is located just above the source while electrode E7 is the furthest. Note the change of polarity on the electrograms of electrodes E32 and E13 at time $t = 0.35$ s.

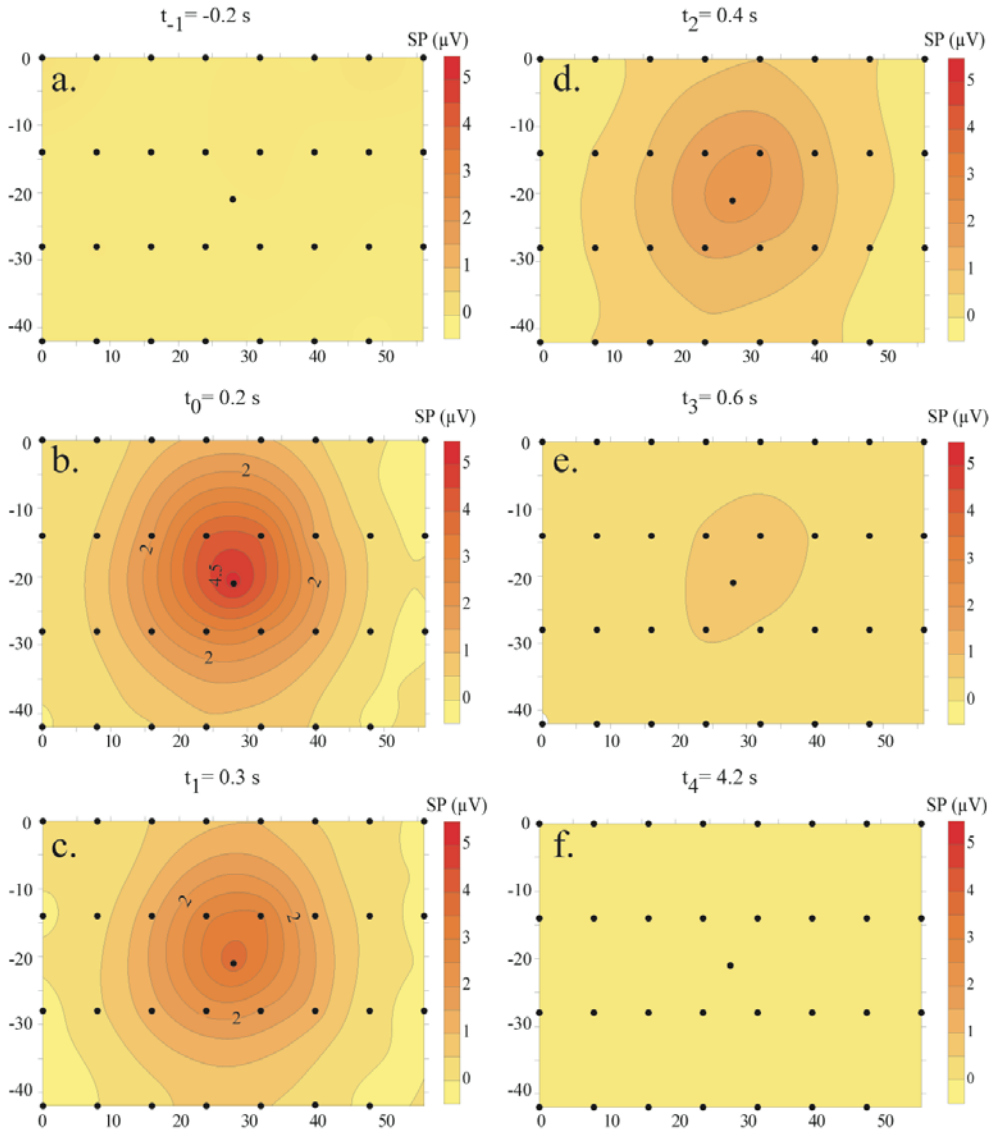

Figure 5. Time-lapse distribution of the self-potential measured at a depth of 3 cm below the ground surface (t = 0 corresponds to the pulse pumping of water through the capillary, experiment #2). At t = 4.2 s, the self-potential anomaly has vanished.

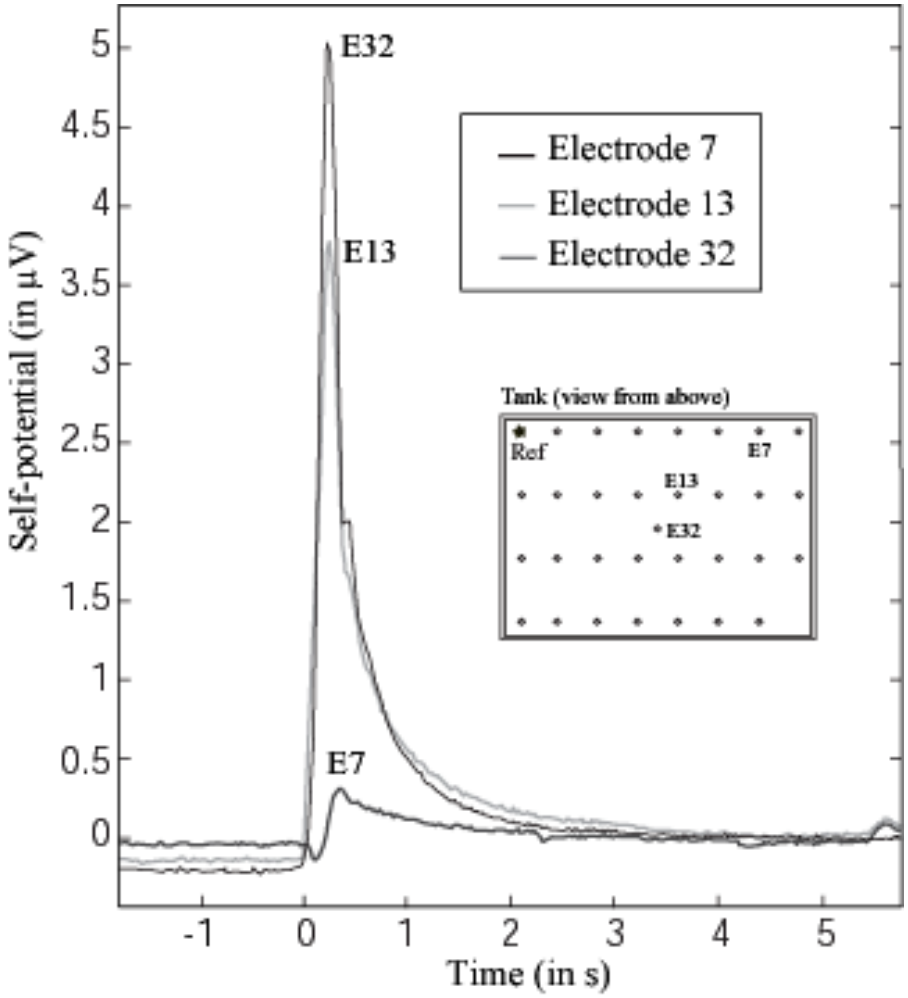

Figure 6. Electrograms for some selected electrodes (Electrodes E7, E13, and E32) located in the vicinity of the top surface of the tank during the pumping experiment (Experiment #2). There is no change of the polarity during the course of the experiment.

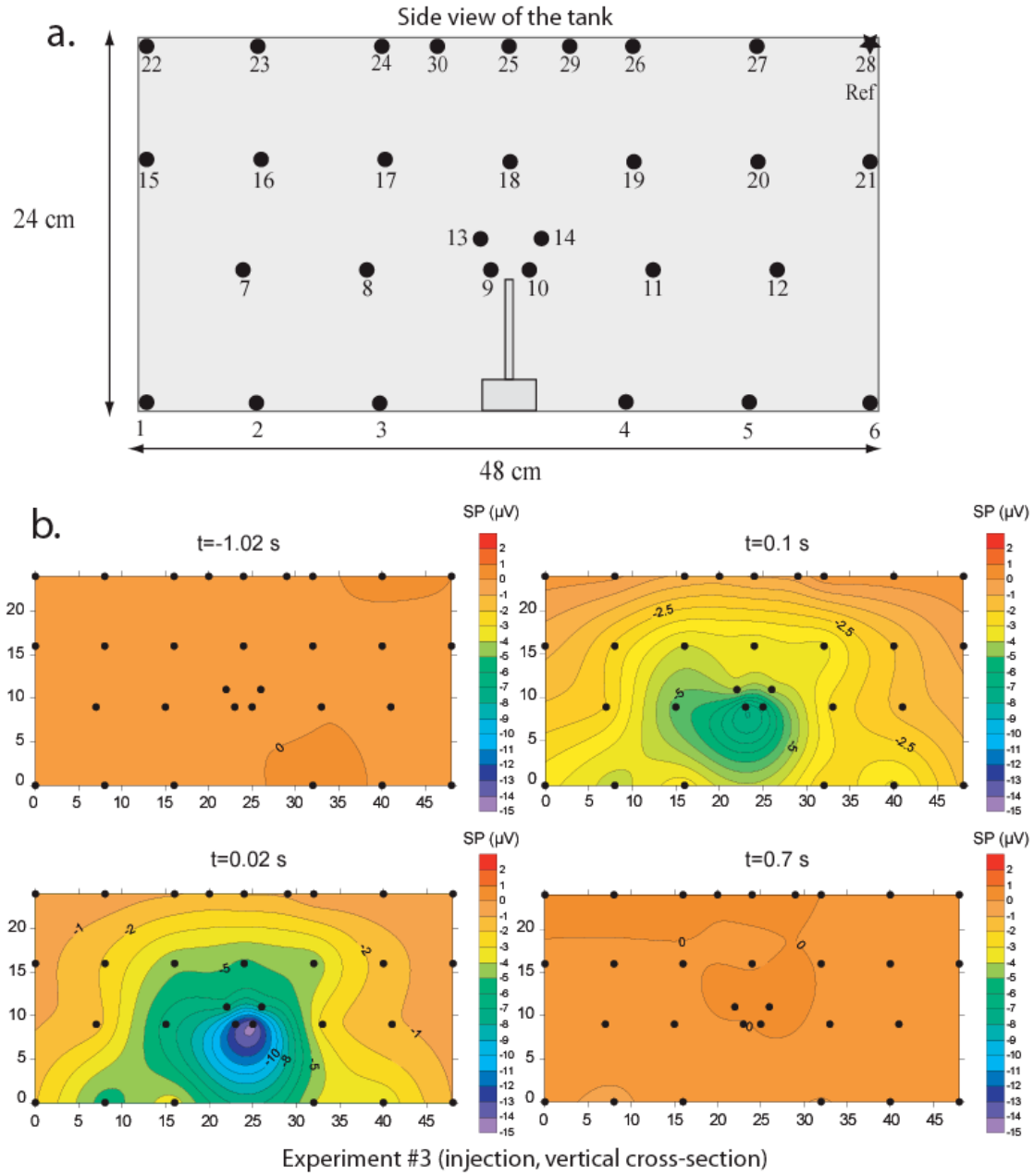

Figure 7. Injection experiment (Experiment #3). **a.** Side view of the tank with the position of the electrodes (#28 is the reference) and the position of the capillary. **b.** Snapshots of the electrical potential distribution of the self-potential at four different time-lapses. The shock created by the hammer stroke is smaller than in Experiment #1.

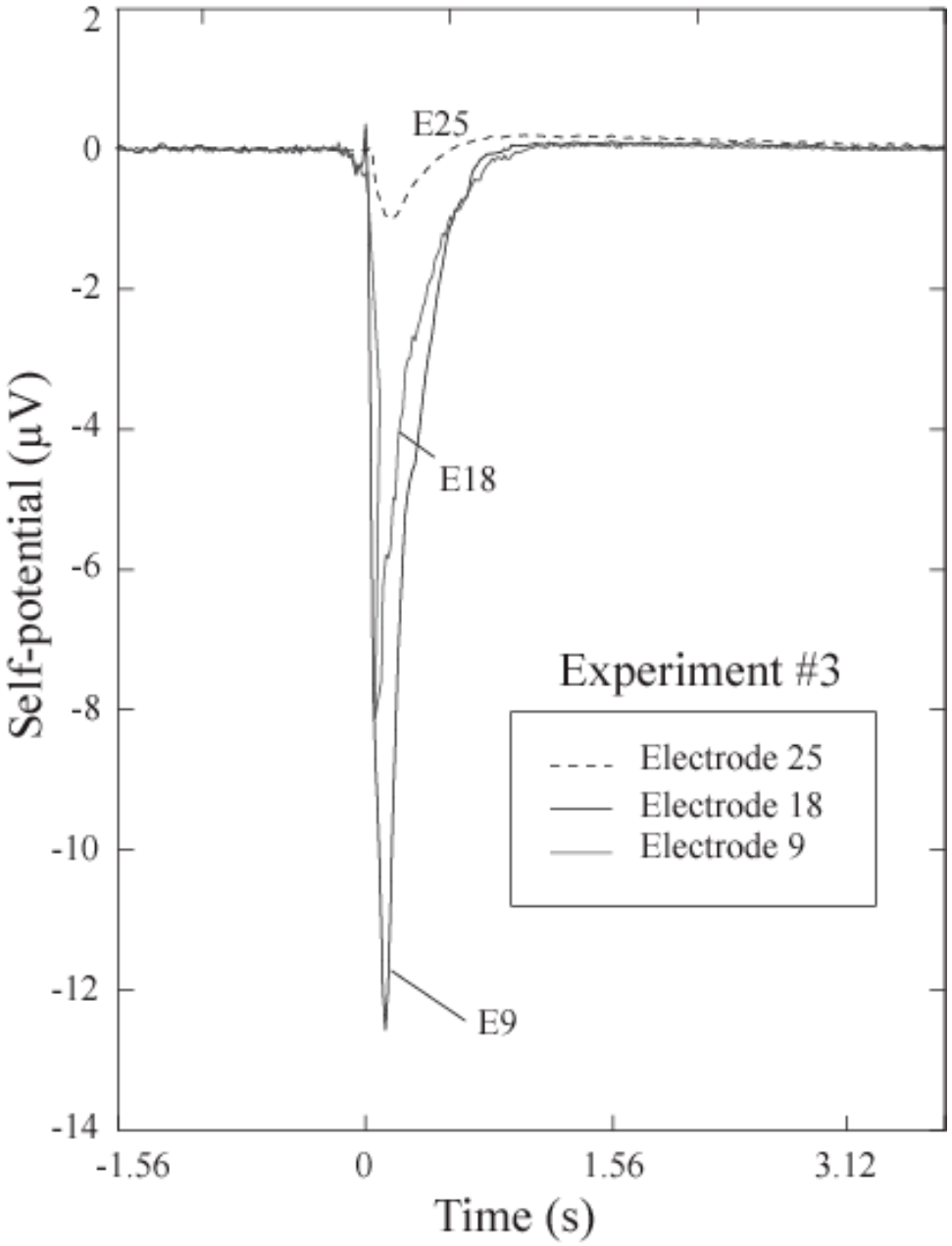

Figure 8. Injection experiment (Experiment #3). Time variation of the self-potential of three selected electrodes.

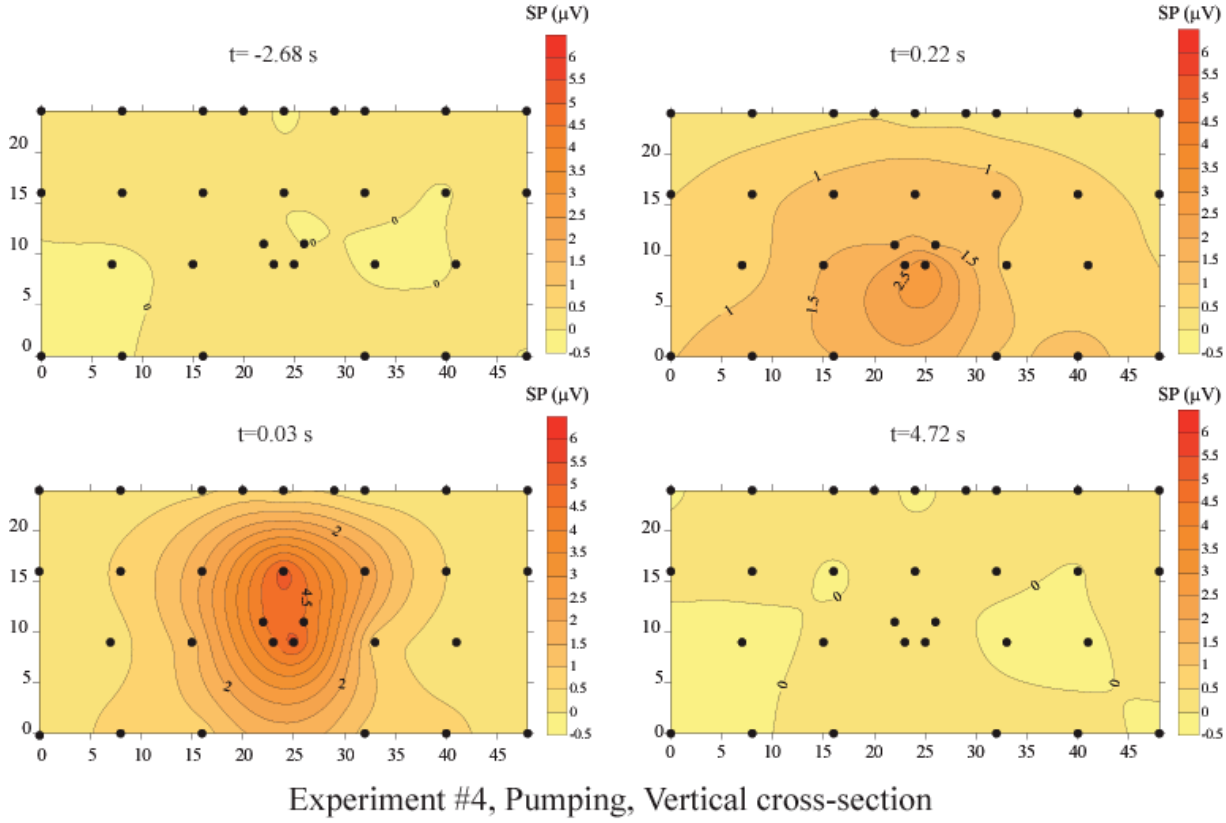

Figure 9. Pumping experiment (Experiment #4). Snapshots of the electrical potential distribution of the self-potential at four different time-lapses. The shock created by the hammer stroke is smaller than in Experiment #2.

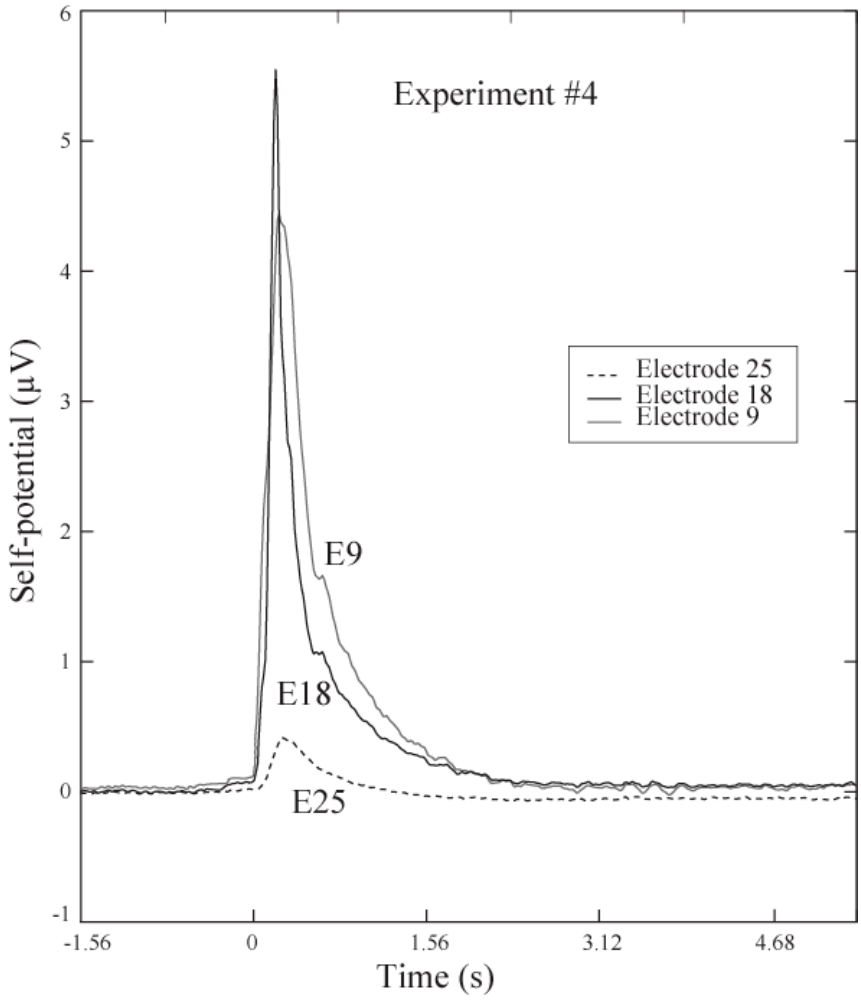

Figure 10. Pumping experiment (Experiment #4). Time variation of the self-potential of three selected electrodes..

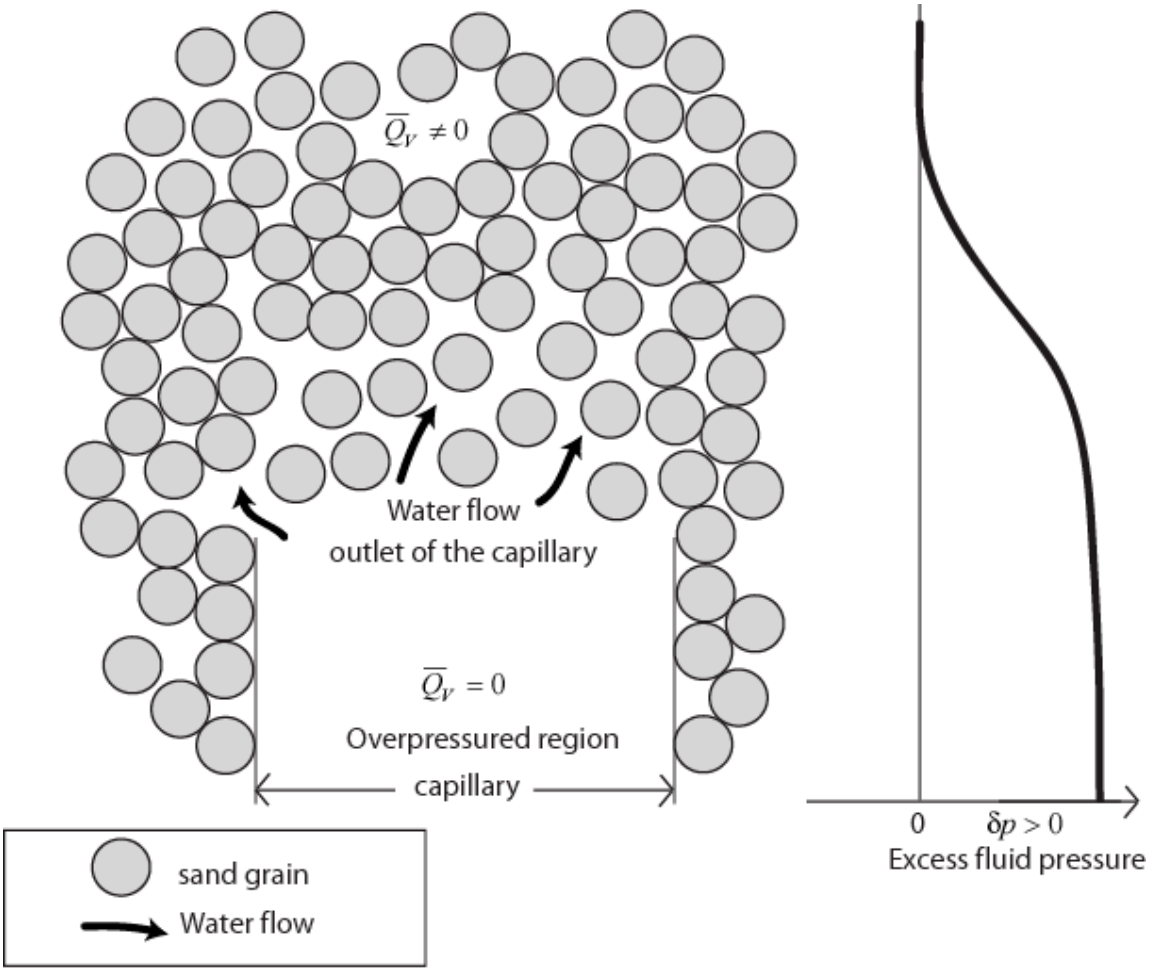

Figure 11. The boundary between the inlet / outlet of the capillary and the surrounding sand is characterized by a drop in the charge density per unit pore volume $\overline{Q_V}$. The resulting dipolar momentum vector **P** is oriented downward. Its position is likely to be located slightly above the capillary outlet. Its strength is expected to decrease over time because of the decrease of the fluid pressure over time due to the diffusion of the pressure field around the outlet of the capillary.

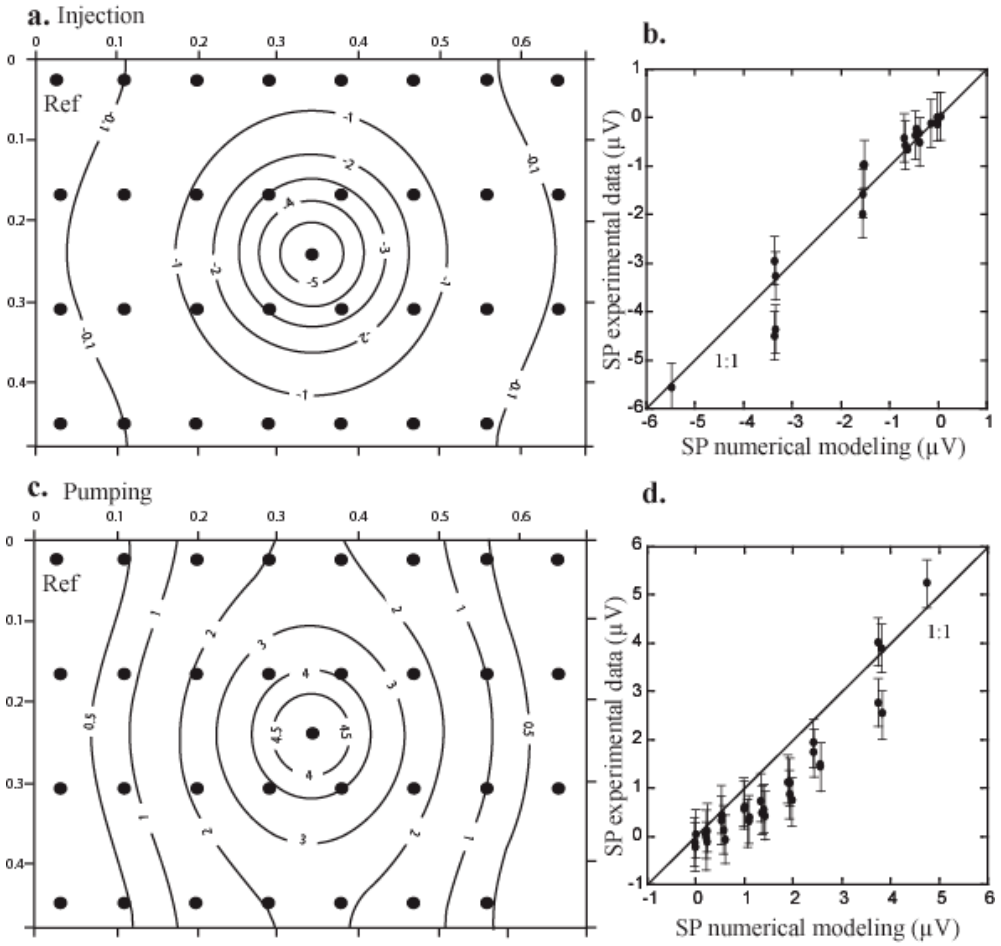

Figure 12. Comparison between the analytical solutions for the self-potential response developed in Appendix A and the measured self-potential distributions. **a.** Self-potential map, at a depth of 3 cm in the tank, for the infiltration experiment. The filled circles correspond to the position of the electrodes in the real sandbox experiment. **b.** Comparison between the analytical solution and the measured self-potential signals at the top surface of the tank (at the peak of the intensity of the self-potential signals (Experiment #1). **c.** Self-potential map for the pumping experiment from the analytical model. **d.** Comparison between the analytical solution and the measured data for the pumping test (Experiment #2).

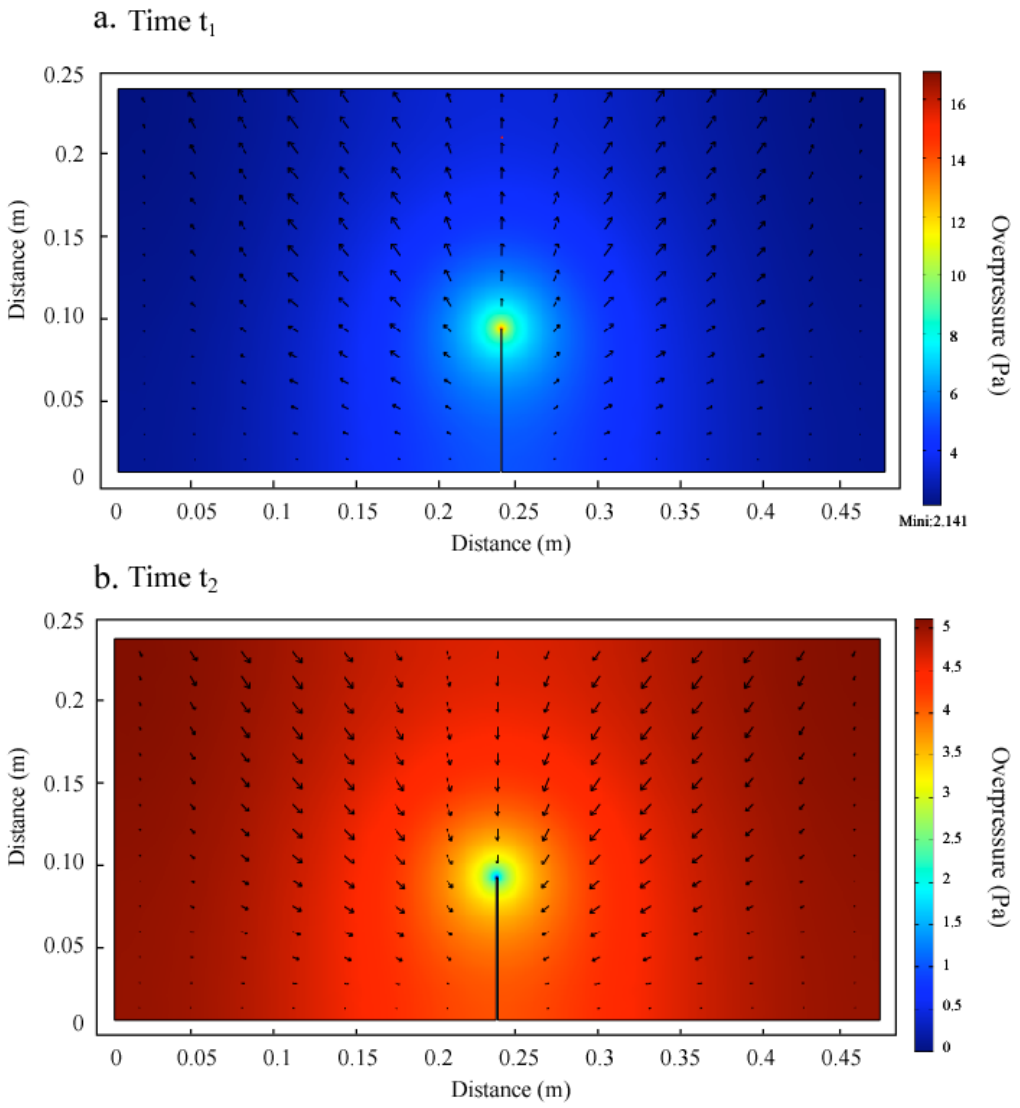

Figure 13. The arrows show the direction of the total displacement **u** (in m) at time t_1 (a) and at time t_2 (b) respectively (see Figure 14). The colors code the fluid pressure above hydrostatic (in Pa). The change of polarity is due the reversal of the fluid flow due to the boundary condition expressed in term of fluid pressure at the end of the capillary. This polarity change is entirely dur to the piston-like effect of the syringe.

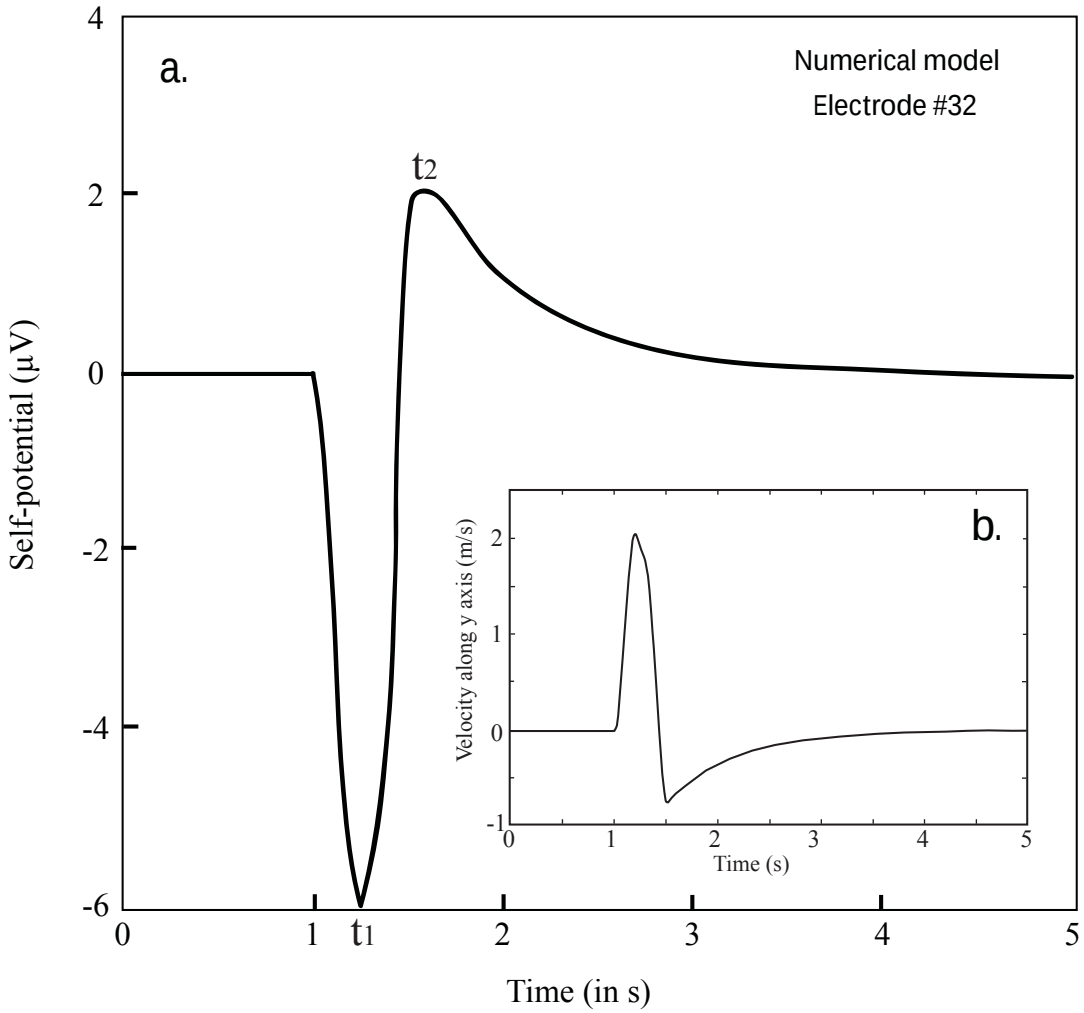

Figure 14. 2D numerical modeling of the self-potential response at electrode #32 (Experiment #1). **a.** Note that the shape of the self-potential curve is similar to the measured self-potential signals (see Figure 4). **b.** Computation of the fluid velocity at the end of the capillary. The reverse of the fluid velocity of the pore water is due to the fact that the fluid pressure is assigned equal to zero at t = 1.5 s.

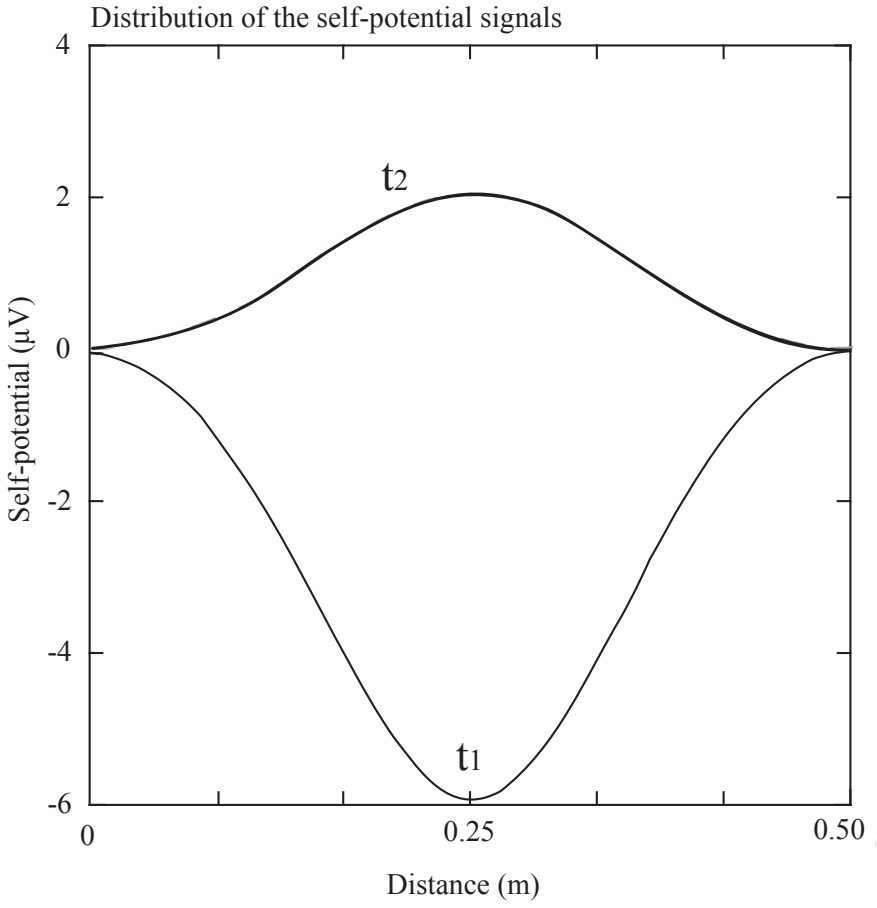

Figure 15. Distribution of the self-potential response at time t_1 and t_2 (see Figure 14) at a depth of 3 cm for the injection experiment.

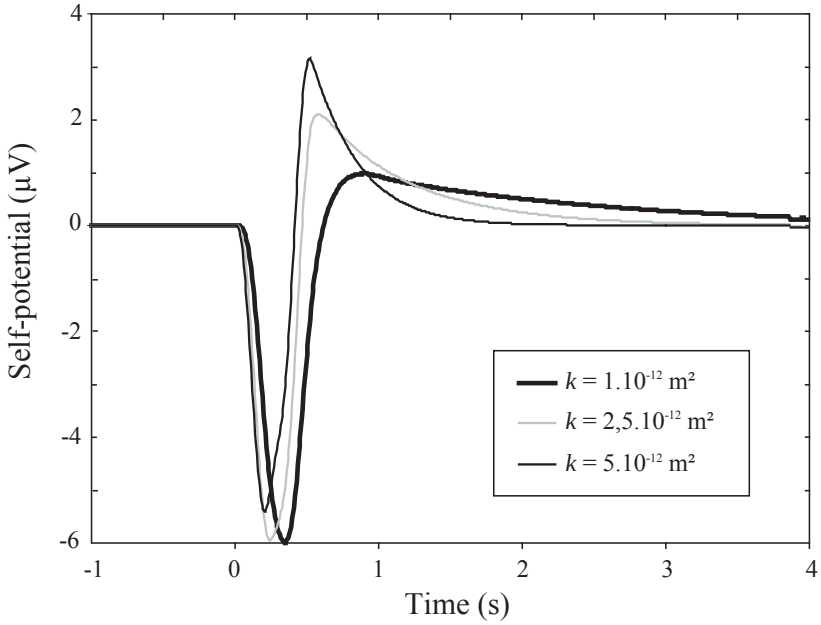

Figure 16. Simulated self-potential response at electrode #32 for different values of the permeability *k* (Experiment #1).

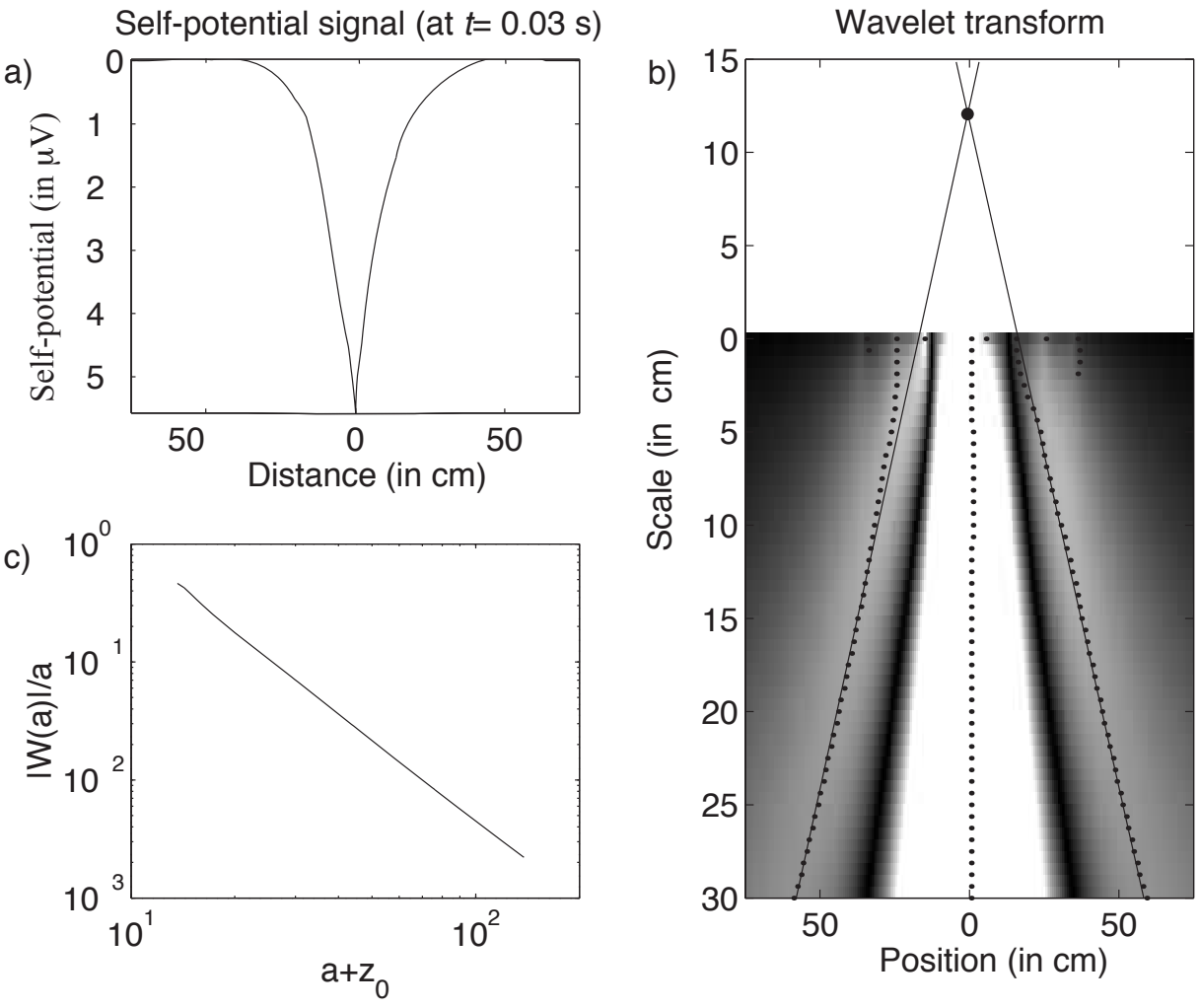

Figure 17. Wavelet analysis of the self-potential data at the maximum development of the self-potential anomaly in the case of the pulse injection of water. **a.** Measured self-potential signals in μV. **b.** Continuous wavelet transform using a first order vertical wavelet, see Eq. (35). The solid lines show the wavelet coefficient maxima that intersect at the position of the source. **c.** The order of the source is estimated from the slope $|W(a)|/a$ versus $a + z_0$ (the slope is equal to 2.2). It follows that the source corresponds to an electrical dipole.

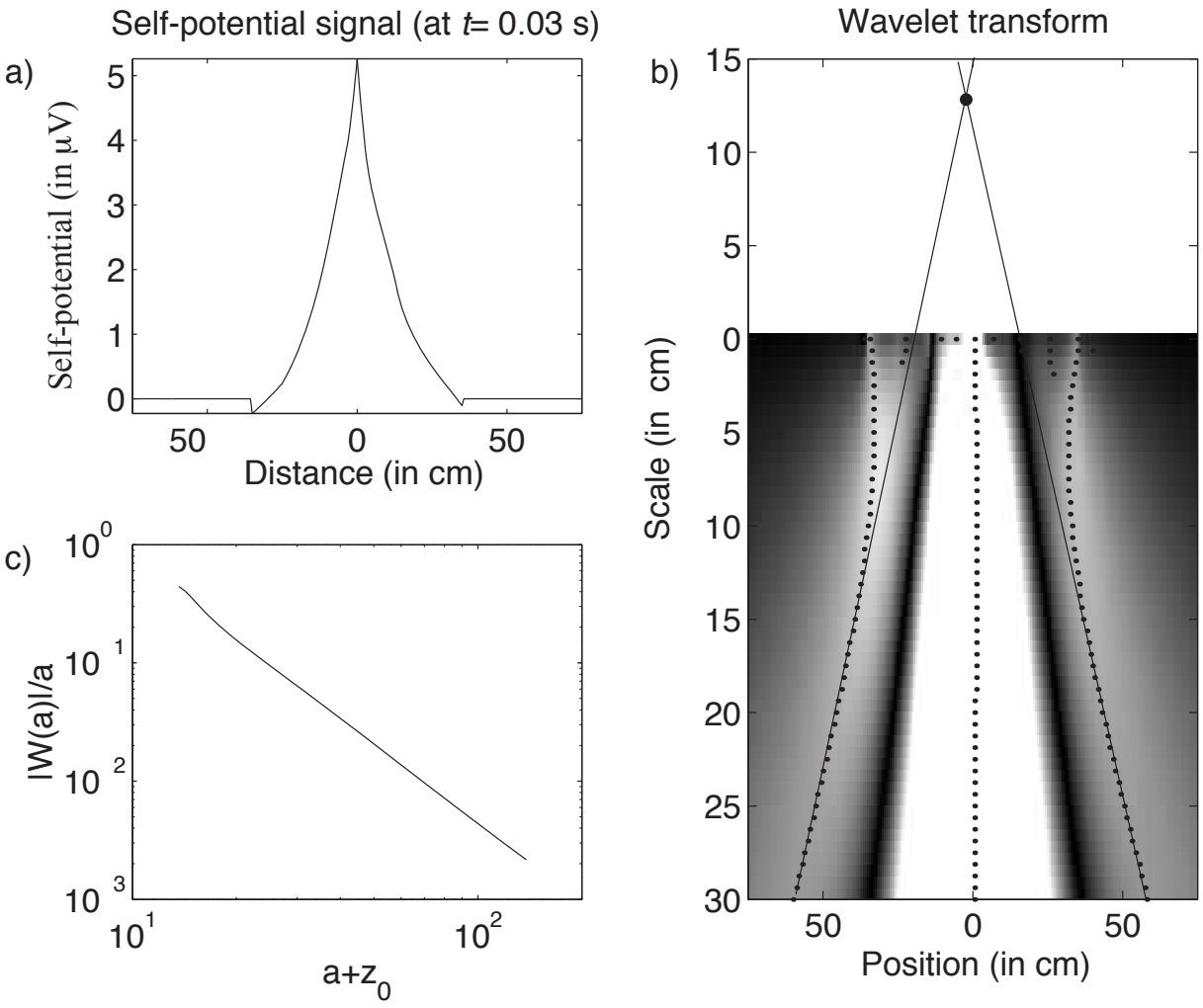

Figure 18. Wavelet analysis of the self-potential data at the maximum development of the self-potential anomaly in the case of the pulse pumping of water. **a.** Measured self-potential signals in μV. **b.** Continuous wavelet transform using a first order vertical wavelet, see Eq. (35). The solid lines show the wavelet coefficient maxima that intersect at the position of the source. **c.** The order of the source is estimated from the slope of $|W(a)|/a$ versus $a + z_0$. The source corresponds to an electrical dipole.

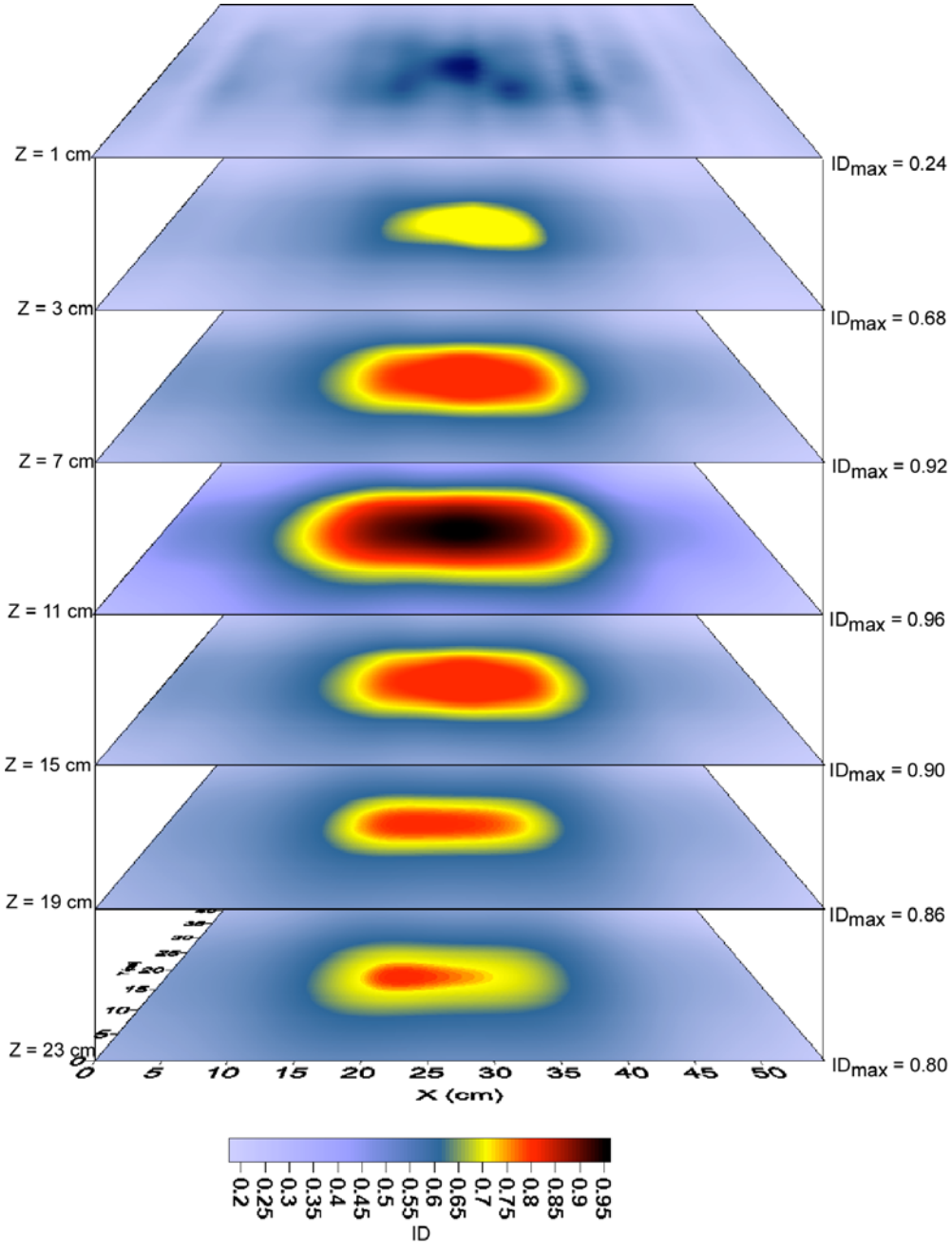

Figure 19. Distribution of the cross-correlation density over the tank (experiment #1). The maximum of the cross-correlation distribution is located at a depth of 14 cm below the top surface of the tank. The numbers on the right side of the tomography represent the maxima of the cross-correlation function for each horizontal plane.

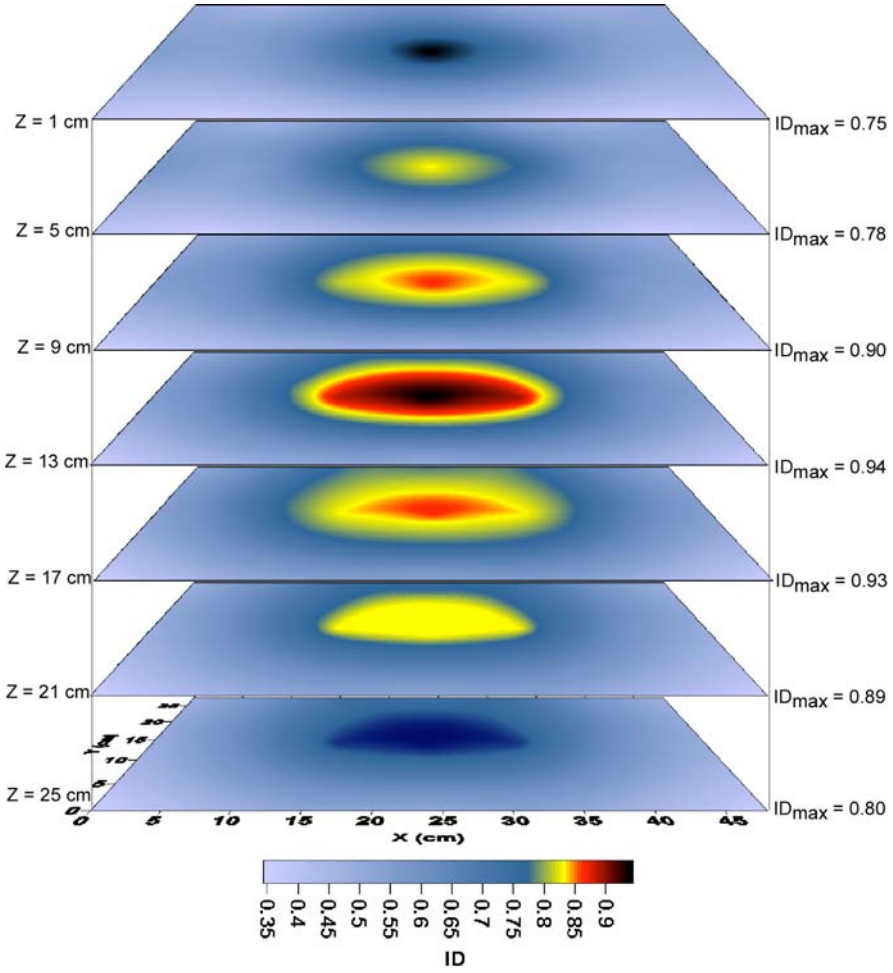

Figure 20. Distribution of the cross-correlation density over the tank for the pumping test (experiment #2). The maximum of the cross-correlation distribution is located at a depth of 16 cm below the top surface of the tank. The numbers on the right side of the tomography represent the maxima of the cross-correlation function for each horizontal plane.

3.5. Conclusion

Dans cette étude, nous nous sommes efforcés de comprendre les mécanismes physiques responsables de la signature de potentiel électrique associé à une perturbation hydromécanique dans un milieu poreux saturé en eau. Nous avons montré, à l'échelle de la cuve, par différentes expériences reproductibles et un voltmètre très sensible, que ce type de source initiée par un très faible changement de pression était détectable et avait une signature électrique caractéristique. Grâce aux deux méthodes associées des transformées en ondelette et une méthode d'intercorrélation, nous avons pu localiser la position de la source et confirmer sa nature dipolaire.

A l'échelle d'un volcan, l'intensité du signal associé à de la fracturation dépend de la profondeur de la source. Pour une profondeur de 1 km, nous pourrions obtenir un signal d'environ 1 mV et à une profondeur de 100 m un signal d'environ 10 mV. Ces signaux sont aujourd'hui mesurables d'autant plus qu'il est possible de s'affranchir du bruit associé aux activités anthropiques et telluriques afin de gagner en précision. Les anomalies associées à de la fracturation et celles induites par un mouvement d'eau dans la zone vadose ou les aquifères ne se produisant pas dans la même gamme de fréquence nous pourrons donc différencier les différents types de signaux.

Ceci ouvre de nouvelles perspectives dans l'utilisation des données de potentiel spontané pour suivre en continu les processus de fracturation non seulement en domaine volcanique mais pourquoi pas sur les glaciers et les failles. Il serait intéressant, connaissant mieux le phénomène dans des conditions bien contraintes avec un sable calibré, de développer de nouveaux protocoles en utilisant d'autres matériaux provenant directement des terrains à étudier en incluant des hétérogénéités argileuses pour se rapprocher davantage d'un système naturel.

3.6. Références

Hornby P, F. Boschetti and F. Horowitz, 1999. Analysis of Potential Field Data in the Wavelet Domain, *Geophysical Journal International*, 137, 137-276.

Iuliano, T., P. Mauriello, and D. Patella, 2002. Looking inside Mount Vesuvius by potential fields integrated probability tomographies, *J. Volcanology Geothermal Res.,* 113, 363-378.

Moore, J. R., and S. D. Glaser, 2006. The origins of the self-potential response during hydraulic fracturing, *Eos Trans.,* AGU Fall Meet. Suppl., Abstract NS21A-04.

Moore, J. R., and S. D. Glaser, 2007. Self-potential observations during hydraulic fracturing, *J. Geophys. Res.,* 112, B02204.

Moreau, F., D. Gibert, M. Holschneider and G. Saracco 1997. Wavelet analysis of potential fields, *Inverse Probl.,* 13, 165-178.

Moreau, F., D. Gibert, M. Holschneider and G. Saracco, 1999. Identification of sources of potential fields with the continuous wavelet transform Basic theory, *J. Geophys. Res.*, 104(B3), 5003-5013.

Patella, D., 1997a. Introduction to ground surface self-potential tomography, *Geophys. Prosp.* 45, 653–681.

Patella, D., 1997b. Self-potential global tomography including topographic effects, *Geophys. Prosp.* 45, 843–863.

Perrier, F., and P. Morat, 2000. Characterization of electrical daily variations induced by capillary flow in the non-saturated zone, *Pure Appl. Geophys.*, 157, 785-810.

Nitsan, U., 1977. Electromagnetic emission accompanying fracture of quartz-bearing rocks, *Geophys. Res. Lett., 4*, 333-336.

Revil, A., L. Ehouarne, and E. Thyreault 2001. Tomography of self-potential anomalies of electrochemical nature, *Geophys. Res. Lett., 28(23),* 4363-4366.

Rizzo, E., B. Suski, A. Revil, S. Straface, and S. Troisi, 2004. Self-potential signals associated with pumping-tests experiments, *J. Geophys. Res.,* 109, *B10203.*

Sailhac, P., A. Galdeano, D. Gibert, F. Moreau, and C. Delor, 2000. Identification of sources of potential fields with the continuous wavelet transform: Complex wavelets and applications to magnetic profiles in French Guiana, *J. Geophys. Res.*, 105, 19,455-19,475.

Surkov, V.V., and V.A. Pilipenko, 1997. Magnetic effects due to earthquakes and underground explosions: a review, *Ann. Geofis.*, XL, 1-13.

Suski, B., E. Rizzo, and A. Revil, 2004. A sandbox experiment of self-potential signals associated with a pumping-test, *Vadose Zone J.*, 3, 1193-1199.

Suski, B., A. Revil, K. Titov, P. Konosavsky, M. Voltz, C. Dagès, O. Huttel, 2006. Monitoring of an infiltration experiment using the self-potential method, *Water Resources Research*, 42.

Yoshida, S., and T. Ogawa, 2004. Electromagnetic emissions from dry and wet granite associated with acoustic emissions, *J. Geophys. Res.,* 109, B09204.

Yoshida, S., M. Uyeshima, and N. Nakatani, 1997. Electric potential changes associated with slip failure of granite: preseismic and coseismic signals, *J. Geophys. Res.*, 102, 14,883-14,897.

Yoshida, S., P. Manjgaladze, D. Zilpimiani, M. Ohnaka, and N. Nakatani, 1994. Electromagnetic emissions associated with frictional sliding of rock, in *Electromagnetic Phenomena Related to Earthquake Prediction*, edited by M. Hayakawa and Y. Fujinawa, 307-322, Terrapub, Tokyo.

Chapitre 4

Applications de la méthode de polarisation spontanée en volcanologie

---

4.1. Introduction

Les signaux de potentiel spontané peuvent être générés par des gradients de potentiels chimiques, des écoulements de fluides ou encore des variations de température. On peut trouver sur les volcans actifs des zones d'anomalies supérieures à 1 Volt comme par exemple sur le Mont Uzen au Japon (Hashimoto et Tanaka, 1995) ou sur le Piton de la Fournaise à la Réunion (Michel et Zlotnicki, 1998). Des anomalies supérieures à 2 ou 3 V ont également été mesurées sur le Mont Fuji au Japon (Aizawa et al., 2005), le volcan Agadak en Alaska (Corwin et Hoover, 1979), et une anomalie de 4 V a été observée sur le Misti au Chili (Thouret et al., 2001; Finizola et al., 2004). Dans le cas des gisements métallifères, le record revient à une anomalie de -10.2 Volts sur la mine aurifère de Yanacocha au Pérou (Goldie, 2004). Comme nous le verrons par la suite toutes ces anomalies sont à priori d'origine électrocinétique.

Dans le cas des zones volcaniques, les mesures de potentiel spontané sont essentiellement utilisées pour cartographier les limites lithologiques (failles, dikes, limites de cratère) et déterminer les configurations des circulations de fluides de subsurface (Zlotnicki et al., 1998 ; Aubert et al., 2000 ; Revil et al., 2004). En plus des variations spatiales, des variations

temporelles de potentiel spontané ont été observées en tant que précurseurs des éruptions volcaniques comme à Miyake-jima au large de Tokyo (Sasai et al. (2002) à l'Etna (Lénat 1995), ou associées à des phénomènes de fracturation hydraulique dans le système volcanique comme c'est le cas au Mérapi en Indonésie (Byrdina et al., 2003). La technique du potentiel spontané est également de plus en plus utilisée comme méthode de surveillance. Les mesures spatio-temporelles de potentiel spontané ont non seulement l'avantage d'être sensibles à la dynamique des systèmes hydrothermaux, mais elle permettent une meilleure compréhension de la configuration des écoulements d'eau météoritiques et du système hydrothermal. Ce dernier aspect a une dimension importante la présence d'aquifères pouvant engendrer des éruptions phréato-magmatiques de fortes intensités mais également devenir une ressource en eau pour les populations locales.

Dans un premier temps nous ferons un rappel des différentes sources possibles des signaux de potentiel spontané en milieu volcanique, puis nous évoquerons les différents types d'anomalies que nous pouvons observer à l'échelle de l'édifice. Nous présenterons deux exemples d'application de la méthode de potentiel spontané à travers deux articles scientifiques l'un soumis dans le "*Journal of Volcanology and Geothermal Research*" et l'autre publié dans le "*Journal of Geophysical Research*". Au cours de quatre missions de terrain réalisées en 2005 et 2006, nous avons utilisé la méthode de polarisation spontanée associée à des tomographies de résistivité électrique, des mesures de température et de flux de CO_2 afin de (1) confirmer l'existence d'un aquifère sur le flanc Est du Stromboli (Iles éoliennes, Sicile, Italie) et déterminer sa profondeur et (2) acquérir une bonne connaissance de la structure interne de l'édifice de la Fossa à Vulcano (Iles éoliennes, Sicile, Italie) dans la perspective de développer un réseau de surveillance adapté à ces volcans.

4.2. Les origines du potentiel spontané

4.2.1. le potentiel électrochimique

Le couplage électrochimique répond au principe d'une pile de concentration et génère via les échanges ioniques un potentiel électrique appelé potentiel de diffusion. Les potentiels de diffusion sont des gradients de potentiel électrique crées sous l'effet d'un gradient de concentration des porteurs de charges (électrons et ions). Dans le cas des électrons le moteur de la densité de courant est un gradient de potentiel redox. La diffusion respective des anions et des cations, de mobilité différente, va engendrer un déséquilibre des charges et donc un courant électrique qui existe tant que la répartition des charges est inégale et n'assure pas l'électroneutralité du système. De tels effets ont été mis en évidence en prospection minière où des lentilles de minerais sulfurés ont été détectées à l'aplomb d'anomalies de potentiel spontané de plusieurs centaines de mV (Figure 4.1).

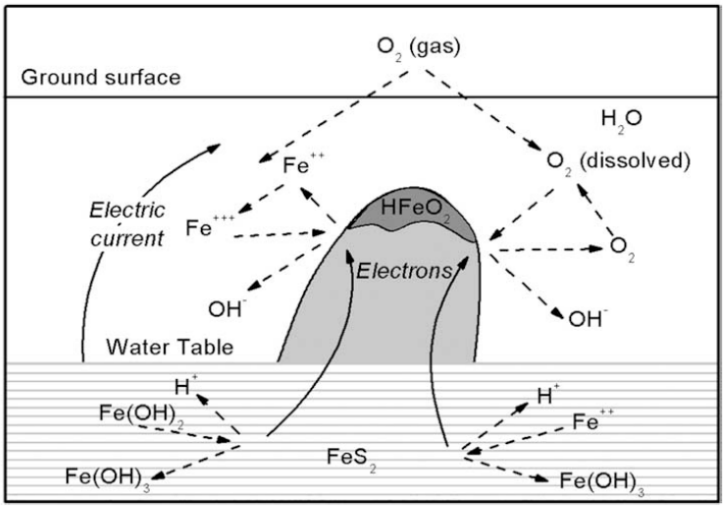

Figure 4.1 : Mécanismes de polarisation spontanée par couplage électrochimique dans la pyrite (d'après Sato et Monney, 1960).

Sur les volcans, des observations géochimiques mettent en évidence des concentrations en ions différentes dans les gaz, les évacuations d'eau et les zones de fumerolles. Les réactions

chimiques entre les gaz volcaniques contenant principalement du sulfure d'hydrogène (H_2S), du dioxyde de soufre (SO_2), du dioxyde de carbone (CO_2) et les eaux souterraines peuvent générer des ions sulfates (SO_4^-) à l'origine d'anomalies négatives en surface, des ions hydrogénocarbonates et carbonates (CO_3^-). En contexte géothermique, ces phénomènes électrochimiques sont considérés comme faibles (de l'ordre de la dizaine de mV) sauf si un conducteur électronique intercepte un front rédox (par exemple la surface piézometrique). On peut également se poser la question de l'effet d'un gradient thermique sur un conducteur électronique en profondeur comme un gisement métallifère). Le signe de ces anomalies (le plus souvent négatives) ainsi que leur longueur d'onde peuvent éventuellement permettre de les distinguer des signaux d'origine thermoélectrique et électrocinétique.

4.2.2. Le couplage thermoélectrique

Si on maintient un gradient de température sur un échantillon de roche, un gradient de potentiel électrique apparaîtra à travers cet échantillon (Nourbehecht, 1963 ; Corwin, 1976 ; Corwin et Hoover, 1979) (Figure 4.2). Ce phénomène est connu sous le nom de couplage thermoélectrique et est le résultat de la diffusion thermique différentielle des ions dans le fluide poral, des électrons dans un conducteur électronique. Ce processus est connu comme l'effet Soret. Le rapport entre le potentiel électrique et le gradient de température $\Delta\varphi/\Delta T$ est le coefficient de couplage thermoélectrique qui peut être calculé à partir des propriétés de l'électrolyte et du milieux poreux par le modèle proposé par Revil (1999). La littérature donne des valeurs de ce coefficient de couplage thermoélectrique allant de -0,1 à +1,5 mV/°C (Yamashita, 1961, Nourbehecht 1963, Revil 1999). Pour les roches volcaniques, même si leur connaissance in situ reste dans le domaine de l'hypothétique, on admet en général des valeurs de l'ordre de 0,2 mV/°C. Cet effet n'est donc pas un phénomène prépondérant, toutefois il doit être pris en compte notamment dans les zones géothermales où de forts gradients de température sont observés (Fitterman et Corwin, 1982 ; Fitterman, 1983) et où ce phénomène existe quelque soit l'intensité du couplage électrocinétique.

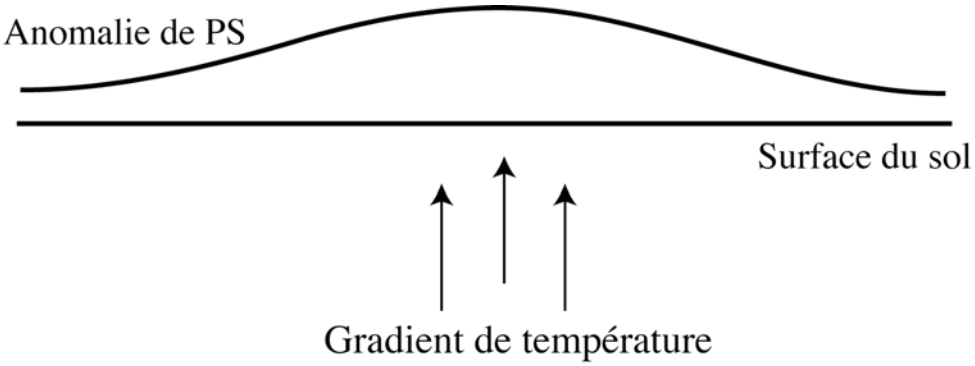

Figure 4.2: Schéma d'un potentiel thermoélectrique produit par un gradient de température (d'après Nourbehecht, 1963). Il est important de noter que la polarité de l'anomalie de potentiel spontané dépend du signe du coefficient de couplage électrothermique qui peut être positif ou négatif.

4.2.3. Le couplage électrocinétique

Les circulations de fluides guidées par les contraintes à travers les roches produisent en général des anomalies positives de potentiel spontané dans le sens d'écoulement des fluides (Fitterman, 1979; Ishido and Mizutani, 1981; Sill, 1983). Des profils de PS s'étendant du sommet aux parties inférieures des flancs des volcans actifs montrent généralement deux zones principales (Sasai et al., 1997; Di Maio et al., 1998; Aubert et al., 2000; Finizola, 2002) : une zone dominée par les circulations hydrothermales, généralement dans la partie supérieure de l'édifice et une zone dominée par des circulations hydrogéologiques dans les parties basses.

D'importantes anomalies positives, supérieures à plusieurs centaines de mV sont souvent observées au sommet de volcans actifs. Ces anomalies sont bien corrélées soit avec des zones de fissures soit avec des cratères sommitaux ou des cônes et sont compensées par une relation inverse et linéaire entre potentiel spontané et altitude loin des zones actives. En contexte volcanique, le phénomène d'électrofiltration est généralement le mécanisme principal générant

des anomalies de potentiel spontané (Ishido et Mizutani, 1981, Morgan et al., 1989, Michel et Zlotnicki, 1998).

4.2.3.1. L'effet topographique

Sur les volcans, une partie de l'eau météorique s'infiltre plus ou moins facilement dans les différentes formations géologiques en fonction de leur perméabilité. La topographie de ces formations guide les écoulements gravitaires. Généralement les eaux souterraines s'écoulent le long des couches horizontales imperméables (Fournier, 1989 ; Aubert et al., 1993) et en particulier sur des barrières de perméabilité associées au toit de la zone hydrothermale comme cela semble être le cas à Stromboli (Revil et al., 2004). Ces écoulements peuvent alimenter des nappes perchées dans le creux d'une barrière de perméabilité comme dans le cratère de Stromboli en Italie (Revil et al., 2004).

L'"effet topographique" se traduit par une relation linéaire inverse entre le potentiel électrique et l'altitude de la surface du sol (Figure 4.3). Cette relation a été mise en évidence sur divers volcans dans des zones non affectées par la convection hydrothermale : sur l'Adagdak (Corwin et Hoover, 1979), le Kilauea (Zablocki, 1978 ; Jackson et Kauahikaua, 1987), le Piton de la Fournaise (Aubert et al., 1993 ; Boubekraoui et al., 1998) et la chaîne des Puys (Fournier, 1989 ; Aubert *et al*., 1990 ; Aubert *et Al*., 1991; Aubert et Atangana, 1996). Cette relation entre potentiel spontané et altitude est souvent écrite sous la forme :

$$\Delta\varphi = C \cdot h + A, \tag{4.1}$$

où $\Delta\varphi$ est la différence de potentiel (en mV), C est le coefficient directeur de la droite reliant le potentiel spontané à l'altitude (en mV/m), h est l'altitude (en m), et A est une constante. La constante A peut être égale à zéro si les relevés sont effectués dans des zones côtières, où l'aquifère se jette au niveau de la mer. Dans ce cas, cette dernière nous fournit notre potentiel électrique de référence. Cette proportionnalité entre potentiel spontané et altitude a été mise en relation avec la nappe phréatique, toutefois, deux interprétations mécanistiques distincts de ces observations ont été proposées. Aubert et Antagana (1996) relient les signaux de potentiel spontané à l'épaisseur de la zone non-saturée. A l'opposé, Fourier (1989) relie les signaux de

potentiel spontané à la distribution de la surface piézométrique de la nappe libre. Nous détaillerons ces deux modèles dans la section 4.4 mais il est important de ne pas considérer ces modèles comme antagonistes. Les deux cas peuvent parfaitement exister dans la nature.

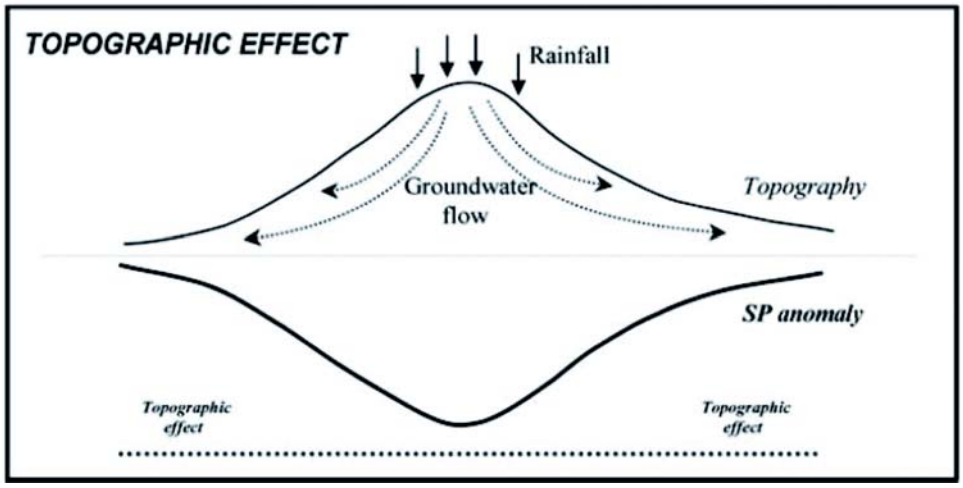

Figure 4.3 : Exemple d'anomalie de potentiel spontané lié à l'effet topographique. D'après Zlotnicki et al. (1998).

4.2.3.2. Les Remontées Hydrothermales.

Sur les volcans actifs, l'effet topographique dû aux écoulements gravitaires est fortement perturbé par des sources hydrothermales peu profondes. Les réservoirs magmatiques, les dikes et les gaz volcaniques fournissent de l'énergie thermique dans les parties hautes de l'édifice. Les sources thermales génèrent des remontées de fluides au-dessus des réservoirs de magma et le long des interfaces tectoniques (limites de cratère, failles…) alors que l'infiltration des eaux météoriques occasionne des circulations vers le bas.

En utilisant un modèle de cellules de convection et en prenant un coefficient de couplage électrocinétique égal à -3.5 mV/MPa, Ishido (1988) a montré que les remontées de fluides chauds

étaient associées à des anomalies positives de potentiel spontané supérieures à 100 mV. Tandis que l'eau météorique infiltre le massif, l'eau est chauffée et des cellules convectives se forment. Une anomalie positive apparaît au-dessus des flux ascendants tandis qu'une anomalie négative se manifeste au-dessus des zones d'écoulements gravitaires. Selon, la chimie des fluides, la lithologie et la température du milieu, l'effet électrocinétique des courants chauds ascendants peut dominer ou être négligeable par rapport à celui des courants froids descendants ; cela se traduit par une anomalie de potentiel spontané en surface positive, négative ou dipolaire. En certaines occasions, l'effet électrocinétique dans la région descendante et froide est plus important que celui de la région ascendante et chaude c'est le cas lorsque le fluide montant est de la saumure car elle a un coefficient de couplage électrocinétique plus faible que l'eau douce descendante. L'anomalie de PS en surface est alors négative.

4.3. Les Principaux Types d'Anomalies de Potentiel Spontané

4.3.1. Les anomalies en V

Si la valeur du potentiel zêta dans les systèmes eau-roches de subsurface est négative, on s'attend à une corrélation entre potentiel spontané et altitude. Cette corrélation négative est générée par les écoulements hydrogéologiques sans remontées hydrothermales. La forme en "V" du profil de potentiel spontané est donc la manifestation de l'effet topographique. Cette configuration est présente sur différents volcans comme l'Adagdak en Alaska (Corwin et Hoover, 1979), la Montagne Pelée en Martinique (Zlotnicki et al., 1998) (Figure 4.4) ou encore le Haruna au Japon (Aizawa, 2008).

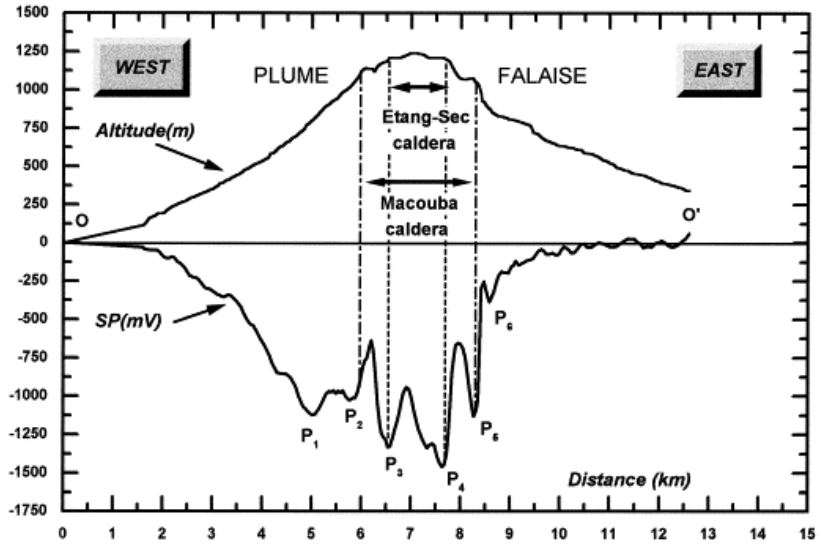

Figure 4.4 : Anomalie de PS sur un profil Ouest-Est de la Montagne Pelée : valeurs de potentiel spontané et topographie vs la distance. D'après Zlotnicki et al., 1988).

4.3.2. Les Anomalies en W

La configuration typique du profil de potentiel spontané sur les volcans est la forme en "W" centrée sur la zone sommitale. Beaucoup d'études mettent en évidence ce type de profils (Ishido, 2004 ; Revil et al., 2008) (Figure 4.5). Zlotnicki et Nishida (2003) expliquent ce type de profil par la coexistence d'anomalies positives et négatives. Dans de nombreux articles scientifiques, la forme en W est interprétée comme la somme d'une anomalie positive associée aux remontées hydrothermales au niveau de la zone sommitale plus une anomalie négative en V liée à l'effet topographique (Nishida et al., 1996 ; Zlotnicki et al., 1998 ; Aizawa et al., 1995). Pour les ïles volcaniques, Ishido (2004) propose toutefois un modèle dans le cas où l'anomalie positive centrale est due à un court-circuit entre la mer et le système hydrothermal de forte conductivité électrique.

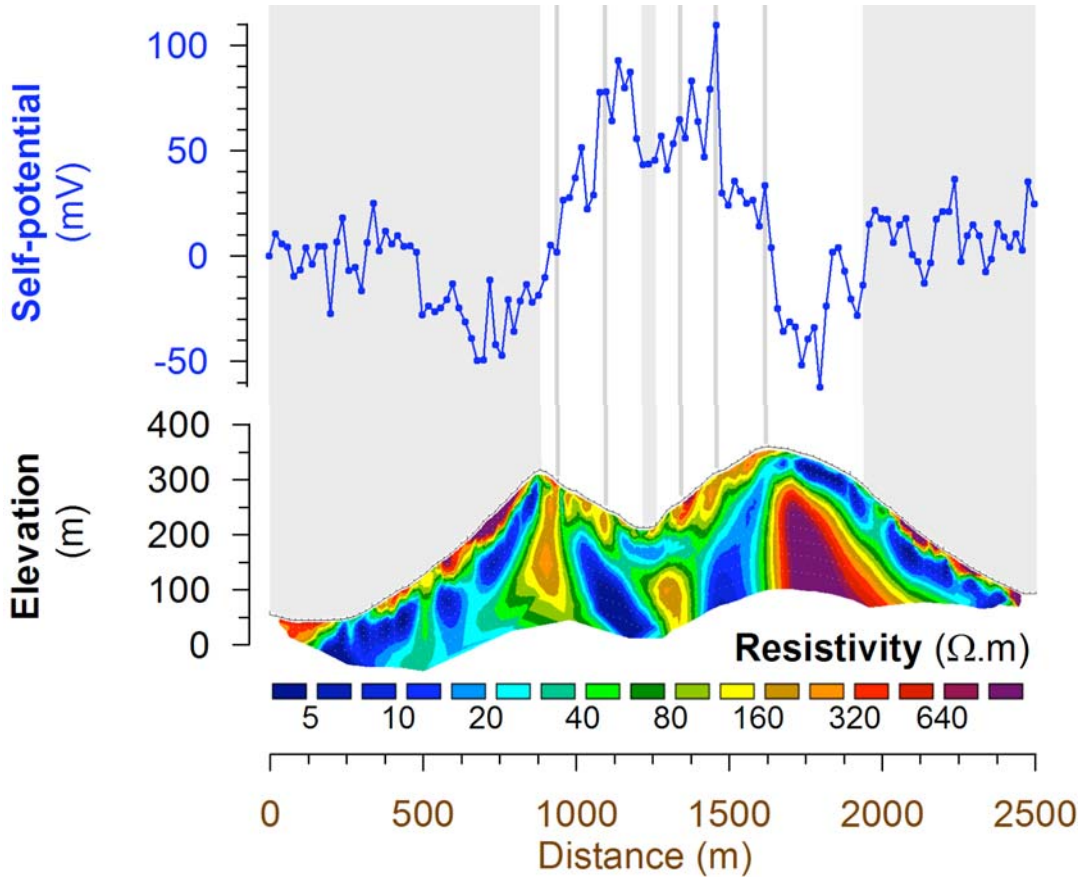

Figure 4.5 : Exemple d'anomalie en « W » sur Vulcano (Italie). L'anomalie positive de potentiel spontané est centrée sur le cratère (Revil et al., 2008)

4.3.3. Les anomalies positives

Sur le Kilauea à Hawaï, des anomalies positives d'environ 1600 mV, ont été reliées sans ambiguïté à des zones de fumeroles et de fissures éruptives récentes (Zablocki, 1976). Sur l'Etna en Sicile, Massenet et Pham (1985) ont montré que ces anomalies pouvaient être observées au-dessus des zones de fissures si ces dernières étaient connectées à une zone active profonde où une source de pression comme une intrusion magmatique peut générer des mouvements de fluides. Au contraire aucune anomalie de potentiel spontané n'est détectée au niveau des zones de fumeroles ou de fissures ouvertes quand ces zones ne sont pas situées au dessus d'une fissure profonde. Sur le Piton de la Fournaise, une anomalie positive de potentiel spontané (supérieure à 1000 mV) très caractéristique, en fer à cheval, coupe la Caldeira en deux (Zlotnicki et al., 1994b;

Malengrau et al., 1994; Michel and Zlotnicki, 1998; Zlotnicki et al., 2001). D'après Michel et Zlotnicki (1998) les fortes précipitations s'infiltrent dans le massif, puis l'eau est canalisée par les limites de cratères et les failles. Ces écoulements gravitaires sont ensuite réchauffés par les réservoirs magmatiques peu profonds et les dikes récents et des flux guidés vers le haut sont générés par la chaleur et les grandes cellules hydrothermales.

Toutefois l'interprétation des anomalies positives comme étant liées à des remontées de fluides chauds est fondée sur deux hypothèses : (1) les signaux de potentiel spontané sont liés à l'effet électrocinétique et (2) le potentiel zêta est négatif dans les systèmes eau-roches de subsurface. Des études récentes sur la caldera du volcan Aso au Japon, ont montrés que plus de la moitié des échantillons étudiés présentaient des valeurs de potentiel zêta positives (Hase et al., 2003). Les anomalies positives de PS peuvent donc être liées à des valeurs positives de potentiel zêta et donc à des écoulements de fluide gravitaires. Aizawa et al. (2008) montrent également que l'on trouve souvent des roches aux potentiels zêta positifs à proximité d'anomalies positives locales de potentiel spontané.

4.4. Localisation d'un aquifère à Stromboli.

4.4.1. Mesures géoélectriques et géochimiques réalisées sur le Stromboli

4.4.1.1. Les mesures de potentiel spontané

Les mesures de potentiel spontané ont été réalisées selon la méthode de la base fixe qui consiste à ne déplacer qu'une électrode (l'électrode de mesure) en gardant l'autre fixe (l'électrode de base). L'électrode mobile est déplacée de façon à mesurer la distribution de potentiel électrique sur toute la surface d'investigation. Les mesures étant faites avec la même base, la lecture du potentiel est directe. Les relevés ont été réalisés tous les 20 m sur deux profils l'un

passant (Profil A) par les zones de la Fossetta, de Rina Grande et des Schicciole et le deuxième traversant les zones de la Fossetta et de Rina Grande. La Figure 4.6 situe la position de ces deux profils. Les deux profils ont la même référence. La différence de potentiel électrique entre l'électrode de référence et l'électrode mobile (électrodes $Cu/CuSO_4$ non polarisable) a été mesurée avec un voltmètre à haute impédance interne d'une sensibilité de 0.1 mV. L'impédance du sol, en général inférieure à 200 kΩ, est très au-dessous de l'impédance du voltmètre (~100 MΩ). Pour améliorer le contact électrique entre le sol et les électrodes, ces dernières sont placées dans des trous d'environ 10 cm de profondeur avec une solution de sulfate de cuivre si nécessaire.

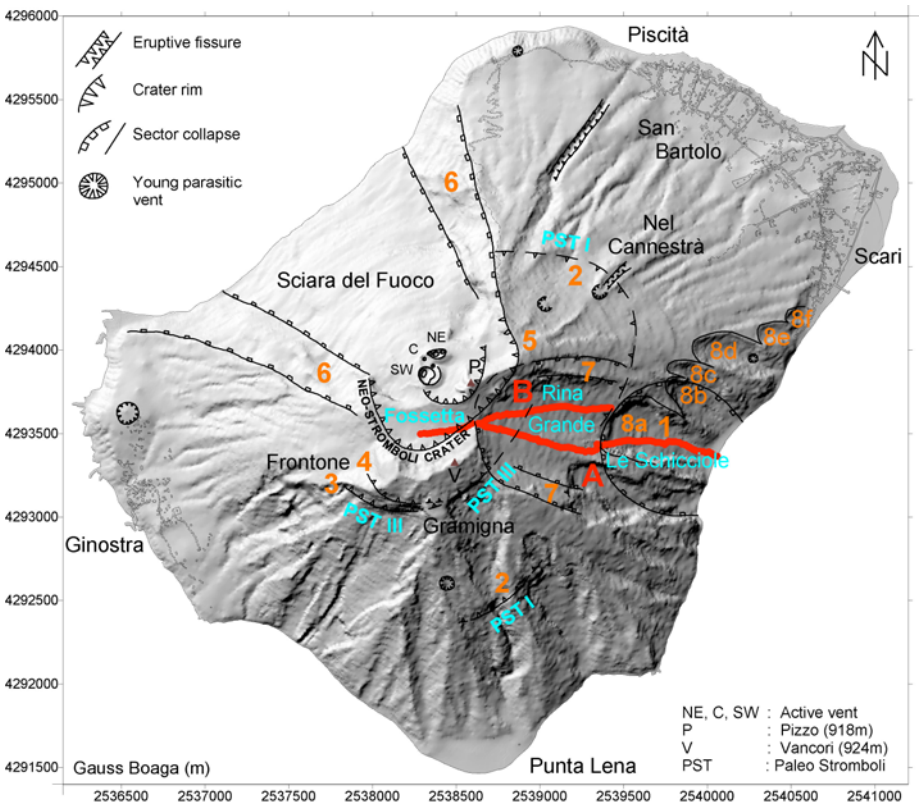

Figure 4.6 : Position des deux profils. Le profil Fossetta, Rina grande, Schicciole (profil A) et le profil Fossetta, Rina Grande (profil B).

4.4.1.2. Les mesures de résistivité électrique

En parallèle des mesures de potentiel spontané, nous avons réalisé des mesures de résistivité électrique grâce à un jeu de 64 électrodes réparties tous les 20 m (aux mêmes positions que celles

de potentiel spontané) le long des profils A et B. Les données ont été acquises avec le système multi-électrodes de l'ABEM (SAS-4000). Nous avons opté pour une configuration Wenner-α car ce dispositif présente non seulement une bonne sensibilité aux variations verticales de résistivité électrique mais aussi un très bon rapport signal/bruit. Le traitement des données est effectué à partir du logiciel d'inversion RES2DINV (Loke and Barker, 1996) basé sur une méthode d'optimisation par moindre carrés généralisés. La topographie a été prise en compte lors de l'inversion des données de résistivité électrique.

4.4.1.3. Les mesures de flux de CO_2

De même que le potentiel spontané et la résistivité électrique, les mesures de flux de CO_2 ont été réalisées tous les 20 m. La méthode utilisée est décrite en détail dans Chiodini et al. (1998). Le dispositif est constitué de plusieurs parties dont les principales sont : la chambre d'accumulation pour les gaz du sol et d'un système de pompage et d'analyse en continu par spectrométrie infrarouge de la concentration en CO_2. On obtient une courbe qui se stabilise sur un palier qui correspond à la concentration du gaz dans le sol. Selon Parkinson (1981) la tangente calculée dans les premiers instants de croissance de cette courbe permet de connaître le flux de CO_2 et donc par extension, connaissant les dimensions de la chambre, la vitesse de remontée du gaz.

4.4.2. Signaux de Potentiel Spontané Associés à des Ecoulements Souterrains

4.4.2.1. La surface SPS

Aubert et Antagana (1996) proposent un modèle selon lequel, les signaux de potentiel spontané mesurés à la surface du sol ont des sources situées dans la zone non-saturée (zone vadose) et sont reliés à son épaisseur. Deux critères sont indispensables pour que le modèle soit valide, la résistivité électrique de la zone non-saturée doit être homogène et supérieure à celle du milieu saturé. Cette relation permet alors de définir une surface équipotentielle appelée surface SPS qui correspond à la limite supérieure de l'aquiclude ou de la zone saturée (Figure 4.7). Pour

un aquifère libre, cette surface correspond au toit de la nappe.

Zhang et Aubert (2003) ont démontré qu'au premier ordre la relation entre le potentiel spontané et l'épaisseur de la zone non-saturée peut s'écrire:

$$\varphi(P) - \varphi_0 = C_v\left[(z - h) - (z_0 - h_0)\right], \tag{4.1}$$

où $\varphi(P)$ est le potentiel spontané mesuré au point de mesure P, C_v est le coefficient de couplage électrocinétique apparent, $z(x,y)$ décrit la topographie de la surface du sol, $h(x,y)$ décrit la topographie de la surface piézométrique, $(z - h)$ représente l'épaisseur de la zone non-saturée au point de mesure P, et $(z_0 - h_0)$ est l'épaisseur de la zone non-saturée au niveau du point de référence où $\varphi_0 = 0$.

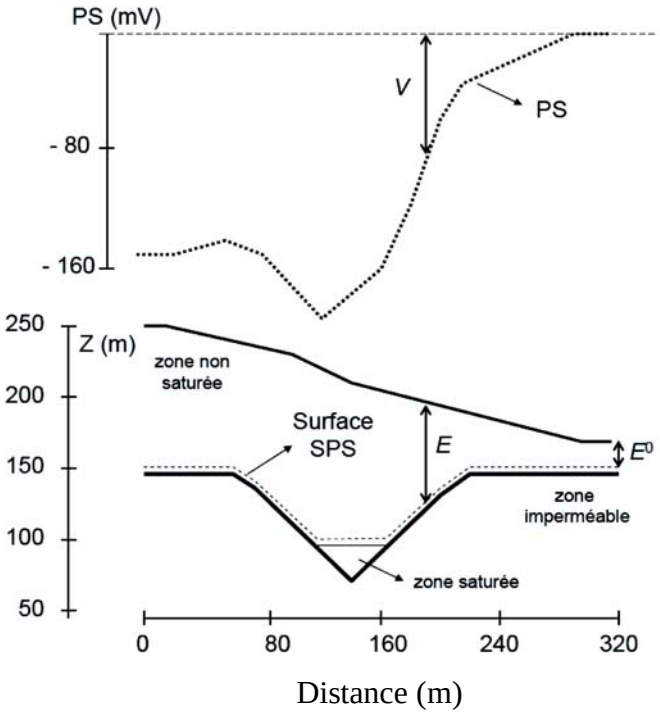

Figure 4.7 : Exemple de représentation de la surface SPS (Aubert et Antagana 1996).

4.4.2.2. Le Modèle de Fournier

Fournier (1989) a proposé que l'effet électrocinétique d'un écoulement d'eau dans un aquifère est équivalent à l'effet d'une couche de dipôles électriques placés au toit de cette nappe et d'intensité proportionnelle à la hauteur piézométrique. Cette analyse repose sur l'hypothèse que le coefficient de couplage électrocinétique *C'* change brutalement au passage de la zone non-saturée à la zone saturée et qu'il est constant dans chacune des deux zones (Figure 4.8). Au premier ordre la relation entre le potentiel spontané et la hauteur piézométrique peut s'écrire lorsque la pente de la surface piézométrique est faible

$$\varphi(P) - \varphi_0 = C'(h - h_0)\,, \tag{4.2}$$

où $C' = C_2 - C_1$ est le coefficient de couplage électrocinétique apparent C_2 et C_1 étant respectivement les coefficient de couplage de la zone saturée et de la zone non saturée, h est la hauteur piézométrique au niveau du point de mesure P, et h_0 est la hauteur piézométrique au niveau du point de référence où $\varphi_0=0$.

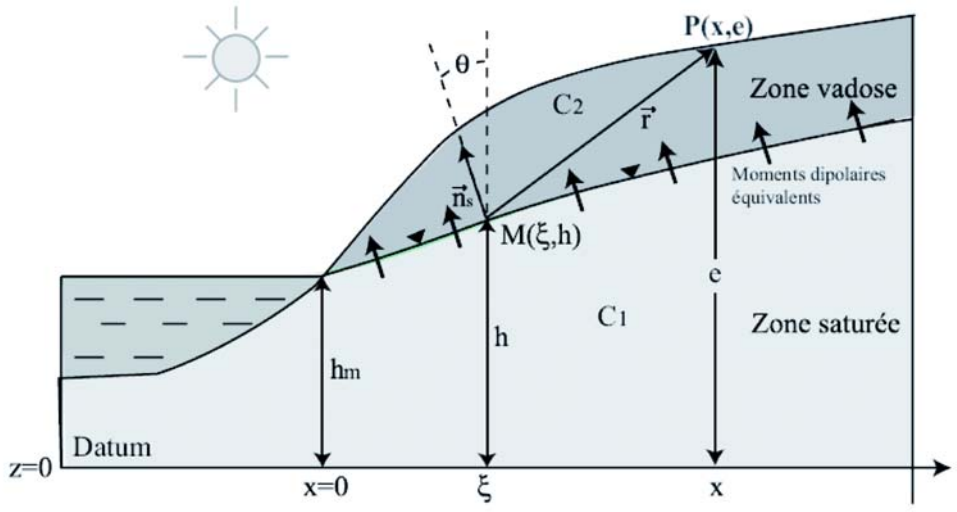

Figure 4.8 : Modèle de la double couche électrique proposé par Fournier (1989). $\vec{r}$ est le vecteur distance entre le point source M(ξ, h) et le point d'observation P(x,e) localisé à la surface du sol, $\vec{n}_s$ est le vecteur normal à la surface piézométrique, h_m est la hauteur piézométrique au point de référence de la mesure du potentiel spontané et C1, C2 sont les coefficients de couplage électrocinétique respectivement de la zone saturée et de la zone vadose.

4.5. Résultats et Interprétations

Les résultats et interprétations des mesures géophysiques et géochimiques réalisées sur le Stromboli ont fait l'objet de la rédaction d'un article soumis dans le "*Journal of Volcanology and Geothermal Research*" intitulé "Localization of freshwater aquifers in active volcanoes with the self-potential method. A case study at Stromboli volcano, Eolian Islands (Italy)" par A. Crespy, A. Revil , A. Finizola, A. Jardani, et T. Ricci. Nous y montrons comment, grâce à l'association de données de potentiel spontané, de résistivité électrique et de flux de CO_2 nous avons mis en évidence la présence d'un aquifère, déterminé sa profondeur et décrit la structure dans laquelle cet aquifère s'est formé.

Localization of freshwater aquifers in a collapse structure inferred by self-potential method. A case study at Stromboli volcano, Aeolian Islands (Italy).

A. Crespy(1), A. Revil (2,3), A. Finizola (4), A. Jardani (2), and T. Ricci (5)

(1) UMR6635 CNRS-CEREGE, Université Aix Marseille III, 13545 Aix-en-Provence, France.

(2) Colorado School of Mines, Department of Geophysics, Golden, CO, 80401, USA.

(3) INSU-CNRS, LGIT (UMR 5559) Université de Savoie, Equipe Volcan, Bâtiment Le Chablais, Domaine Universitaire, 73376 Le Bourget-du-Lac, France.

(4) Laboratoire GéoSciences Réunion, Université de la Réunion, Institut de Physique du Globe de Paris, CNRS, UMR 7154, Equipe Géologie des Systèmes Volcaniques, 15 rue René Cassin, 97715 Saint-Denis cedex 9, La Réunion, Indian Ocean, France.

(5) Università Roma Tre & INGV- Sezione Roma 1, Via della Vasca Navale 79 – 00146, Roma, Italy

---

Corresponding author :

Intended for publication in Journal of Volcanology and Geothermal Research

Abstract. A geophysical survey was conducted over the Eastern flank of Stromboli volcano in the Aeolian islands in Italy to look for the presence of a freshwater aquifer. Electrical resistivity tomograms, soil CO_2 flux, and self-potential data were obtained along two profiles crossing the Fossetta, Rina Grande and Schicciole areas. Ground water flow generates an electrical current density called the streaming current density. The resulting self-potential signals can be measured at the ground surface of the Earth. The combination of these data was used to provide insights regarding the position of the water table of a relatively shallow aquifer (the maximum depth of the water table is estimated to be on the order of 150 m). We use a first-order approximation (called the SPS method) of the relationship between the thickness of the vadose zone and the self-potential anomaly to determine the shape of the water table along these profiles. The value of the streaming potential coupling coefficient in the field is consistent with laboratory measurements. This demonstrates that the process connecting the hydraulic heads to the self-potential signal is scale independent because the coupling coefficient is the same at the scale of the core and at the scale of the flank of the volcano.

Keywords: Stromboli, self-potential, aquifer, electrical resistivity

1. Introduction

The localization of aquifers in active volcanoes is a fundamental step in assessing several geological hazards like phreato-magmatic eruptions and landslides (Petrinovic and Piñol, 2006; Lorenz and Kurszlaukis, 2007; Weinstein, 2007). It is also important because water is a scarce resource in some volcanic areas, and the supply of fresh water is becoming an increasing problem resulting especially from the increase of the populations and touristic activities (Cruz and França, 2006). At Stromboli Island, for instance, the population increases from 350 inhabitants in winter to over 5000 inhabitants over the summer.

In hydrogeology, the presence of aquifers is evidenced by drilling and the estimate of the permeability can be obtained by pumping or slug tests. However, drilling a set of boreholes in volcanic formations can be very expensive and a difficult task owing due to the topography and the mechanical resistance of some of the volcanic rocks. Geophysical methods represent a non-intrusive approach to handle this problem. Traditionally, electromagnetic methods (like AudioMagneTotelluric (AMT) and Time Domain ElectroMagnetic (TDEM) methods) have been used to look for aquifers in active volcanoes (e.g., Krivochieva and Chouteau, 2003). Electrical resistivity can be very sensitive to the water content but unfortunately the electrical resistivity is also known to be affected by the presence of clays (Revil et al., 1998; Revil, 1999) and zeolites (Revil et al., 2002) resulting from hydrothermal alteration and weathering (Coppo et al., 2008). Therefore electromagnetic methods cannot be used as stand-alone methods to determine the presence of aquifers in volcanic areas.

The only non-intrusive geophysical method that is sensitive to the flow of the ground water from the ground surface is the self-potential method. The self-potential method consists on the passive measurements of the electrical potential distribution at the ground surface of the Earth

with a sensitive voltmeter having a high input impedance (usually >10 MOhm) and two non-polarizing electrodes (Fournier,1989; Corwin, 1990; Aubert et al.,1993). One of these electrodes is used as a reference station while the roving electrode is used to scan the electrical potential at a set of stations along a profile or a closed loop (Finizola et al., 2003, 2004). Unusual variation of the electrical potential with respect to the potential of the reference station is called a self-potential anomaly. These self-potential anomalies are always associated with natural polarization mechanisms occurring at depth and especially to the divergence of a source current density associated with of the chemical potential of charge carriers (Revil and Linde, 2006).

In volcanic areas, self-potential anomalies are generally associated with the occurrence of a streaming current. Thermoelectric, electrodiffusional, and electro-redox contributions can generally be neglected (Nourbehecht, 1963; Sill, 1983; Revil et al. 2002). While different theories have been proposed to relate the self-potential anomalies to the depth of the water table (Jackson and Kauahikaua 1987; Fournier, 1989; Aubert et al., 1993), the theoretical background connecting the self-potential anomalies to the pattern of the ground water flow was not fully established until recently. Recent works have proposed a complete theory (e.g., Revil et al., 1999a, b) including the effect of the temperature (Reppert and Morgan, 2003), the effect of the saturation of the water phase (Linde et al., 2007; Revil et al., 2007), and the effect of the Reynolds number in the inertial laminal flow regime (Bolève et al., 2007; Crespy et al., 2007; Kuwano et al., 2007; Revil, 2007). However, even with this background theory in mind, self-potential anomalies can be notoriously difficult to interpret because of the role of the chemistry of the pore fluid and the mineralogy of the rock (see Aizawa et al., 2008, Aizawa, 2008). While the self-potential method has been used in a number of studies to determine the presence of aquifers in active volcanoes (Aubert on Merapi (2000), Bedrosian on Mount St Helen, 2007),

there were no work, to our knowledge, where a combination of methods like self-potential and DC-resistivity tomography plus laboratory measurements were used to address this problem.

In the present paper, we show that the combination of self-potential data, DC-resistivity, and the measurements of the flux of the CO_2 plus some laboratory measurements of the value of the streaming potential coupling coefficient can be used to assess the presence of an aquifer on the flank of an active volcano. Finizola et al. (2002) performed a self-potential survey at the scale of the island of Stromboli and suspected the presence of a cold aquifer on one of the flank of this very active volcano because of the presence of a negative self-potential anomaly in this area (see also Finizola et al., 2006). In the present study, we present new field results to determine the depth of this aquifer using the combination of methods discussed above.

2. Geological Setting

Stromboli is a stratovolcano forming the northernmost island of the Aeolian volcanic arc in the Southern Tyrrhenian sea. It rises from a depth of 2000 m below sea level to an elevation of 924 m above sea level. So it is a volcanic edifice of over 3000 m in which two-thirds are submarine (Segre, 1968). It is one of two active volcanoes (with Vulcano) of the Aeolian archipelago, whose existence is related to the subduction of the African plate under the Eurasian plate (Barberi et al., 1974). Geological surveys (Rosi, 1980 ; Francalanci, 1987; Keller et al., 1993) show that the subaerial part of the main cone was built up during the last 100 ka and can be divided into seven phases, separated by erosional deposits or by collapses of calderas or flanks (Pasquarè et al. 1993): PaleoStromboli I (PST I), PaleoStromboli II (PST II), PaleoStromboli III, Scari complex, Vancori period, Neostromboli and recent Stromboli. The transition between the NeoStromboli and the recent Stromboli cycle occurred most probably 5,000 years B.P (Gillot and

Keller 1993). On a structural point of view, the eastern aerial flank of Stromboli have been affected by several collapses. The oldest one, the Schicciole (see label "1" on fig. 1) affect the PaleoStromboli Units. Then, a succession of caldera collapses occurred (see label "2","3" and "4" in fig. 1). PST I caldera have been identified by geological evidences between Gramigna and Punta Lena in the southern part of the island (Hornig-Kjarsgaard et al., 1993) and a break in slope in the northern part of the island suggest the continuity of the structural boundary crossing the eruptive fissure of Nel Cannestrà (Pasquarè et al., 1993). PST III and lower Vancori caldera ("4" in fig. 1) are only observable between Gramigna and Frontone. Then, occurred the formation of NeoStromboli crater about 13.000 years BP (Hornig-Kjarsgaard et al., 1993). This latter have been affected by sereval collapse structures : The Sciara del Fuoco collapse, 5.000 yrs ago B.P (Hornig-Kjarsgaard et al., 1993), ("6" in Fig.1) and the Rina Grande sector collapse ("7" in Fig. 1). This latter cut the Vancori units in the northern and southern part of the collapse structure and affected only partially the boundary of NeoStromboli crater in the upper part of the collapse structure. Finally a succession of six adjacent flank failure structure (see 8a, 8b, 8c, 8d, 8e and 8f in Fig. 1) occurred in the lower eastern part of the edifice, probably link to the reactivation of a fault, N 64 in direction, located in the upper part of these six collapse structures (Finizola et al., 2002).

3. Field Survey

Electrical resistivity measurements were obtained using a set of 64 brass electrodes along two profiles (1) in the Fossetta, southern part of Rina Grande and the Schicciole areas, (profile A in Fig. 1 and Fig. 2) and (2) in the Fossetta and the northern part of the Rina Grande area (profile

B in Fig. 1 and Fig. 3). The spacing between the electrodes in the field was 20 meters along the curvilinear coordinates following ground surface. We used the Wenner-α configuration for its good signal-to-noise ratio. The data were inverted using RES2DINV (Loke and Barker, 1996) using a finite element grid for the forward analysis. Topography was included in the inversion of the resistivity data.

The CO_2 soil concentration measurements were obtained with a spacing of 20 m along the same profiles at the position of the brass electrodes. The methodology is described in details in Chiodini et al. (1998).

Self-potential measurements were also made at the same stations using a pair of non-polarizing $Cu/CuSO_4$ electrodes. The difference of electrical potential between the reference electrode (arbitrary placed at the beginning of the profile) and the moving electrode was measured with a high-impedance voltmeter. In most cases, the impedance of the ground, was < 200 kΩ, so much below the internal impedance of the voltmeter (~100 MΩ). At each station, a small hole (~10 cm deep) was dug to improve the electrical contact between the electrode and the ground and eventually a little bit of cupper sulfate was added to the ground to improve the electrical contact. The choice of the reference position is discussed in the section 4.3.

4. Modeling Self-potential Signals

4.1 Background Theory

The hydroelectric coupling generating streaming potential can be explained by the following mechanism. Minerals forming the volcanic rocks develop an electric double layer when

they are in contact with water (Lorne et al., 1999; Revil and Leroy, 2001; Leroy and Revil, 2004). An excess of electrical charges, generally negative, exists therefore onto the mineral surface. This fixed charges is counterbalanced by mobile charges located in the vicinity of the mineral water interface in the so called diffuse layer (Gouy, 1910). Groundwater flow through a porous medium drags the excess of charge of the electrical diffuse layer in the flow direction. The streaming current density $\mathbf{j}_S$ associated with ground water flow (in A m^{-2}) is a source electrical current density corresponding to the drag of the excess of electrical charge carried by the flow of the pore water. This source current density is therefore a convective term. The total current density **j** (in A m^{-2}) is the sum of the conduction current density given by the classical Ohm law and this streaming current density (Sill, 1983; Revil et al. 2007; Jardani *et al* 2007).

$$\mathbf{j} = -\sigma \nabla \varphi + \mathbf{j}_S \tag{1}$$

where φ is the self-potential (in V), σ is the electrical conductivity of the porous material (in S m^{-1}), and where the source current density is approximately related to the seepage velocity (Darcy velocity) by $\mathbf{j}_S = \overline{Q}_V \mathbf{u}$ (Revil & Leroy, 2004; Revil *et al.*, 2005) and $\overline{Q}_V$ (in C m^{-3}) is the excess of charge density of the pore water at saturation.

The excess of electrical charge $\overline{Q}_V$ can be derived from streaming potential measurements in the laboratory using $\overline{Q}_V = -C\sigma / K$; where $C = (\partial \varphi / \partial H)_{\mathbf{j}=0}$ is the streaming potential coupling coefficient (Revil *et al.*, 2005).

The continuity equation for the electrical charge is,

$$\frac{\partial Q}{\partial t} + \nabla \cdot \mathbf{j} = 0, \tag{2}$$

where Q is the charge per unit volume of the material. However, porous rocks are globally neutral (the charge contained in the pore water is balanced by the charge existing onto the surface of the minerals) and therefore $\nabla \cdot \mathbf{j} = 0$. This means that $\mathbf{j}$ is conservative. Combining equation (1) and the continuity equation yield the classical Poisson equation for electrical potential,

$$\nabla \cdot (\sigma \nabla \varphi) = \nabla \cdot \mathbf{j}_S , \tag{3}$$

where the right-hand side of Equation (3) corresponds to the source term associated with the Darcy velocity distribution and the heterogeneity in the distribution of the excess charge coefficient $\overline{Q_V}$. The self potential distribution is therefore obtained by solving first the boundary value problem for the hydraulic head. The solution is then used to determine the seepage velocity distribution. Knowing the distribution of the excess of electrical charge per unit volume, the source term of the Poisson equation can be obtained and the Poisson equation can be solved with appropriate boundary conditions. The ground surface is considered to be an insulating boundary and therefore the normal component of the current density vanished at this boundary ($\mathbf{n} \cdot \nabla \varphi = 0$ where $\mathbf{n}$ is the unit vector normal to the ground surface). These equations can be coupled to the hydraulic problem, which can be solved numerically and its solution used to determine the self-potential signals. An alternative to this brute-force approach is to use a first-order solution between the self-potential signals and the piezometric levels as done below.

4.2 Experimental Measurements

We determine in this section a reasonable value for the streaming potential coupling coefficient. As explained in Section 4.1, the coupling coefficient represents the sensitivity

between the electrical potential difference produced in response to a pore fluid pressure gradient. We measure this coupling coefficient for a set of 7 samples from the Rina Grande area.

The samples were first crushed, washed to remove organic matter, and sieved to obtain a grain size comprises between 100 and 200 μm. The samples were saturated with NaCl electrolytes at different ionic strengths during several days. In order to be certain that equilibrium is reached, the conductivity and the pH of the solution was measured over time.

Streaming potential measurements were performed in the laboratory using a Zêtacad (Figure 4). The sample is enclosed in a glass holder allowing fluid flow only through the two end faces. We measure the electrical potential difference between the two end-faces of the sample submitted to a known pore fluid pressure difference in drained conditions. The results (see Figure 5) show that the coupling coefficient depends strongly on the conductivity of the pore water as predicted by the theory (e.g., Morgan et al. 1989; Revil, 2002). The ground water at the Schicciole spring, which is located in between the Rina Grande and the Schicciole areas, was sampled. Measurements of its electrical conductivity yields 1.2×10^{-1} S m^{-1} (at 25°C). According to Figure 6, the coupling coefficient is therefore equal to -1.2 mV m^{-1}.

4.3 Use of a First-order Model

On the flanks of active volcanoes, a linear reverse relationship between self-potential signals and the altitude is often observed (see Corwin and Hoover, 1979; Jackson and Kauahikaua, 1987; Lénat, 1987; Aubert and Yéné Atangana, 1996). According to Zablocki, (1978) and Jackson and Kauahikaua (1987), the amplitude of the self-potential anomalies is proportional to the thickness of the vadose zone. Zhang and Aubert (2003) demonstrated that the

following first-order relationship can be used to relate the self-potential signals to the thickness of the vadose zone,

$$\varphi(x,y,z) - \varphi_0(x_0,y_0,z_0) = c_V\left\{\left[z(x,y) - h(x,y)\right] - \left[z_0(x_0,y_0) - h_0(x_0,y_0)\right]\right\}, \quad (4)$$

where $\varphi(x, y, z)$ is the electrical potential at a self-potential station P(x, y, z) located at the ground surface; c_v is an apparent streaming potential coupling (in mV m^{-1}) coefficient; $z(x, y)$- $h(x, y)$ represents the thickness of the vadose zone below the self-potential station P and $z_0(x_0, y_0)$- $h_0(x_0, y_0)$ represents the thickness of the vadose zone below the reference station.

From the experimental studies checked by drilling, Aubert and Yene Atangana (1996) specified the conditions necessary to verify this correlation, namely a superficial layer characterized by high resistivity overlying a deep layer characterized by a lower resistivity. These conditions are generally well satisfied in volcanic areas. In our case, we can see on the both profiles that the superficial layer is more conductive than the substratum. We can assume that this superficial layer corresponds with a zone full of very conductive ashes above an old fractured lava flow.

In the case of volcanic areas, c_v is usually in the range -(1.5 –4) mV m^{-1} (Aubert and Yene Atangana, 1996). We used resistivity data from the both profiles in the Fossetta - Rina Grande areas (Fig. 2 and Fig. 3) to assess the depth of the rooth of the aquifer. Based on the results obtained for the electric resistivity values of the aquifer identified in the north-eastern part of the island (Finizola et al., 2006) and based on the resistity value close to the Schicciole water spring (Figure 2), we fixed at 70 Ohm.m the boundary between satured and no satured zone. Depth of the aquifer have been calculated each 20m in correlation to each SP measurements. These results are shown in figure 7 which exhibits a good correlation. The slope of the linear regression

provides an estimate of the value of c_v equal to -2.03 mV m^{-1}, which is on the same order of magnitude of the value of the intrinsic coupling coefficient measured in the laboratory (-1.3 mV/m). Using Eq. (4), we can calculate the altitude of the water table (Aubert called this surface the SPS surface).

The electrical tomography configuration allows to determine a consistent reference for the self-potential profiles. On the basis of the values of electrical resistivity, we can divide the profile A (Fig. 2) into four sectors: two highly resistive named R1 and R2 (> 2000 Ω m) and two very conductive bodies, C1 and C2 (<300 Ω m). We can note that the Schicciole source is situated on the other side of a huge resistive structure, so it seems to be unlikely that the source is connected to the Rina Grande aquifer. Thus, we chose to take the reference near the basis of the very conductive zone and close to the surface at the point 360 m. We remember that the first 360 m are the same on the both profiles (see common profile in Figure 1 and grey rectangle in Figure 1 and 3), thus the reference is similar.

Concerning the profile B (Figure 3) we can suppose three main zones, the first RC quite heterogenous, the second R very resistive and the last C very conductive. Indeed, along Profile A, we can observe a low conductive zone R1 associated with a very low variation of the self-potential and CO_2 signals, it is the same on the profile B in the part RC. B1 is characterized by a very low resistivity, and clear positive anomalies of self-potentials and CO_2. This increase is also visible on the profile B. The positive anomaly in C1 is directly followed by a decrease of SP and CO_2 anomalies. This pattern is representative of the presence of an aquifer (Finizola et al., 2006).

In R2 sector as in R1 sector, we can note a very good correlation between the two CO_2 peaks and SP minimum. This correlation have been already shown by Finizola et al. 2002, and interpreted as more fractured and permeable areas allowing preferential fluid flow. We can see a

fairly clear transition zone between the R2 and C2 which seems to coincide with the Schicciole collapse that occurred during the stage of PaleoStromboli edification. As the area C1, C2 is a very conductive zone accompanied by a very low CO_2 flux and slight SP variations. This low SP/altitude correlation suggests in this part the profile an aquifer parallel to the topography. This hypothesis is rather well supported by the electrical resistivity tomography section. These two conductive bodies demonstrate the presence of porous and permeable structure in this part of the edifice. That can be associated with perched aquifers.

On the profile B (Fig.3), in the area of Rina Grande, the conductive body C in correlation with a negative SP anomaly also suggests the presence of an aquifer. The part R is characterized by a very strong vertical resistivity transition located in the upper part of Rina Grande sector collapse (see fig. 1 and fig. 3). This latter is probably associated with the caldera boundary of PaleoStromboli III as suggested by Finizola et al. (2002) through SP and CO_2 data analysis. On the level of the vertical resistivity transition the both profiles are 50 m apart, this important resistive structure exists only on the profile B and consequently seems to be a residue of the PaleoStromboli III crater rim. Based on the results obtained coupling SP and electrical resistivity tomography, we can suppose by this morphological structure that the depth of the vadose zone (Fig. 8) corresponds to the level of the sliding plane of the collapse structure of Rina Grande. The depth of this latter is at about an average of 150 m.

Moreover, we can see on figure 8 the strong influence of the resistive body on the depth of the water table inferred by SP measurements. Indeed, we can note that the Rina Grande sector collapse affects mainly the area located at an elevation below 750m a.s.l. Up to this elevation, the collapse structure remained at a shallow depth. In the highest part of this collapse structure, along the gliding plane, the permeability is higher, as shown by the CO_2 flux values. The fact that the

302 collapse structure of Rina Grande is shallow, up to 750 m a.s.l. is also supported by the
303 geological outcrop of NeoStromboli crater rim at about 800m of elevation not affected by the
304 Rina Grande sector collapse. That clearly displays that the gliding plane of Rina Grande sector
305 collapse at about 800m of elevation was not deep enough to affect the entire structure of
306 NeoStromboli crater boundary. Considering the huge transition in the depth of the gliding plane
307 of Rina Grande at about 750m a.s.l. and the geological lateral boundary of this collapse structure
308 (Fig. 1), it was possible to estimate a global volume of Rina Grande sector collapse structure
309 between the upper part of the Schicciole collapse structure and the top of Rina Grande collapse
310 structure. This volume is about 50.106 m^3. It corresponds twice the volume that affected the
311 aerial and submarine part of the edifice during the collapse of Sciara del Fuoco on 30 December
312 2002 (Maramai et al., 2005).
313

314 ## 5. Concluding statements

315

316 A combination of electrical methods (resistivity and self-potential) revealed the presence of an
317 aquifer that can be associated with the gliding plane of Rina Grande sector collapse. The area of
318 the sector collapse has been clearly subdivided in two parts: The sector below 750 m a.s.l. where
319 the collapse structure reach an average depth of about 120 m and the sector above 750 m a.s.l.
320 where the collapse structure is shallow and have not affected totally the NeoStromboli crater rim.
321 The resistive body that had probably a main role in this differential collapse structure (in depth)
322 of Rina Grande could be the old boundary of PaleoStromboli III caldera. On the top of the Rina
323 Grande sector collapse, the high CO_2 flux values suggest that the gliding plane of Rina Grande is
324 acting nowadays as a more permeable structural boundary. These results display that the eastern

flank of Stromboli volcano need also to be consider carefully for potential structure of flank instability.

Acknowledgments. The INSU-CNRS, Instituto di Metodologie per l'Analisi Ambientale (IMAA) del CNR, the Laboratoire GéoSciences Réunion-IPGP, the CNR, the Istituto Nazionale di Geofisica e Vulcanologia (INGV). This is the IPGP contribution nb XXXX.

References

Aizawa K, M. Uyeshima and K. Nogami 2008. Zeta potential estimation of volcanic rocks on 11 island arc-type volcanoes in Japan: Implication for the generation of local self-potential anomalies, Journal of Geophysical Research, 113(B2), B02201.

Aizawa K., 2008. Classification of self-potential anomalies on volcanoes and possible interpretations for their subsurface structure, Journal of Volcanology and Geothermal Research, In Press.

Aubert, M. and Q. Yene Atangana, 1996. Self-potential method in hydrogeological exploration of volcanic areas. Ground-water 34 6, pp. 1010–1016.

Aubert, M., Dana, I., Gourgaud, A., 2000. Internal structure of the Merapi summit from self-potential measurements. *J. Volcanol. Geotherm. Res.,* 100, 337-343.

Barberi, F., Rosi, M., Sodi, A. 1993. Volcanic hazard assessment at Stromboli based on review of historical data. Acta Vulcanol. 3 : 173-187.

Barberi, F., Civetta, L., Gasparini, P., Innocenti, F., Scandone, R., Villari, L., 1974. Evolution of a section of the Africa-Europe plate boundary; paleomagnetic and volcanological evidence from Sicily. Earth Planet. Sc. Lett., 22 (2), 123-132.

Bedrosian, P. A., J. Unsworth M., Malcolm J.S. Johnston, 2007. Hydrothermal circulation at Mount St. Helens determined by self-potential measurements, *Journal of Volcanology and Geothermal Research,* 160(1-2), 137-146.

Bolève, A., A. Crespy, A. Revil, F. Janod, and J. L. Mattiuzzo, Streaming potentials of granular media: Influence of the Dukhin and Reynolds numbers, J. Geophys. Res., 112, B08204, doi:10.1029/2006JB004673, 2007.

Chiodini G., Cioni R., Guidi M. & Raco C. (1998). Soil CO2 flux measurements in volcanic and geothermal areas. Applied Geochemistry, 13 (5): 543-552.

Coppo N, Schnegg PA, Heise W, et al., 2008. Multiple caldera collapses inferred from the shallow electrical resistivity signature of the Las Canadas caldera, Tenerife, Canary Islands, Journal of Volcanology and Geothermal Research, 170(3-4), 153-166.

Corwin, R. F.: 1990, 'The Self-Potential Method for Environmental and Engineering Applications in S. H. Ward (ed.), Geotechnical and Environmental Geophys., Vol. 1, Soc. Explor. Geophys., Tulsa, p. 127.

Corwin, R.F., Hoover, D.B., 1979. The Self-Potential method in geothermal exploration. Geophysics 44, 226-245.

Crespy, A., A. Bolève, and A. Revil, Influence of the Dukhin and Reynolds numbers on the apparent zeta potential of granular media, Journal of Colloid and Interface Science, 305, 188-194, 2007.

Cruz J. V., and Z. França 2006. Hydrogeochemistry of thermal and mineral water springs of the Azores archipelago (Portugal), Journal of Volcanology and Geothermal Research, 151, 4 , *382-398.*

Finizola, A., S. Sortino, J.-F. Lénat, M. Aubert, M. Ripepe, and M. Valenza (2003). The summit hydrothermal system of Stromboli. New insights from self-potential, temperature, CO2 and fumarolic fluid measurements. Structural and monitoring implications, Bull. Volcanol., 65, 486-504.

Finizola A., A. Revil, E. Rizzo, S. Piscitelli, T. Ricci, J. Morin, B. Angeletti, L. Mocochain, F. Sortino, 2006. Hydrogeological insights at Stromboli volcano (Italy) from geoelectrical, temperature, and CO_2 soil degassing investigations, Geophys. Res. Lett., 33, L17304, doi:10.1029/2006GL026842.

Finizola, A., S. Sortino, J.-F. Lénat and M. Valenza (2002). Fluid circulation at Stromboli volcano (Aeolian Islands, Italy) from self-potential and CO2 surveys, J. Volcanol. Geotherm. Res., 116, 1-18.

Francalanci, L., 1987. Evoluzione vulcanologica e magmatologica dell'isola di Stromboli (Isole Eolie) : Relazioni tra magmatismo calc-alcalino e shoshonitico, Tesi di Dottorato, Dipartimento di Scienze della Terra, Firenze, 351 pp.

Gillot, P.Y., Keller, J., 1993. Radiochronological dating of Stromboli. Acta Vulcanol. 3, 69-77.

Gouy, G. 1910. Sur la constitution de la charge électrique à la surface d'un électrolyte. J. Phys. Theor. Appl., 9, 455-468.

Hornig-Kjarsgaard, I., J. Keller, U. Koberski, E. Stadlbauer, L. Francalanci, and R. Lenhart, Geology, stratigraphy and volcanological evolution of the island of Stromboli, Aeolian arc, Italy., Acta Vulcanologica, 3, 21-68, 1993.

Jackson, D.B., Kauahikaua, J., 1987. Regional SP anomalies at Kilauea. Volcanism in Hawaii. USGS Prof. paper 1350, chap. 40, pp. 947–959.

Keller, J., Hornig-Kjarsgaard, I., Koberski, U., Stadlbauer, E., Lenhart, R., 1993. Geological map of the island of Stromboli. Acta Vulcanol., 3.

Krivochieva S., and M. Chouteau, 2003. Integrating TDEM and MT methods for characterization and delineation of the Santa Catarina aquifer (Chalco Sub-Basin, Mexico), Journal of Applied Geophysics, 52, 1, 23-43.

Kuwano O, Nakatani M, Yoshida S 2007. Reply to comment by A. Revil on "Effect of the flow state on streaming current" , Geophys. Res. Lett., 34(9) L09312.

Lénat, J.F., 1987. Structure et dynamique interne d'un volcan basaltique intraplaque océanique: Le Piton de la Fournaise (l'île de la Réunion). Thèse de doctorat ès sciences. Université Blaise Pascal, Clermont-Ferrand.

Leroy, P., Revil, A., 2004. A triple-layer model of the surface electrochemical properties of clay minerals. J. Colloid Interface Sci. 270 (2), 371–380.

Linde, N., D. Jougnot, A. Revil, S.K. Matthaï, T. Arora, D. Renard, and C. Doussan, Streaming current generation in two-phase flow conditions, Geophysical Research Letters, 34(3), L03306, doi: 10.1029/2006GL028878, 2007.

Lorenz V., and S. Kurszlaukis 2007. Root zone processes in the phreatomagmatic pipe emplacement model and consequences for the evolution of maar–diatreme volcanoes, Journal of Volcanology and Geothermal Research, 159(1-3), 4-32.

Lorne, B., Perrier, F., Avouac, J.P., 1999[a]. Streaming potential measurements, 1, Properties of the electrical double layer from crushed rock samples. J. Geophys. Res., 104, 17,857-17,877.

Morgan, F. D., Williams, E. R., and T. R. Madden, 1989, Streaming potential of westerly granite with applications, J. Geophys. Res., 94, 12,449-12461.

Nourbehecht, B., 1963. Irreversible thermodynamic effects in inhomogeneous media and their applications in certain geoelectric problems, PhD thesis, Mass. Inst. of Technol., Cambridge, Mass.

Pasquarè, G., Francalanci, L., Garduno, V.H., Tibaldi, A., 1993. Structure and geologic evolution of the Stromboli volcano, Aeolian Islands, Italy. Acta Vulcanol., 3, 79-89.

Petrinovic I.A., and F. C. Piñol 2006. Phreatomagmatic and phreatic eruptions in locally extensive settings of Southern Central Andes: The Tocomar Volcanic Centre (24°10′S–66°34′W), Argentina, Journal of Volcanology and Geothermal Research, 158, 1-2, 37-50.

Reppert PM, Morgan FD. 2003. Temperature-dependent streaming potentials: 1. Theory, Journal of Geophysical Research, 108(B11), 2546.

Revil A., Comment on "Effect of the flow state on streaming current" by Osamu Kuwano, Masao Nakatani, and Shingo Yoshida, Geophys. Res. Lett., 34, 9, L09311.

Revil A., N. Linde, A. Cerepi, D. Jougnot, S. Matthäi, and S. Finsterle, Electrokinetic coupling in unsaturated porous media, Journal of Colloid and Interface Science, 313(1), 315-327, 10.1016/j.jcis.2007.03.037, 2007.

Revil, A., and N. Linde, Chemico-electromechanical coupling in microporous media, Journal of Colloid and Interface Science, 302, 682-694, 2006.

Revil A., Finizola A., Sortino F., Ripepe M., 2004. Geophysical investigations at Stromboli volcano, Italy. Implications for ground water flow and paroxysmal activity. Geophysical Journal International, 157, 426-440.

Revil, A., 2002. The hydroelectric problem of porous rocks: thermodynamic approach and introductionof a percolation threshold. Journal of Geophysical research, 151, 944-949.

Revil, A., D. Hermitte, E. Spangenberg, and J. J. Cochémé, Electrical properties of zeolitized volcaniclastic materials, Journal of Geophysical Research, 107(B8), 2168, 10.1029/2001JB000599, 2002.

Revil, A., Leroy, P., 2001. Hydroelectric coupling in a clayey material. Geophys. Res. Lett. 28 (8), 1643–1646.

Revil A., 1999, Ionic diffusivity, electrical conductivity, membrane and thermoelectric potentials in colloids and granular porous media: a unified model, Journal of Colloid and Interface Science, 212, 503-522.

Revil, A., and Glover, P.W.J. 1998, Nature of surface electrical conductivity in natural sands, sandstones, and clays, Geophysical Research Letters, 25(5), 691-694.

Rosi, M., 1980. The Island of Stromboli. Rend. Soc. It. Miner. Petrol. 36, 345-368.

Segre, A.G., 1968. Notizie sulla morfologia submarina di Stromboli, Stromboli 11, 45-49.

Sill, W. R., 1983. Self-potential modeling from primary flows, Geophysics, J8, 76-86.

Weinstein Y. 2007. A transition from strombolian to phreatomagmatic activity induced by a lava flow damming water in a valley, Journal of Volcanology and Geothermal Research, 159, 1-3, 267-284.

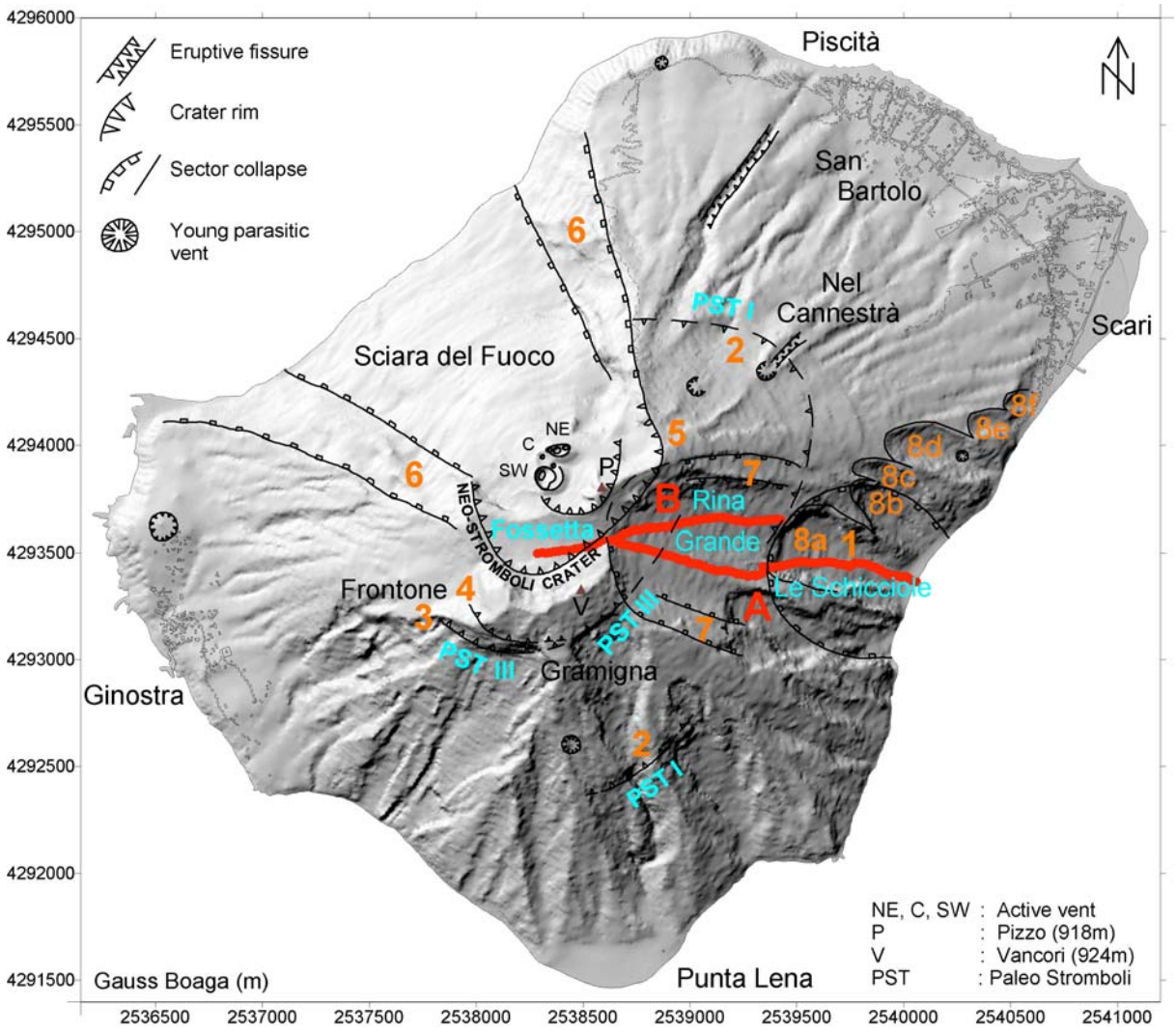

Figure 1. Map of Stromboli volcano with the both profiles. The Fossetta-Rina Grande Schicciole profile (Profile A) and the Fossetta Rina grande (Profile B).

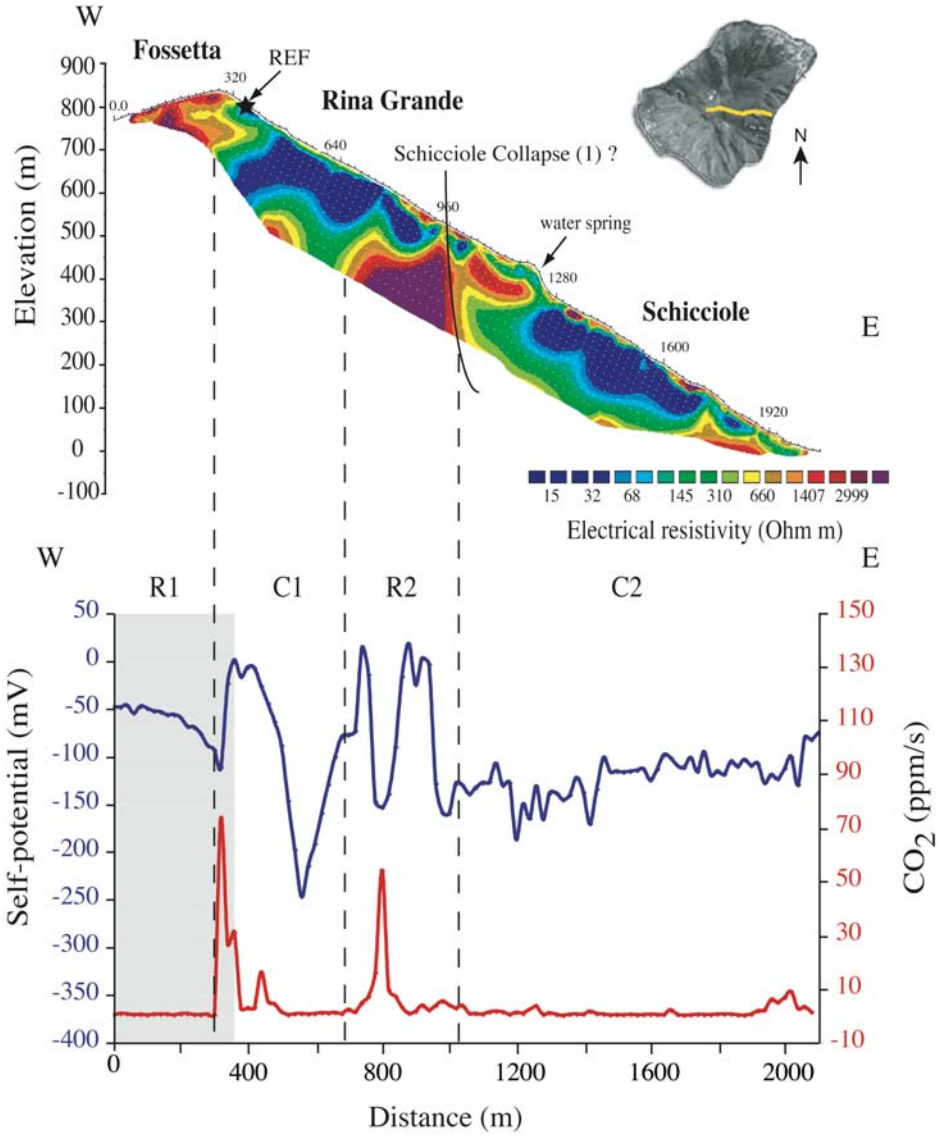

Figure 2. Self-potential, CO_2 measurements made along the electrical resistivity profile between the Fossetta, Rina Grande and the Schicciole areas. The grey area at the bottom of the figure indicates the common part of the profiles between Profiles A and B. The black star corresponds to the reference of the SP profile.

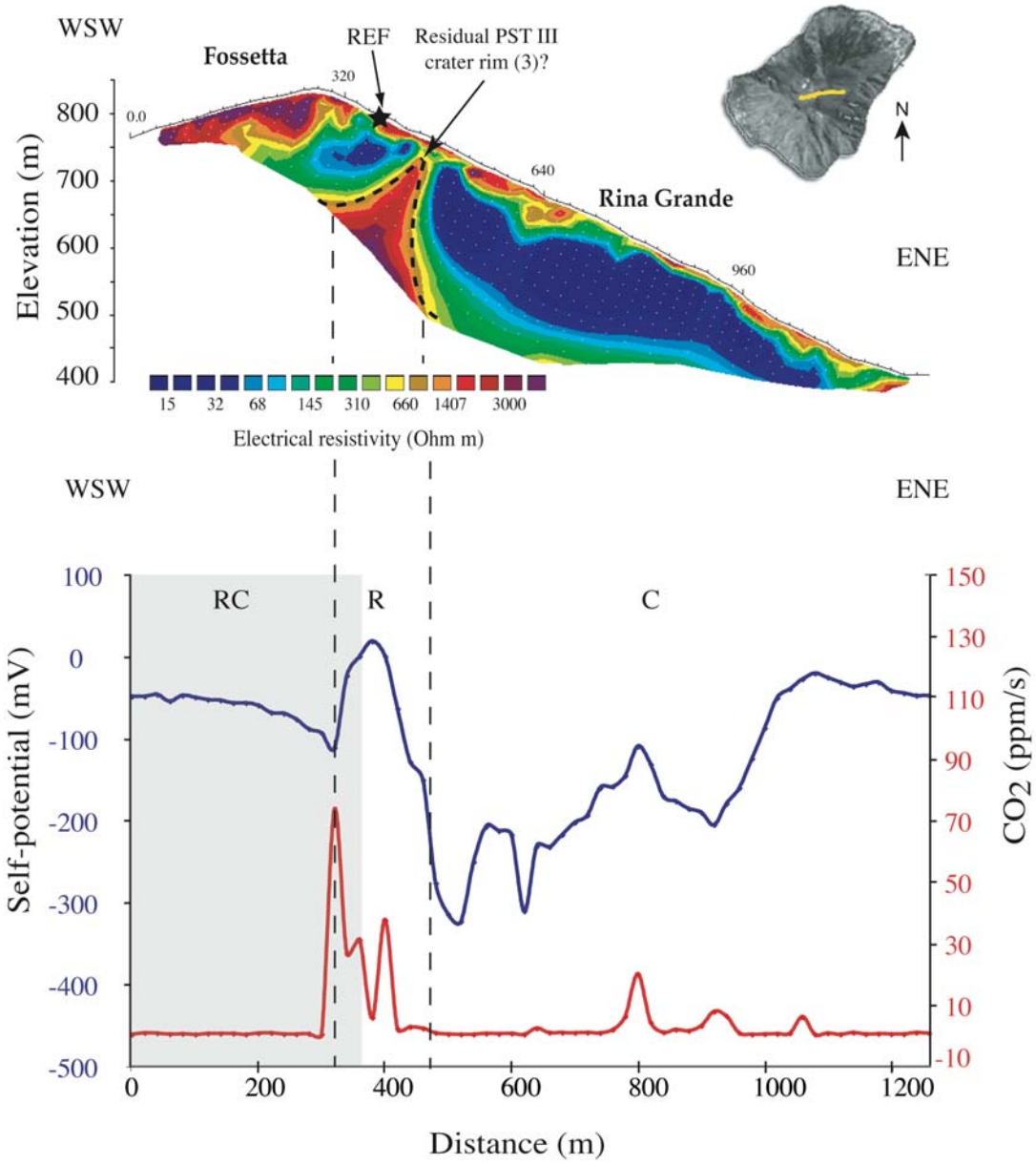

Figure 3. Self-potential, CO_2 measurements made along the electrical resistivity profile through the Fossetta and Rina Grande areas. The grey part represents the common part between profile A and B.

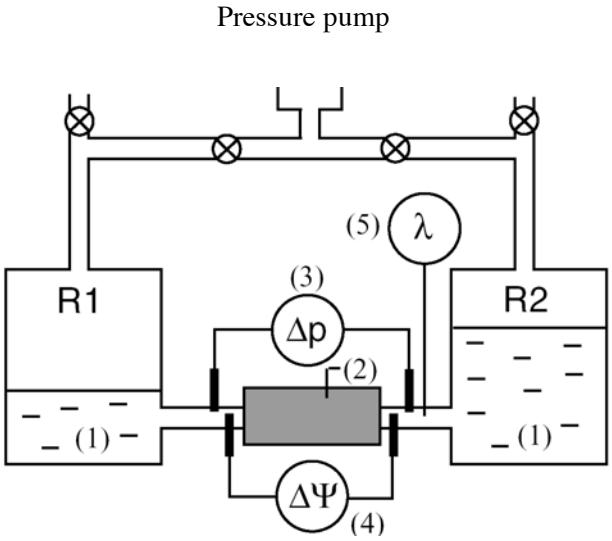

Figure 4. Experimental setup (ZetaCad) used to measure the streaming potential coupling coefficient. The sketch shows the pore fluid reservoirs R1 and R2 (1), sample tube (2), pressure sensors (3), voltage electrode connected to an impedance meter (4), and measurements of the electrical conductivity of the electrolyte (5). The pressure level in the reservoir is controlled by adjusting the pressure with N_2 gas.

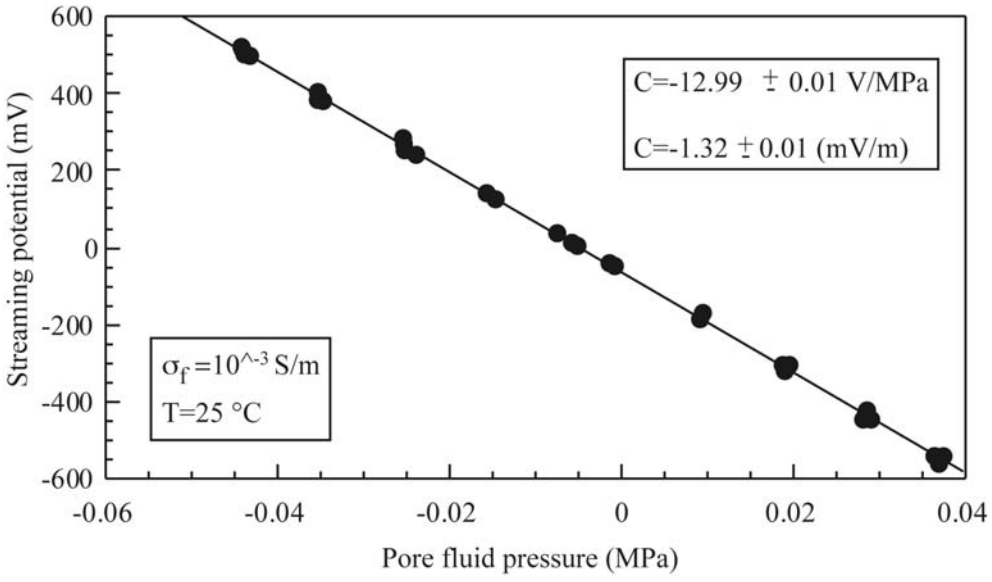

Figure 5. Laboratory measurements of the electrokinetic coupling coefficient. The streaming potential coupling coefficient is given as a slope of the recorded electric potential versus the fluid pressure differentials imposed between the two end-faces of a core sample.

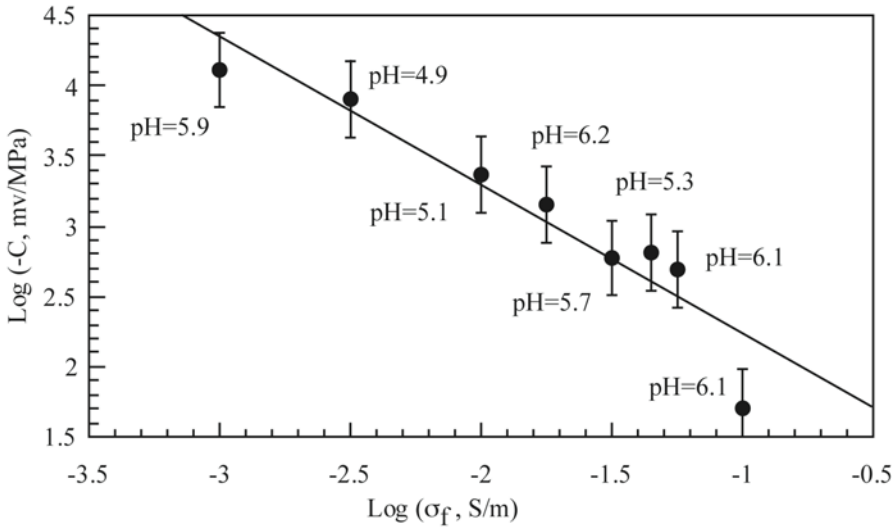

Figure 6. Intrinsic value of the streaming potential coupling coefficient *C* versus the value of the fluid conductivity σ_f. The pH values indicated on the figure represent the pH of solution in thermodynamic equilibrium with the core sample and the atmosphere.

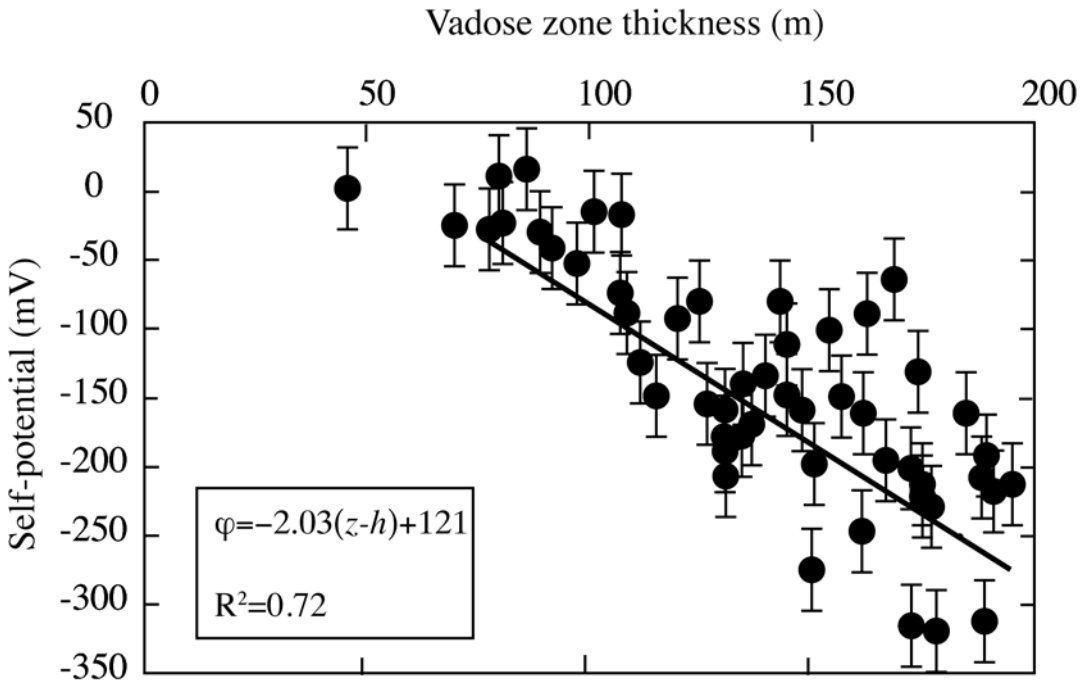

Figure 7. Correlation between self-potential data and the depth of the aquifer.

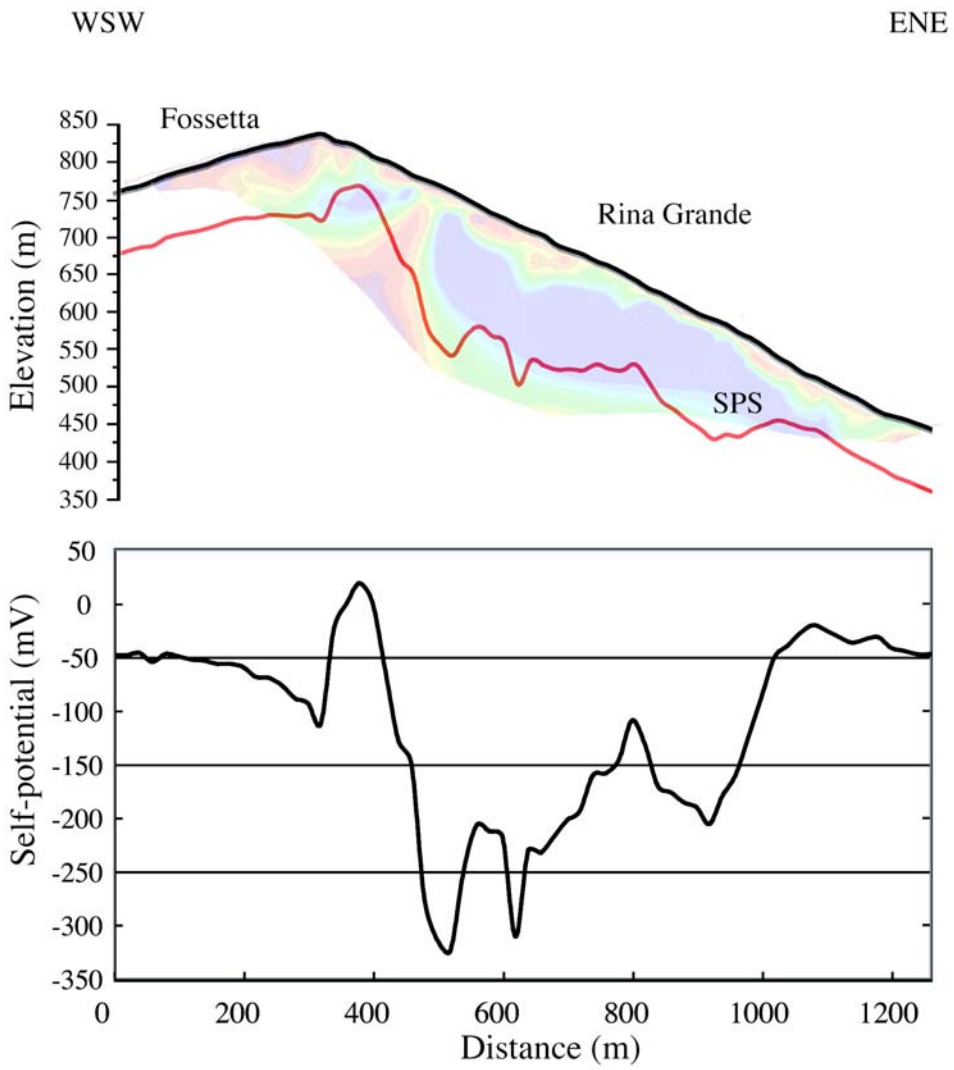

Figure 8. Topographic and SPS (red line) profiles superimposed on the resistivity profile B and SP profile (lower part).

4.6. Etude de la Structure Interne de Vulcano

Comme sur le Stromboli, des mesures géophysiques géochimiques ont été effectuées sur Vulcano afin de comprendre la structure interne de l'édifice. Ces travaux ont été motivés par le risque que représente l'activité du volcan: les coulées pyroclastiques, les retombées de bombes, les explosions phréatiques lors de ces périodes d'activité. De plus l'altération prononcée de ses flancs peut conduire à des glissements de terrain et à des tsunamis si ceux-ci se produisent sur le bord de mer de l'édifice de la Fossa par exemple.

La taille relativement restreinte de l'édifice et son système hydrothermal très actif en font un "laboratoire" intéressant pour étudier les possibilités des méthodes géophysiques dans la représentation de la structure interne des volcans ou dans la surveillance des changements d'activité. Neuf profils de résistivité électrique, de potentiel spontané, de température, et de flux de CO2 ont été réalisés. Le nombre de profils effectués nous a permis d'obtenir une représentation haute résolution de la structure du volcan. La Figure 4.9 nous montre la position de ces profils. Les méthodes de mesures et l'espace entre électrodes restent les mêmes que ceux utilisés sur le Stromboli.

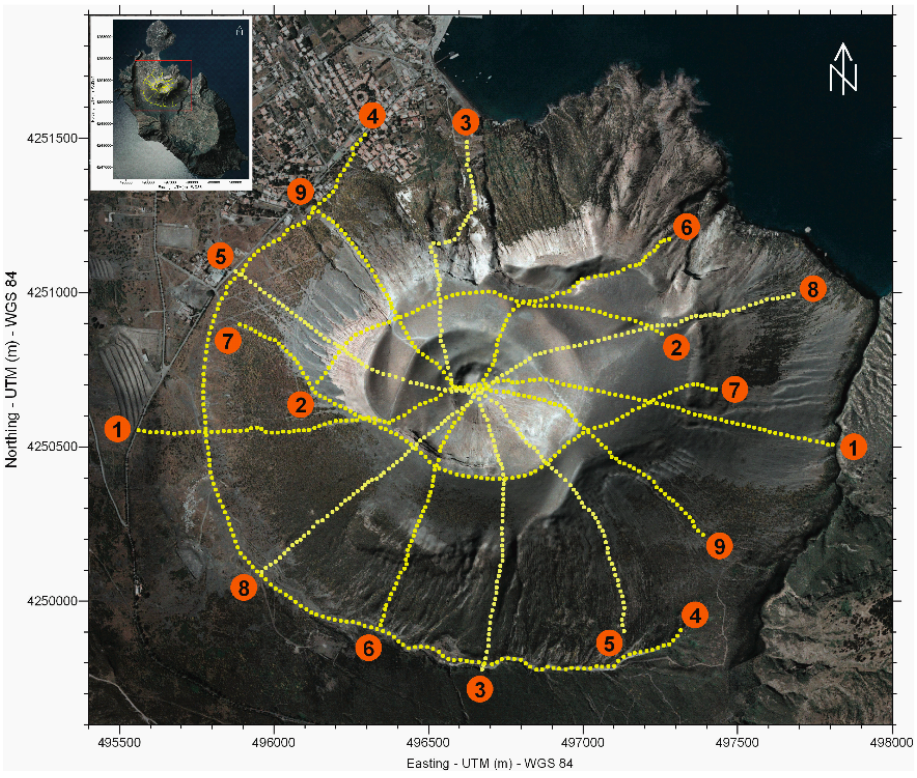

Figure 4.9 : Position des neuf profils traversant le cratère appelé la Fossa.

Les données recueillies lors des trois missions de terrain auxquelles j'ai participé ont fait l'objet de la publication d'un article scientifique intitulé " The inner structure of La Fossa di Vulcano (Vulcano Island, southern Tyrrhenian Sea, Italy) revealed by high resolution electric resistivity tomography coupled with self-potential, temperature, and CO_2 diffuse degassing measurements" publié dans Journal of Geophysical Research par Revil et al. (2008).

The inner structure of La Fossa di Vulcano (Vulcano Island, southern Tyrrhenian Sea, Italy) revealed by high resolution electric resistivity tomography coupled with self-potential, temperature, and CO_2 diffuse degassing measurements

Revil A. [1, 2, 3], Finizola A. [4, 5], Piscitelli S. [6], Rizzo E. [6], Ricci T. [7], Crespy A. [2], Angeletti B. [2], Balasco M. [6], Barde Cabusson S. [8], Bennati L. [8,9], Bolève A. [3, 10], Byrdina S. [11, 8], Carzaniga N. [12], Di Gangi F. [4], Morin J. [13, 5], Perrone A. [6], Rossi M. [11], Roulleau E. [14], and Suski B. [15]

[1] Colorado School of Mines, Dept. of Geophysics, Golden, CO, USA
[2] CNRS, Université Aix Marseille III, Aix en Provence, France
[3] CNRS-LGIT (UMR 5559), University of Savoie, Equipe Volcan, Chambéry, France
[4] Istituto Nazionale di Geofisica e Vulcanologia, Sezione di Palermo, Palermo, Italy
[5] Laboratoire GéoSciences Réunion, UR, IPGP, UMR 7154, La Réunion, France
[6] IMAA-CNR, Laboratory of Geophysics Tito Scalo (PZ), Italy
[7] Università Roma Tre and INGV- Sezione Roma 1, Roma, Italy
[8] LMV, Université Blaise Pascal, Clermont-Ferrand, France
[9] Dept. of Earth & Atmospheric Sciences, Purdue University, West Lafayette, USA
[10] Sobesol, Savoie Technolac, BP 230, F-73375 Le Bourget du Lac Cedex, France
[11] IPGP- Jussieu, CNRS, Paris, France
[12] Università Milano-Bicocca, Milan, Italy
[13] Université Paris 1, Panthéon-Sorbonne, Paris, France
[14] GEOTOP-UQAM-McGill, Montréal, Canada
[15] Université de Lausanne (UNIL), Institut de Géophysique, Lausanne, Switzerland

Corresponding author: André Revil (arevil@mines.edu)

Keywords: Electrical resistivity, self-potential, soil CO_2 degassing, hydrothermal system

Abstract. La Fossa cone is an active stratovolcano located on Vulcano Island, in the Aeolian Archipelago (southern Italy). Its activity is characterized by explosive phreatic and phreato-magmatic eruptions producing wet and dry pyroclastic surges, pumice fall deposits, and highly viscous lava flows. Nine 2D electrical resistivity tomograms (ERT) (electrode spacing 20 meters, with a depth of investigation > 200 meters) were obtained to image the edifice. In addition, we also measured the self-potential, the CO_2 flux from the soil, and the temperature along these profiles at the same locations. These data provide complementary information to interpret the ERT profiles. The ERT profiles allow to identify the main structural boundaries (and their associated fluid circulations) defining the shallow architecture of the Fossa cone. The hydrothermal system is identified by very low values of the electrical resistivity (< 20 Ω m). Its lateral extension is clearly limited by the crater boundaries, which are relatively resistive (> 400 Ω m). Inside the crater, it is possible to follow the plumbing system of the main fumarolic areas. On the flank of the edifice, a thick layer of tuff is also marked by very low resistivity values (in the range 1 to 20 Ω m) because of its composition in clays and zeolites. The ashes and pyroclastic materials ejected during the nineteenth century eruptions and partially covering the flank of the volcano corresponds to relatively resistive materials (several hundreds to several thousands Ω m). We carried out laboratory measurements of the electrical resistivity and the streaming potential coupling coefficient of the main materials forming the volcanic edifice. A 2D simulation of the ground water flow is performed over the edifice using a commercial finite element code. Input parameters are the topography, the ERT cross-section, and the value of the measured streaming current coupling coefficient. From this simulation, we computed the self-potential field and we found good agreement with the measured self-potential data by adjusting the boundary conditions for the flux of water. Inverse modeling shows that self-potential data can be used to determine the pattern of ground water flow and potentially to assess water budget at the scale of the volcanic edifice.

1. Introduction

Vulcano is a small volcanic island (3 x 7 km) located at the southernmost of the Aeolian Islands in the Southern Tyrrhenian Sea in Italy (38°24'N, 14°58'E). This island was shaped during five main volcanic stages during the past 120,000 years. The two overlapping calderas of the island, the 2.5-km-wide Caldera del Piano on the south east and the 3-km-wide Caldera della Fossa on the north west of the island (Figures 1), were formed at about 98,000-77,000 and 24,000-13,000 years ago, respectively. Volcanism has migrated to the north of the island over time. La Fossa cone, which is the target of the present investigation, occupies the 3-km-wide Caldera della Fossa at the north-west end of the island. This edifice has been active throughout the Holocene and constitutes the location of most of the historical eruptions of Vulcano island. In the vicinity of the Fossa cone, the Vulcanello edifice forms a low, roughly circular peninsula, on the northern tip of Vulcano (Figure 1). This area was formed as an island beginning in 183 BC and was connected to the Vulcano island in 1550 AD during its last eruption. The latest eruption from Vulcano consisted of explosive activity from the Fossa cone from 1888 to 1890 (e.g., *Frazzetta et al.* [1983, 1984]).

There are two main reasons why we choose to investigate La Fossa cone. The first reason is related to the geohazards associated with the activity of the active La Fossa cone. The population of the island increases to nearly 5,000 inhabitants during the summer from a few hundreds during the winter. The main geohazards at Vulcano are related to sin-eruptive pyroclastic surges, bombs and block fallout, phreatic explosions, gas hazard, debris flows, and landslides of altered flanks and the subsequent formation of tsunamis. The second reason is related to the relatively modest dimensions of this edifice and its strong hydrothermal activity. The Fossa cone is therefore a perfect natural laboratory to test the ability of geophysical methods to image the substructure of an active volcano. In addition, we are interested to see how geophysical signals can be used to monitor changes in its activity.

The use of deep DC electrical resistivity tomography has recently gained in interest to

map the substructure of volcanoes and active faults (e.g., *Storz et al.* [2000]; *Colella et al.* [2004]; *Diaferia et al.* [2006]; *Finizola et al.* [2006]; *Linde and Revil* [2007]). However, electrical resistivity tomography alone is notoriously difficult to interpret unequivocally. The main reason is that electrical resistivity of volcanic rocks depends on too much parameters including the water content, salinity, temperature, and cation exchange capacity of the porous material (e.g., *Waxman and Smits* [1968]; *Revil et al*. [2002], and references therein). Therefore, it is essential to add additional information to electrical resistivity tomograms to improve their interpretation in terms of geological and hydrogeological units (see *Revil et al.* [2004b], *Finizola et al*. [2006], *Coppo et al.* [2008]).

Self-potential signals correspond to the passive measurement of the distribution of the electrical potential at the ground surface of the Earth. Once filtered, these signals evidenced polarization mechanisms at depth. One of them is related to ground water flow and is know as the streaming potential. *Gex* [1992] and *Di Fiore et al*. [2004] have performed self-potential measurements at the island of Vulcano. However, while these works were very useful, only specific parts of the volcano were covered by these investigations and self-potential signals were not interpreted quantitatively in terms of ground water flow pattern.

In this paper, we interpret a set of new high-resolution electrical resistivity tomograms crossing the Fossa cone of Vulcano Island. By high resolution, we mean that the spacing between the electrodes is only of 20 meters. This allows a resolution that is much higher than electromagnetic methods (e.g., TDEM) and classical large scale resistivity surveys without the use of a long cable (> 1 km). To help the interpretation of these tomograms, additional measurements of temperature, self-potential, and CO_2 flux from the soil were carried out along the resistivity profiles at the same locations than the electrodes used for the resistivity surveys. The temperature and CO_2 flux reveal the position of the permeable flow pathways of the hydrothermal system. We show that forward and inverse modeling of the self-potential data allow constraining the pattern of ground water flow. All these measurements result in a

unique data set, at a kilometer scale, over an active volcano. This data set reveals for the first time the inner substructure of La Fossa cone stratovolcano, showing the main geological structure and the extent of the hydrothermal system inside the edifice.

2. Geological Background

Vulcano Island represents the southernmost portion of a NW-SE elongated volcanic ridge that comprises seven islands forming the Aeolian Archipelago (southern Italy). This archipelago is related to the subduction of the African plate underneath the European Plate [*Keller*, 1980; *Ellam et al.*, 1989]. The ridge is affected by a regional, NW-SE to N-S striking fault system [*Gasparini et al.*, 1982]. In ancient times, the Romans believed that Vulcano was the chimney to the forge of the god Vulcan. The glow of eruptions was thought to be from his forges and the island had grown because of his periodic clearing of cinders and ashes. The earthquakes that either preceded or accompanied the explosions of ashes were considered to be due to Vulcan himself making weapons for the other gods.

Nowadays, we know that the island has been shaped during five distinct stages. These stages are Vulcano Primordiale, Piano Caldera, Lentia Complex, La Fossa Caldera, and Vulcanello. The history of Vulcano begins with the formation of a stratovolcano. The collapse of this stratovolcano produces the Piano caldera (see CP in Figure 1, *Santacroce et al.* [2003]). Then, this caldera was partially filled with pyroclastic deposits and lava flows. The stratovolcano and its caldera form the southern part of the island of Vulcano. The Fossa cone grew within the Fossa caldera, which constitutes the northern part of the island (Figure 1).

The Fossa cone is a small stratovolcano with an altitude of 391 m a.s.l. (meters above sea level, see Figures 2 and 3). The diameter of its base is about 2 kilometers. The Fossa cone began to form 6,000 years ago [*Dellino and La Volpe*, 1997; *De Rosa et al.*, 2004]. Six volcanic successions: Punte Nere, Palizzi, Caruggi, Forgia Vecchia, Pietre Cotte and Gran Cratere (post-1739), with different vent locations and eruptive histories, shaped the edifice

[*Dellino and La Volpe*, 1997; *De Rosa et al.*, 2004, *De Astis et al.*, 2007]. Each succession follows the same evolution starting with pyroclastic surges and ending with the emission of highly viscous lava flows. All the explosive and effusive products of La Fossa cone have high potassium contents and a chemical composition ranging from trachytic to the more evolved rhyolitic composition [*Keller*, 1980].

The last eruption of the Fossa cone occurred from 1888 to 1890. In the same century, Vulcano produced three eruptions lasting more than one month (1822-23, 1873, and 1886). The violence of the last eruption (1888-1890) was marked by the fall of volcanic bombs and blocks, about ~1 m in diameter, at ~1 km from the vent. Breadcrust bombs, distinctive of this style of eruption, were ejected about 500 m. These bombs are characterized by an aphyric glassy matrix of rhyolitic composition and xenoliths of trachytic composition [*De Fino et al.*, 1991]. Explosions were intermittent and separated by quiet periods lasting a few minutes to a few days. Explosions varied in strength. Only the largest explosions, separated by longer quiet periods, could throw blocks and bombs. No domes or lava flows were produced at the end of this eruption.

Nowadays, the peculiarity of La Fossa volcano is the occurrence of thermal and seismic crisis. The last one occurred in 2004-2006 (*Granieri et al.* [2006]; *Aubert et al.* [2007]) and was characterized by strong increases of the temperature of the fumaroles and an increase of the surface area covered by the fumarolic field (see below). Chemical changes in the fumaroles and the occurrence of shallow seismic activity were indicative of an increase of the input of magmatic fluids (*Granieri et al.* [2006]). However, during such episodes, there was no evidence of magmatic rising.

There are three types of upper formations of the Fossa cone: (1) The former is constituted of the Palizzi pumice deposit, mainly scattered along the southern slope of La Fossa Cone and with a maximum thickness of 2 m at the break in slope of the volcano [*Frazzetta et al.*, 1983]. The pumice fragments range in size from several centimeters to about

30 cm, with a mean value of about 10 cm. The glass matrix of the fragments has a trachytic composition. (2) The latter constituting the substratum is formed by a very impermeable fine-grained hydromagmatic tuff (Figure 2) and (3) the grey ashes from Gran Cratere that were deposited all over the edifice during the 1888-1890 eruption.

3. Field Investigations

In October 2005, May 2006, and October 2006, we performed three geophysical surveys (electrical resistivity, self-potential, temperature, and soil CO_2 flux) that were organized along nine profiles crossing the entire Fossa cone. The position of these profiles is shown on Figure 2. Note that because we know nothing about the temporal variation of these, we did not tried to provide a 3D reconstruction of these data in the present work. We present in this section the methodology employed for the various measurements

3.1. Electrical Resistivity Profiles

Because of their sensitivity to porosity, water saturation, and the presence of clays and zeolites minerals, DC-electrical resistivity and electromagnetic methods (e.g., time-domain electromagnetics) are efficient tools to image active volcanoes (*Fitterman et al.* [1988]; *Zohdy and Bisdorf* [1990], *Lénat et al.* [2000]). DC-Electrical resistivity measurements were obtained along the nine profiles displayed in Figure 2. The measurements were performed using a set of 64 brass electrodes with a spacing of 20 meters. We use a shielded cable of 1.26 km made of 8 segments of 160 m each. Two or three roll-alongs of the electrodes were performed to complete each profile. Contact between the electrodes and the ground was improved by adding salty water at the base of each electrode to decrease the contact resistance between the ground and the electrodes. We used the Wenner array for its good signal-to-noise ratio. Reciprocity measurements (performed on one profile) show an uncertainty smaller than 7%. Dipole-dipole measurements provide complementary information with respect to the

Wenner array. However, we did not perform such measurements because of time constraints.

The resistivity data were inverted with RES2DINV [*Loke and Barker,* 1996], which uses the smoothness-constrained method [*Constable et al.,* 1987] to perform the inverse problem:

$$(\mathbf{J}^T\mathbf{J} + \alpha\mathbf{F})\mathbf{d} = \mathbf{J}^T\mathbf{g} - \alpha\mathbf{F}\mathbf{r}\,, \tag{1}$$

where **F** is a smoothing matrix, **J** is the Jacobian matrix of partial derivatives, **r** is a vector containing the logarithm of the model resistivity values, α is the damping factor, **d** is the model perturbation vector, and **g** is the discrepancy vector. The discrepancy vector, **g**, contains the difference between the calculated and measured apparent resistivity values. The magnitude of this vector is given by a RMS (root-mean-squared) value. The algorithm seeks to reduce this quantity in an attempt to find a better model after each iteration. The model perturbation vector, **d**, is the change in the model resistivity values calculated using the above equation which normally results in an "improved" model. The uniqueness of the solution of the inverse problem is an issue here (see, for example, discussions in *Linde and Revil* [2006]). This means that for the same data set, there are several possible resistivity models that fit the data equally well (e.g., *Auken and Christiansen* [2004]; *Binley and Kemna* [2005]). Additional information can be helpful to stabilize the inversion process. Starting from an initial model, RES2DINV looks for an improved model with calculated apparent resistivity values closer to the measured values. We used various initial models to test the stability of the inversion process. Starting the iterations with either a uniform resistivity model or the apparent resistivity pseudosection did not alter the final result.

Topography was also included in the inversion process. Topography was extracted from a very precise digital elevation map (DEM of 1x1m) of La Fossa cone provided by Maria Marsella (see also *Baldi et al.* [2002]). Northing and easting UTM coordinates were obtained from a portable GPS receiver. Four electrical resistivity tomograms are displayed in

Figures 4 to 7. Accounting for the complex geometry of the volcano, a 3D inversion of ERT would be necessary to define the complex structural heterogeneities of the Fossa edifice. However, we show below that 2D inversion of ERT provides an image that is consistent with the other data (self-potential, temperature, and CO_2 flux) in order to define the architecture of the volcano.

3.2. Temperature

Thermal probes and a digital thermometer were used to measure the temperature of the ground. Each temperature measurement was done in four steps. (1) We hammered a steel rod (2 cm in diameter) into the ground to a depth of 30 ± 2 cm. (2) Then a thermal probe was inserted into the hole at the precise depth of 30 ± 1 cm by means of a graduated wooden stick. (3) The hole around the stick was filled and compacted. (4) After 10 to 15 minutes (this duration is required to achieve thermal equilibrium), a temperature reading is performed (see *Finizola et al.* [2002, 2003]). The duration to reach thermal equilibrium was checked by looking at the time variation of the temperature. We observed that the temperature stabilized in less than 10 minutes.

The temperature profile provides an independent way to see the extension of the hydrothermal body in the vicinity of the ground surface. The temperature was measured with a sensitivity of 0.2 °C. Due to the maximum amplitude of diurnal variation at Vulcano at 30 cm depth during the summer season (1.2°C), and due to the maximum amplitude of seasonal variation, from 12.2 to 27.2°C respectively in January and August (*Lo Cascio and Navarra* [1997]), a temperature above 30°C can be considered as indicative of the underground geothermal system. A map of the interpolated temperature is shown on Figure 8.

It is important to note that our CO_2 flux, self-potential, and temperature measurements were obtained at different periods during the last 2004-2006 crisis, which began in November 2004 (*Granieri et al.*, [2006]). However, the amplitude the anomalies are not of primary

importance because we will only use temperature anomalies as a way to detect qualitatively preferential fluid flow pathways in the hydrothermal system.

3.3. CO_2 Diffuse Degassing

The CO_2 diffuse degassing measurements were obtained with a spacing of 20 m (uncertainty < 5%). The methodology is described in details in *Chiodini et al*. [1996, 1998]. The accumulation chamber method allows to measure quickly the CO_2 fluxes from the soil in a wide interval from 0.2 to several hundreds g m^{-2} day^{-1}. This method does not require corrections or assumptions on the characteristics of the soil. The instrumentation consists in an IR spectrometer, to measure CO_2 fluxes from 0 to 2000 μmol/mol (2 % vol.), an accumulation chamber (type A: dead volume 30 cm^3), and a PDA to plot the CO_2 increase. The accumulation chamber is stood on the ground so that the atmospheric air can not penetrate inside. The gas permeating from the soil accumulates in the dead volume, thus the CO_2 concentration increases; every second the gas is analyzed by the IR spectrometer and reinjected in the accumulation chamber so as not to deplete the CO_2 concentration. The PDA software displays a curve representing the variation of the concentration of CO_2 versus time. This rate is directly proportional to the flux of CO_2 from the soil, expressed in g m^{-2} day^{-1} (the constant of proportionality depends on the instrument dead volume and on the atmospheric pressure).

Carbon dioxide anomalies have their origin in magma degassing inside the volcanic system. The gas follows the same preferential pathways as the hydrothermal fluids, providing information about the permeability distribution of the edifice, high fluxes suggest permeable pathways from the hydrothermal system to the ground surface due to the presence of fractures.

A recent study (*Granieri et al*. [2006]) shown that in quiet periods La Fossa crater area releases diffusively about 200 ton day-1 of CO_2 from a surface of 0.5 km^2 while during crises

the CO_2 output may increase of one order of magnitude. These data suggest that a significant volume of degassing magma exists at depth and that during crises the increasing of CO_2 diffuse degassing is due to the opening of new fractures at shallow level and the consequent increasing of the permeability of the soil. This could be due to the shallow seismicity or to a generalised increase of the pore pressure in the volcanic system.

3.4. Self-potential

The self-potential (SP) method measures the distribution of the electric potential at the surface of the Earth (and or in boreholes) with respect to a reference electrode (e.g., *Corwin and Hoover* [1979]; *Lénat* [2007]). Sources of self-potential fields include large-scale Earth currents due to ionospheric activity, chemical potential gradients (*Maineult et al*. [2005, 2006]), redox potentials (*Linde and Revil* [2006]), and electrokinetic conversion associated with fluid movement through porous materials (the so-called streaming potential). In active volcanoes, the main source of self-potential anomalies is related to the flow of the ground water (*Massenet and Pham* [1985], *Ishido et al.* [1997]; *Bedrosian et al.* [2007]). Self-potential is the only method that is directly sensitive to the pattern of ground water flow and to changes in the seepage velocity (see *Perrier et al*. [1998], *Kulessa et al*. [2003a, b], *Rizzo et al*. [2004], *Suski et al*. [2004], *Hase et al*. [2005]; *Titov et al*. [2005], *Jardani et al*. [2006b, 2007], *Suski et al*. [2006], *Wishart et al*. [2006]).

To perform the self-potential measurements, we used a pair of non-polarizing $Cu/CuSO_4$ electrodes. The microporous nature of the end-contacts of these electrodes (made of a low-permeability wood) avoids leakage of the $CuSO_4$ solution during contact between with the ground. Wood is also much more durable than the ceramics that is more commonly used to make commercial electrodes. The difference of electrical potential between the reference electrode (arbitrarily placed at the beginning of the profile) and the moving electrode was measured with a calibrated high impedance voltmeter (METRIX MX20,

sensitivity of 0.1 mV, input impedance of ~100 MΩ). When interpreting self-potential data, we have to consider that the value of the self-potential itself is meaningless. Only the gradient of the self-potential data (that is the electrical field) has a physical meaning.

Before and after each series of measurements, the reference electrode and the roving electrode were put face-to-face to check that the difference of potential between the two electrodes was less than 2 mV (if this is not the case, the static value is removed to all the measurements). At each station, a small hole (~10 cm deep) was dug to improve the electrical contact between the electrode and the ground. For each self-potential measurement, the value of the electrical resistance was also measured prior the self-potential measurement. Most of the time, the moisture in the soil was sufficiently high to insure low enough impedance contact between the scanning electrode and the ground. However, if the contact resistance was high (>1 MΩ), a small amount of a saturated $CuSO_4$ solution was placed at the bottom of the hole to decrease the contact resistance between the electrode and the ground. We did not observe the type of drift reported by *Corwin and Hoover* [1979] associated with watering the electrodes. The standard deviation on the measurements is determined by performing twenty measurements few meters around the same station. At Vulcano, it is on the order of 12 mV in average. This relatively large standard deviation is mainly due to the strong heterogeneity of the resistivity distribution near the surface of the ground. In the following, we will consider that the self-potential measurement is a random process described by a Guassian distribution (as shown by *Linde et al*. [2007]) with a standard deviation of 12 mV.

To perform the self-potential measurements, a long wire was used to connect the two electrodes to aMetrix MX20 voltmeter. The distance between two successive measurement stations was 20 m. The total length of the wire was 400 m, and consequently, 20 measurements were realized with the same reference. The advantage of this procedure was to avoid cumulative errors by changing the reference too often along the same profile. Every 400 m, a new reference station was established. As the profiles were several kilometers long,

several base stations were used to cover a profile. After the survey, the entire self-potential profile was reconstructed using the first reference station as the unique reference for the entire profile.

4. Laboratory Measurements

In this section, we report laboratory measurements of the electrical conductivity and streaming potential of a collection of 21 core samples from the edifices of La Fossa di Vulcano and Stromboli (a nearby volcano that is strongly active). Electrical conductivity measurements were performed on each sample in the frequency range from 20 Hz to 100 kHz, at room temperature (20 ± 2°C), using NaCl solutions with the following pore fluid conductivities σ_f = 0.1 S m^{-1} and 0.5 S m^{-1} (pH 7). The conductivity of the pore water sampled at the base of the volcano, in different wells, is in the range 0.1 to 2.8 S m^{-1} and the pH is in the range 5.4 to 7.9 with a mean equal to 6.7 (*Cortesi et al*. [2001]). We believe that a water conductivity of 0.1 S m^{-1} is representative of fresh (meteoric) waters while high conductivities are indicative of a mixture of fresh water and sea water and possibly hydrothermal fluids. The water flowing along the slopes is locally affected by fumarolic fields is also enriched with the fumarolic acid condensates coming from the pericrateric high-temperature fumaroles along the fluid flow pathways highlighted by the resistivity tomograms and temperature anomalies.

We use a Waynekerr-6425 impedancemeter for the resistivity measurement. The samples were placed between two stainless steel electrodes. Two circular pieces of brine-saturated filter paper were used to ensure good electrical contacts between the sample and the electrodes. The jacketed samples were first washed with demineralized water and dried at 60°C for 2 days. The jacket was made of a hydrophobic adhesive. The samples were held under vacuum prior to be saturated with a degassed brine at 0.1 S m^{-1} (see *Revil et al.* [2002] for a detailed version of the procedure). Following the initial measurements, the salinity of the

brine was then changed by placing the samples in a 0.5 S m^{-1} electrolyte and by letting the brine diffuses to the sample through the two end-faces for 1 week (see *Revil* [1995] for tests of the effectiveness of this procedure). The results are reported in Table 1.

Electrical conductivity is sensitive to the water content, the mineralization of the pore water (salinity), the cation exchange capacity of the clay minerals (surface conductivity), and temperature (see *Waxman and Smits* [1968], *Revil et al.* [1998, 2002], *Kalscheuer et al.* [2007]; *Niwas et al.* [2007]; *Jin et al*. [2007]; *Tabbagh and Cosenza* [2007]; *Shevnin et al*. [2007]). In this paper, we assume a simple linear conductivity model,

$$\sigma = \frac{1}{F}\left[\sigma_f + (F-1)\sigma_S\right], \tag{2}$$

which can be considered as a first-order approximation of the non-linear models proposed by *Revil et al.* [1998, 2002]. In Equation (2), F is the electrical formation factor (a powerlaw function of porosity widely known as Archie's law) and σ_S is the surface conductivity occurring mainly in the Stern layer at the water-mineral interface (*Revil and Glover* [1998]). Surface conductivity usually results from the cation exchange capacity of clay minerals and zeolites and is indicative of the alteration of the rock (see *Roberts and Lin* [1997]; *Revil et al.* [2002]; *Bernard et al.* [2007]). An electrochemical model of surface conductivity has been developed recently by *Leroy and Revil* [2004] that can be used to determine the effect of the composition of the pore fluid and mineralogy upon the surface conductivity of the material. Using Eq. (2) and the resistivity data reported in Table 1, we determined the value of the formation factor and surface conductivity and their uncertainties. These values are reported in Table 2. We note that the tuff of Vulcano is characterized by a very high surface conductivity, which explains the very low electrical resistivity observed by the resistivity surveys for this formation (see Figures 4 to 7).

We also performed measurements of the streaming potential coupling coefficient C at room temperature (20 ± 2°C) for 21 rock samples. The streaming potential coupling

coefficient is the key-material property required to compute the self-potential contribution associated with ground water flow (see Section 5 below) (e.g., *Tosha et al.* [2003]). The experimental setup for the measurement of the streaming potential coupling coefficient is shown Figure 9a. A given hydraulic head is imposed on the cylindrical sample placed at the bottom of the tube by adding water to the water column in the tube in such a way that the hydraulic head is maintained constant above the rock sample. The gradient of the fluid pressure is controlled by the hydraulic head in the tube (imposed by the head of a much more important reservoir in contact with it) and the length of the sample. The electrical potential resulting from the flow of the pore water is measured with two non-polarizable $Ag/AgCl_2$ electrodes (Ref321/XR300, Radiometer Analytical) located in the vicinity of the end-faces of the sample (Figure 9a). The difference of the electrical potential measured between the end-faces of the porous pack divided by the length of the sample is the streaming electrical field associated with the flow of the brine through the sample. The voltages are measured with a Metrix MX-20 voltmeter (internal impedance 100 MΩ, sensitivity 0.1 mV).

In the viscous-laminar flow regime (characterized by low Reynolds numbers, see *Bolève et al.* [2007a]), the difference of the electrical potential measured in the vicinity of the end-faces of the porous medium is proportional to the imposed hydraulic head H (Figures 10b and 10c) (this trend is non-linear in the inertial-laminar flow regime). The slope of the linear trend of streaming potential vs. head is the streaming potential coupling coefficient (e.g., *Revil et al.* [2004a], *Bolève et al.* [2007a, b]),

$$C = \left(\frac{\partial \varphi}{\partial H} \right)_{\mathbf{j}=0}. \tag{3}$$

The values of the streaming potential coupling coefficient for the different samples are reported in Table 1.

After completion of the electrical conductivity and streaming potential measurements, we determined the porosity and matrix density from classical triple weight measurements.

The samples were first washed with demineralized water for 1 week to let the salt diffusing out from the samples. Then the samples were dried at 60°C for 4 days and their weights measured. Finally, the samples were saturated with degassed water under vacuum and let stand for 2 additional days to allow complete saturation of the connected porosity. Weight measurements of the saturated samples were carried out after that time. The saturated samples were weighted in air and water (buoyancy weight). Values of the porosity are reported in Table 2. A correlation between the formation factors and the connected porosities (not shown here) indicates that the formation factor is related to the porosity by an Archie's law $F = \phi^{-m}$ with $m \approx 2.0 \pm 0.1$.

5. Interpretation and Discussion

5.1. Uncertainty Associated with the Resistivity Data

The analysis of the uncertainty associated with the interpretation of the self-potential data in terms of ground water flow will be discussed below in Section 5.5. We discuss below the uncertainty associated with the resistivity data, which show large RMS error (up to 25% at the fourth iteration). We performed a sensitivity analysis using Profile 1. We were especially interested by this profile to see if the resistive structure found at depth below the bottom part of the crater (see Figure 11a) was an artifact or not.

To perform the sensitivity analysis, we followed the following steps (1) We used a simple resistivity distribution for this profile (see Figure 10a); (2) We used the finite-element code RESMOD to simulate the acquisition of the data using the resistivity distribution and the known topography; (3) We contaminated these synthetic data with various levels of (white) noise; (4) we run RES2DINV on these profiles to invert the synthetic apparent resistivity data; and (5) we compare the inverted results with the input resistivity data. The results are the following (see Figure 10): (1) the resistive structure below the bottom of the crater is

probably not an artifact because it cannot be reproduced without the presence of a resistive body at this location, (2) the deep resistive body on the flanks of the volcanoes have a higher resistivity values than obtained from the resistivity tomograms (by using a trial and error approach, we obtained a resistivity value of 4000 ± 1000 Ω m), (3) the high RMS error is essentially due to the noise existing in the raw data because of the relatively low current injected in the ground. However, adding white noise to the data does not change the result of the inversion. It just change the RMS value. Consequently, the inverse modeling is very robust to the presence of such a noise.

5.2. The Flanks

Along the East-West direction (see Profile 1 for example), we observe a relatively simple architecture from the electrical resistivity tomogram. A resistive ash layer (100-1000 Ω m, 500 Ω m according to Figure 10) covers a conductive tuff layer (5 to 50 Ω m, see Figures 4 and 11). At depth, a highly and continuous resistive body is observed on both sides of the volcano (Figures 4 and 11). We interpret this body as corresponding to massive lava flow units with resistivity in the range 100 to 5000 Ω m (4000 Ω m according to Figure 10). No thermal anomalies are observed at the ground surface along the flanks. The self-potentials exhibit a classical W-shape (*Ishido* [2004]), which is traditionally interpreted as the effect of the upwelling of hydrothermal fluids in the central part of the edifice and the downward flow of meteoritic groundwater along the flanks of the edifice (*Michel and Zlotnicki* [1998], *Revil et al.* [2003]). This self-potential anomaly is quantitatively modeled in Section 5.5.

Profile 3 is nearly perpendicular to Profile 1 (see Figure 5). This profile shows a very complex pattern by comparison with Profile 1 and the existence of thermal anomalies. This complex pattern results from the evolution of the volcano over time (see Figure 5). It crosses in the northern part of the profile, temperature anomalies related to the crater boundaries of Forgia Vecchia. The first (and the most important) of the two Forgia Vecchia craters, Forgia

Vecchia I, was formed during the 6th century B.C. (*Giacomelli and Scandone* [2002]). The second crater, Forgia Vecchia II, was formed in 1727 A.D. (*Frazzetta and La Volpe* [1991]), just before the extrusion of the Pietre Cotte obsidian lava flow that occurred in 1739 A.D. (*De Fiore* [1922]).

5.3. The Hydrothermal System

Fumarolic activity indicates that the extension of the hydrothermal system is constrained by the boundary of the main crater, except for the area of Forgia Vecchia (see location Figure 1). The temperature map (Figure 8) shows that the main structural morphological crater boundaries, identified by previous geological mapping, serve as preferential fluid flow pathways for the upwelling of hot fluids. These structural boundaries are: (1) the southern crater rim of Caruggi cycles [*De Astis et al.*, 2007] representing the ex-Commenda cycle (2) the Fossa I crater rim located in the eastern part of the edifices. (3) Different imbricated crater boundaries constituting the present day cone of Vulcano also called La Fossa cone or Gran Cratere (post-1739), and (4) a small temperature peak on Forgia Vecchia crater rim, in the northern part of the edifice. This shows that all the geological crater boundaries, constituting the actual cone of Vulcano, act as preferential flowpaths for heated hydrothermal fluids. The hydrothermal system is mainly contained inside the boundary of the craters including Forgia Vecchia. All the crater boundaries exhibit thermal anomalies (Figures 4 to 8). These boundaries are planes of mechanical weakness along which cracks are periodically reopened by tectonic activity of the volcano during crises affecting La Fossa di Vulcano (see *Granieri et al.* [2006]).

We have no idea about the resistive body lying below the bottom part of the crater (Figure 11a). However, this body if not an artifact due to the influence of the topography on the inversion of the resistivity data (see Figure 10). It could be either a low-porosity body (the

neck of the old magmatic chamber) or dry steam in the hydrothermal system. A future study will monitor the resistivity and self-potential changes along a profile crossing the crater of La Fossa to see how stable is this anomaly and the positive self-potential anomaly observed in the crater.

Figure 12 shows the architecture of the Fossa cone along a SW-NE profile. The area of the highest temperature fumarolic activity (noted “F1” in Figure 12) can be extended to a depth of 200 meters corresponding to a conductive region. The high conductivity region is probably related to the presence of alteration products (clays and zeolites) combined with the high temperatures inside this zone (see *Lénat et al.* [2000]; *Revil et al.* [2003]; *Bernard et al.* [2007]). Figure 13 shows a picture of the southern part of the crater. All the structures observed at the ground surface can be observed on the resistivity tomogram (compare Figures 12° and 13).

Below the sea level, high values of the conductivity are associated with the intrusion of the sea water. This can explain the disapearance of some of the structures below the sea level (e.g., on the right-hand side of Profile 1, see Figure 4). Therefore, when interpreting resistivity profiles, we have to keep in mind that the relationship between resistivity and lithology is far from being univoque.

5.4. Flow Pattern at Vulcano

We use the finite-element code Comsol Multiphysics 3.3 to determine the distribution of the streaming electrical potential associated with ground water flow (see *Bolève et al.* [2007b]). Such numerical simulations can be used to assess the geometry of ground water flow of volcanoes and geothermal systems. The physics of these streaming potentials can be explained as follows: The existing charge at the surface of the minerals in contact with water is counterbalanced by an excess of electrical charges of opposite polarity located in the pore

water. The flow of pore fluid drags the excess of electrical charge contained creating an electrical current density called the streaming current.

In this section, we use the resistivity profile measured along the East-West profile to simulate ground water flow along this profile and to compute the resulting self-potential profile. Using the recent model developed by *Revil et al.* [2005] and *Revil and Linde* [2006], the total current density **j** (in A m^{-2}) is given by,

$$\mathbf{j} = \sigma\mathbf{E} + \overline{Q}_V \mathbf{u}\,, \tag{4}$$

where **u** is the Darcy's velocity (in m s^{-1}), $\mathbf{E} = -\nabla\varphi$ is the macroscopic electrical field (in V m^{-1}), φ is the electrical (self-) potential (in V), and $\overline{Q}_V$ is the excess of charge (of the diffuse layer) of the pore water per unit pore volume (in C m^{-3}). The streaming potential coupling coefficient defined by Eq. (3) and the excess of charge $\overline{Q}_V$ are related to each other and to the hydraulic conductivity K (in m s^{-1}) by $C = \partial\varphi / \partial H = -\overline{Q}_V K / \sigma$ where H is the hydraulic head (*Revil et al.* [2005]). This formulation has been recently extended to unsaturated conditions by *Linde et al.* [2007b] and *Revil et al.* [2007].

According to Eq. (4), the distribution of the self-potential is sensitive to the pattern of the Darcy velocity **u**. Therefore, the mechanism generating the flow itself (gravitational flow, free or forced convection) is rather unimportant regarding the distribution of the self-potential signals. We determine the flow pattern by using Darcy's law:

$$\mathbf{u} = -K\nabla H\,, \tag{5}$$

where $\Delta H = \delta p / \rho_f g$ is the change in hydraulic head (above or below the hydrostatic initial distribution H_0), δp is the excess of pressure above or below the hydrostatic level, ρ_f is the pore fluid density (in kg m^{-3}), and g is the acceleration of the gravity (in m s^{-2}). The Darcy's law is combined with the continuity equation for the mass of the pore fluid to give:

$$S\frac{\partial H}{\partial t} = \nabla\cdot(K\nabla H)\,, \tag{6}$$

where t is time, S (in m^{-1}) is the poro-elastic storage coefficient at saturation. The following computation is performed for steady state conditions and therefore the flow is given by solving $\nabla \cdot (K \nabla H) = 0$. The flow can be imposed by using appropriate boundary conditions and conservation of pore water flux. Here, we impose the flux at the boundaries of the system.

The continuity equation, for the electrical charge is $\nabla \cdot \mathbf{j} = 0$. Combining this equation with Eq. (4) results in Poisson equation for the electrical potential with a source term that depends only on the seepage velocity in the ground:

$$\nabla \cdot (\sigma \nabla \varphi) = \Im, \tag{7}$$

where $\Im$ is the volumetric current source density (in A m^{-3}) given by,

$$\Im = \overline{Q}_V \nabla \cdot \mathbf{u} + \nabla \overline{Q}_V \cdot \mathbf{u}, \tag{8}$$

The resistivity distribution determined along profile 1 (see Figure 4) was imported into the commercial finite-element software Comsol Multiphysics 3.3. The resistivity cross-section was discretized in several blocks (each block was then discretized using triangular meshing). The blocks represent the ash, tuff, inner massive lava flow units, and the hydrothermal system. In addition to the value of the resistivity, we need the values of the permeability and the streaming current coupling coefficient plus boundary conditions for the current density (or the electrical potential) and the hydraulic head (or the flux of water) to determine the ground-water flow under steady-state conditions. We use C = -5 mV m^{-1} and k = 10^{-10} m^2 for the ashes, C = -3 mV m^{-1} and k = 10^{-14} m^2 for the tuff, C = -5 mV m^{-1} and k = 10^{-11} m^2 for the hydrothermal system. We assign a zero permeability to the massive lava flow units; accordingly the coupling coefficient in this unit does not matter. We have also to worry about the temperature dependence of the material properties because of the elevated field temperatures in the volcanic edifice. However, the resistivity data are taken directly from the ERT profiles so they include the effect of the temperature. *Revil et al.* [2002] have shown that the value of the streaming potential coupling coefficient of volcaniclastic rocks is independent

of the temperature so we do not have to worry about the direct influence of the temperature upon the coupling coefficient used to perform the simulation in this study.

The simulated ground water flow pattern is shown on Figure 14. There is a downward flow inside the ashes and the tuff materials along the flanks of the volcano while there is an upward flow inside the boundary of the crater. As shown from the CO_2 data, there is no seal (very low permeability unit) inside the crater (except maybe at the bottom part of the crater). The upward flow of the hot pore water is responsible for pronounced evaporation of water inside the crater boundaries. To check if this pattern of ground-water flow is compatible with the self-potential data, we determine the resulting self-potential distribution along Profile 1. The simulated self-potential profile agrees quite well with the measured self-potential profile. In turn, this means that we could invert the measured self-potential data to determine the distribution of the Darcy velocity of the water phase inside the edifice. This is performed in the next section.

5.5. Inversion of Self-Potential Data

The self-potential data are governed by a Poisson equation with a source term given by the divergenece of the source (streaming) current density. Inverting Poisson equations is a well-established problem in the interpretation of magnetic and gravity data. Recently, various algorithms have been proposed to invert self-potential data in terms of the divergence of the current density (*Minsley et al.* [2007]), the three components of the current density itself (*Jardani et al.* [2007]; *Linde et Revil* [2007b]), or the position of the source (*Jardani et al.* [2006a]).

In this paper, we follow the methodology proposed recently by *Jardani et al.* [2007]. The relationship between the electrical current density and the measured SP signals can be written as,

$$\varphi(P) = \int_{\Omega} \mathbf{K}(P,M)\,\mathbf{j}_S(M)\,dV\,, \tag{9}$$

where $\mathbf{j}_S$ is the source current density (in both saturated and unsaturated conditions) described in Section 2 and $\mathbf{K}(P,M)$ is the kernel connecting the SP data measured at a set of non-polarizing electrodes P (with respect to a reference electrode) and the source of current at point M in the conducting ground of support Ω. The components of the kernel corresponds to the Green's function of the problem. The kernel depends on the number of measurement stations at the ground surface, the number of discretized elements in which the source current density is going to be determined, and the resistivity distribution of the medium. The inversion of the SP data follows a two-step process. The first step is the inversion of the distribution of the current density $\mathbf{j}_S$. The second step is the determination of $\mathbf{u}$ using the distribution of $\mathbf{j}_S$ and assuming values for the excess charge density and, eventually, an a prior distribution of the current density determined by a prior model of ground water flow.

We propose to determine the current density by finding the minimum of the following objective function ψ,

$$\psi = (\mathbf{Km} - \varphi_d)^T \mathbf{W}_d (\mathbf{Km} - \varphi_d) + \lambda^2 (\mathbf{m} - \mathbf{m}_0)^T \mathbf{W}_k^m (\mathbf{m} - \mathbf{m}_0)\,, \tag{10}$$

where λ is the regularization parameter ($0 < \lambda < \infty$, see *Tikhonov and Arsenin* [1977]), $\mathbf{K} = (\mathbf{K}_{ij}^x, \mathbf{K}_{ij}^z)$ is a Nx$2M$ matrix corresponding to the kernel, which can be measured by each component of a current density source $\mathbf{m} = (\mathbf{j}_i^x, \mathbf{j}_i^z)$, N is the number of self-potential stations and M is the number of discretized cells composing the ground, $2M$ represents the number of elementary current sources to consider (one horizontal component and one vertical component per cell for a 2D problem), $\mathbf{m}$ is the vector of $2M$ model parameters (source current density), $\boldsymbol{m}_0$ is an a prior distribution of the source current density, $\mathbf{W}_d = \mathrm{diag}\{1/\varepsilon_1,...,1/\varepsilon_N\}$ is a square diagonal weighting NxN matrix (elements along the diagonal of this matrix are the reciprocal of the standard deviation ε_i of the data), and φ_d is vector of N elements corresponding to the self-potential measurements at the surface of the

volcano. In our analysis, we took a mean deviation standard of 12 mV by analyzing the self-potential data along Profile 1 (mean and standard deviation). The standard deviation is mainly due to heterogeneity in the resistivity distribution just around the self-potential measurement stations.

The matrix $\mathbf{W}_k^m$ corresponds to a kth order derivative. The first and second order derivative are given by,

$$\mathbf{W}_1^m = \begin{bmatrix} 1 & -1 & 0 & 0 & \dots & 0 \\ 0 & 1 & -1 & 0 & \dots & 0 \\ \vdots & & \ddots & \ddots & & \vdots \\ \vdots & & & \ddots & \ddots & \vdots \\ 0 & \dots & 0 & 1 & -1 & 0 \\ 0 & \dots & 0 & 0 & 1 & -1 \end{bmatrix}, \tag{11}$$

$$\mathbf{W}_2^m = \begin{bmatrix} 1 & -2 & 1 & 0 & \dots & 0 \\ 0 & 1 & -2 & 1 & \dots & 0 \\ \vdots & & \ddots & \ddots & & \vdots \\ \vdots & & & \ddots & \ddots & \vdots \\ 0 & \dots & 1 & -2 & 1 & 0 \\ 0 & \dots & 0 & 1 & -2 & 1 \end{bmatrix}. \tag{12}$$

To account for the depth sensitivity of the source, we use a depth weighting diagonal matrix **S**. If the medium has a homogeneous resistivity distribution, it is defined from the depth weighting function:

$$\mathbf{S} = \begin{bmatrix} \frac{1}{(z_{m_1} + \varepsilon)^\beta} & 0 & \cdots & 0 \\ 0 & \frac{1}{(z_{m_2} + \varepsilon)^\beta} & \cdots & 0 \\ \vdots & \vdots & \ddots & \vdots \\ 0 & 0 & \cdots & \frac{1}{(z_{m_{2M}} + \varepsilon)^\beta} \end{bmatrix}, \tag{13}$$

where the small value ε is used to prevent the singularity when z is close to zero. The depth weighting (Nx3M) matrix is required to reduce the large sensitivity of the shallow cells (*Li*

and Oldenburg [1998], *Boulanger and Chouteau* [2001], and *Chasseriau and Chouteau* [2003]). In the general case, the depth weighting is given by (e.g., *Spinelli* [1999]),

$$\mathbf{S} = \mathrm{diag}\left(\frac{1}{N} \sqrt{\sum_{j=1}^{N} (K_{ij})^2} \right). \tag{14}$$

The solution of the problem is to find the unknown vector **m** corresponding to the minimum of the cost function given by $\partial\psi / \partial\mathbf{m} = 0$. This minimum is given by (*Hansen* [1992]):

$$\mathbf{m}_w = \left[\mathbf{K_w}^T (\mathbf{W}_d^T \mathbf{W}_d) \mathbf{K_w} + \lambda (\mathbf{W}_m^T \mathbf{W}_m) \right]^{-1} \left(\mathbf{K_w}^T (\mathbf{W}_d^T \mathbf{W}_d) \varphi_d + \lambda (\mathbf{W}_m^T \mathbf{W}_m) \mathbf{m}_0 \right). \tag{15}$$

where $\mathbf{K}_w = \mathbf{K}\mathbf{S}^{-1}$. The model vector is finally then given by $\mathbf{m}^* = \mathbf{S}\mathbf{m}_\mathbf{w}$. Because the model is linear with respect to the source current density, the solution, in terms of streaming current density, is obtained directly from Eq. (13). However, the solution of the inverse problem depends on the value of the regularization parameter and the value of the a prior model $\mathbf{m}_0$. To determine the value of the regularization parameter, *Hansen* [1998] proposed to plot the norm of the regularized smoothing solutions versus the norm of the residuals of the data misfit function. The resulting curve is hyperbolic and has therefore an L-shape. The determination of the regularization parameter, which is chosen at the corner of the L-shape plot, is known as the L-shape method. This is this method that we follow below.

An alternative method is the cross-validation method (*Desbat and Girard* [1995]). The cross-validation method allows choosing the best estimate of the regularization parameter in terms of the overall error prediction of the self-potential data. The total error prediction $\mathrm{E}(\lambda)$ is defined by,

$$\mathrm{E}(\lambda) = \frac{1}{N} \sum_{i=1}^{N} \left(\varphi_i^d - \varphi_i^*(\lambda) \right)^2, \tag{14}$$

where φ_i^d are the measured self-potential data and $\varphi_i^*(\lambda)$ are the estimate of the self-potential data at each self-potential station for a choice of the regularization parameter λ. The

best choice of the regularization parameter is obtain to reach the condition $\mathrm{Min}\, E(\lambda)$.

The determine the resolution of the inverse problem,w e can introduce the resolution matrix of the self-potential problem. The forward model is given by $\overline{\varphi} = \mathbf{Km}$ where $\overline{\varphi}$ is the self-potential vector. The solution of the inverse problem is given by $\mathbf{m}^* = \mathbf{T}\overline{\varphi}$ where $\mathbf{T}$ is the inverse transformation matrix. The resolution matrix $\mathbf{R}$ is defined by $\mathbf{m}^* = \mathbf{Rm}$ with $\mathbf{R} = \mathbf{KT}$ [*Menke*, 1989]. The resolution matrix contains all the information related to the uncertainty of the solution $\mathbf{m}^*$ for any cell of the investigated source volume.

The steps we follow to invert the self-potential data on Profile 1 are the following:

(1) We determine an a prior model of fluid flow using the geometrical structure inferred from the electrical resistivity tomogram along this profile, a prior permeability value that we believe to be reasonable for the four types of formations used to interpret the resistivity tomogram, and boundary conditions for the flow. The result is shown on Figure 14 and provides already a good fit of the self-potential data. Then we use this ground water flow solution to determine $\boldsymbol{m}_0$, the a prior distribution of the source current density (Figure 15). This solution has not to be very precise but physically meaningful to place a prior constraints on the inversion of the self-potential data and to reduce the non-uniqueness of the solution.

(2) The second step is the determination of the kernel. For each discretized cell, we consider a collection of *M* elementary source (in 2D, there are 2*M* components of the current density to retrieve) and *N* observation stations *P*. When computing the elements of $\boldsymbol{K}$, one has to remember that the electrical potential is determined relatively to a reference electrode. In our case, the reference electrode is placed at the first station at the beginning of the profile). By definition, the electrical potential at the reference is taken as equal to zero and this condition should be fulfilled for all the elements of $\boldsymbol{K}$ by removing the potential computed at this location from the self-potential distribution determined over the field. By computting the kernel, we also take into account the ground topography. In computing the kernel, we can also to choose to restrain the solution to subvolumes of the volcanoes. In the present case, we

consider that the very resistive units are low-porosity units which can be consider as seals with a null permeability.

(3) The third step is the determination of the regularization parameter using the L-shape method.

(4) The final problem is the determination of the best fit solution using Eq. (15). The result of the inversion with the use if an a prior model is shown in Figure 16.

We find that the source is mainly located below the crater (sources along the flanks are very minor, see Figure 16). Interestingly, the localization of the inverted source current density is consistent with the position of the source model inferred recently by *Gambino and Guglielmino* [2008] for the subsidence of the Fossa edifice that occurred during the period 1990-1996. During this period, electro-optical distance and leveling measurements were used by *Gambino and Guglielmino* [2008] to infer a shallow prolate ellipsoid responsible for the deformation of La Fossa Edifice. They explained the deformation as a transient migration of hydrothermal fluids along this source model. Because the current density evidences preferential fluid migration along a conduit, it is likely that deformation and self-potential point out the same preferential fluid flow pathway below the carter of La Fossa volcano.

6. Concluding Statements

The inner structure of La Fossa di Vulcano (Vulcano Island, southern Tyrrhenian Sea, Italy) is revealed by high resolution electric resistivity tomography coupled with self-potential, temperature, and CO_2 gas flux measurements. These measurements provide an idea of the architecture of the edifice including the geometry of the ash, tuff, lava flow units, and the spatial organization of the hydrothermal system. Numerical modeling of the flow system along the east-west profile shows the downward percolation of water in the ash and tuff, and upward flow of ground water inside the crater that is required to explain the observed self-potential data measured along this profile.

Because of its relatively small size and importance in terms of geohazards, La Fossa di Vulcano is a very interesting natural laboratory to see how various geophysical methods can be integrated to reveal the architecture of a volcano and to monitor its thermohydromechanical behavior. In the near-future, we plan to perform a three-dimensional joint inversion of electrical resistivity and gravity data. Such a joint inversion would probably be able to identify structural discontinuities of the edifice and to estimate both density and resistivity values for each sub-unit using a structural joint inversion approach (*Gallardo and Meju* [2004]) or sequential inversion approach with discret values for the resistivity and the mass density (e.g, *Krahenbuhl and Li* [2006]). The combination of various sources of information (shallow passive seismic data, self-potential, ground deformation, and variation of the gravity field) is probably required to distinguish magmatic versus hydrothermal phenomena and their implications in the assessment of geoharzards.

Acknowledgments. The INSU-CNRS, Instituto di Metodologie per l'Analisi Ambientale (IMAA) del CNR, the Laboratoire GéoSciences Réunion-IPGP, the CNR, the Istituto Nazionale di Geofisica e Vulcanologia (INGV), and the Dipartimento per la Protezione Civile through the DPC research program (V3.5 Vulcano, 2005-2007) are thanked for financial supports. We also thank Xavier Rassion and Etienne Wheris for their help in the field, without forgetting Peppe Sansone for his inimitable Sicilian recipes. We thank also A. Jardani for his help and Maria Marsella for facilitating the use of Vulcano DEM. This is the IPGP contribution nb 2294. We thank the Associate Editor, an anonymous referee, and David Fitterman for their very useful comments of our manuscript.

References

Aubert, M., S. Diliberto, A. Finizola, Y. Chébli (2007), Double origin of hydrothermal convective flux variations in the Fossa of Vulcano (Italy), doi 10.1007/s00445-007-0165-y, *Bull. Volcanol.* In press.

Auken, E., and A.V. Christiansen (2004), Layered and laterally constrained 2D inversion of resistivity data, *Geophysics, 69,*752–761.

Baldi, P., S. Bonvalot, P. Briole, M. Coltelli, K. Gwinner, M. Marsella, G. Puglisi, D. Remy (2002), Validation and comparison of different techniques for the derivation of digital elevation models and volcanic monitoring (Vulcano Island, Italy), *International Journal of Remote Sensing, 22,* 4783-4800.

Bedrosian, P.A., M.J. Unsworth, M.J.S. Johnston (2007), Hydrothermal circulation at Mount St. Helens determined by self-potential measurements, *J. Volcan. Geotherm. Res., 160 (1-2),* 137-146.

Bernard, M.-L., M. Zamora, Y. Geraud, and G. Boudon (2007), Transport properties of pyroclastic rocks from Montagne Pelee volcano (Martinique, Lesser Antilles), *J. Geophys. Res., 112(B5),* B05205.

Binley, A., and A. Kemna (2005), DC resistivity and induced polarization methods, in: Y. Rubin, S. Hubbard (Eds.), *Hydrogeophysics,* Springer, 129–156, Chapter 5.

Bolève, A., A. Crespy, A. Revil, F. Janod, and J.L. Mattiuzzo (2007a), Streaming potentials of granular media: Influence of the Dukhin and Reynolds numbers, *J. Geophys. Res., 112,* B08204, doi:10.1029/2006JB004673.

Bolève A., A. Revil, F. Janod, J. L. Mattiuzzo, and A. Jardani (2007b), Forward modeling and validation of a new formulation to compute self-potential signals associated with ground water flow, *Hydrology and Earth System Sciences, 11(5),* 1661-1671.

Boulanger, O., and M. Chouteau (2001), Constraints in 3D gravity inversion, *Geophysical Prospecting,* 49(2), 265-280.

Chasseriau, P., and M. Chouteau (2003), 3D gravity inversion using a model of parameter covariance, *J. Applied Geophys., 52(1),* 59-74.

Chiodini, G., R. Cioni, M. Guidi, L. Marini, and B. Raco (1998), Soil CO_2 flux measurements in volcanic and geothermal areas, *Appl. Geochem., 13,* 543-552.

Chiodini, G., Frondini F., and Raco B. (1996), Diffuse emission of CO_2 from the Fossa crater, Vulcano Island (Italy). *Bull. Volcanol*., 58, 41– 50.

Colella, A., V. Lapenna, and E. Rizzo (2004), High-resolution imaging of the High Agri Valley basin (Southern Italy) with Electrical Resistivity Tomography. *Tectonophysics*, 386, 29-40.

Coniglio, S., and F. Dobran (1995), Simulations of magma ascent and pyroclast dispersal at Vulcano (Aeolian Islands, Italy), *J. Volcanol. Geotherm. Res., 65*, 297-317.

Constable, S.C., R.L. Parker, C.G. Constable (1987), Occams inversion— a practical algorithm for generating smooth models from electromagnetic sounding data, *Geophysics, 52*, 289–300.

Coppo N., P.-A. Schnegg, W. Heise, P. Falco, and R. Costa (2008), Multiple caldera collapses inferred from the shallow electrical resistivity signature of the Las Cañadas caldera, Tenerife, Canary Islands, *Journal of Volcanology and Geothermal Research, 170 (3-4)*, 153-166.

Cortecci, G., E. Dinelli, L. Bolognesi, T. Boschetti, and G. Ferrara (2001), Chemical and isotopic compositions of water and dissolved sulfate from shallow wells on Vulcano Island, Aeolian Archipelago, Italy, *Geothermics 30*, 69-91.

Corwin, R. F., and D. B. Hoover (1979), The self-potential method in geothermal exploration, *Geophysics*, *44*, 226-245.

De Astis, G., P. Dellino, L. La Volpe, F. Lucchi, C.A. Tranne, (2007), Geological Map of the Vulcano Island (1:10.000). La Volpe L., De Astis G., editors.

De Fiore, O. (1922), Vulcano (Isole Eolie). *Monografia – Zeitsch. Fur Vulk.*, 3, 3-393 (Rep. Swets and Zeitlinger N.V., Amsterdam, 1969).

Dellino, P., and L. La Volpe (1997), Stratigrafia, dinamiche eruttive e deposizionali, scenario eruttivo e valutazioni di pericolosità a La Fossa di Vulcano. In: "*CNR-GNV Progetto Vulcano 1993-1995* " L. La Volpe, P. Dellino, M. Nuccio, E. Privitera, and A. Sbrana (Ed), Felici, Pisa, 214-237.

De Rosa, R., N. Calanchi, P.F. Dellino, L. Francalanci, F. Lucchi, M. Rosi, P.L. Rossi, and C.A. Tranne (2004), *32nd International Geological Congress, Field Trip Guide Book* – P42, Volume n° 5: Geology and volcanism of Stromboli, Lipari, and Vulcano (Aeolian Islands); Firenze 20-28 agosto 2004.

Di Fiore, B., P. Mauriello, and D. Patella (2004), On the localisation of long-standing self-potential sources at Vulcano (Italy) by probability tomography, *Quadernidi Geofisica, 35*, .27-32.

Diaferia, I., M. Barchi, M. Loddo, D. Schiavone, and A. Siniscalchi (2006), Detailed imaging

of tectonic structures by multiscale Earth resistivity tomographies: The Colfiorito normal faults (central Italy), *Geophys. Res. Lett.*, *33*, L09305, doi:10.1029/2006GL025828.

Ellam, R.M., C.J. Hawkesworth, M.A. Menzies, and N.W. Rotgers (1989), The volcanism of Southern Italy – Role of subduction and the relationship between potassic and sodic alakline magmatism, Journal of Geophysical Research, *J. Geophys. Res.*, *94(B4)*, 4589-4601.

Finizola, A., A. Revil, E. Rizzo, S. Piscitelli, T. Ricci, J. Morin, B. Angeletti, L. Mocochain, and F. Sortino (2006), Hydrogeological insights at Stromboli volcano (Italy) from geoelectrical, temperature, and CO_2 soil degassing investigations, *Geophys. Res. Lett.*, *33*, L17304, doi:10.1029/2006GL026842.

Finizola, A., S. Sortino, J.-F. Lénat, M. Aubert, M. Ripepe, and M. Valenza (2003), The summit hydrothermal system of Stromboli. New insights from self-potential, temperature, CO_2 and fumarolic fluid measurements. Structural and monitoring implications, *Bull. Volcanol.*, *65*, 486-504, doi:10.1007/s00445-003-0276-z.

Finizola, A., S. Sortino, J.-F. Lénat, and M. Valenza (2002), Fluid circulation at Stromboli volcano (Aeolian Islands, Italy) from self-potential and CO_2 surveys, *J. Volcanol. Geotherm. Res.*, *116*, 1-18.

Fitterman, D. V., W. D. Stanley, and R. J. Bisdorf (1988), Electrical structure of Newberry volcano, Oregon, *J. Geophys. Res.*, 93(B9), 10,119–110,134.

Frazzetta, G., and L. La Volpe (1991), Volcanic history and maximum expected eruption at "La Fossa di Vulcano" (Aeolian Islands, Italy). *Acta Vulcanol.*, *1*, 107-113.

Frazzetta, G., L. La Volpe, and M.F. Sheridan (1983), Evolution of the Fossa cone, Volcano, *J. Volcanol. Geotherm. Res.*, *17*, p. 329-360.

Frazzetta, G., P.Y. Gillot, L. La Volpe, M.F. and Sheridan (1984), Volcanic hazards at Fossa of Volcano: Data from the last 6,000 years, *Bulletin of Volcanology*, *47*, 105-125.

Gambino, S., and F. Guglielmino (2008), Ground deformation induced by geothermal processes: a model for La Fossa crater (Vulcano Island, Italy), Journal of Geophysical Research.

Gasparini, C., G. Iannaccone, and R. Scarpa (1982), Seismotectonics of the Calabrian Arc, *Tectonophysics*, *84*, 267-286.

Gex, P. (1992), Etude géophysique des environs du cratère de Vulcano, Italie (Geophysical survey in the region of the crater of Vulcano, Italy) (in french), *Bulletin de la Société Vaudoise des Sciences Naturelles*, *82*(2), 157-172.

Giacomelli, L., and R. Scandone (2002), Vulcani e eruzioni. *Pitagora Editrice*, Bologna, pp. 278.

Granieri, D., M. L. Carapezza, G. Chiodini, R. Avino, S. Caliro, M. Ranaldi, T. Ricci, and L. Tarchini (2006), Correlated increase in CO2 fumarolic content and diffuse emission from La Fossa crater (Vulcano, Italy): Evidence of volcanic unrest or increasing gas release from a stationary deep magma body?, *Geophys. Res. Lett., 33*, L13316, doi:10.1029/2006GL026460.

Gallardo, L. A., and M. A. Meju (2004), Joint two-dimensional DC resistivity and seismic travel time inversion with cross-gradient constraints, *J. Geophys. Res., 109*, B03311, doi:10.1029/2003JB002716.

Hansen, P.C. (1998), *Rank-Deficient and Discrete Ill-Posed Problems: Numerical Aspects of Linear Inversion*, SIAM, Philadelphia, 247 pp.

Hase, H., T. Hashimoto, S. Sakanaka, W. Kanda, and Y. Tanaka (2005), Hydrothermal system beneath Aso volcano as inferred from self-potential mapping and resistivity structure, *J. Volcanol. Geotherm. Res., 143*, 259-277.

Ishido, T., T. Kiruchi, N. Matsushima, Y. Yano, S. Nakao, M. Sugihara, T. Tosha, S. Takakura, and Y. Ogawa (1997), Repeated self-potential profiling of Izu-Oshima Volcano, Japan, *J. Geomag. Geoelectr., 49*, 1267-1278.

Ishido, T. (2004), Electrokinetic mechanism for the "W"-shaped self-potential profile on volcanoes, Geophys. Res. Lett., 31 (15): Art. No. L15616.

Jardani, A. A. Revil, F. Akoa, M. Schmutz, N. Florsch, and J.P. Dupont (2006a), Least-squares inversion of self-potential (SP) data and application to the shallow flow of the ground water in sinkholes, *Geophys. Res. Lett.*, *33*(19), L19306, doi: 10.1029/2006GL027458.

Jardani, A., J.P. Dupont, and A. Revil (2006b), Self-potential signals associated with preferential ground water flow pathways in sinkholes, *J. Geophys. Res.*, *111*, B09204, doi: 10.1029/2005JB004231.

Jardani, A., A. Revil, A. Bolève, J.P. Dupont, W. Barrash, and B. Malama (2007), Tomography of groundwater flow from self-potential (SP) data, *Geophys. Res. Lett., 34*, L24403, doi:10.1029/2007GL031907.

Jin, G., C. Torres-Verdin, S. Devarajan, E. Toumelin, and E. C Thomas. (2007), Pore-scale analysis of the Waxman-Smits shaly-sand conductivity model, *Petrophysics, 48 (2)*, 104-

120.

Kalscheuer T., M. Commer, S.L. Helwig, A. Hördt, and B. Tezkan (2007), Electromagnetic evidence for an ancient avalanche caldera rim on the south flank of Mount Merapi, Indonesia, *Journal of Volcanology and Geothermal Research, 162 (1-2), 15, 81-97.*

Keller, J. (1980), The island of Vulcano, *Soc. Italiana Min. Petr., 36,* 368-413.

Krahenbuhl, R.A., and Y. Li (2006), Inversion of gravity data using a binary formulation, *Geophys. J. Int., 167*, 543–556.

Kulessa, B., B. Hubbard, and G.H. Brown, (2003a), Cross-coupled flow modeling of coincident streaming and electrochemical potentials, and application to subglacial self-potential (SP) data, *J. Geophys. Res., 108(B8)*, 2381, doi: 10.1029/2001JB1167.

Kulessa, B., B. Hubbard, G.H. Brown, and J. Becker (2003b), Earth tide forcing of glacier drainage, *Geophys. Res. Lett, 30(1)*, 1011, doi: 10.1029/2002GL105303.

Lénat, J.F. (2007), Retrieving self-potential anomalies in a complex volcanic environment: an SP/elevation gradient approach, *Near-Surface Geophysics, 5(3)*, 161-170.

Lénat, J.F., D. Fitterman, D.B. Jackson, and P. Labazuy (2000), Geoelectrical structure of the central zone of Piton de la Fournaise volcano (Reunion), *Bulletin of Volcanology, 62 (2)*, 75-89.

Leroy, P. and A. Revil (2004), A triple layer model of the surface electrochemical properties of clay minerals, *Journal of Colloid and Interface Science, 270(2),* 371-380.

Li, Y., and D.W. Oldenburg (1998), 3-D inversion of gravity data, *Geophysics, 63(1)*, 109-119.

Linde, N., A. Revil, A. Bolève, C. Dagès, J. Castermant, B. Suski, and M. Voltz (2007), Estimation of the water table throughout a catchment using self-potential and piezometric data in a Bayesian framework, *Journal of Hydrology, 334*, 88-98.

Linde, N., and A. Revil (2006), A comment on "Electrical tomography of La Soufrière of Guadeloupe Volcano: Field experiments, 1D inversion and qualitative interpretation", by Nicollin, F. et al., (Earth Planet Sci. Lett. 244 (2006) 709-724), *Earth Planet Sci. Lett., 258*, 619-622, 10.1016/j.epsl.2006.02.020, 2007.

Linde, N., A. Revil, A. Bolève, C. Dagès, J. Castermant, B. Suski, and M. Voltz (2007a), Estimation of the water table throughout a catchment using self-potential and piezometric data in a Bayesian framework, *Journal of Hydrology, 334*, 88-98, 2007.

Linde, N., and A. Revil (2007b), Inverting residual self-potential data for redox potentials of contaminant plumes, Geophysical Research Letters, 34, L14302,

doi:10.1029/2007GL030084.

Lo Cascio, P., and E. Navarra (1997), Guida Naturalistica Alle Isole Eolie. L'EPOS, Palermo. 112 pp.

Loke, M.H. and R. D. Barker (1996), Rapid least-squares inversion of apparent resistivity pseudosections by a quasi-Newton method, *Geophysical Prospecting, 44*, 131-152.

Maineult, A., Y. Bernabé, and P. Ackerer (2005), Detection of advected concentration and pH fronts from self-potential measurements, *J. Geophys. Res.*, 110(B11), B11205, doi: 10.1029/2005JB003824.

Maineult, A., Y. Bernabé, and P. Ackerer (2006), Detection of advected, reacting redox fronts from self-potential measurements, *Journal of Contaminant Hydrology*, 86, 32-52

Massenet, F., and V. N. Pham (1985), Experimental and theoretical basis of self-potential phenomena in volcanic areas with reference to results obtained on Mount Etna (Sicily), *Earth Planet. Sci. Lett., 73*, 415-429.

Michel, S., and J. Zlotnicki (1998), Self-potential and magnetic surveying of La Fournaise volcano (Réunion island): Correlations with faulting, fluid circulation, and eruption, *J. Geophys. Res., 103*, 17,845 – 17,857.

Minsley, B.J., J. Sogade, and F.D. Morgan (2007), Three-dimensional source inversion of self-potential data, *J. Geophys. Res., 112*, B02202, doi: 1029/2006JB004262.

Niwas, S., P.K. Gupta, and O.A.L. de Lima (2007), Nonlinear electrical conductivity response of shaly-sand reservoir, *Current Science, 92 (5)*, 612-617.

Perrier, F., M. Trique, B. Lorne, J.P. Avouac, S. Hautot, and P. Tarits (1998), Electrical potential variations associated with yearly lake level variations, *Geophys. Res. Lett., 25*, 1955-1959.

Revil, A. (1995), *Conductivité Electrique et Potentiel Spontané dans les Mileux Poreux: De la Théorie à l'Analyse des Mesures en Forage*, Ph-D Thesis, Université Louis Pasteur à Strasbourg.

Revil, A., and Glover, P.W.J. (1998), Nature of surface electrical conductivity in natural sands, sandstones, and clays, *Geophysical Research Letters, 25(5)*, 691-694.

Revil, A., L.M. Cathles, S. Losh, and J.A. Nunn (1998), Electrical conductivity in shaly sands with geophysical applications, *J. Geophys. Res., 103(B10)*, 23,925-23,936.

Revil, A., H. Schwaeger, L.M. Cathles, and P. Manhardt (1999), Streaming potential in porous media. 2. Theory and application to geothermal systems, *J. Geophys. Res., 104(B9)*, 20,033-20,048.

Revil, A., D. Hermitte, E. Spangenberg, and J. J. Cochémé (2002), Electrical properties of zeolitized volcaniclastic materials, *J. Geophys. Res., 107(B8)*, 2168, 10.1029/2001JB000599.

Revil, A., G. Saracco, and P. Labazuy (2003), The volcano-electric effect, *J. Geophys. Res., 108(B5),* 2251, doi: 10.1029/2002JB001835.

Revil, A., V. Naudet, and J.D. Meunier (2004a), The hydroelectric problem of porous rocks: Inversion of the water table from self-potential data, *Geophys. J. Intern., 159*, 435-444.

Revil, A., A. Finizola, F. Sortino, and M. Ripepe (2004b), Geophysical investigations at Stromboli volcano, Italy. Implications for ground water flow, *Geophys. J. Intern., 157*, 426-440.

Revil, A., P. Leroy, and K. Titov (2005), Characterization of transport properties of argillaceous sediments. Application to the Callovo-Oxfordian Argillite, *J. Geophys. Res., 110*, B06202, doi: 10.1029/2004JB003442.

Revil, A., and N. Linde (2006), Chemico-electromechanical coupling in microporous media, *Journal of Colloid and Interface Science, 302,* 682-694, 2006.

Revil, A., N. Linde, A. Cerepi, D. Jougnot, S. Matthäi, and S. Finsterle (2007), Electrokinetic coupling in unsaturated porous media, *Journal of Colloid and Interface Science, 313(1)*, 315-327, 10.1016/j.jcis.2007.03.037.

Rizzo, E., B. Suski, A. Revil, S. Straface, and S. Troisi (2004), Self-potential signals associated with pumping-tests experiments, *J. Geophys. Res., 109*, B10203, doi: 10.1029/2004JB003049.

Roberts, J.J., and W. Lin (1997), Electrical properties of partially saturated Topopah Spring tuff: Water distribution as a function of saturation, *Water Resources Res., 33(4)*, 577-587.

Santacroce, R., R. Cristofolini, L. La Volpe, G. Orsi, and M. Rosi (2003), Italian active volcanoes, *Episodes IUGS, 26(3)*, 227-234.

Shevnin, V., A. Mousatov, A. Ryjov, and O. Delgado-Rodriquez (2007), Estimation of clay content in soil based on resistivity modelling and laboratory measurements, *Geophys. Prospect.,55 (2)*, 265-275.

Storz, H., W. Storz, and F. Javobs (2000), Electrical resistivity tomography to investigate geological structures of the earth's upper crust, *Geophys. Prospect., 48,* 455– 471.

Suski, B., A. Revil, K. Titov., P. Konosavsky, C. Dagès, M. Voltz, and O. Huttel (2006), Monitoring of an infiltration experiment using the self-potential method, *Water Resour. Res., 42*, W08418, doi:10.1029/2005WR004840.

Suski, B., E. Rizzo, and A. Revil (2004), A sandbox experiment of self-potential signals associated with a pumping-test, Vadose Zone Journal, 3, 1193-1199.

Tabbagh A. and Ph. Cosenza (2007), Effect of microstructure on the electrical conductivity of clay-rich systems, *Physics and Chemistry of the Earth, Parts A/B/C, 32(1-7*), 154-160.

Tikhonov, A.N., and V.Y. Arsenin (1977), *Solutions of Ill-posed Problems*, John Wiley & Sons, Washington.

Titov, K., A. Revil, P. Konasovsky, S. Straface, and S. Troisi (2005), Numerical modeling of self-potential signals associated with a pumping test experiment, *Geophys. J. Intern., 162*, 641-650.

Tosha, T., N. Matsushima, and T. Ishido (2003), Zeta potential measured for an intact granite sample at temperatures to 200 degrees C , *Geophysical Res. Lett., 30(6)*, 1295.

Waxman, M.H. and Smits, L.J.M. (1968), Electrical conduction in oil-bearing sands, *Society of Petroleum Engineers Journal, 8*, 107-122.

Wishart, D. N., L. D. Slater, and A. E. Gates (2006), Self potential improves characterization of hydraulically-active fractures from azimuthal geoelectrical measurements, *Geophys. Res. Lett., 33*, L17314, doi:10.1029/2006GL027092.

Zhdanov, M. (2002), *Geophysical Inverse Theory and Regularization Problems*, Elsevier, Amsterdam.

Zohdy, A.A.R., and R. J. Bisdorf (1990), Schlumberger soundings near Medicine Lake, California, *Geophysics, 55(8)*, 956-964.

Table 1. Measurements of the electrical resistivity, the streaming potential coupling coefficient of various samples from Stromboli and La Fossa di Vulcano (called respectively "S-" and "V-"). S-Bi: Vancori Basalt (Stromboli), S-LFi: Lava Flow (Piscità, Stromboli), S-Ti: Tuff (Pizzo, Stromboli), V-LFi: Lava flow (Vulcano), V-Lbi: Lava Flow (Borehole, see position in Figure 1, Vulcano), and V-Ti: Tuff (Vulcano). The uncertainties associated with the measurements of the resistivity and the coupling coefficient are approximately 5% (determined from the reproducility of the measurements).

Samples	Resistivity (in Ω m) σ_f = 0.1 S m^{-1}	C (in mV m^{-1}) σ_f = 0.1 S m^{-1}	Resistivity (in Ω m) σ_f = 0.5 S m^{-1}	C (in mV m^{-1}) σ_f = 0.5 S m^{-1}
S-B1	698	-3.9	167	-1.79
S-B2	638	-2.6	192	-0.54
S-B3	707	-4.1	222	-0.75
S-LF1	802	-5.2	180	-0.90
S-LF2	728	-4.1	179	-1.71
S-LF3	421	-	53	-
S-LF4	575	-2.1	205	-0.61
S-LF5	327	-2.0	113	-1.47
S-LF6	1040	-2.4	160	-1.05
S-T1	656	-2.0	125	-0.87
S-T2	452	-2.9	102	-0.89
S-T3	626	-5.1	135	-0.62
S-T4	713	-3.4	130	-0.80
V-LF1	378	-5.4	74	-2.22
V-LF2	265	-4.2	63	-1.09
V-LF3	345	-3.4	57	-0.92
V-Lb1	227	-4.3	61	-0.91
V-Lb2	306	-2.8	55	-0.96
V-Lb3	712	-3.8	94	-0.77
V-Lb4	315	-2.5	40	-1.31
V-T1	22	-3.4	7.8	-0.12

Table 2. Formation factor and surface conductivity determined from the electrical conductivity measurements. “S-“ and “V-“ stand for Stromboli and Vulcano samples. S-Bi: Vancori Basalt (Stromboli), S-LFi: Lava Flow (Piscità, Stromboli), S-Ti: Tuff (Pizzo, Stromboli), V-LFi: Lava flow (Vulcano), V-Lbi: Lava Flow (Borehole, see position Figure 1, Vulcano), and V-Ti: Tuff (Vulcano).

Samples	F	σ_S (in 10^{-4} S m^{-1})	Porosity
S-B1	90 ± 4	4.3 ± 1	0.15
S-B2	112 ± 6	7.6 ± 2	0.09
S-B3	132 ± 7	7.3 ± 2	0.13
S-LF1	95 ± 4	2.9 ± 1	0.12
S-LF2	97 ± 4	4.4 ± 2	0.13
S-LF3	28 ± 2	9.2 ± 2	0.18
S-LF4	130 ± 8	10.5 ± 3	0.12
S-LF5	71 ± 3	18.1 ± 3	0.12
S-LF6	82 ± 3	1.55 ± 0.20	0.10
S-T1	63 ± 3	0.7 ± 0.3	0.12
S-T2	54 ± 2	5.3 ± 1.0	0.12
S-T3	71 ± 4	3.3 ± 1.0	0.10
S-T4	65 ± 4	0.1 ± 0.1	0.10
V-LF1	38 ± 3	2.8 ± 0.1	0.44
V-LF2	34 ± 2	11.4 ± 2.4	0.48
V-LF3	29 ± 2	3.0 ± .4	0.48
V-Lb1	34 ± 4	18.3 ± 2.5	0.14
V-Lb2	28 ± 2	0.4 ± 0.1	0.14
V-Lb3	49 ± 4	4.5 ± 1.0	0.13
V-Lb4	21 ± 1	12.6 ± 2	0.14
V-T1	4.8 ± 1	310 ± 20	-

Captions

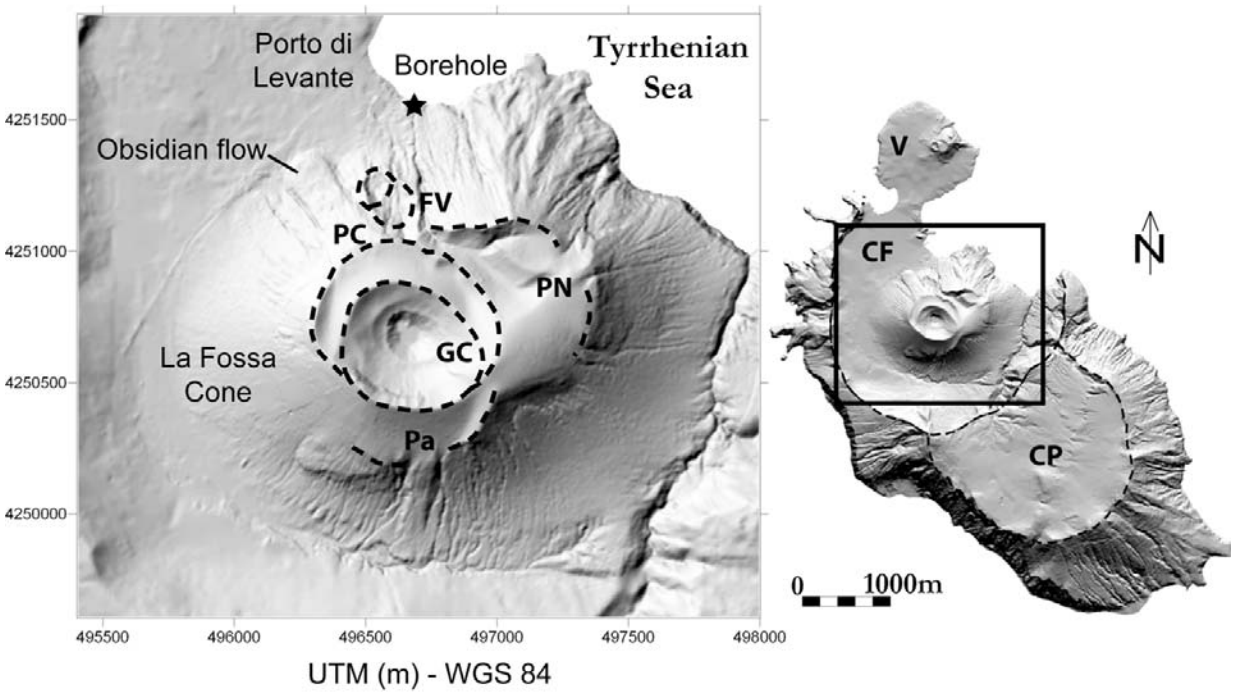

Figure 1. Map of the Island of Vulcano (Italy). Left-hand side: PN, Punte Nere; Pa, Palizzi; FV, Forgia Vecchia; PC, Pietre Cotte; GC, Gran Cratere. Right-hand side: V, Vulcanello, CF, Caldera della Fossa; and CP, Caldera del Piano.

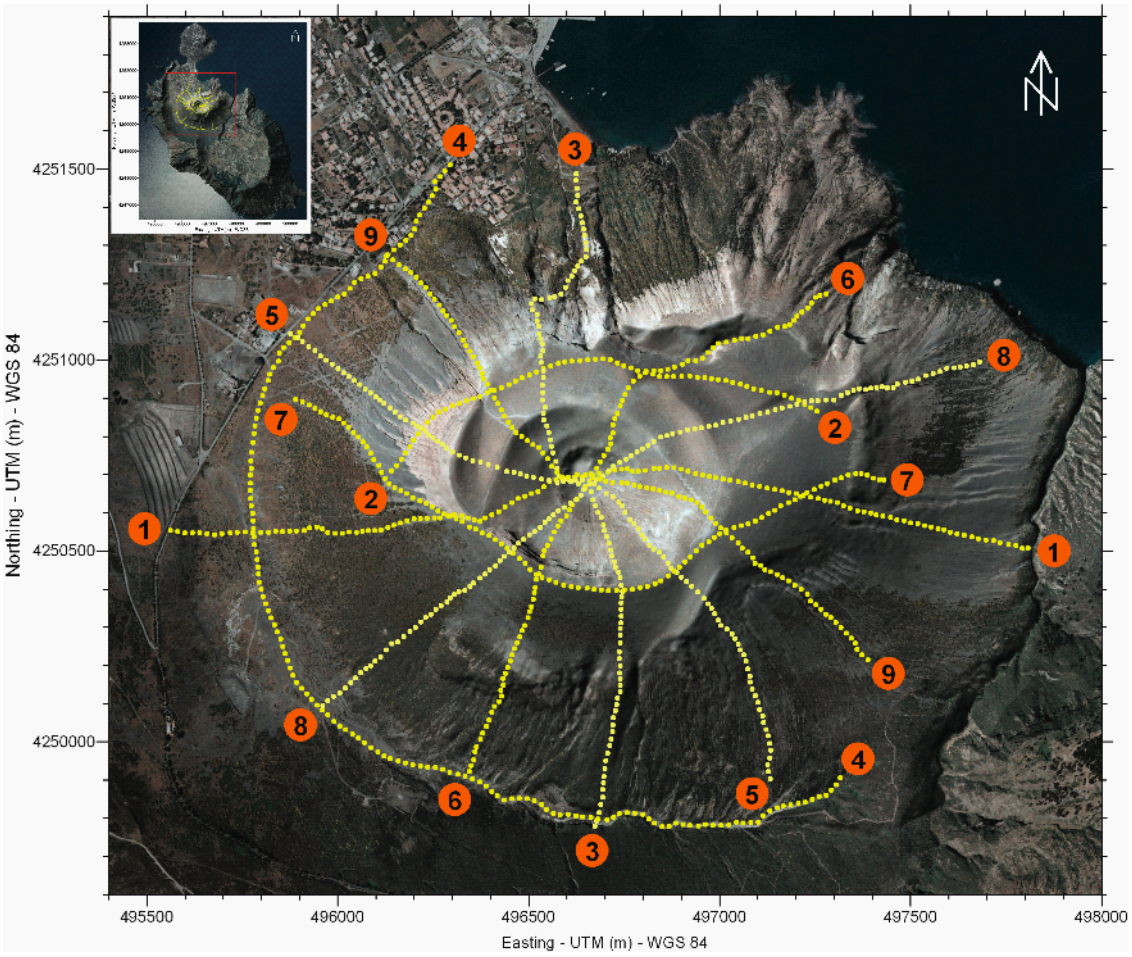

Figure 2. Position of the investigated area on the Fossa cone. Nine profiles (labeled from 1 to 9) have been performed crossing the Fossa edifice. The bright areas on the flanks of the volcano correspond to the hydromagmatic tuff discussed in the main text.

Figure 3. The Fossa cone observed from the south.

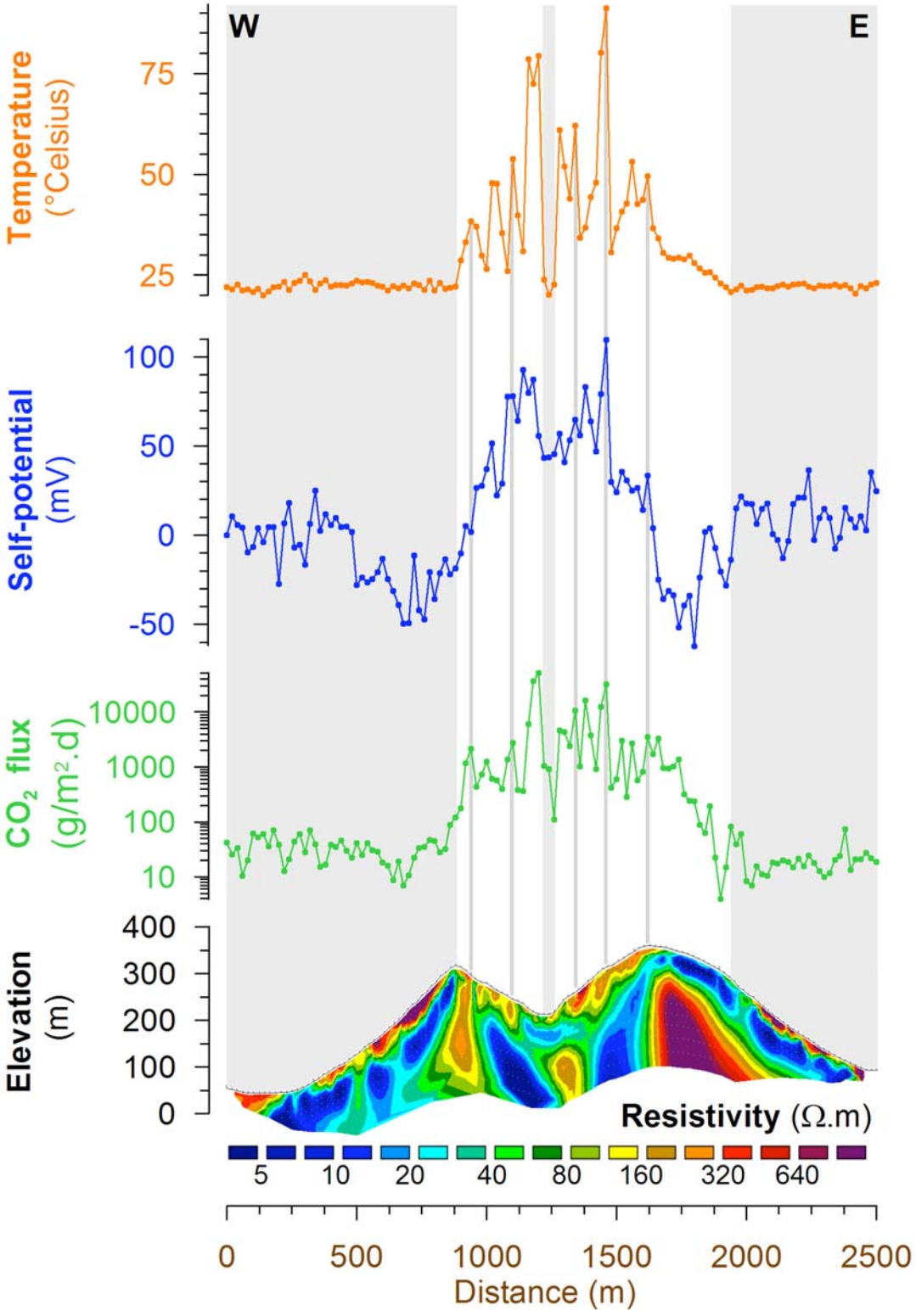

Figure 4. Temperature, self-potential, soil CO_2 flux, and electrical resistivity tomogram along Profile 1; These data show that the main activity is constrained inside the crater, which is characterized by self-potential, CO_2, and temperature anomalies. Note that the ground surface of the central part of the crater is cold.

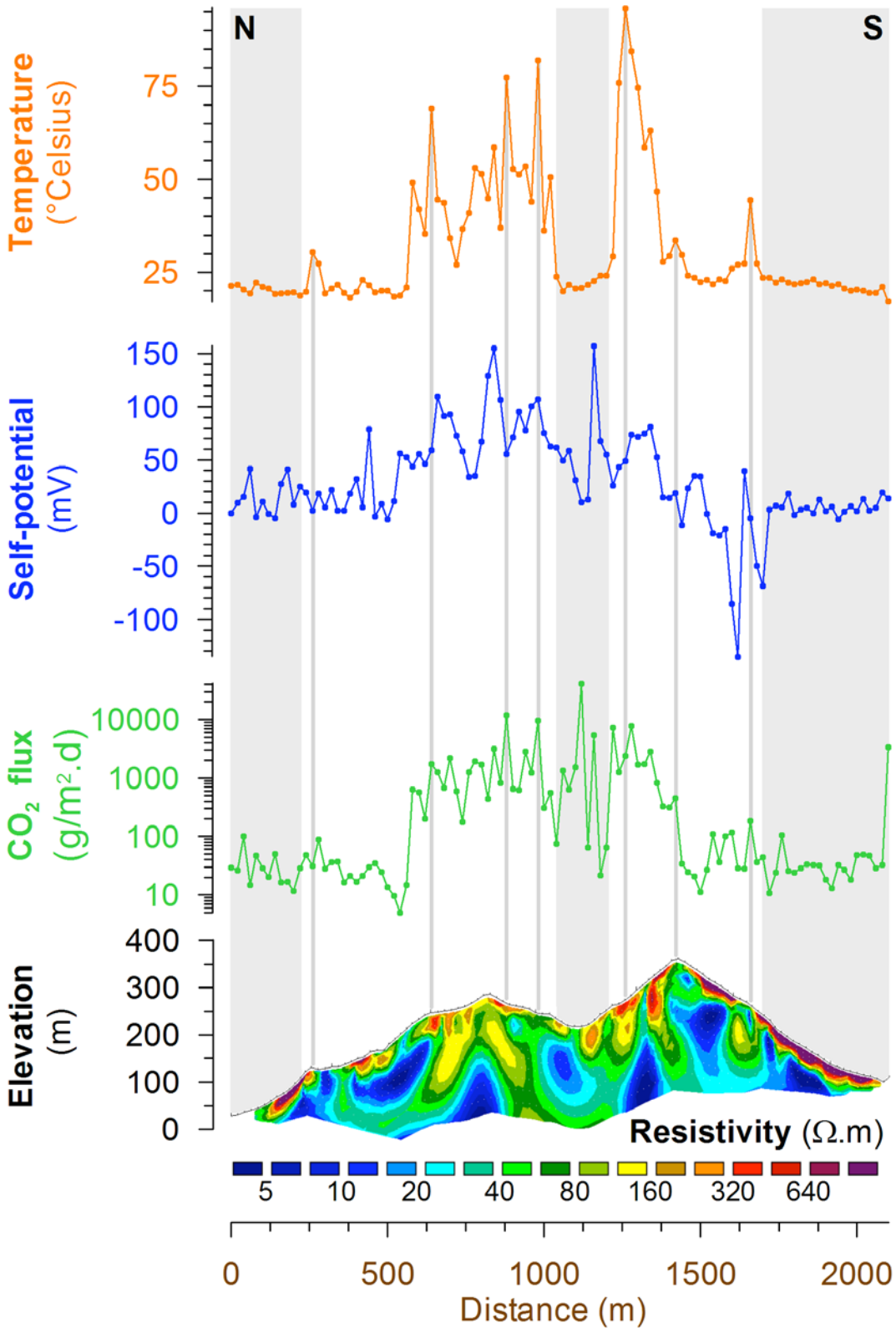

Figure 5. Temperature, self-potential, soil CO_2 flux, and electrical resistivity tomogram along Profile 3. Note that the bottom part of the crater is cold. On the northern flank of the edifice (the left side of the figure), a conductive area is laterally limited by two thermal anomalies. These anomalies represent the boundary of the Forgia Vecchia crater which last eruption occured in 1727.

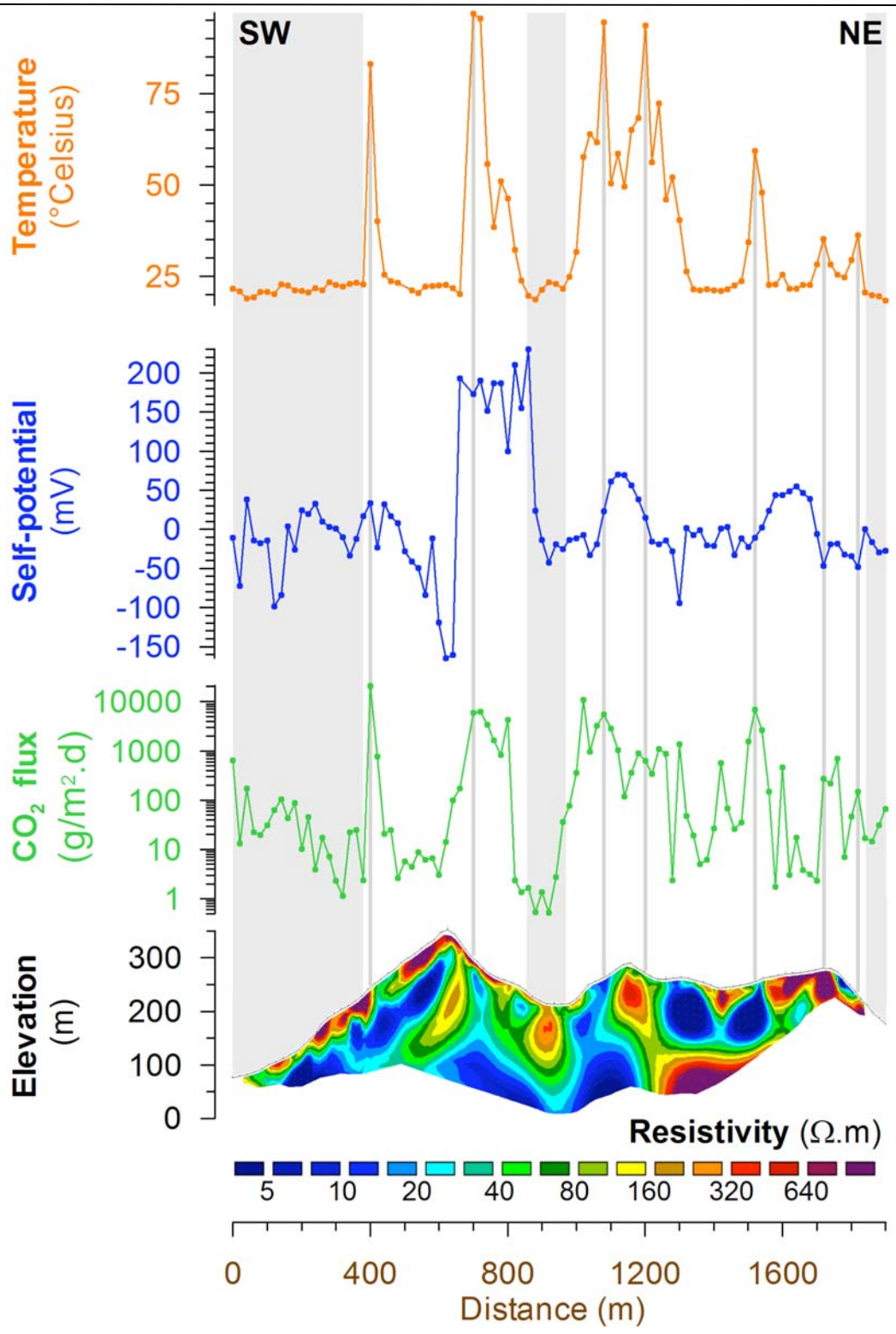

Figure 6. Temperature, self-potential, soil CO_2 flux, and electrical resistivity tomogram along Profile 6. Note the M-shape of the temperature, self-potential, and CO_2 anomalies inside the crater.

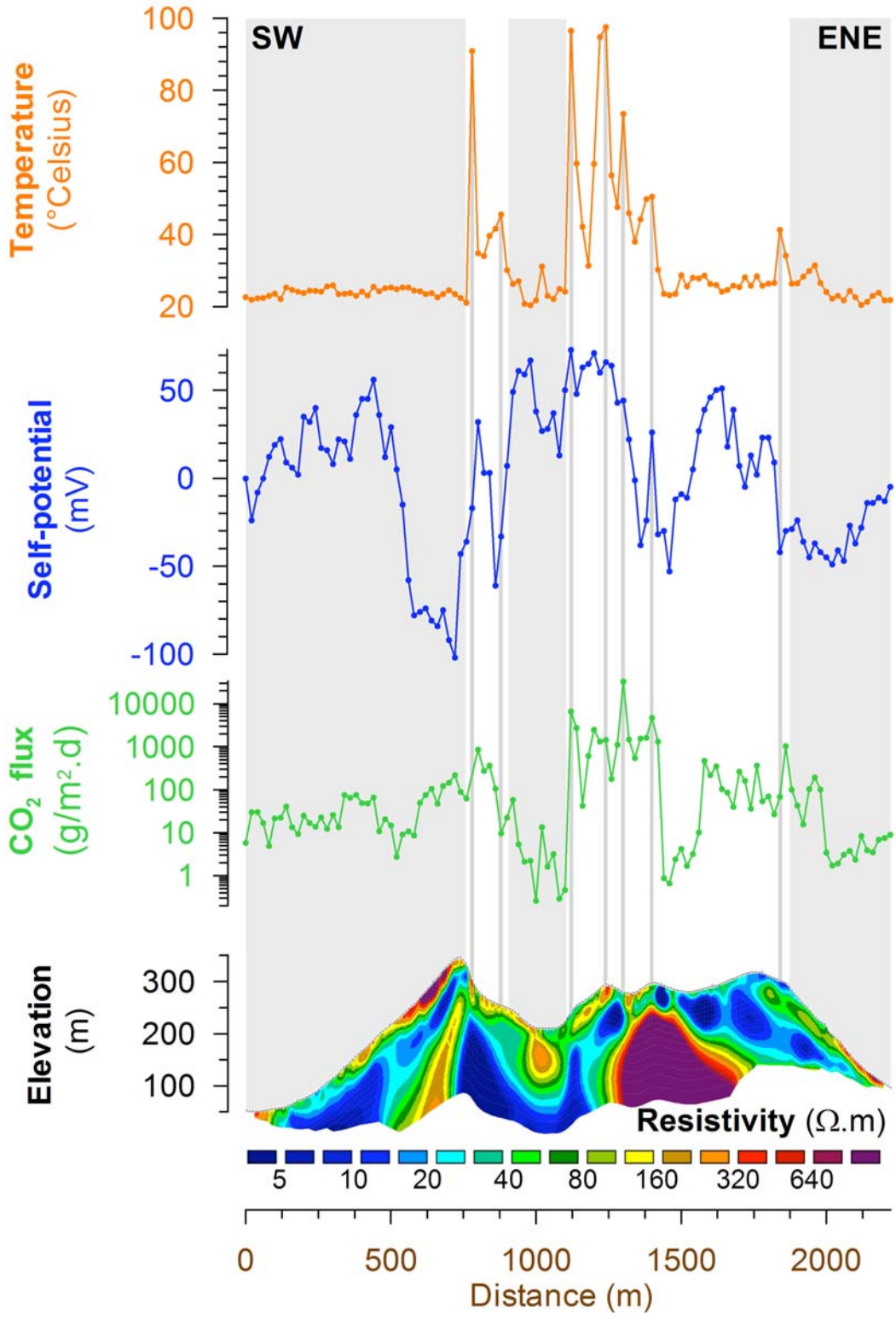

Figure 7. Temperature, self-potential, soil CO_2 flux, and electrical resistivity tomogram along Profile 8.

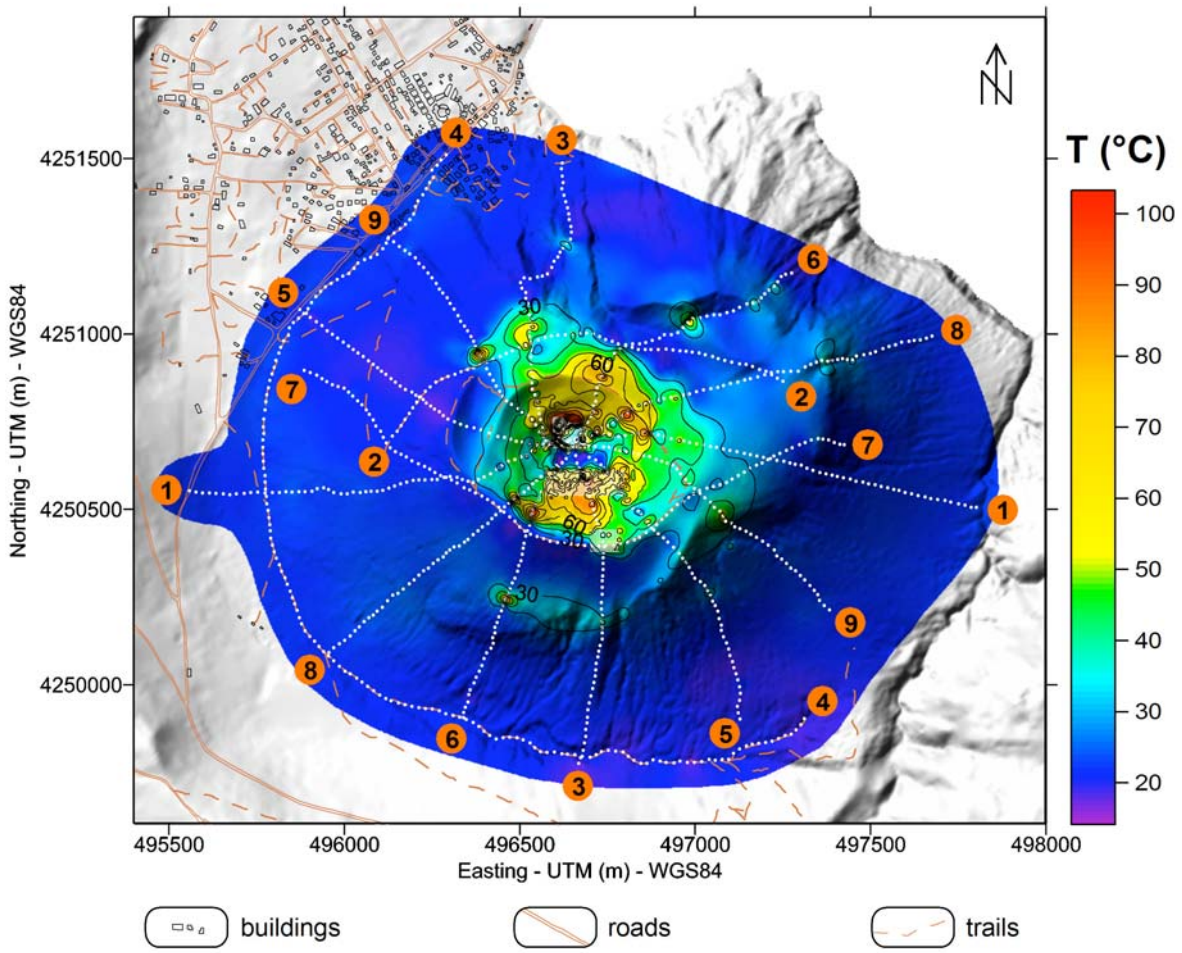

Figure 8. Map of the temperature at a depth of 30 cm superimposed on the DEM of La Fossa cone. The white dots correspond to the location of the temperature measurements of the present study. The dots inside the La Fossa crater correspond to the detailed temperature survey (at the same depth of 30 cm) reported by *Aubert et al*. [2007]. Note that the bottom of the crater is cold (<30°C). Thermal anomalies are sometimes observed on the flanks of the volcano. In this case, these anomalies are indicative of the boundaries of ancient craters.

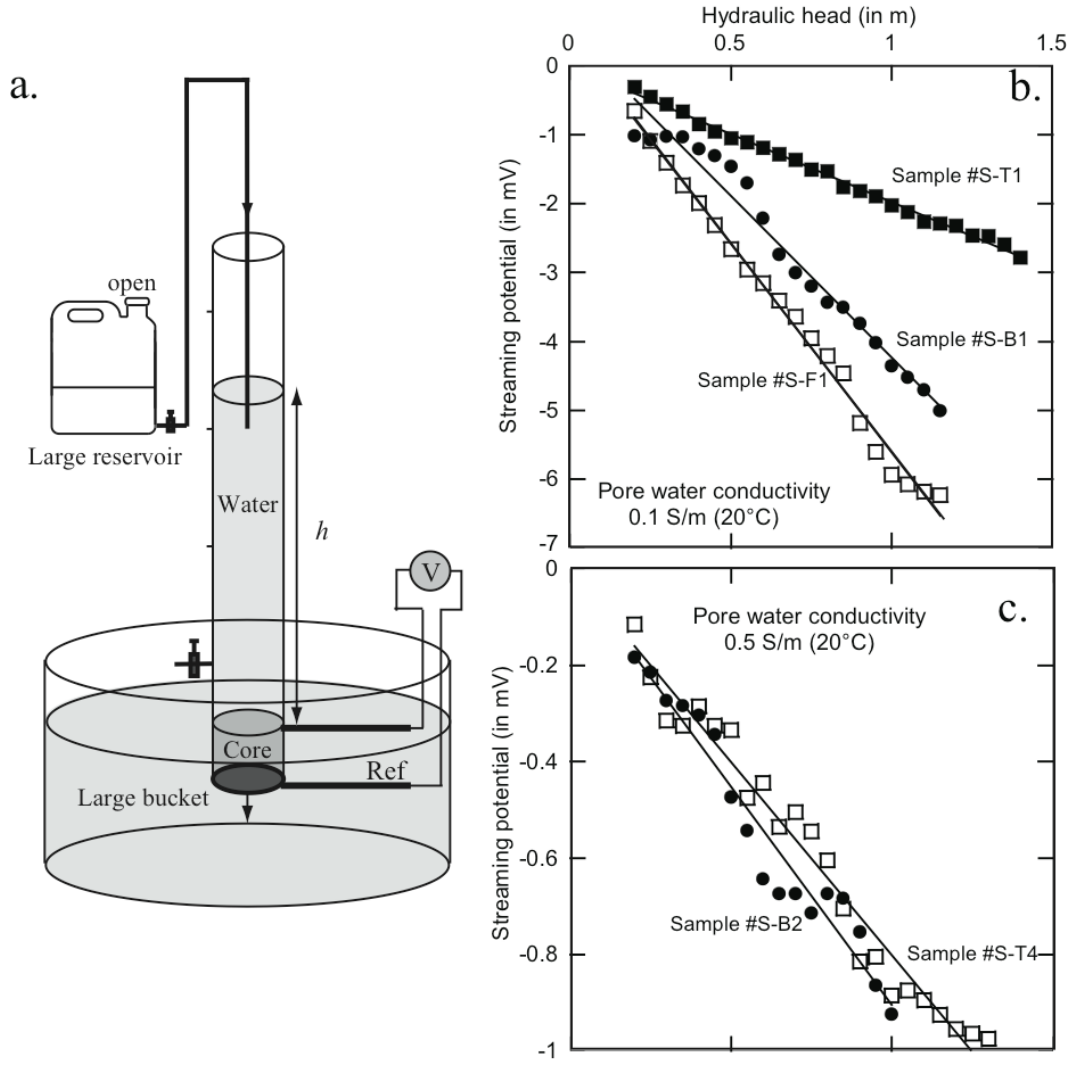

Figure 9. Examples of typical runs for five different volcanic rock samples. **a.** Sketch of the experimental setup used to measure the streaming potential coupling coefficient. The jacketed sample is placed at the bottom of a Plexiglas tube. The record of the self-potentials during the flow of the electrolyte through the sample is done with Ag/AgCl electrodes ("Ref" is the reference electrode). The hydraulic heads are maintained constant at different levels with the help of the large reservoir and the valve. The electromotive force is recorded at these levels between the end-faces of the core sample with a high-impedance voltmeter. **b.** Streaming potentials versus hydraulic heads using a solution at 0.1 S m^{-1} (this value is typical of the conductivity of the pore water flowing in the shallow aquifers of Vulcano). **c.** Same with a solution at 0.5 S m^{-1}. In both cases, we observe linear relationships. Tthe streaming potential coupling coefficient is equal to the slope of these linear trends. The denomination of the samples is the same as in Tables 1 and 2.

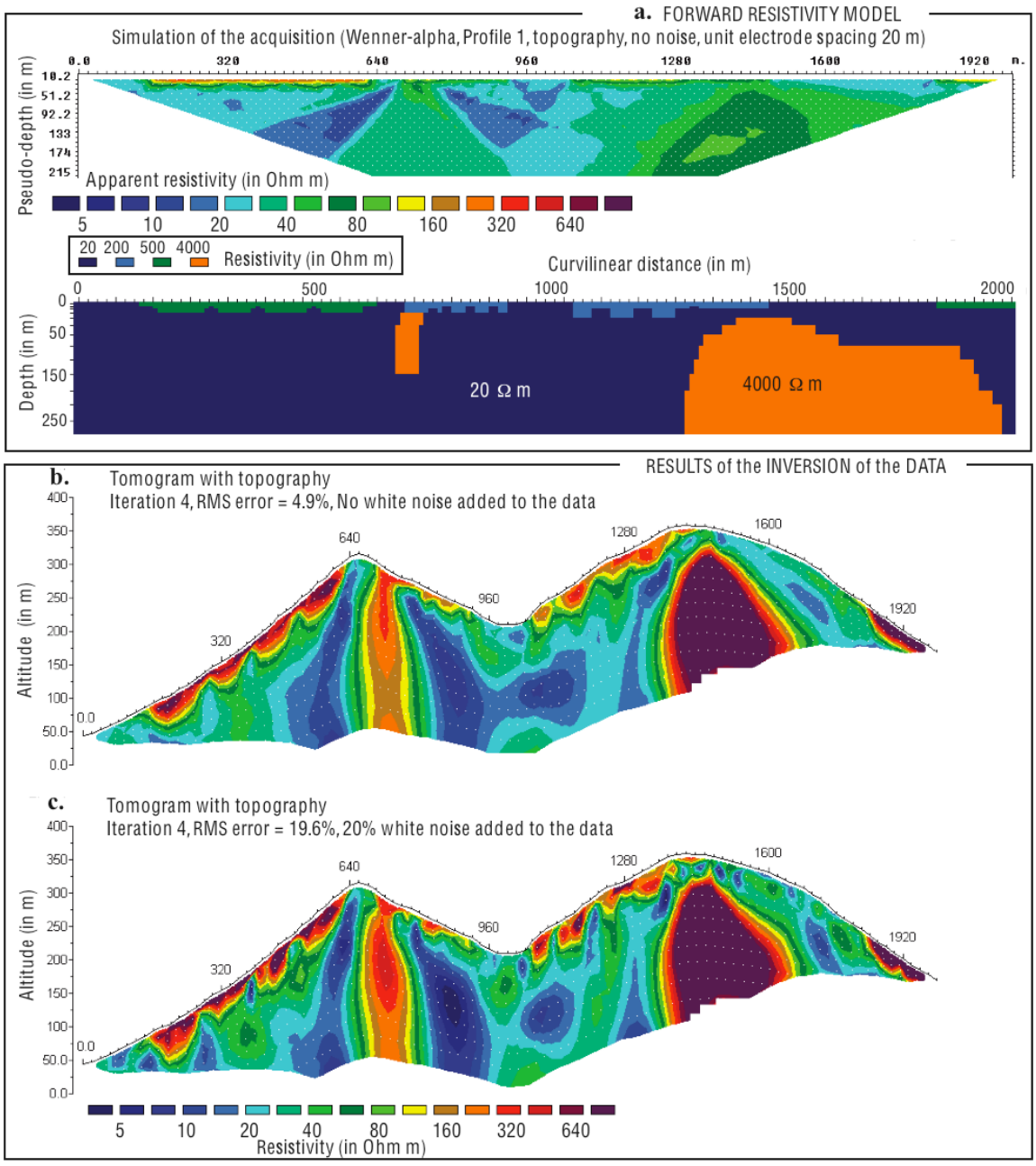

Figure 10. Sensitivity analysis of the resistivity data along profile 1. **a.** We have used a simple resistivity structure by trial and error that can reproduce the resistivity data. In the example shown here, we did not try to model the resistivity anomaly observed in the inversion of the data below the bottom of the crater (see Figure 11a). **b, c.** The resistivity anomaly below of the bottom of the crater is not found even with 20% of white noise added to the data. It seems therefore that this strcuture is not an artefact. The high RMS error found with this profile (25% at the fourth iteration) seems therefore the result of random noise existing in the data because of the low injected current.

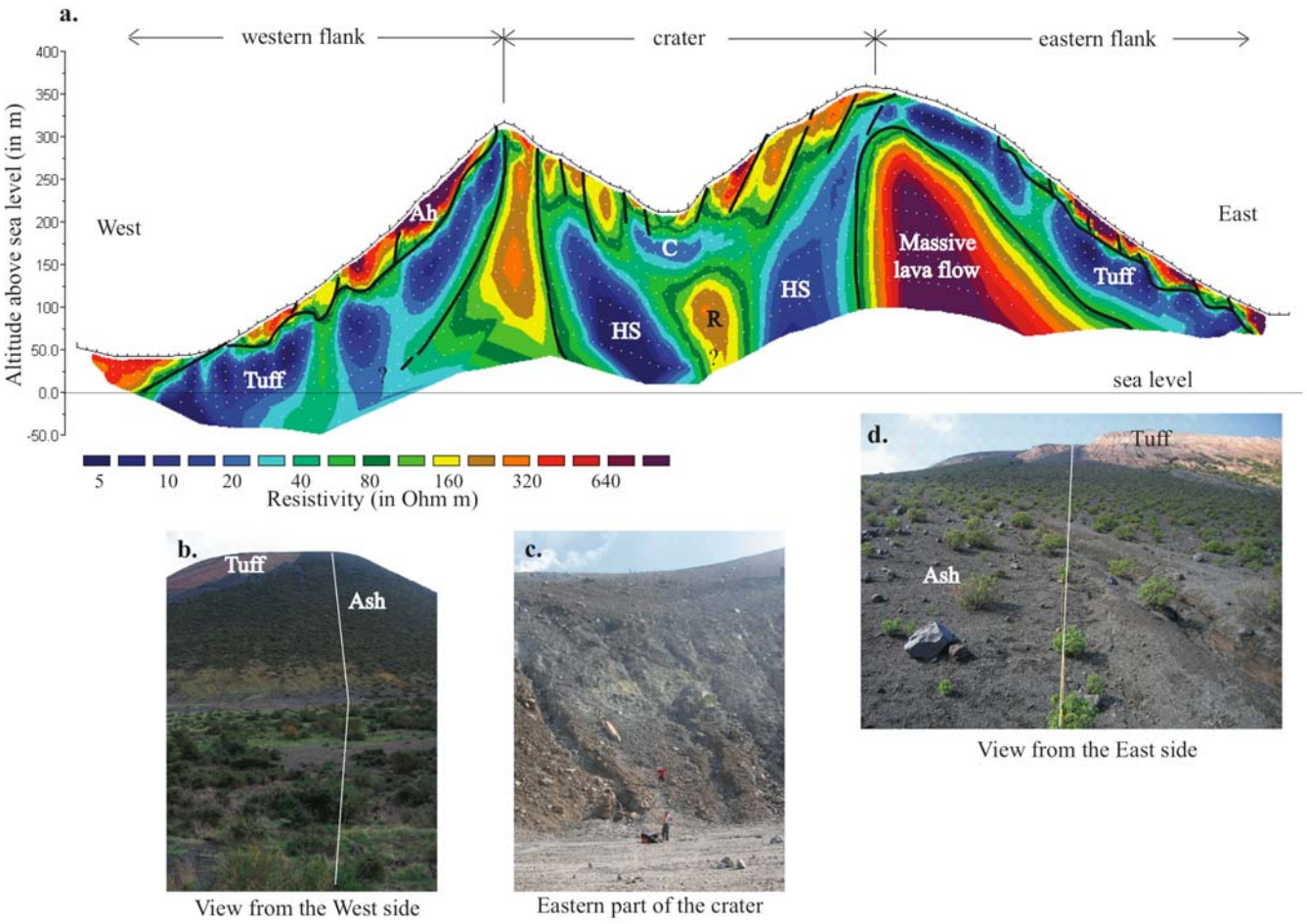

Figure 11. a. Architecture of the Fossa cone along the profile 1 (resistivity tomogram). “Ah” and “HS” stand for respectively Ash and Hydrothermal System. “C” and “R” stand for “Conductive” and “Resistive” body, respectively. **b.** and **d.** Pictures of the Fossa cone from the west and east sides, respectively, showing the position of the ashes relatively to the position of the hydromagmatic tuff (the line shows the position of the profile). **c.** Picture taken inside the crater showing the pyroclastic deposits.

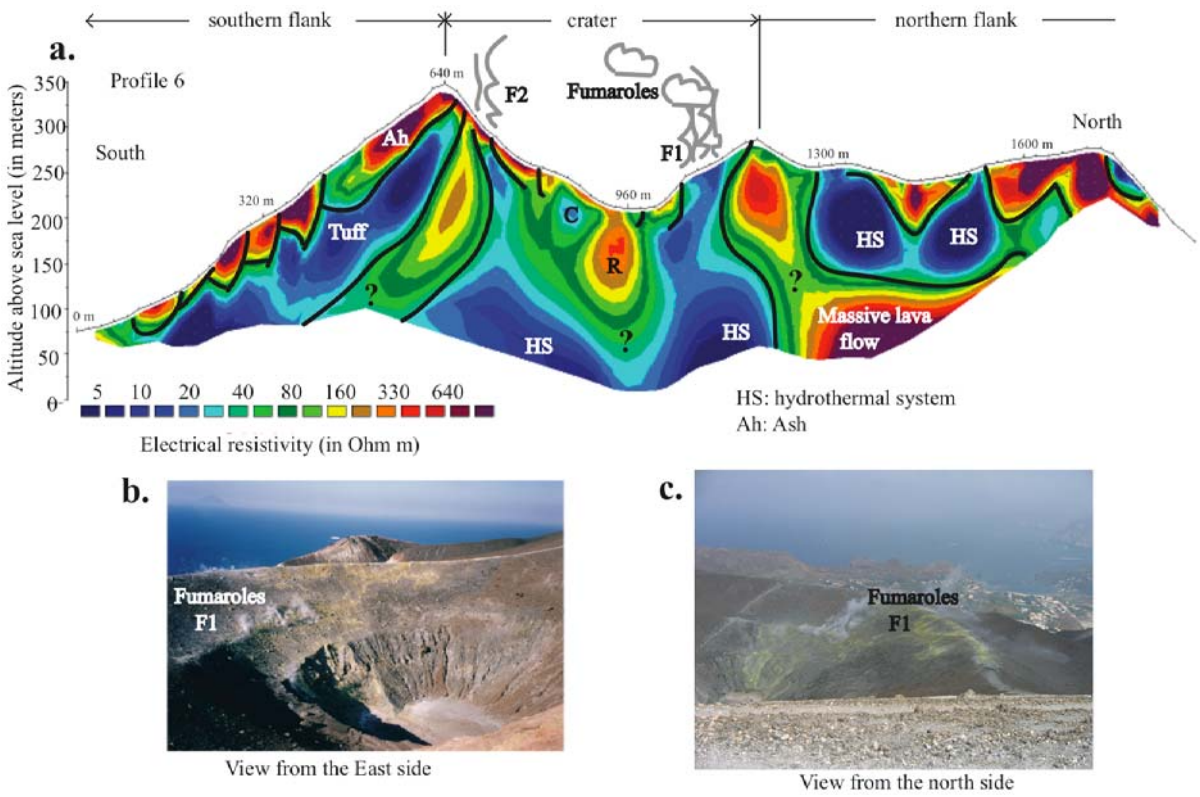

Figure 12. Architecture of the Fossa cone along the profile 6. The root of the area of fumarolic activity can be extended to a depth of 200 meters below the ground surface. F1 and F2: fumaroles, Ah: ash, HS: hydrothermal system. The internal part of the crater is characterized by a pocket of high conductivity (C) and a high resistivity structure (R).

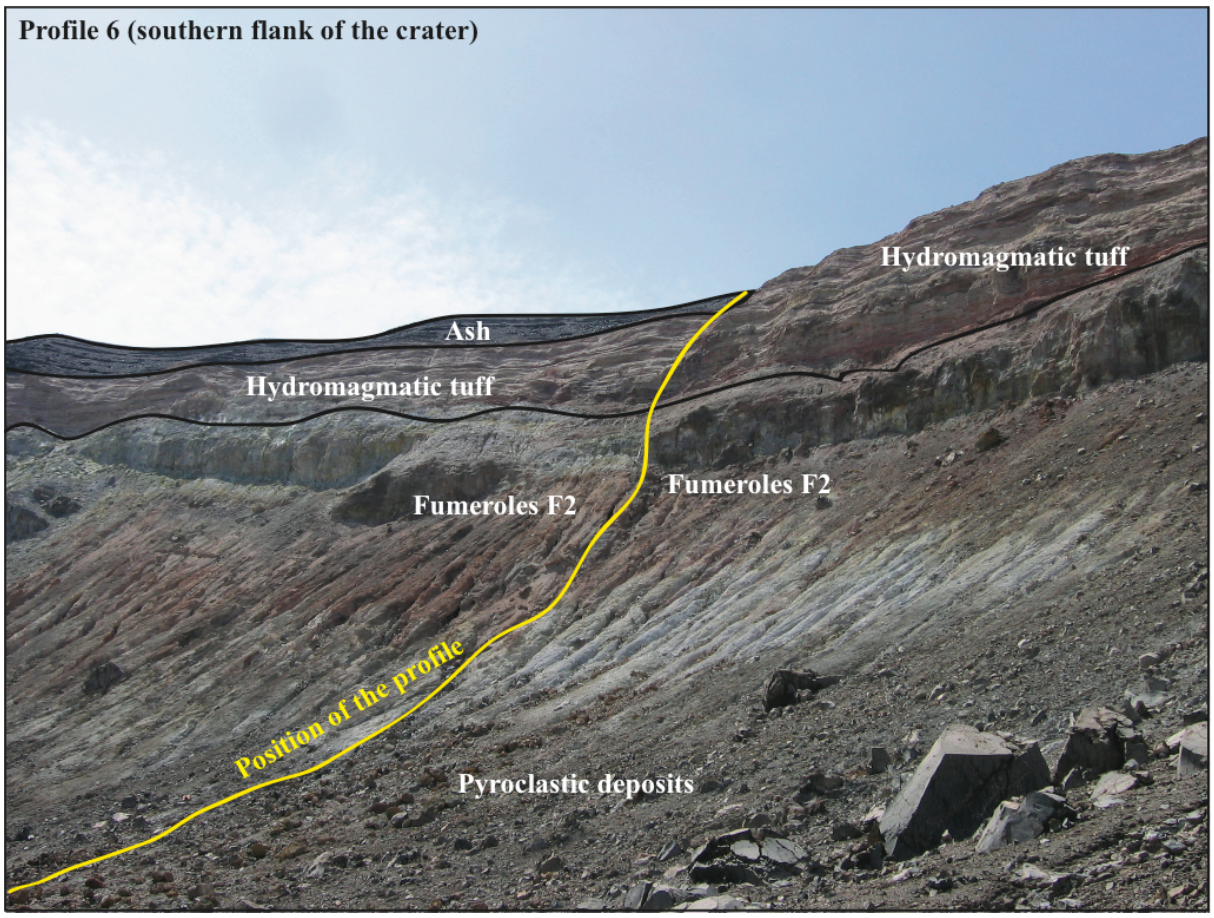

Figure 13. Architecture of the southern part of the crater along Profile 6 with the position of the fumerole 2 (F2).

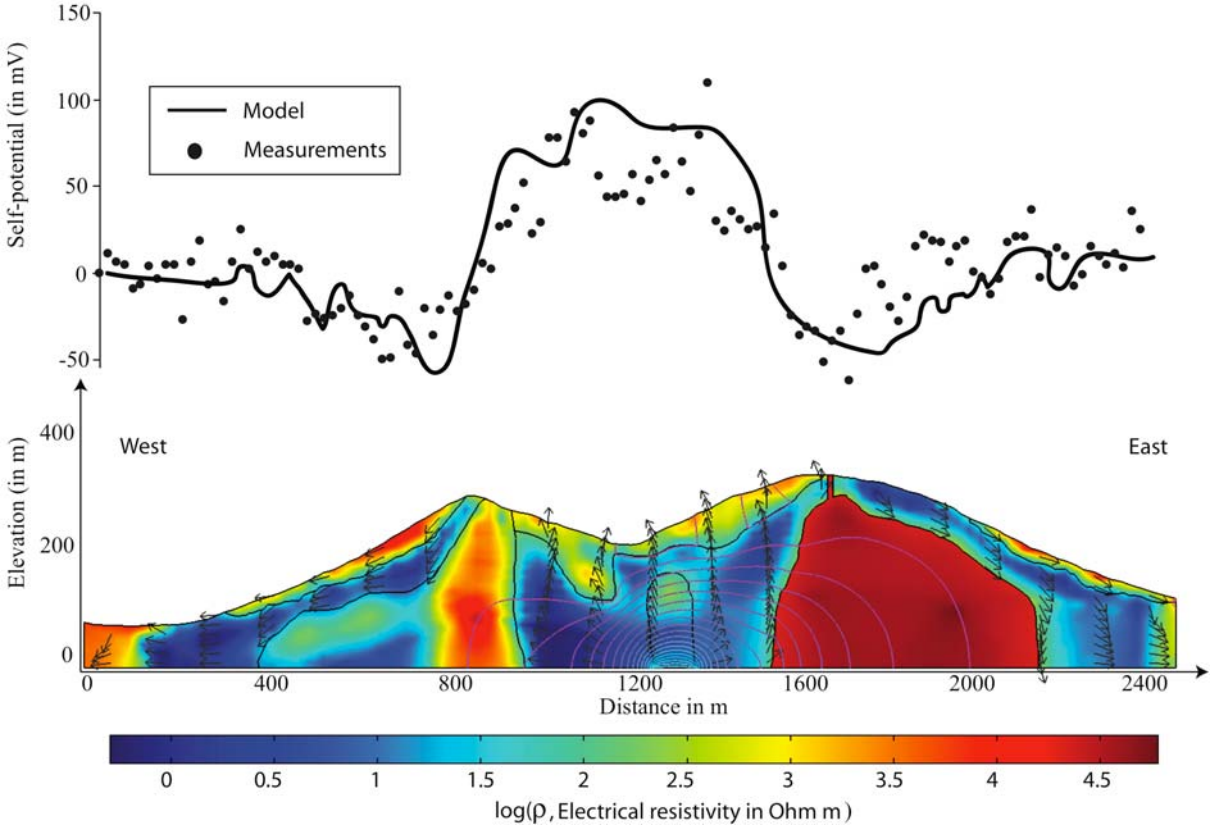

Figure 14. Finite element model of ground-water flow (the arrows represent the normalized seepage velocities) and resulting self-potential distribution at the ground surface of the Fossa Cone obtained using a finite-element code (Comsol Multiphysics 3.3). The negative self-potential anomaly along the flanks of the volcan results from the percolation of the ground water in shallow aquifers while the positive self-potential anomaly inside the crater is due to the upflow of the hydrothermal fluids (profile 1).

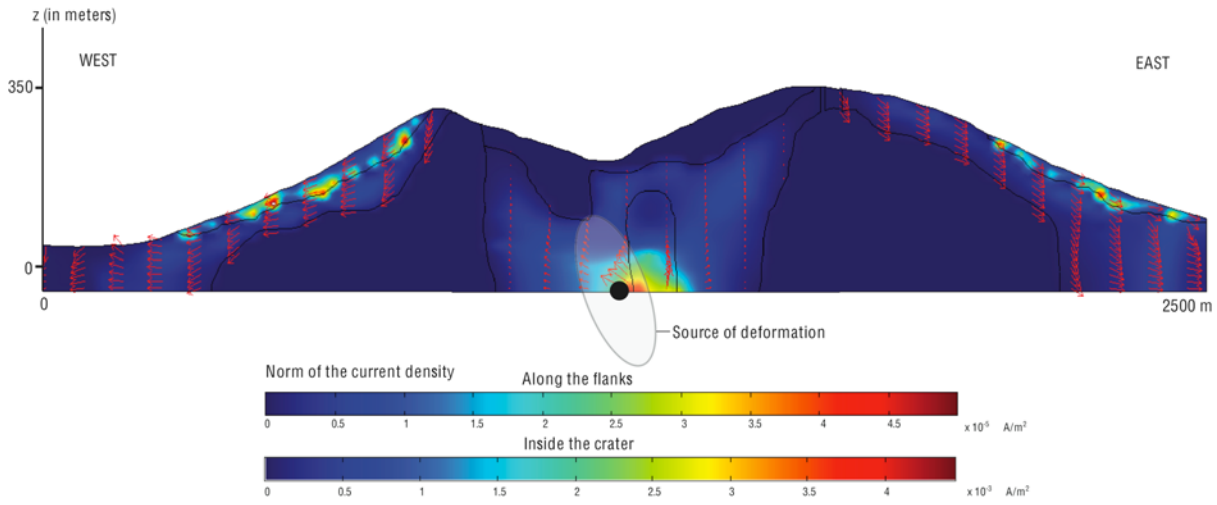

Figure 15. Determination of the sources of current density in the system associated with the flow of the ground water. The ellipsoid corresponds to the deflation source volume observed by *Gambino and Guglielmino* [2008] for the period 1990-1996 inverting electro-optical and levelling measurements in an elastic homogeneous and isotropic half-space.

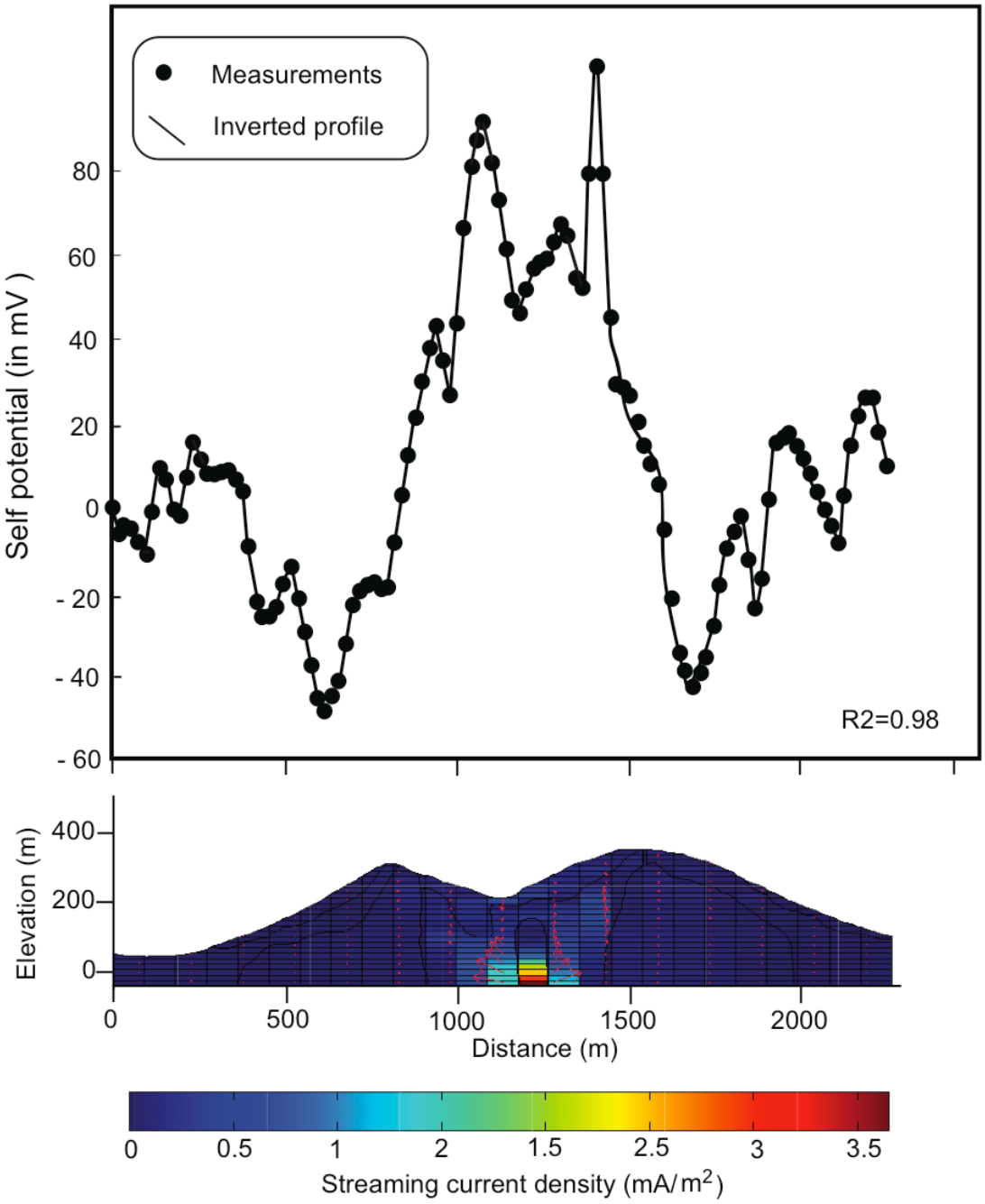

Figure 16. Inversion of the self-potential data in terms of the streaming current density. **a.** Comparison between the measured self-potential data and the self-potential determined from the inverted model (R^2 = 0.98). **b.** Result of the inversion of the self-potential data with a depth weigthing matrix and a derivative operator of order one. The arrows represent the direction of the current density vector.

4.7. Conclusion

Sur des structures volcaniques actives, le potentiel spontanée constitue de toute évidence une méthode efficace pour identifier des zones de remontées de fluides, et les zones purement hydrogéologiques caractérisées par des écoulements gravitaires souterrains. Sur les flancs des édifices volcaniques la transition entre zone hydrogéologique et système hydrothermal est particulièrement bien marquée car ces derniers se manifestent en potentiel spontané par des anomalies positives de quelques centaines à quelques milliers de millivolts.En pratique, cela revient à inverser le gradient potentiel spontané/altitude qui passe d'une valeur négative en zone hydrogéologique à une valeur positive en zone hydrothermale. De ce fait, le minimum du potentiel spontané constitue la limite d'extension du système hydrothermal.

Les résultats issus de l'utilisation de méthodes géophysiques et géochimiques couplées sur Stromboli et Vulcano montrent clairement le potentiel que possèdent ces méthodes pour une meilleure compréhension de la structure interne des édifices dans la mesure où elle nous éclairent sur ses caractéristiques lithologiques (zones de failles, limites de cratère…) mais également sur la dynamique des mouvements de fluides de subsurface que ce soient des fluides hydrothermaux ou encore des nappes d'eau douce. L'importance de ses informations n'est plus à démontrer puisqu'elles procurent un savoir nécessaire à la prévention du risque volcanique ou, comme nous l'avons vu à la recherche de ressources en eau. La méthode de potentiel spontané est complémentaire de méthode de résistivité soit de type galvanomètrique soit par induction (e.g., avec le système SkyTEM expérimenté au Galapagos par d'Ozouville et al. (2008).

4.8. Références

Aizawa, K., R. Yoshimura, N. Oshiman, K. Yamazaki, T. Uto, Y. Ogawa, S.B. Tank, W. Kanda, S. Sakanaka, Y. Furukawa, T. Hashimoto, M. Uyeshima, T. Ogawa, I. Shiozaki, T. Hurst, 2005. Hydrothermal system beneath Mt. Fuji volcano inferred

from magnetotellurics and electric self-potential, *Earth Planet. Sci. Lett.*, 235, 343–355.

Aizawa K., M. Uyeshima, K. Nogami, 2008. Zeta potential estimation of volcanic rocks on 11 island arc-type volcanoes in Japan: Implication for the generation of local self-potential anomalies, *J. Geophys. Res.*, 113.

Aizawa, K., 2008. Classification of self-potential anomalies on volcanoes and possible interpretations for their subsurface structure, *J. Volcanol. Geotherm. Res.*, 175, 253-268.

Aubert, M., I. Dana, A. Gourgaud, 2000. Internal structure of the Merapi summit from self-potential measurements, *J. Volcanol. Geotherm. Res.,* 100, 337-343.

Aubert, M., P. Antraygues, E. Soler, 1993. Interpretation of the self-potential measurements in hydrogeological exploration of a volcanic massif. On the existence of groundwater flow paths on the south flank of the Piton de la Fournaise (Réunion Island). *Bull. Soc. Géol. France*, 64, 17-25.

Aubert, A., I. Dana, M. Livet, 1990. Identification of the boundaries between two watersheds in a volcanic area by self-potential method. *C. R. Acad. Sci. Paris,* 311, 990-1004.

Aubert, M., I. Dana, J.C. Dupuy, 1991. Application of the self-potential method to the detection of underground water courses in a volcanic area, *C. R. Acad. Sci. Paris,* 312, 325-330.

Aubert, M., Q. Atangana, 1996. Self-potential method in hydrogeological exploration of volcanic areas, *Ground Water,* 34(6), 1010-1016.

Aubert, M., I. Dana, A. Gourgaud, 2000. Internal structure of the Merapi summit from self-potential measurements, *J. Volcanol. Geotherm. Res.,* 100, 337-343.

Boubekraoui, S., M. Courteaud, M. Aubert, Y. Albouy, J. Coudray, 1998. New insights into the hydrogeology of a basaltic shield volcano from a comparison between self-potential and electromagnetic data : Piton de la Fournaise, Indian ocean, *J. Appl. Geoph.,* 40, 165-177.

Byrdina, S., S. friedel, J. Wassermann, and J. Zlotnicki, 2003. Self-potential variations associated with ultra-long period seismic signals at Merapi Volcano, *Geophys. Res. Lett., 30*(22), 2156.

Chiodini G., R. Cioni, M. Guidi and C. Raco, 1998. Soil CO_2 flux measurements in volcanic and geothermal areas, Applied Geochemistry, 13(5), 543-552.

Corwin, R.F, and D.B. Hoover, 1979. The self-potential method in geothermal exploration. *Geophysics,* 44 (2), 226-245.

D'Ozouville, N., E. Auken, K. Sorensen, S. Violette, G. de Marsily, B. Deffontaines, et G. Merlen, 2008. Extensive perched aquifer and structural implications revealed by 3D resistivity mapping in a Galapagos volcano, Earth and Planetary Science Letters, 269, 517-521.

Di Maio, R., P. Mauriello, D. Patella, Z. Petrillo, S. Piscitelli, A. Siniscalchi, 1998. Electric and electromagnetic outline of the Mount Somma – Vesuvius structural setting, *J. Volcanol. Geotherm. Res.,* 82, 219-238.

Finizola A., F. Sortino, J-F. Lénat, M. Valenza, 2002. Fluid circulation at Stromboli volcano (Aeolian Islands, Italy) from self-potential and soil gas surveys, *J. Volcanol. Geotherm. Res.*, 116, 1-2, 1-18.

Fittermann, D.V. and R.F. Corwin, 1982. Inversion of self-potential data from Cerro Prieto geothermal field, Mexico, 47(6), 938-945.

Fittermann, D.V., 1983. Modeling of self-potential anomalies near vertical dykes, *Geophysics*, 48, 171-180.

Fitterman, D., 1979. Theory of Electrokinetic-Magnetic Anomalies in a Faulted Half-Space, *J. Geophys. Res.*, 84 (B11), 6031-6040.

Finizola, A., J. F. Lénat, O. Macedo, D. Ramos, J. C. Thouret, and F. Sortino, 2004. Fluid circulation and structural discontinuities inside Misti volcano (Peru) inferred from self-potential measurements, *J. Volcanol. Geotherm. Res.,* 135(4), 343– 360.

Finizola, A., F. Sortino, J.-F. Lénat, M. Valenza, 2002. Fluid circulation at Stromboli volcano (Aeolian Islands, Italy) from self-potential and CO2 surveys, *J. Volcanol. Geotherm. Res.*, 116, 1–18.

Fournier, C., 1989. Spontaneous potential and resistivity surveys applied to hydrogeology in a volcanic area : case history of the chaîne des puys (Puy-de-Dôme, France), *Geophys. Prospecting*, 37, 647-668.

Goldie, M., 2004. Self-potentials associated with the Yanacocha high sulfidation gold deposit in Peru, *Geophysics,* 67(3), 684-689.

Hase, H., T. Ishido, S. Takakura, T. Hashimoto, K. Sato, and Y. Tanaka, 2003. Zêta potential measurement of volcanic rocks from Aso caldera, *Geophys. Res. Lett.*, 30(23), 2210.

Hashimoto, T., Y. Tanaka, 1995. A large self-potential anomaly on Unzen volcano, Shimbara peninsula, Kyushu island, *Japan. Geophys. Res. Lett.,* 22, 191–194.

Ishido, T., and H. Mizutani, 1981. Experimental and theoretical basis of electrokinetic phenomena in rock-water systems and its applications to geophysics, *J. Geophys. Res.,* 86, 1763-1775.

Ishido, T., 2004. Electrokinetic mechanism for the "W"-shaped self-potential profile on volcanoes, *Geophys. Res. Lett.*, 31, L15616.

Ishido, T., 1988. Self-Potential Generation by Subsurface Water Flow through Electrokinetic Coupling, in G. P. Merkler et al. (eds), *Detection of Subsurface Flow Phenomena*, Springer-Verlag, Lecture Notes in Earth Sciences 27, 121.

Jackson, D.B., and J. Kauahikaua, 1987. Regional self-potential anomalies at Kilauea volcano. *"Volcanism in Hawaii"* chapter 40 U.S.G.S. Professional paper 1350, 947-959.

Lénat, J.-F., 1995. Geoelectric methods in volcano monitoring. In: McGuire, B., Kilburn, C.R.J., Murray, J. (Eds.), *Monitoring Active Volcanoes: Strategies, Procedures and Techniques*. University College London.

Loke, M. H. and R. D. Barker, 1996. Rapid least-squares inversion of apparent resistivity pseudosections by a quasi-newton method, *Geophysical Prospecting*, 44, 131–152.

Malengreau, B., J.F. Lénat, A. Bonneville, 1994. Cartographie et surveillance temporelle des anomalies de Polarisation Spontanée (PS) sur le Piton de la Fournaise, *Bull. Soc. Géol. Fr.*, 165,3, 221-232.

Massenet, F. and V. N. Pham, 1985. Experimental and Theoretical Basis of Self-Potential Phenomena in Volcanic Areas with Reference to Results Obtained on Mount Etna (Sicily), *Earth Planet. Sci. Lett.* 73, 415–429.

Michel, S., and J. Zlotnicki, 1998. Self-potential and magnetic surveying of La Fournaise volcano (Réunion Island): Correlations with faulting, fluid circulation, and eruption, *J. Geophys. Res.* 103, 17,845-17,857.

Morgan, F. D., E. R. Williams, and T. R. Madden, 1989. Streaming potential of westerly granite with applications, *J. Geophys. Res.,* 94, 12,449-12461.

Nishida, Y., N. Matsushima, A. Goto, Y. Nakayama, A. Oyamada, M. Utsugi and H. Oshima, 1996, Self-Potential Studies in Volcanic Areas (3) Miyake-jima, Esan and Usu, *J. Fac. Sci.*, Hokkaido Univ. Ser. 7, 10, 63.

Nourbehecht, B., 1963. Irreversible thermodynamic effects in inhomogeneous media and their applications in certain geoelectric problems, *Ph.D. thesis,* Mass. Inst. of Technol., Cambridge.

Parkinson, K. J., 1981. An improved method for measuring soil respiration in the field, *J. Appl. Ecol.,* 18, 221-228.

Revil A., 1999. Ionic diffusivity, electrical conductivity, membrane and thermoelectric potentials in colloids and granular porous media: a unified model, *J. Colloid Interface Sci.*, 212, 503-522.

Revil, A., A. Finizola, F. Sortino, M. Ripepe, 2004. Geophysical investigations at Stromboli volcano, Italy: implications for ground water flow and paroxysmal activity, *Geophys. J. Int.*, 157, 426–440.

Revil A., A. Finizola, S. Piscitelli, E. Rizzo, T. Ricci and A. Crespy, 2008. Inner structure of La Fossa di Vulcano (Vulcano Island, southern Tyrrhenian Sea, Italy) revealed by high-resolution electric resistivity tomography coupled with self-potential, temperature, and CO_2 diffuse degassing measurements, *J. Geophys. Res.*, 113, B07207.

Sasai, Y., M. Uyeshima, J. Zlotnicki, H. Utada, T. Kagiyama, T. Hashimoto, Y. Takahashi, , 2002. Magnetic and electric field observations during the 2000 activity of Miyaki-jima volcano, Central Japan, *Earth Planet. Sci. Lett.*, 203, 769–777.

Sasai, Y., J. Zlotnicki, Y. Nishida, P. Yvetot, P. Morat, H. Murakami, Y. Tanaka, Y. Ishikawa, S. Koyama, and W. Sekiguchi, 1997. Electromagnetic Monitoring of Miyake-jima Volcano, Izu Bonin Arc, Japan: A Preliminary Report, *J. Geomag. Geoelectr.,* 49, 1293.

Sato, M. H.M. Mooney, 1960. The electrochemical mechanism of sulfide self potentials, *Geophysics,* 35, 226-249.

Sill, W.R., 1983. Self-potential modeling from primary flows, *Geophysics,* 48, 76-86.

Thouret, J.-C., A. Finizola, M. Forani, A. Legeley-Padovani, J. Suni, M. Frechen, 2001. Geology of El Misti volcano near the city of Arequipa, Peru, *GSA. Bull.*, 113, 1593–1610.

Yamashita, S., 1961. The Electromotive Force Generated within the Ore body by the Temperature Difference, *J. Min. Coll., Akita Univ. Ser.,* A 1, 69

Zablocki, C.J., 1978. Streaming potentials resulting from the descent of meteoric water. A possible source mechanism for Kilauean self-potential anomalies. *Geothermal Ressources Council Transactions,* 2 : 747-748.

Zablocki, C. J., 1976. Mapping Thermal Anomalies on an Active Volcano by the Self-Potential Method, Kilauea, Hawaii, *Proc. 2nd U.N. Symp. on the Development and Use of Geothermal Resources*, San Francisco, **2**, 1299.

Zhang G.-B. and M. Aubert 2003. Quantitative interpretation of self-potential anomalies in hydrogeological exploration of volcanic areas: a new approach, *Near Surf. Geophys.*, 69–75.

Zlotnicki, J., G. Boubon, J.P. Viodé, J.F. Delarue, A. Mille, F. Bruère, 1998. Hydrothermal circulation beneath Mount Pelée inferred by self potential surveying. Structural and tectonic implications, *J. Volcanol. Geotherm. Res.,* 84, 73-91.

Zlotnicki, J., M. Feuillard, G. Hammouya, 1994. Water circulations on La Soufrière volcano inferred by self-potential surveys (Guadeloupe, Lesser Antilles). Review of volcanic activity, *J. Geomag. Geoelectr.,* 46, 797-813.

Zlotnicki, J., S. Michel, C. Annen, 1994. Anomalies de polarisation spontanée et systèmes convectifs sur le volcan du Piton de la Fournaise (Ile de la Réunion, France), *C.R. Acad. Sci. Paris,* t.318 - II, 1325-1331.

Zlotnicki, J., Y. Nishida, 2003. Review of morphological insights on self-potential anomalies on volcanoes, *Surv. Geophys.* 24, 291–338.

Zlotnicki, J., J. L. Le Mouël, Y. Sasai, P. Yvetot, and M. H. Ardisson, 2001. Self-potential changes associated with the volcanic activity. Short-term signals associated with March, 9, 1998 Eruption, *Ann. Geofis.,* 44(2), 335.

Conclusions et Perspectives

Les principaux résultats de cette thèse ont été:

(1) d'étendre la théorie de l'électrofiltration au régime d'écoulement laminaire inertiel (pour de fortes valeurs du nombre de Reynolds) et de prendre en compte l'effet de la conductivité de surface à travers l'influence d'un autre nombre adimensionnel, le nombre de Dukhin. Cette nouvelle théorie a été validée par des expériences sur billes de verre en laboratoire. Ajouter des hétérogénéités puis travailler sur de nouveaux matériaux avec toute une gamme de taille de particules pourrait nous permettre de nous rapprocher des conditions naturelles.

(2) de caractériser et localiser les sources électriques associées à des perturbations hydromécaniques. Pour cela nous avons présenté une extension de la théorie de l'électrofiltration au cas d'un milieu poroélastique saturé en eau. Nous avons développé une expérience en cuve à l'aide d'un système de mesure ultra-sensible. Nous avons montré que ce type de source initié par un très faible changement de pression était détectable et avait une signature électrique caractéristique. Grâce à l'association des méthodes de transformées en ondelettes et d'intercorrélation, nous avons pu localiser la source et définir sa nature dipolaire. Il serait intéressant, pour se rapprocher d'un système naturel, de développer de nouveaux protocoles en utilisant d'autres matériaux provenant directement des terrains à étudier en incluant des hétérogénéités de résistivité électrique et de perméabilité. A l'échelle d'un volcan, l'intensité du signal associée à de la fracturation dépend de la profondeur de la source. Ces signaux sont aujourd'hui mesurables d'autant plus qu'il est possible de s'affranchir (par filtrage) du bruit associé aux activités anthropiques et telluriques afin de gagner en précision.

(3) de situer et déterminer la profondeur d'aquifères en terrains volcaniques et de mieux comprendre la structure interne d'édifices comme Stromboli et Vulcano dans l'intention de mettre en place de nouveaux systèmes de surveillance.

A la suite de ces travaux, nous avons imaginé de nouvelles expériences à effectuer au Laboratoire à Bas Bruit de Rustrel (ancienne base militaire de lancement des missiles nucléaires du plateau d'Albion). La capsule blindée dans laquelle se tenaient les officiers de tir a un niveau de bruit électromagnétique 100 fois inférieur au bruit d'un cerveau humain dans sa phase de sommeil la plus calme. Nous pourrions dans ce cas coupler des données électriques à des données électromagnétiques précises.

L'application du potentiel spontané dans l'étude des processus hydromécaniques ouvrent de nouvelles perspectives concernant l'utilisation des données de potentiel spontané pour le suivi en continu des processus de fracturation, non seulement en domaine volcanique mais aussi sur les glaciers et les zones de failles actives.

Sur les flancs des édifices volcaniques, la transition entre zone hydrogéologique et système hydrothermal est particulièrement bien marquée car les systèmes hydrothermaux se manifestent par des anomalies positives de quelques centaines à quelques milliers de millivolts tandis que les zones d'écoulements gravitaires sont le plus souvent associées à des anomalies négatives. De ce fait, le minimum de potentiel spontané constitue la limite d'extension du système hydrothermal. Comme nous avons pu le constater sur le Stromboli et Vulcano, l'association de méthodes géophysiques et géochimiques devient un outil indispensable dans la compréhension du fonctionnement général des volcans. Sur le Stromboli, il serait intéressant de procéder à des analyses biologiques et chimiques de l'eau de l'aquifère afin de déterminer si son utilisation est possible pour l'approvisionnement des populations locales ou l'irrigation. Sur Vulcano il est envisagé de réaliser une inversion trois dimensions des données de résistivité électrique et de gravité afin d'identifier plus précisément les discontinuités structurales de l'édifice. La combinaison de données sismiques, de potentiel spontané et de gravité permettrait certainement d'imager plus finement la géométrie de l'édifice. Ce dernier point est très important dans l'évaluation du risque volcanique et par conséquent dans la protection des populations.

Bibliographie

A

Agapiou J.S. and M.F. De Vries, 1989. An experimental determination of the thermal conductivity of a stainless steel powder metallurgy material, *J. Heat Transfer,* 111, 281–286.

Aizawa K., M. Uyeshima, K. Nogami, 2008. Zeta potential estimation of volcanic rocks on 11 island arc-type volcanoes in Japan: Implication for the generation of local self-potential anomalies, *J. Geophys. Res.*, 113, B02201, doi:10.1029/2007JB005058.

Aizawa, K., 2008. Classification of self-potential anomalies on volcanoes and possible interpretations for their subsurface structure, *J. Volcanol. Geotherm. Res.*, 175, 253-268.

Aizawa, K., R. Yoshimura, N. Oshiman, K. Yamazaki, T. Uto, Y. Ogawa, S.B. Tank, W. Kanda, S. Sakanaka, Y. Furukawa, T. Hashimoto, M. Uyeshima, T. Ogawa, I. Shiozaki, T. Hurst, 2005. Hydrothermal system beneath Mt. Fuji volcano inferred from magnetotellurics and electric self-potential, *Earth Planet. Sci. Lett.*, 235, 343–355.

Arora, T., A. Revil, N. Linde, and J. Castermant, 2007. Non-intrusive determination of the redox potential of contaminant plumes using the self-potential method, *Contaminant Hydrology*, 92, 274-292.

Aubert, M., P. Antraygues, E. Soler, 1993. Interpretation of the self-potential measurements in hydrogeological exploration of a volcanic massif. On the existence of groundwater flow paths on the south flank of the Piton de la Fournaise (Réunion Island). *Bull. Soc. Géol. France*, 64, 17-25.

Aubert, M., Dana, I., Gourgaud, A., 2000. Internal structure of the Merapi summit from self-potential measurements. *J. Volcanol. Geotherm. Res.,* 100, 337-343.

Aubert, M. and Yene Atangana, Q., 1996. Self-potential method in hydrogeological exploration of volcanic areas, *Ground-water*, 34 (6), 1010–1016.

Aubert, A., I. Dana, M. Livet, 1990. Identification of the boundaries between two watersheds in a volcanic area by self-potential method, *C. R. Acad. Sci. Paris,* 311, 990-1004.

Aubert, M., I. Dana, J.C. Dupuy, 1991. Application of the self-potential method to the detection of underground water courses in a volcanic area, *C. R. Acad. Sci. Paris,* 312, 325-330.

B

Bernabé Y., 1998. Streaming potential in heterogeneous networks, *J. Geophys. Res.*, 103, 20827–20841.

Bernabé, Y., and A. Revil, 1995. Pore-scale heterogeneity, energy dissipation and the transport properties of rocks, *Geophys. Res. Lett.*, 22, 1529-1532.

Byrdina, S., S. friedel, J. Wassermann, and J. Zlotnicki, 2003. Self-potential variations associated with ultra-long period seismic signals at Merapi Volcano, *Geophys. Res. Lett., 30*(22), 2156.

Block, G. I., and J. G. Harris, 2006. Conductivity dependence of seismoelectric wave phenomena in fluid-saturated sediments, *J. Geophys. Res.,* 111, B01304, doi:10.1029/2005JB003798.

Boubekraoui, S., M. Courteaud, M. Aubert, Y. Albouy, J. Coudray, 1998. New insights into the hydrogeology of a basaltic shield volcano from a comparison between self-potential and electromagnetic data : Piton de la Fournaise, Indian ocean, *J. Appl. Geoph.,* 40, 165-177.

C

Chiodini G., R. Cioni, M. Guidi and C. Raco, 1998. Soil CO_2 flux measurements in volcanic and geothermal areas, *Applied Geochemistry*, 13(5), 543-552.

Corwin, R., and H. Morrison, 1977. Self-Potential Variations Preceding Earthquakes in Central California, *Geophys. Res. Lett.,* 4(4), 171-174.

Corwin, R.F, and D.B. Hoover, 1979. The self-potential method in geothermal exploration. *Geophysics,* 44 (2), 226-245.

Corwin, R. F., 1990. The Self-Potential Method for Environmental and Engineering Applications in S. H. Ward (ed.), *Geotechnical and Environmental Geophys.*, Vol. 1, Soc. Explor. Geophys., Tulsa, 127.

Crespy, A., A. Bolève, and A. Revil, 2007. Influence of the Dukhin and Reynolds numbers on the apparent zeta potential of granular media, *J. Colloid Interface Sci.,* 305, 188-194.

D

D'Ozouville, N., E. Auken, K. Sorensen, S. Violette, G. de Marsily, B. Deffontaines, et G. Merlen, 2008. Extensive perched aquifer and structural implications revealed by 3D

resistivity mapping in a Galapagos volcano, *Earth and Planetary Science Letters*, 269, 517-521.

Di Maio, R., P. Mauriello, D. Patella, Z. Petrillo, S. Piscitelli, A. Siniscalchi, 1998. Electric and electromagnetic outline of the Mount Somma – Vesuvius structural setting, *J. Volcanol. Geotherm. Res.,* 82, 219-238.

Doussan, C., L. Jouniaux, and J.-L. Thony, 2002. Variations of self-potential and unsaturated water flow with time in sandy loam and clay loam soils, *Journal of Hydrology*, 267, 173–185.

Dukhin, S. S. and B. V Derjaguin, 1974. Surface and Colloid Science (Wiley-Interscience, New York).

F

Finizola, A., J. F. Lénat, O.Macedo, D. Ramos, J. C. Thouret, and F. Sortino, 2004. Fluid circulation and structural discontinuities inside Misti volcano (Peru) inferred from self-potential measurements, *J. Volcanol. Geotherm. Res.,* 135(4), 343– 360.

Finizola A., F. Sortino, J-F. Lénat, M. Valenza, 2002. Fluid circulation at Stromboli volcano (Aeolian Islands, Italy) from self-potential and soil gas surveys, *J. Volcanol. Geotherm. Res.*, 116, 1-2, 1-18.

Fitterman, D., 1978. Electrokinetic and Magnetic Anomalies Associated With Dilatant Regions in a Layered Earth, *J. Geophys. Res.*, 83(B12), 5923-5928.

Fitterman, D., 1979. Theory of Electrokinetic-Magnetic Anomalies in a Faulted Half-Space, *J. Geophys. Res.*, 84 (B11), 6031-6040.

Fittermann, D.V. and R.F. Corwin, 1982. Inversion of self-potential data from Cerro Prieto geothermal field, Mexico, 47(6), 938-945.

Fittermann, D.V., 1983. Modeling of self-potential anomalies near vertical dykes, *Geophysics*, 48, 171-180.

Fournier, C, 1989. Spontaneous potential and resistivity surveys applied to hydrogeology in a volcanic area : case history of the chaîne des puys (Puy-de-Dôme, France), *Geophys. Prospecting*. 37, 647-668.

Fox, R.W., 1830. The electromagnetic properties of metalliferous veins in the mines of Cornwall. In: *Proc. R. Soc*. London 2, 411.

Freund, F., A. Takeuchi, and B.W.S. Lau, 2006. Electric currents streaming out of stressed igneous rocks. A step toward understanding pre-earthquake low frequency EM emissions, *Physics and Chemistry of the Earth*, 31, 389-396.

G

Gex, P., 1980. Electrofiltration phenomena associated with several dam sites, *Bulletin of the Society Vaud Science and Nature*, 357(75), 39-50.

Goldie, M., 2004. Self-potentials associated with the Yanacocha high sulfidation gold deposit in Peru, *Geophysics,* 67(3), 684-689.

Guichet X., and P. Zuddas, 2003. Effets of secondary minerals on electrokinetic phenomena during water-rock interation, *Geophys. Res. Lett, 30*, No. 13, 1714, doi : 10.1029/2003GL017480.

H

Haartsen, M. W., and M. N. Toksöz, 1996. Dynamic streaming currents from seismic point sources in homogeneous poroelastic media, *Geophys. J. Int.,* 132, 256– 274.

Hase, H., T. Ishido, S. Takakura, T. Hashimoto, K. Sato, and Y. Tanaka, 2003. Zêta potential measurement of volcanic rocks from Aso caldera, *Geophys. Res. Lett.*, 30(23), 2210.

Hashimoto, T., Y. Tanaka, 1995. A large self-potential anomaly on Unzen volcano, Shimbara peninsula, Kyushu island, *Japan. Geophys. Res. Lett.,* 22, 191–194.

Hearst, J.R., P.H. Nelson, and F.L. Paillett, 2000. Well logging for physical properties, Wiley-VCH Verlag GmBH, Germany.

Hornby P, F . Boschetti, F. Horowitz, 1999. Analysis of Potential Field Data in the Wavelet Domain, *Geophysical Journal International*, 137, 137-276.

I

Ishido, T., and H. Mizutani, 1981. Experimental and theoretical basis of electrokinetic phenomena in rock-water systems and its applications to geophysics, *J. Geophys. Res.,* 86, 1763-1775.

Ishido, T., 2004. Electrokinetic mechanism for the "W"-shaped self-potential profile on volcanoes, *Geophys. Res. Lett.*, 31, L15616.

Ishido, T., 1988. Self-Potential Generation by Subsurface Water Flow through Electrokinetic Coupling, in G. P. Merkler et al. (eds), *Detection of Subsurface Flow Phenomena*, Springer-Verlag, *Lecture Notes in Earth Sciences*, 27, 121.

Iuliano, T., P. Mauriello, and D. Patella, 2002. Looking inside Mount Vesuvius by potential fields integrated probability tomographies, *J. Volcanology Geothermal Res.,* 113, 363-378.

J

Jackson, D.B., and J. Kauahikaua, 1987. Regional self-potential anomalies at Kilauea volcano. *"Volcanism in Hawaii"* chapter 40 U.S.G.S. Professional paper 1350, 947-959.

Jardani A., J.P. Dupont, and A. Revil, 2006. Self-potential signals associated with preferential ground water flow pathways in sinkholes, *J. Geophys. Res.*, 111, B09204, doi: 10.1029/2005JB004231.

Jardani, A., Revil, A., Barrash, W., Crespy, A., Rizzo, E., Straface, S., Cardiff, M., Malama, B., Miller, C., and Johnson, T. (2008) Reconstruction of the Water Table from Self-Potential Data: A Bayesian Approach, Ground Water, doi:10.1111/j.1745-6584.2008.00513.x

L

Lénat, J.F., B. Robineau, S. Durand and P. Bachélery, 1998. Etude de la zone sommitale du volcan Karthala (Grande Comore) par polarisation spontanée, *C.R. Acad. Sci.,* 327, 781-788.

Lénat, J.-F., 1995. Geoelectric methods in volcano monitoring. In: McGuire, B., Kilburn, C.R.J., Murray, J. (Eds.), *Monitoring Active Volcanoes: Strategies, Procedures and Techniques*. University College London, 248–274.

Leroy, P., and A. Revil, 2004, A triple-layer model of the surface electrochemical properties of clay minerals, *Journal of Colloid and Interface Science*, 270, 371-381.

Linde, N., D. Jougnot, A. Revil, S. Matthäi, T. Arora, D. Renard, and C. Doussan, 2007. Streaming current generation in two-phase flow conditions, *Geophysical Research Letters, 34(3)*, L03306, doi: 10.1029/2006GL028878.

Loke, M. H. and Barker, R. D., 1996. Rapid least-squares inversion of apparent resistivity pseudosections by a quasi-newton method. *Geophysical Prospecting*, 44, 131–152.

Lorne, B, F. Perrier and J.P. Avouac, 1999a. Streaming potential measurements 1. Properties of the electrical double layer from crushed rock samples, *J. of Geophys. Res.* 104 pp. 857–877.

M

Malengreau, B., J.F. Lénat, A. Bonneville, 1994. Cartographie et surveillance temporelle des anomalies de Polarisation Spontanée (PS) sur le Piton de la Fournaise, *Bull. Soc. Géol. Fr.*, 165,3, 221-232.

Marshall, D.J., and T.R. Madden, 1959. Induced polarization, a study of its causes, *Geophysics,* 4(4), 790-816.

Massenet, F. and V. N. Pham, 1985. Experimental and Theoretical Basis of Self-Potential Phenomena in Volcanic Areas with Reference to Results Obtained on Mount Etna (Sicily), *Earth Planet. Sci. Lett.* 73, 415–429.

Mendelson, K. S., and M. H. Cohen, 1982. The effect of grain anisotropy on the electrical properties of sedimentary rocks, *Geophysics*, 47(2), 257–263.

Michel, S., and J. Zlotnicki, 1998. Self-potential and magnetic surveying of La Fournaise volcano (Réunion Island): Correlations with faulting, fluid circulation, and eruption, *J. Geophys. Res.* 103, 17,845-17,857.

Moore, J. R., and S. D. Glaser, 2006. The origins of the self-potential response during hydraulic fracturing, *Eos Trans. AGU*, *87*(15), Fall Meet. Suppl., Abstract NS21A-04.

Moore, J.R. and S.D. Glaser, 2007. Self-Potential Observations During Hydraulic Fracturing, *J. Geophys. Res.*, Vol. 112, B02204, 1-17.

Morgan, F. D., E. R. Williams and T. R. Madden, 1989. Streaming potential of westerly granite with applications, *J. Geophys. Res., 94*, 12,449-12461.

Moreau F., D. Gibert, M. Holschneider and G. Saracco 1997. Wavelet analysis of potential fields, *Inverse Probl.,* 13, 165-178.

Moreau F., D. Gibert, M. Holschneider and G. Saracco, 1999. Identification of sources of potential fields with the continuous wavelet transform Basic theory, *J. Geophys. Res.*, 104(B3), 5003-5013.

N

Naudet, V., A. Revil, J.-Y. Bottero, and P. Bégassat, 2003. Relationship between self-potential (SP) signals and redox conditions in contaminated groundwater, *Geophys. Res. Lett.,* 30(21), 2091, doi : 10.1029/2003GL018096.

Naudet, V., A. Revil, E. Rizzo, J.-Y Bottero, and P. Begassat, 2004. Groundwater redox conditions and conductivity in a contaminant plume from geoelectric investigations, *Hydrology and Earth System Science*, 8 (1), 8-22.

Nishida, Y., N. Matsushima, A. Goto, Y. Nakayama, A. Oyamada, M. Utsugi and H. Oshima, 1996, Self-Potential Studies in Volcanic Areas (3) Miyake-jima, Esan and Usu, *J. Fac. Sci.*, Hokkaido Univ. Ser. 7, 10, 63.

Nitsan, U., 1977. Electromagnetic emission accompanying fracture of quartz-bearing rocks, *Geophys. Res., Lett.,* 4, 333-336.

Nourbehecht, B., 1963. Irreversible thermodynamic effects in inhomogeneous media and their applications in certain geoelectric problems, *Ph.D. thesis,* Mass. Inst. of Technol., Cambridge.

O

O'Brien R.W. and W.N. Rowlands, 1993. Measuring the surface conductance of kaolinitic particles, *J. Colloid Interface Sci.* 159 (2), 471–476.

Overbeek, J.T.G., 1952. Electrochemistry of the double layer. *Colloïd Science*, 1, 115-193.

P

Palciauskas, V. V., and P. A. Domenico, 1989. Fluid pressures in deforming porous rocks, *Water Resour. Res.*, 25, 203-213.

Parkinson, K. J., 1981. An improved method for measuring soil respiration in the field. *J. Appl. Ecol.,* 18, 221-228.

Patella, D., 1997a. Introduction to ground surface self-potential tomography. *Geophys. Prosp.,* 45, 653–681.

Patella, D., 1997b. Self-potential global tomography including topographic effects. *Geophys. Prosp.,* 45, 843–863.

Pengra, D., S. Xi Li, and P. Wong, 1999. Determination of rock properties by low-frequency AC electrokinetics, *J. Geophys. Res.*, 104(B12), 29485-29508.

Perrier, F., and P. Morat, 2000. Characterization of electrical daily variations induced by capillary flow in the non-saturated zone, *Pure Appl. Geophys.*, *157*, 785-810.

Perrier, F., G. Petiau, G. Clerc, V. Bogorodsky, E. Erkul, L. Jouniaux, D. Lesmes, J. Macnae, J, Meunier, D. Morgan, D. Nascimento, G. Oettinger, G. Schwartz, H. Toh, M. Valiant, K. Vozoff, and O. Yazici-Çakin, 1997. A one-year systematic study of electrodes for long period measurements of the electric field in geophysical environments, *J. Geomag. Geoelectr.*, 49, 1677-1696.

R

Revil, A. and Leroy, P., 2001. Hydroelectric coupling in a clayey material. *Geophysical Research Letters*, 28, 1643–1646.

Revil, A. and Leroy, P., 2004. Governing equations for ionic transport in porous shales, *J. Geophys. Res.*, 109(B03208), doi 10.1029/2003JB002755.

Revil, A., Finizola, A., Sortino, F., Ripepe, M., 2004. Geophysical investigations at Stromboli volcano, Italy: implications for ground water flow and paroxysmal activity, *Geophys. J. Int.* 157, 426–440.

Revil and N. Linde, 2006. Chemico-electromechanical coupling in microporous media, *J. Colloid Interface Sci.,* 302, 682–694.

Revil, A., P. Pezard, and P. Glover, 1999a. Streaming potential in porous media 1. Theory of the zeta potential, *J. Geophys. Res.*, 104 (B9), 20021-20031.

Revil, A., H. Schwaeger, L. Cathles III, and P. Manhardt, 1999b. Streaming potential in porous media 2. Theory and application to geothermal systems, J. Geophys. Res., 104(B9), 20033-20048.

Revil, A., and P.W.J. Glover, 1997. Theory of the ionic-surface conduction in porous media, *Phys. Review, B*, 55(3), 1,757-1,773.

Revil, A., P. Leroy, and K. Titov, 2005. Characterization of transport properties of argillaceous sediments. Application to the Callovo-Oxfordian Argillite, *J. Geophys. Res.*, 110, B06202.

Revil, A., D. Hermitte, E. Spangenberg, and J.J Cochmé, 2002b, Electrical properties of zeolitized volcaniclastic materials, *J. Geophys Res.*, 107(B8), 2168, doi:10.1029/2001JB000599.

Revil A., 1999. Ionic diffusivity, electrical conductivity, membrane and thermoelectric potentials in colloids and granular porous media: a unified model, *Journal of Colloid and Interface Science*, 212, 503-522.

Revil, A., L. Ehouarne, and E. Thyreault 2001. Tomography of self-potential anomalies of electrochemical nature, *Geophys. Res. Lett., 28(23),* 4363-4366.

Revil, A., G. Saracco, and P. Labazuy, 2003. The volcano-electric effect, *J. Geophys. Res.*, 108(B5), 2251.

Revil A., A. Finizola, S. Piscitelli, E. Rizzo, T. Ricci and A. Crespy, 2008. Inner structure of La Fossa di Vulcano (Vulcano Island, southern Tyrrhenian Sea, Italy) revealed by high-resolution electric resistivity tomography coupled with self-potential, temperature, and CO_2 diffuse degassing measurements, *J. Geophys. Res.*, 113, B07207.

Rizzo, E., B. Suski, A. Revil, S. Straface, and S. Troisi, 2004. Self-potential signals associated with pumping-tests experiments, *J. of Geophys. Res.,* 109, B10203, doi: 10.1029/2004JB003049.

S

Sailhac, P., A. Galdeano, D. Gibert, F. Moreau, and C. Delor, 2000. Identification of sources of potential fields with the continuous wavelet transform: Complex wavelets and applications to magnetic profiles in French Guiana. *J. Geophys. Res.*, 105, 19,455-19,475.

Sasai, Y., M. Uyeshima, J. Zlotnicki, H. Utada, T. Kagiyama, T. Hashimoto, Y. Takahashi, , 2002. Magnetic and electric field observations during the 2000 activity of Miyaki-jima volcano, Central Japan, *Earth Planet. Sci. Lett.*, 203, 769–777.

Sasai, Y., J. Zlotnicki, Y. Nishida, P. Yvetot, P. Morat, H. Murakami, Y. Tanaka, Y. Ishikawa, S. Koyama, and W. Sekiguchi, 1997. Electromagnetic Monitoring of Miyake-jima Volcano, Izu Bonin Arc, Japan: A Preliminary Report, *J. Geomag. Geoelectr.,* 49, 1293.

Sato, M. Mooney, H.M., 1960. The electrochemical mechanism of sulfide self potentials, *Geophysics* 35, 226-249.

Sill, W.R., 1983. Self-potential modeling from primary flows, *Geophysics* 48, 76-86

Somasundaran, P., R. D. Kulkarni, 1973. A New Streaming Potential Cell and Study of Temperature Effects Using It, *J. Coll. Interf. Sci.,* 45, 591-600.

Surkov, V. V., and V. A. Pilipenko, 1997. Magnetic effects due to earthquakes and underground explosions: a review, *Ann. Geofis.*, XL, 1-13.

Suski, B., E. Rizzo, and A. Revil, 2004. A sandbox experiment of self-potential signals associated with a pumping-test, *Vadose Zone J.*, *3*, 1193-1199.

Suski, B., A. Revil, K. Titov, P. Konosavsky, M. Voltz, C. Dagès, O. Huttel, 2006. Monitoring of an infiltration experiment using the self-potential method. *Water Resources Research*, 42, W08418, doi:10.1029/2005WR004840.

T

Teng, H., and T.S. Zhao, 2000. An extension of Darcy's law to non-Stokes flow in porous media, *Chemical Engineering Science*, 55, 2727-2735.

Thouret, J.-C., A. Finizola, M. Forani, A. Legeley-Padovani, J. Suni, M. Frechen, 2001. Geology of El Misti volcano near the city of Arequipa, Peru, *GSA. Bull.*, 113, 1593–1610.

W

Waxman, M.H., and L.J.M. Smits, 1968. Electrical conductivities in oil-bearing shaly sands, *Journal of the Society of Petroleum Engineering*, 8, 107–122.

Y

Yamashita, S., 1961. The Electromotive Force Generated within the Ore body by the Temperature Difference, *J. Min. Coll.*, Akita Univ., Ser., 1, 69.

Yoshida, S., and T. Ogawa, 2004. Electromagnetic emissions from dry and wet granite associated with acoustic emissions, *J. Geophys. Res., 109*, B09204, doi:10.1029/2004JB003092.

Yoshida, S., M. Uyeshima, and N. Nakatani, 1997. Electric potential changes associated with slip failure of granite: preseismic and coseismic signals, *J. Geophys. Res.*, 102, 14,883-14,897.

Yoshida, S., P. Manjgaladze, D. Zilpimiani, M. Ohnaka, and N. Nakatani, 1994. Electromagnetic emissions associated with frictional sliding of rock, in *Electromagnetic Phenomena Related to Earthquake Prediction*, edited by M. Hayakawa and Y. Fujinawa, 307-322, Terrapub, Tokyo.

Z

Zablocki, C.J., 1978. Streaming potentials resulting from the descent of meteoric water. A possible source mechanism for Kilauean self-potential anomalies, *Geothermal Ressources Council Transactions,* 2, 747-748.

Zablocki, C. J., 1976. Mapping Thermal Anomalies on an Active Volcano by the Self-Potential Method, Kilauea, Hawaii, *Proc. 2nd U.N. Symp. on the Development and Use of Geothermal Resources*, San Francisco, 2, 1299.

Zhang G.-B. and Aubert M., 2003. Quantitative interpretation of self-potential anomalies in hydrogeological exploration of volcanic areas: a new approach, *Near Surf. Geophys.*, 69–75.

Zlotnicki, J., Boubon, G., Viodé, J.P., Delarue, J.F., Mille, A., Bruère. F., 1998. Hydrothermal circulation beneath Mount Pelée inferred by self potential surveying. Structural and tectonic implications, *J. Volcanol. Geotherm. Res.,* 84, 73-91.

Zlotnicki, J., Nishida, Y., 2003. Review of morphological insights on self-potential anomalies on volcanoes. *Surv. Geophys.* 24, 291–338.

Zlotnicki, J., Feuillard, M., Hammouya, G., 1994a. Water circulations on La Soufrière volcano inferred by self-potential surveys (Guadeloupe, Lesser Antilles). Review of volcanic activity , *J. Geomag. Geoelectr.,* 46, 797-813.

Zlotnicki, J., J. L. Le Mouël, Y. Sasai, P. Yvetot, and M. H. Ardisson, 2001. Self-potential changes associated with the volcanic activity. Short-term signals associated with March, 9, 1998 Eruption, *Ann. Geofis.,* 44(2), 335.

Zlotnicki, J., S. Michel, C. Annen, 1994b. Anomalies de polarisation spontanée et systèmes convectifs sur le volcan du Piton de la Fournaise (Ile de la Réunion, France). *C.R. Acad. Sci. Paris,* t.318 - II, 1325-1331.

Liste des figures

CHAPITRE 1

Figure 1.1: Schéma de la distribution ionique de la double couche électrique……**9**
Figure 1.2 : Système de mesure de laboratoire du coefficient de couplage électrocinétique (1) Réservoirs de fluide poral R1 et R2. (2) Echantillon. (3) Capteurs de pression. (4) Electrodes non-polarisables permettant la mesure de la différence de potentiel et reliées à un voltmètre. (5) Mesures de la conductivité électrique de l'électrolyte. La pression est contrôlée par de l'azote qui n'a aucun effet sur le pH et la salinité de l'électrolyte……**17**
Figure 1.3 : Dispositif expérimental pour déterminer le coefficient de couplage électrocinétique. **a.** Dispositif expérimental montrant l'échantillon situé en bas d'un tube de plexiglass. La différence de potentiel électrique aux bornes de l'échantillon est mesurée avec un voltmètre Metrix MX-20 et de deux électrodes non polarisables $Ag/AgCl_2$. **b.** Représentation graphique de la réponse de potentiel électrique en fonction de différentes charges hydrauliques. Le coefficient de couplage correspond à la pente de la tendance linéaire……..**18**

CHAPITRE 2

Figure 2.1 : Variation des valeurs du coefficient de couplage électrocinétique en fonction de la perméabilité suivant la relation $Cc = 200 + 3{,}7 \times 10^{27}\, k^{1{,}5}$. D'après Moore and Glaser (2007)……**23**
Figure 2.2 : Influence de la température sur le potentiel ζ (silice, pH 7, KNO_3). Données expérimentales de Somasundaran and Kulkarni (1973) et Ishido et Mizutani (1981)…….**24**
Figure 2.3 : Relation typique entre pH et valeurs du potentiel ζ (selon Hase et al., 2003),……**26**

CHAPITRE 3

Figure 3.1. Vue d'ensemble du dispositif expérimental……**110**
Figure 3.2: Photographie des électrodes Ag/AgCl……**111**
Figure 3.3 : Appareil d'électro-encéphalographie d'après :www.biosemi.com……**112**
Figure 3.4 : Représentation 3D de la cuve. Un total de 32 électrodes est réparti à trois cm de la surface de la cuve. La cuve est remplie de sable bien calibré et saturé par une solution dont la conductivité électrique et la composition est de l'électrolyte. L'électrode de référence est figurée en rouge……..**113**
Figure 3.5 : (**a**) Vue de dessus de la surface de la cuve montrant la position des électrodes (Expériences 1 et 2). Les électrodes sont placées à une profondeur de 3 cm. L'étoile rouge représente la position de l'électrode de référence. L'électrode 32 est placée juste au-dessus de la sortie du capillaire. (**b**) Schéma représentant la position des électrodes sur un plan vertical (Expériences 3 et 4)……**114**

CHAPITRE 4

Figure 4.1 : Mécanismes de polarisation spontanée par couplage électrochimique dans la pyrite (d'après Sato et Monney, 1960)……**177**
Figure 4.2 : Schéma d'un potentiel thermoélectrique produit par un gradient de température (d'après Nourbehecht, 1963). Il est important de noter que la polarité de l'anomalie de potentiel spontané dépend du signe du coefficient de couplage électrothermique qui peut être positif ou négatif……**179**
Figure 4.3 : Exemple d'anomalie de potentiel spontané lié à l'effet topographique. D'après Zlotnicki et al. (1998)……**181**
Figure 4.4 : Anomalie de PS sur un profil Ouest-Est de la Montagne Pelée : valeurs de potentiel spontané et topographie vs la distance. D'après Zlotnicki et al., 1988)……..**183**
Figure 4.5 : Exemple d'anomalie en « W » sur Vulcano (Italie). L'anomalie positive de potentiel spontané est centrée sur le cratère (Revil et al., 2008)……**184**
Figure 4.6 : Position des deux profils. Le profil Fossetta, Rina grande, Schicciole (profil A) et le profil Fossetta, Rina Grande (profil B)……..**186**
Figure 4.7 : Exemple de représentation de la surface SPS (Aubert et Antagana 1996)…….**188**
Figure 4.8 : Modèle de la Double Couche Electrique proposé par Fournier (1989)……**189**
Figure 4.9 : Position des neuf profils traversant le cratère appelé la Fossa……..**215**

Liste des symboles

ε_0 : permittivité électrique du vide (ε_0= 8, 84.10^{-12})

ε_r : constante diélectrique relative

e : charge élémentaire de l'électron (1.602×10^{-19} C)

N : nombre d'Avogadro (6, 023 × 10^{23} mol.L^{-1})

I : force ionique de l'eau (mol m^3)

k_b: constante de Boltzman (k_b=1,3806 × 10^{-23} J.K^{-1})

Δp : différence de pression contrôlant le débit hydrique (en Pa)

$\Delta\varphi$: différence de potentiel électrique (en V)

σ_f: conductivité électrique du fluide(en S m^{-1})

ε_f : constante diélectrique du fluide (en F m^{-1})

ζ : potentiel zêta (en V)

η_f: viscosité dynamique du fluide (en Pa s)

C_{HS} : coefficient de couplage électrocinétique (mV/Pa)

$\mathbf{J}$: densité de courant (A m^{-2}),

σ : conductivité électrique du milieu (S m^{-1})

φ : potentiel électrique macroscopique (V)

ρ_f : masse volumique du fluide (kg m^{-3})

$\mathbf{g}$: accélération due à la gravité (m s^{-2})

$\mathbf{U}$: vitesse de Darcy (m s^{-1})

p : pression du fluide poral (Pa),

F : le facteur de formation

ϕ : porosité

h : charge hydraulique (m)

K : conductivité hydraulique (m s^{-1})

L : coefficient de couplage électrocinétique (m^2 V^{-1} s^{-1})

$\mathbf{J_s}$: densité de courant

σ : contrainte moyenne (en Pa)

ε : déformation volumique du milieu poreux

R, ξ, et H : coefficients de Biot

$\Im$: densité de courant volumique (en A m^{-3})

$\overline{Q_V}$: excès de charge effectif (en C m^{-3})

C : coefficient de couplage électrocinétique (mV/Pa)

C' : coefficient de couplage électrocinétique associé aux variations de hauteurs d'eau (en mV m^{-1})

T_0 : température de référence (25°C)

ξ_{app} : potentiel zêta apparent (V)

k_0 : perméabilité intrinsèque du milieu poreux (m^2)

Re : nombre de Reynolds

Du : nombre de Dukhin

ψ : ondelette analysante

$\varphi_0(x)$ *:* champ de potentiel mesuré

a : paramètre de dilatation

b : paramètre de position

$P_a(x)$: filtre de prolongement vers le haut

γ : ordre de l'ondelette analysante

Q : nombre de frontières de l'espace discrétisé

Γ_q : intensité de l'accumulation de charges électriques à l'interface q

$\boldsymbol{r}_q$: distance entre la charge q et le point d'observation P

I_x : fonction scannante

E : module du champ électrique $\boldsymbol{E}(\boldsymbol{r})$

C_v^p : coefficient de normalisation

C_v : coefficient de couplage électrocinétique apparent

$\vec{r}$: vecteur distance

$\vec{n}_s$: vecteur normal à la surface piézométrique

Théorie de l'électrofiltration : Nouveaux développements, validations expérimentales et applications à l'hydrogéologie et au volcanisme.

La méthode de polarisation spontanée (PS) consiste en la mesure du potentiel électrique naturellement présent dans le sol. Elle est la seule méthode sensible aux écoulements d'eau souterrains. Les principaux objectifs de cette thèse ont été de (1) déterminer l'influence de la conductivité de surface et du régime d'écoulement sur le coefficient de couplage électrocinétique (paramètre crucial pour l'interprétation des signaux de PS), (2) de montrer l'efficacité de la PS dans la mise en évidence des phénomènes hydromécaniques et (3) de caractériser les écoulements de fluides en contexte volcanique. Nous avons développé un modèle corrigeant le coefficient de couplage électrocinétique à la fois des effets de la conductivité de surface et du nombre de Reynolds. La validité de ce modèle a été confirmée grâce à des expériences réalisées sur billes de verre. Lors d'expériences en cuve, la méthode du potentiel spontané associée à un appareillage de haute sensibilité nous a permis de caractériser la signature électrique liée à des phénomènes hydromécaniques. Utilisées à partir des enregistrements de PS réalisés à la surface de la cuve les méthodes d'analyse en ondelettes et d'intercorrelation ont montré la nature dipolaire de la source électrique liée à de telles perturbations et ont permis sa localisation. Sur le Stromboli en Italie, nous avons utilisé une approximation au premier ordre de la relation entre l'épaisseur de la zone vadose et l'anomalie de PS afin de déterminer la profondeur d'un aquifère situé sur le flanc est du volcan.

Mots clés: **Potentiel Spontané, PS, électrofiltration, coefficient de couplage électrocinétique, aquifère.**

Theory of electrofiltration : New developments, experimental validations, hydrogeology and volcanism applications.

The self-potential method consists on the passive measurement of the electrical potential distribution at the ground surface of the Earth. This is the only method thqt is sensitive to the flow of the ground water. The main objectives of this work were (1) to determine the influence of the surface conductivity and the flow regime upon the streaming coupling coefficient (a critical parameter to interpret SP signals), (2) to show the efficiency of the SP in the localization of hydromechanical disturbances, (3) to characterize ground water flow and aquifers in a volcanic context. For indifferent electrolytes, like sodium chloride, we derived two simple scaling laws for the dependence of the streaming potential coupling coefficient with the surface conductivity and Reynolds number. The validity of these laws was checked successfully against a new set of experimental data using glass bead. In sandbox experiments, the self-potential method associated with a high sensitivity equipment has enabled us to characterize the electrostatic signature of hydromechanical disturbances. The wavelet analysis and the cross-correlation method showed the dipolar nature of the electrical source linked to such disturbances and can be used to locate the source. On Stromboli in Italy, we used a relationship between the thickness of the vadose zone and the self-potential anomaly to determine the shape of the water table along the flank of the volcano.

Key words: **Self-potential, SP, electrofiltration, streaming potential coupling coefficient, aquifer.**

Discipline : **Géosciences**

Adresse du centre de recherche:
CEREGE-CNRS-Université Aix-Marseille III (Paul Cézanne), Europôle de l'Arbois, BP 80, 13545 Aix en Provence cedex 04